X-RAY EMISSION
FROM COMPACT OBJECTS

Askar Ibragimov

Division of Astronomy
Department of Physics
University of Oulu
Finland

Abstract

The thesis is devoted to the observational studies of the black-hole binary Cyg X-1 and the accretion-powered millisecond pulsar SAX J1808.4–3658. Most of the work has been done using data from the *Rossi X-ray Timing Explorer (RXTE)* satellite, that provides an excellent timing resolution and large photon statistics owing to the unprecedented collection area of its main detector, Proportional Counting Array.

Broad-band spectral analysis is a direct way to detect and separate various spectral components present in the X-ray band. It helps to reveal the underlying physics of a compact object. In our work devoted to the broad-band spectroscopy of Cyg X-1, we used 42 spectra in the energy range 3–1000 keV, when the source was simultaneously observed by the *RXTE* and *CGRO* satellites. We have studied the observed variability patterns and spectral parameter correlations and discussed the presence and origin of the spectral components. We have also compared the observed correlations to the predictions of the the dynamic corona (Malzac, Beloborodov, & Poutanen, 2001) and the truncated disc (e.g., Zdziarski et al. 2002) theoretical models.

We have investigated the physics behind the 152-day superorbital long-term variability seen in Cyg X-1. Decade-long daily data from *RXTE*/All Sky Monitor allowed us to obtain statistically good variability profiles. The origin of this variability is believed to be due to the accretion disc precession. Taking into account several models for the emission, we have constrained some system parameters; in particular, we obtained the disc precession angle of $10^{\rm o} - 20^{\rm o}$. We demonstrated that the thermal Comptonization model explains very well the observed decrease from 1 to 300 keV of the variability amplitude. In a subsequent paper we have discovered that the orbital variability properties of Cyg X-1 are connected to its superorbital phase. This effect can be explained by a combination of the accretion disc precession and absorption of the X-rays by an accretion bulge located near the disc edge.

We conducted a comprehensive study of spectral and temporal characteristics of the accretion-powered millisecond pulsar SAX J1808.4–3658. Our main finding is that the variety of observational data support the physical picture where the accretion disc inner edge recedes from the neutron star as the outburst progresses and flux decays. In order to explain the complex pulse profile evolution, we suggest that at a certain moment the secondary emitting spot becomes visible to an observer, and this effect, together with other consequences due to changes in the accretion flow geometry, causes the observed complex pulse evolution. In the following theoretical paper, we perform modelling of the pulse profiles that includes the effect of partial screening of the antipodal emitting

spot, and demonstrate that there is an agreement between the theoretical pulse shapes and the observed ones.

These works discuss several new observational facts and are important for understanding the physics and accretion disc geometry in accreting black holes and neutron stars.

Acknowledgments

It's been a while since I visited the "Otdel 52" in IKI, Moscow, and asked Prof. Rashid Sunyaev if I could do some scientific task related to the High Energy Astrophysics. He then directed me to Marat Gilfanov, with whom we started the work now known as "Paper I" in the current PhD thesis. That work also led me to the University of Oulu where I was able to complete this and other works with guidance and help of my supervisor, Juri Poutanen. Shortly after, while presenting the work on a Finnish Lapland conference I met Andrzej Zdziarski, who also became a collaborator and offered me a great deal of support throughout all of my PhD. I also should say, this thesis would never happen without help of Valery Suleimanov, who started to work with me back then during my time as a student in Kazan University and, effectively, led me to the topic of High Energy Astrophysics. I am deeply grateful to all of you for being patient with me, sharing your knowledge and providing such a great and reliable support, which is far beyond any formal limits.

I am also grateful to colleagues who helped me with various aspects of my research and been more than just colleagues but reliable, good friends. I wish to thank Indrek Vurm, Jari Kajava, Chris Done, Marek Gierliński, Jacob Hartman, Magnus Axelsson and Linnea Hjalmarsdotter; also, all the staff of Oulun yliopisto, IKI Space Research Institute in Moscow, CAMK Warszawa, Durham University and ISSI Bern for the help and hospitality during my visits. A special thanks goes to the people who are involved in this PhD defense – my evaluators Didier Barret and Diana Hannikainen and my opponent Rudy Wijnands, who also helped me out in the past with few questions related to my work.

I am also deeply grateful to my family, back in Kazan, and my very close friends from Oulu and Russia, for supporting me in my life and rooting for me in my work. Your presence and support is invaluable to me and I am always indebted to you.

List of original papers

Paper I: Ibragimov A., Poutanen J., Gilfanov M., Zdziarski A. A., Shrader C. R.: Broad-band spectra of Cygnus X-1 and correlations between spectral characteristics. 2005, MNRAS, 362, 1435

Paper II: Ibragimov A., Zdziarski A. A., Poutanen J.: Superorbital variability of X-ray and radio emission of Cyg X-1 — I. Emission anisotropy of precessing sources. 2007, MNRAS, 381, 723

Paper III: Poutanen J., Zdziarski A. A., Ibragimov A.: Superorbital variability of X-ray and radio emission of Cyg X-1 — II. Dependence of the orbital modulation and spectral hardness on the superorbital phase. 2008, MNRAS, 389, 1427

Paper IV: Ibragimov A., Poutanen J.: Accreting millisecond pulsar SAX J1808.4-3658 during its 2002 outburst: evidence for a receding disc. Accepted to MNRAS (astro-ph/0901.0073).

Paper V: Poutanen J., Ibragimov A., Annala M.: On the nature of pulse profile variations and timing noise in accreting X-ray millisecond pulsars. Submitted to ApJ Letters.

Contents

Chapter 1

Accreting binaries

About one third of all the stars in our Galaxy are, in fact, members of binary systems – when two stars are gravitationally bound together and rotating around a single centre of mass. Under some circumstances, matter can be transferred from one star to the other due to the influence of gravity. When the accretor is a neutron star or a black hole, the accreting matter in the vicinity of the compact object heats up to $10^7 - 10^9$ K and emits in the X-ray band. Such systems are called X-ray binaries. Nowadays, about 300 X-ray binaries are known in our Galaxy (Liu, van Paradijs, & van den Heuvel, 2007).

There are two distinct observational classes, low- and high-mass X-ray binaries (LMXB and HMXB, respectively). LMXBs have a companion of spectral class A – M and mass lower than about $2M_\odot$. The mass transfer in the systems occurs via Roche lobe overflow. Most LMXBs are transients, i.e. these are radiating non-permanently, experiencing periods of quiescence, which range from a few days to more than ten years. By contrast, HMXBs are much more massive systems, with companions such as Be-stars ($M > 5M_\odot$) or OB supergiants ($M > 15M_\odot$). In these objects the mass transfer occurs because the compact object crosses gaseous disc around Be star or because of the strong stellar wind generated by the giant companion (with the mass loss reaching up to $10^{-5}M_\odot$/year). All known HMXBs are persistent sources. The "intermediate mass" X-ray binaries are rarely observed, as they do not supply enough stellar wind and their evolution makes the Roche lobe transfer phase very short. Her X-1 and Cyg X-2 are the few known examples.

Accretion acts as a power source for the X-ray binary systems: if all the kinetic energy of the gas converted to radiation, the released power will be of the amount

$$L \approx \frac{GM\dot{M}}{R},\tag{1.1}$$

where M and R are the mass and the radius of the central object and $\dot{M}$ is the accretion rate. Therefore, the energy release depends strongly on the ratio M/R, making it most effective in compact objects. The accretion efficiency (in other words, the released fraction of rest mass energy) for a neutron star is about 0.15, while nuclear burning of hydrogen has efficiency of only about 0.007.

Figure 1.1. An artistic view of Cyg X-1 high-mass black hole binary. Image from http://www.spacetelescope.org/.

The Eddington luminosity is the limiting luminosity corresponding to the balance between the gravitational force and radiation pressure force. In the case of spherical accretion of pure hydrogen it is

$$L_{\text{E}} = \frac{4\pi G M m_{\text{p}} c}{\sigma_{\text{T}}} \simeq 1.3 \times 10^{38} \left(\frac{M}{M_\odot}\right) \text{erg s}^{-1}, \tag{1.2}$$

where m_{p} is the proton mass and σ_{T} is the Thomson cross section for photon scattering off free electrons. The ratio L/L_{E} is often used as a "scaling factor" to characterize accretion properties.

Since the accreting matter carries some angular momentum, it should be carried away to allow matter to accrete. The matter does not experience free-fall but rather forms an *accretion disc*, where angular momentum transfers outwards while the matter spirals down towards the compact object. The exact properties of accretion discs are the subject of intensive research since the 1960s.

1.1   Emission of a flow: accretion solutions

The emission of the accretion disc is one of the observed components in X-ray binaries and in order to compute theoretical spectra it is necessary to have a model of

accretion flow. In the canonical accretion disc model by Shakura & Sunyaev (1973), the assumption is that viscous stress converts the gravitational potential energy into heat and the heat, in turn, is radiated locally. The theory uses the so-called α-prescription, where all the physics of viscous stress is parameterized via the phenomenological scale coefficient α, which relates the total pressure to the shear stress. This solution produces a geometrically thin and optically thick disc. The model predicts the temperature profile across the disc to be $T(r) \sim r^{-3/4}$ and one can then obtain a standard "multicolour blackbody disc spectrum" by integrating the local blackbody spectra along the radius. A modification to this approach, which takes into account the pseudo-Newtonian potential (Paczyński & Wiita, 1980), is presented by Gierliński et al. (1999). Although the spectral model fits well the "disc" component in the observed spectra, its parameters should not be taken literally as the corrections for relativistic effects must be considered (Li et al., 2005; Davis et al., 2005).

Recently, magneto-rotational instability (MRI) has been identified as the physical process that produces the stress (Balbus & Hawley, 1991; Balbus, 2005). The Shakura-Sunyaev prescription is subject to the instability due to the ionization of hydrogen (at low luminosities, $L/L_E \sim 0.001$ for an orbital period of ~ 1 hour, see Lasota 2001). Despite many works that claim that the Shakura-Sunyaev disc is subject to radiation instability at high luminosities ($L/L_E \sim 0.06$, e.g. Lightman & Eardley 1974; Shakura & Sunyaev 1976; Piran 1978), a recent study by Hirose, Krolik, & Blaes (2009) shows that in fact radiation-dominated discs may be thermally stable. The instability would affect the source lightcurve and would be obvious for an observer, while in fact the discs of accreting systems remain mostly stable at least till $L/L_E \sim 0.7$.

The energy can thermalize locally (to meet the Shakura-Sunyaev assumption), but this is not always the case. If the flow is hot enough, then it can become optically thin to electron-photon collisions. These conditions then result in the accreting flow configuration that differs considerably from the Shakura-Sunyaev regime. Gravitational energy is carried mostly by protons, while electrons can take only a small part of it via Coloumb interactions, but they radiate more efficiently; this would lead to incomplete thermalization of protons with electrons and therefore to a two-temperature flow. Due to low optical depth, the shape of the emitted spectrum will be due to Comptonization, bremsstrahlung and cyclo-synchrotron emission. Shapiro, Lightman, & Eardley (1976) computed two-temperature flows without advection (the effect of carrying part of the energy away together with the flow); however, advection of gravitational energy by protons is quite important, and this is accounted for in the Advection-Dominated Accretion Flow models by Ichimaru (1977); Narayan & Yi (1995); Esin, McClintock, & Narayan (1997). In these papers, advection is treated as a cooling process only, but if the advection fraction becomes negative, the process can heat up matter, producing a Luminous Hot Accretion Flow (Yuan, 2001, 2003; Yuan & Zdziarski, 2004). The other effects that can affect the solution are: wind from the disc (Narayan & Yi, 1995; Blandford & Begelman, 1999), convection (Blandford & Begelman, 1999; Abramowicz & Igumenshchev, 2001), the existence of magnetic fields (Meier, 2005) and a jet (Falcke, Körding, & Markoff, 2004). These solutions all result in hot, quasi-spherical flows. It is believed that in such regions Comptonization of soft "seed" photons takes place,

producing the observed Compton continuum.

1.2 Comptonization

Compton scattering is the scattering of photons against free (or, if the photons are very energetic, bound) electrons. During scattering, photons and electrons can exchange energies. The commonly known Thomson scattering is the simplified case when energy exchange is negligible. The detailed description of all possible scattering regimes is beyond the scope of this introduction, but we are especially interested in the case when relatively cool seed photons encounter a hot electron cloud. These seed photons can be supplied by the accretion disc or, if a magnetic field is available, produced as synchrotron emission by the same electrons that later participate in Compton scattering (such a process is called synchrotron-self-Compton emission and is used, in particular, to explain spectra of jets from blazars; it can be also of importance to accreting binaries).
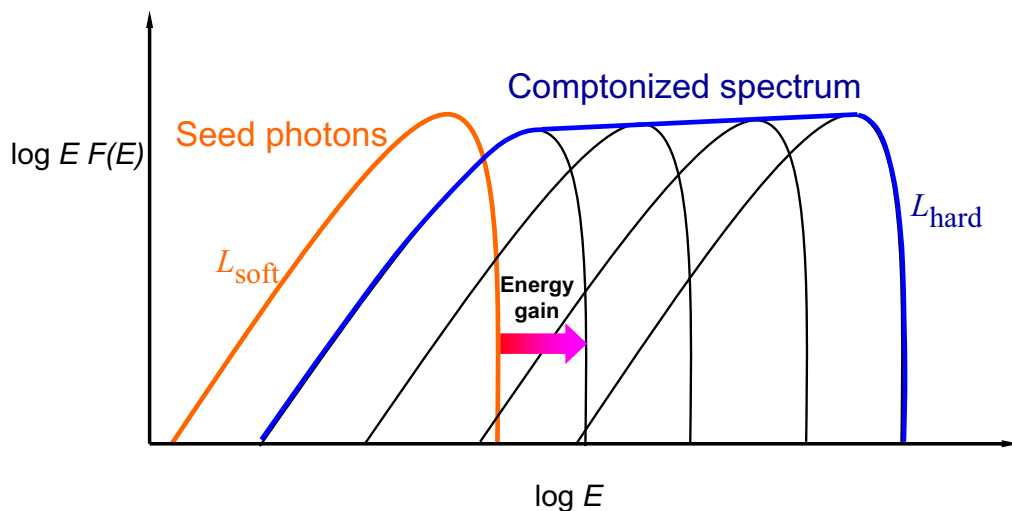
Figure 1.2. The schematic illustration of the Comptonization process. Figure courtesy by Marek Gierliński.

A single scattering of a photon against an electron in the case of a Maxwellian electron distribution will result in the photon's average relative energy gain of

$$\left\langle \frac{\Delta E}{E} \right\rangle = 4\frac{kT}{m_e c^2}, \tag{1.3}$$

where E is the photon energy, ΔE is the change of photon energy, k is the Boltzmann constant, T is the temperature of the electron cloud and m_e is the electron rest mass. "Comptonization" is the term for the effect of multiple scattering of low energy photons

by hot electrons, during which the photons can be up-scattered to very high energies (as sketched in Fig. 1.2). Such a process is governed by the Kompaneets parameter $y = 4\frac{kT}{m_e c^2}\max(\tau_\text{T}, \tau_\text{T}^2)$, where τ_T is the Thomson optical depth of the electron cloud. Based on the value of the parameter, we can distinguish:

- *Very unsaturated Comptonization*, $y \ll 1$. Just a few scatterings are possible, resulting in a very steep powerlaw with the photon energy index $\alpha \gg 1$ (where $\alpha = -d\ln F_E/d\ln E$ and F_E is the flux). Such a regime is achieved, for example, when the cosmic microwave background radiation is scattered on the hot electron gas in galaxy clusters (Sunyaev-Zeldovich effect).

- *Unsaturated Comptonization*, $y \sim 1$ and $\alpha \sim 1-2$. This regime describes the hard X-ray spectra of galactic black holes, neutron stars and active galactic nuclei. If the electron cloud has a Maxwellian velocity distribution, then the photon spectrum experiences a cutoff around the energy of kT. If the velocity distribution is non-thermal (commonly, a powerlaw), then no cutoff is present in power-law continuum (as e.g. in the soft state of Cyg X-1, see Fig. 1.3). In reality, some hybrid combinations of thermal and non-thermal Comptonization are observed (Coppi, 1999).

- *Saturated Comptonization*, $y \gg 1$, when all photons scatter for a very long time and end up in a Bose-Einstein distribution at around $E = kT$ preceded by a flat spectrum with $\alpha \sim 0$. This regime is possible in high accretion rate systems.

In our Papers I and IV, we model the numerous spectra of the Cyg X-1 black hole binary and accretion millisecond X-ray pulsar SAX J1808.4–3658 using the Comptonization model COMPPS (Poutanen & Svensson, 1996). The model was also used in Paper II to obtain energy-dependent emissivity patterns of a Comptonizing slab.

1.3   Compton reflection and iron line

The hard X-rays, produced by Comptonization process in a region around the central compact object, can irradiate the accretion disc, producing the Compton reflection component (see Fig. 1.3). Magdziarz & Zdziarski (1995) derived approximations to Green's functions for the reflection of Xγ-rays by cold electrons.

This irradiation also gives rise to a fluorescent iron 6.4 keV line and iron edge at 7 keV (and can also lead to the ionization of matter, however present observations from Cyg X-1 are consistent with neutral reflecting medium). The iron line (as well as reflection) is produced in the strong gravity field and in the disc material orbiting rapidly the central compact object, and thus becomes relativistically "smeared" by a combination of Doppler shifts, gravitational redshift and light bending (e.g. Reynolds & Nowak 2003). Even though analysis of the iron line is complex, its exact shape can give us important information about the accretion flow in the vicinity of the compact object, such as the object's spin and the actual inner disc radius. The width of the iron line and the amplitude of the reflection are usually well correlated, indicating their origin

from the same media (e.g. Ibragimov et al. 2005). In recent works by Beckwith & Done (2004); Dovčiak, Karas, & Yaqoob (2004); Li et al. (2005), iron line and continuum modelling in the relativistic regime was considered.
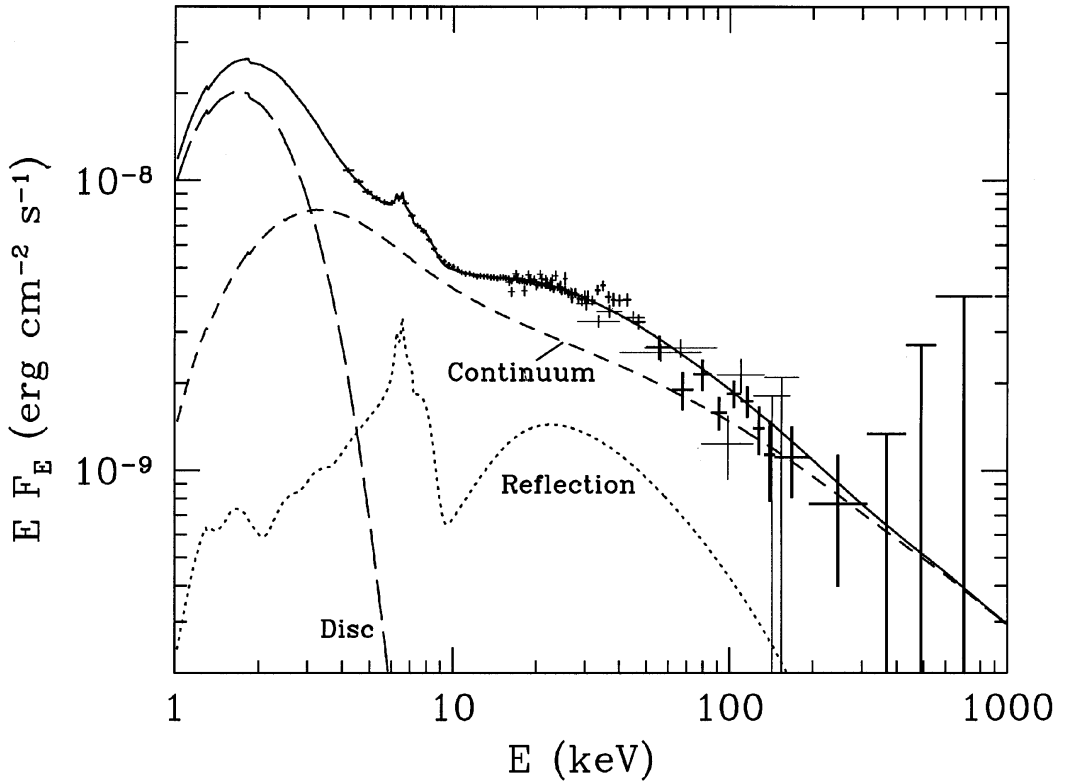

Figure 1.3. The simultaneous RXTE and CGRO/OSSE observation of Cyg X-1 in the soft state on 1996 June 17. The solid line show a best-fit model. The emission components are marked in the figure. Figure from Gierliński et al. (1999).

Chapter 2

Black hole binaries

In 1939, Oppenheimer & Snyder (1939) made the first precise calculations describing the birth of a black hole (hereafter BH). Optical observations of Cyg X-1 (Bolton, 1972; Webster & Murdin, 1972) brought to light the first strong observational evidence of this class of object. Today, about 20 objects are known to contain a compact objects that is too massive to be a neutron star ($M > 3M_\odot$). Population estimates result in $10^8 - 10^9$ black holes in our Galaxy (Brown & Bethe, 1994; Timmes, Woosley, & Weaver, 1996). Stellar-mass black holes are one of the endpoints of stellar evolution and are responsible for the heavy element abundance in the Universe; observations of BHs can constrain theories about their formation and the evolution of binary systems; some BHs in binary systems might be related to "hypernovae" believed to power gamma-ray bursts. Studies of fast quasi-periodic oscillations and high-energy spectra could help in understanding e.g. the accretion physics and jet formation in the vicinity of the BHs.

It is usually quoted, that a "black hole has no hair" (Ruffini & Wheeler, 1971), i.e. it possesses only mass and spin. These parameters, along with geometrical constraints, should completely determine the accretion flow that we observe through its radiation. Mass acts like a "scale factor", while spin controls the geometry. Depending on the spin, the innermost stable circular orbit (ISCO) around BH ranges from $6R_g$ for Schwarzschild (non-rotating) BH to $1R_g$ for a maximally-rotating Kerr BH (here, $R_g = GM/c^2$ is the gravitational radius and $R_S = 2R_g$ is the Schwarzschild radius).

2.1 Spectral states

The most dramatic phenomenon observed in accreting systems is the existence of different spectral states, that switch from one to another every few years (see Fig. 2.1). While Cyg X-1 mainly shows the so-called "hard" and "soft" states with some intermediate states (nomenclature of the states is not quite robust across the literature, see e.g. Zdziarski & Gierliński 2004 and Remillard & McClintock 2006 for various state definitions), several other states are observed in other BH binaries. These states differ considerably in almost every observational characteristic.

- *Hard state.* The hard state spectrum has its energy peak at about 100 keV
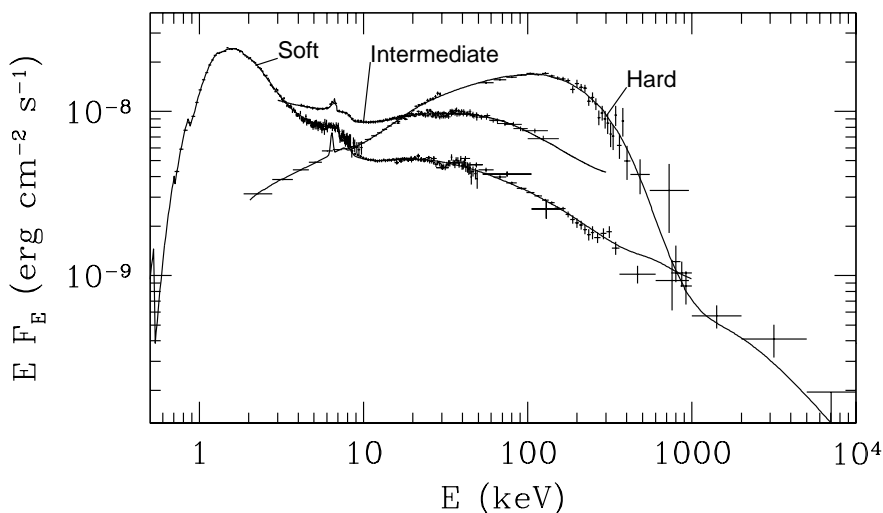
Figure 2.1. Spectral states of Cyg X-1 (Gierliński et al., 1999).

and is believed to originate from thermal Comptonization in a hot electron cloud (Shapiro, Lightman, & Eardley, 1976; Ichimaru, 1977; Sunyaev & Truemper, 1979; Sunyaev & Titarchuk, 1980; Poutanen, 1998; Zdziarski & Gierliński, 2004). The strong cutoff around 100 keV is observed (which is expected from a thermal electron cloud), but some weak MeV tail also exists, suggesting the presence of non-thermal particles (McConnell et al., 1994; Ling et al., 1997). This state is accompanied by a steady radio jet (Fender, 2001).

- *Soft state.* This state consists of a prominent ∼ 1 keV black-body and a power-law-like tail (see Figs. 1.3 and 2.1). The spectral component reminiscent of a black-body is associated with the optically thick accretion disc (Shakura & Sunyaev, 1973) with a temperature of about 0.4–1.5 keV. Above that, a powerlaw tail exists that shows no cutoff till at least 10 MeV (McConnell et al., 2002), which can be explained by the emission of purely non-thermal plasma (Poutanen & Coppi, 1998; Gierliński et al., 1999; Coppi, 1999; Zdziarski et al., 2001; Zdziarski & Gierliński, 2004). No QPOs are observed in this state. This state is sometimes also referred to as *thermal dominant*.

- *Very high state.* The state observed during the brightest phases of many BH binaries; characterized by the very bright disc emission that is similar to the soft state, but also with a prominent high-energy tail that is steeper than in hard or soft state (photon index above 2.4, e.g., Miyamoto et al. 1991, 1993; Done, Wardziński, & Gierliński 2004; Abe et al. 2005).

- *Ultrasoft state.* Similar to the soft state with a very small amount of high-energy emission.

- *Intermediate state.* A state which takes place between the soft and hard states, but does not have the luminosity of the very high state (Ebisawa et al., 1994; Belloni et al., 1996). Sometimes, due to similarity of properties, also referred to as the very high state.

Theoretical grounds for the explanation of the observed spectra were addressed in accretion disc models (see reviews by Beloborodov 1999; Done, Gierliński, & Kubota 2007) and in the works devoted to the computation of the Comptonized emission in various geometries (Poutanen & Svensson, 1996; Coppi, 1999). In the recent work of Poutanen & Vurm (2009) the authors model a spherical inner accretion flow, similar to advection-dominated (Esin, McClintock, & Narayan, 1997) or luminous hot accretion flows (Yuan, 2003; Yuan & Zdziarski, 2004). The model can explain the hard state as being produced by the synchrotron-self-Compton mechanism, without any input of emission from the accretion disc and with a low magnetic field. Explanation of the soft state spectra requires input from a disc and presense of a magnetically-dominated emission region. The model provides a good match with the observed Cyg X-1 soft and hard state spectra. Difference in the required amount of seed photons from the disc suggests similarities to the "truncated disc" model, as explained below.

2.2 "Truncated disc" model framework

From the theoretical point of view, we have two stable accretion flows: a Shakura-Sunyaev disc and a "hot inner flow" (see Section 1.1). The combination of these two solutions, likely switching from one to another at some "truncation radius", is at the core of the "truncated disc" model, aimed to explain the origin of spectral states. The soft and hard state configurations are sketched in detail in Fig. 2.2. In the hard state, the disc turns into a hot inner flow (probably penetrating it to some extent) at some radius, and the flow manifests itself by creating the thermal Comptonization continuum, while the disc provides some reflection and seed photons for the Comptonization. In the soft state, the hot flow is greatly suppressed and the disc extends almost towards the ISCO, and therefore we mainly see emission from the disc itself. Comptonization however probably takes place in active regions (flares) above the disc or some other form of the hot, optically thin medium (Done, Gierliński, & Kubota, 2007). These regions are likely to contain non-thermal electrons which lead to nonthermal Comptonization continuum. In Fig. 2.3 we illustrate a variety of "additional" states along with proposed configurations of the truncated disc.

Our Paper I discusses the application of this framework to the observational data of Cyg X-1. While the observed correlation between the spectral slope and the reflection scaling factor (see Fig. 11 in Paper I) is not well reproduced by the truncated disc model, a clear anticorrelation between the Quasi-Periodic Oscillation frequency (probably related to the truncation radius) and coronal compactness follows the relation expected from the truncation disc configuration (Fig. 10 in Paper I).

Soft X-rays
from disc

Comptonized
hard X-rays

Compton reflected X-rays

Cool outer disc

Hot inner flow

Black hole

Radio jet

Soft X-rays
from disc

Comptonized
hard X-rays

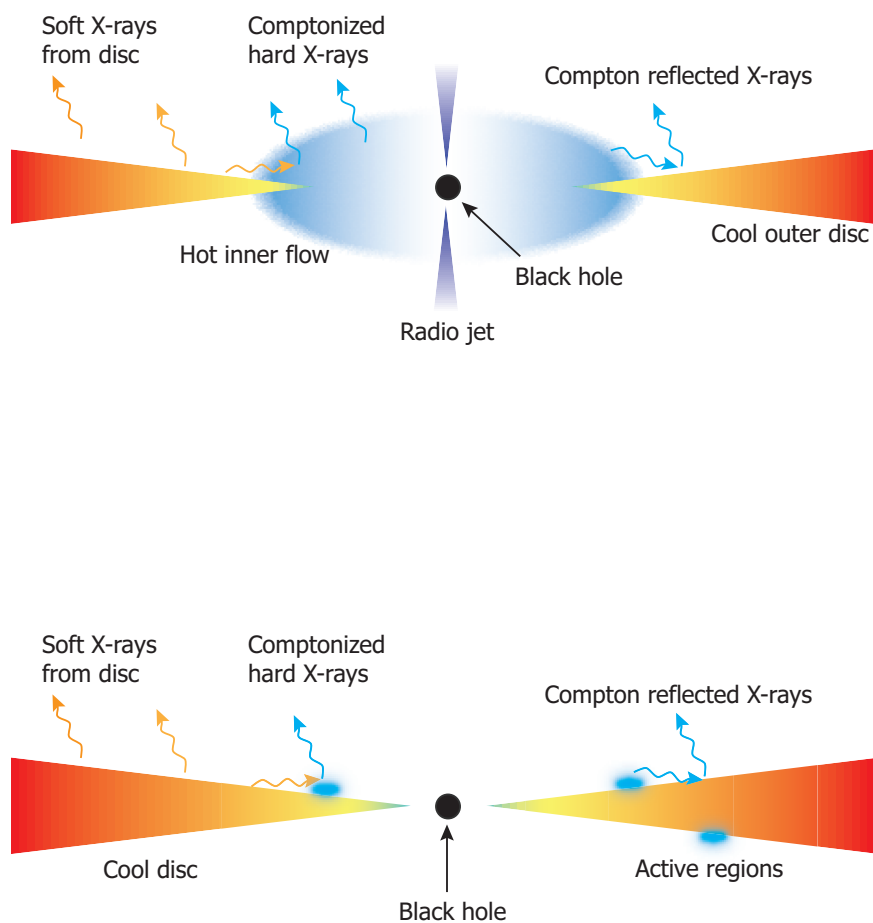Compton reflected X-rays

Cool disc

Active regions

Black hole

Figure 2.2. The geometries of hard and soft states according to the "truncated disc" model. Adapted from Zdziarski et al. (2002).
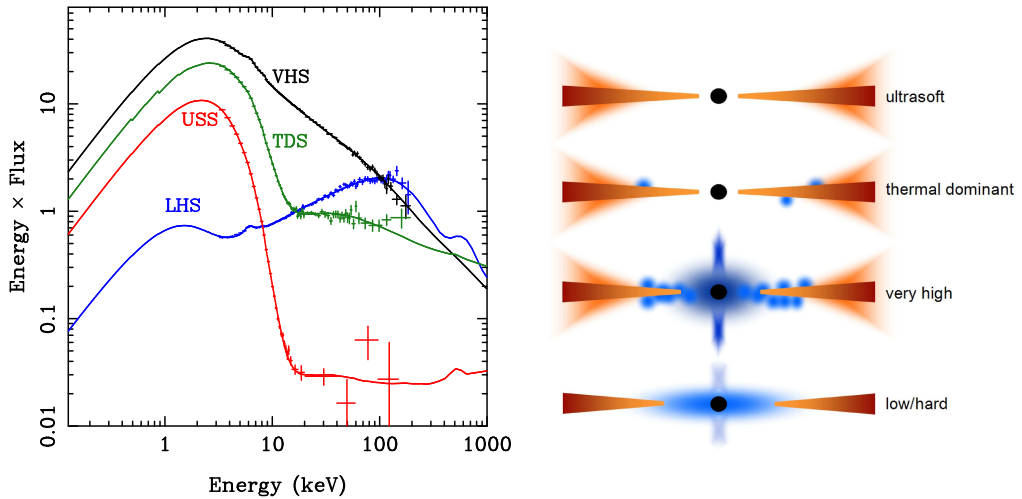
Figure 2.3. A selection of states taken from the 2005 outburst of GRO J1655−40. Abbreviations VHS, TDS, USS and LHS refer to the very high, soft (thermal dominant), soft with extremely weak tail (ultrasoft) and hard states. The right hand panel shows the proposed accretion geometry configurations of the "truncated disc" model with sketched accretion disc, hot inner flow, its associated jet and active regions above the disc. Figure from Done, Gierliński, & Kubota (2007).

2.3   Variability

Cyg X-1 displays variability on all timescales, from milliseconds to years. The main large-scale variability phenomena are state transitions, large outbursts, orbital modulation (due to absorption in the companion wind at certain orbital phase) and superorbital modulation. X-ray outbursts in low-mass X-ray BH binaries lasting between ∼20 days and many months are explained by an instability arising in the accretion disc. When the accretion rate from the donor star can not maintain continuous viscous flow, matter builds up in the outer disc and when the critical density is reached, the outburst is triggered. Such an explanation predicts recurrent outbursts with period of $1 − 20$ years, and indeed, half of known BH binaries show such a behaviour (but this model, described in Lasota 2001, does not explain outbursts that happen at longer or shorter timescales). In day-to-day variability patterns, Cyg X-1 shows two clear "modes": spectral normalization change and "pivoting" around 10 keV (Zdziarski et al. 2002 and Paper I).

The power density spectra (PDS, usual frequencies for *RXTE*/PCA are in the range of 0.002 – 4096 Hz) vary greatly with the spectral state. These are usually decomposed as a sum of Lorentzians plus a powerlaw component in the hard state and just a powerlaw in the soft state. These observed Lorentzians are commonly referred to as Quasi-Periodic Oscillations and studied extensively (e.g., Pottschmidt et al. 2003; Gleissner et al. 2004a,b; Axelsson, Borgonovo, & Larsson 2005, 2006; Axelsson et al.

2008; Wilms et al. 2006). The similarities between black hole and neutron star PDS suggest that most of these features are physically connected not to the nature of the central object but instead to the accretion flow (although a difference would follow from the presence of a solid surface in the case of neutron stars). Some particular radii are picked up by variability, and when a source makes a transition from the hard to the soft state, the frequencies of QPOs increase. This fact strongly supports the "truncated disc" model (that was initially developed for explaining spectral, not temporal, changes).

In Cyg X-1 the long-term variability phenomena include orbital (e.g., Brocksopp et al. 1999b) and superorbital variations (see Brocksopp et al. 1999a; Pooley et al. 1999; Özdemir & Demircan 2001; Benlloch et al. 2001, 2004; Karitskaya et al. 2001; Lachowicz et al. 2006). Orbital variability of 5.6 days occurs due to the obscuration of the central source of X-rays by the focused wind from the companion, the OB supergiant HD 226868. The bound-free absorption in the wind causes strong modulation in X-rays, while the free-free absorption modulates the radio emission. The superorbital variability observed at almost all wavelengths has a period of ∼150 days and is possibly caused by the disc precession, the properties of which we investigate in detail in our papers II and III.

Chapter 3

Accretion-powered millisecond pulsars

3.1 Pulsating emission from neutron stars

Neutron stars (hereafter NS) are one of the most fascinating bodies in the universe. They contain over a solar mass of matter within ~ 10 km radius. The density of a NS is about 10^{15} g/cm^3. Such a high density can not be reproduced artificially, therefore NS could serve as a laboratory to study condensed matter. Also, these are excellent subjects to test the effects of General Relativity. In 1967, Bell and Hewish discovered radio pulsars, and Gold (1968) identified these as rotating neutron stars. The famous Crab pulsar was discovered in the remnants of the Crab supernova from 1054, confirming the scenario of NS origin from a supernova explosion. Reliable observational determinations of NS masses in radio pulsars give a quite narrow range of 1.35 ± 0.04 $M_\odot$ (Thorsett & Chakrabarty, 1999), and 1–2 $M_\odot$ is obtained from several other binary systems containing a NS (Page & Reddy, 2006). Stellar evolution theory predicts proto-neutron stars with masses of $1.2-1.8 M_\odot$. The expected population of NS in our Galaxy is about 10^8. In Fig. 3.1 we present a sketch of the NS structure (for an overview of recent studies on NS theory see Heiselberg & Pandharipande 2000; Page & Reddy 2006), where the inner core region is marked by a question mark, as there is no consensus of its composition.

It is very difficult to observe very dim, non-accreting NS, though a few objects of this kind are known ("The Magnificent Seven", e.g., Haberl 2007). Rotating NS generate pulsed emission, hence the name *pulsars*. *Radio pulsars* are objects where the magnetic and rotational angles are misaligned, so they emit radiation in the form of radio waves. In general, their periods are around 1 s (see Fig. 3.2). From the frequency derivative of the observed pulse periods it is known that their magnetic fields are about 10^{12} G. A distinct class are *millisecond pulsars* with periods below 10 ms and very low period derivatives suggesting a magnetic field strength of about 10^8–10^{10} G. In the 1970s, it was discovered that *X-ray pulsars* exist. These are mostly NS accreting matter from high-mass ($M > 10 M_\odot$) companions. The accretion flow follows the magnetic field lines that
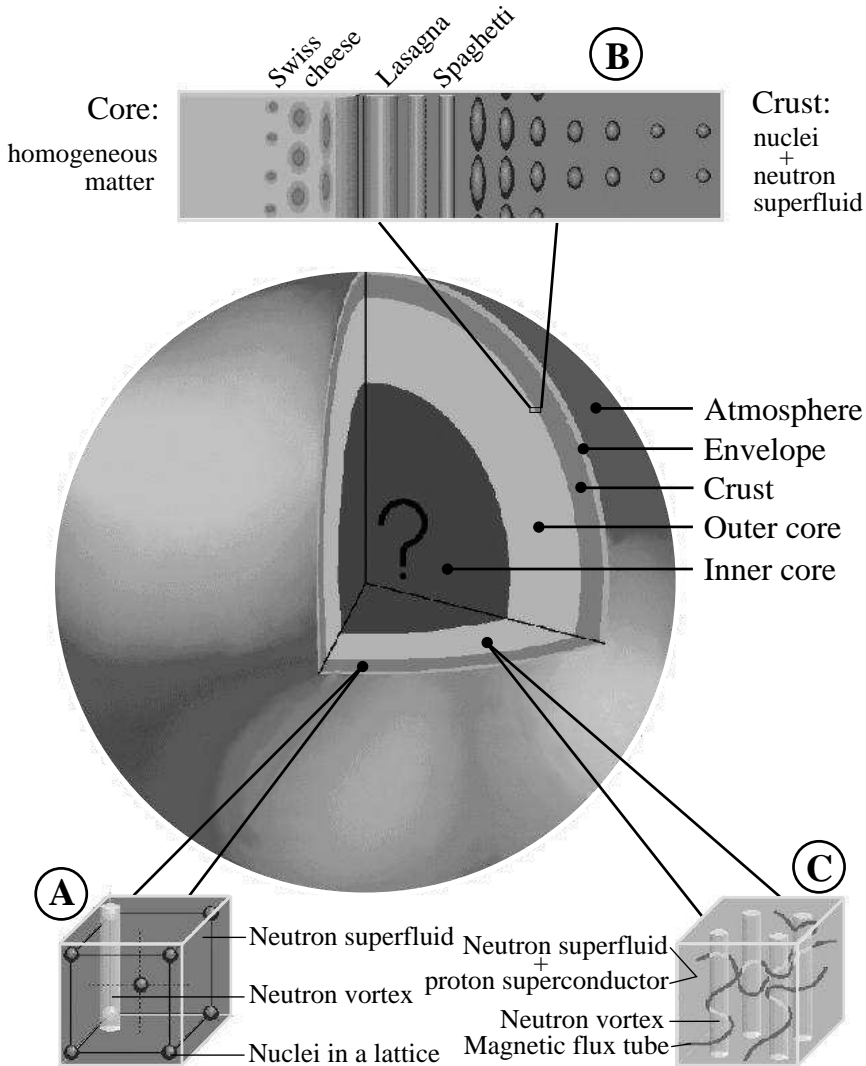
Figure 3.1. Inside a neutron star. Figure from Page & Reddy (2006).

disrupt the accretion disc at some radius and lead matter towards the magnetic poles, as sketched in Fig. 3.3.

In the accreting disc, magnetic pressure becomes equal to the ram pressure of the accreting matter at the Alfvén radius

$$R_{\mathrm{m}} = \Big[\frac{B_0^2 R^6}{2\dot{M}\sqrt{GM}} \Big]^{2/7}, \tag{3.1}$$

where B_0 is the magnetic field, M and R are the NS mass and radius and $\dot{M}$ is the accretion rate. We can compare R_{m} to the corotation radius R_{co}, where the Keplerian
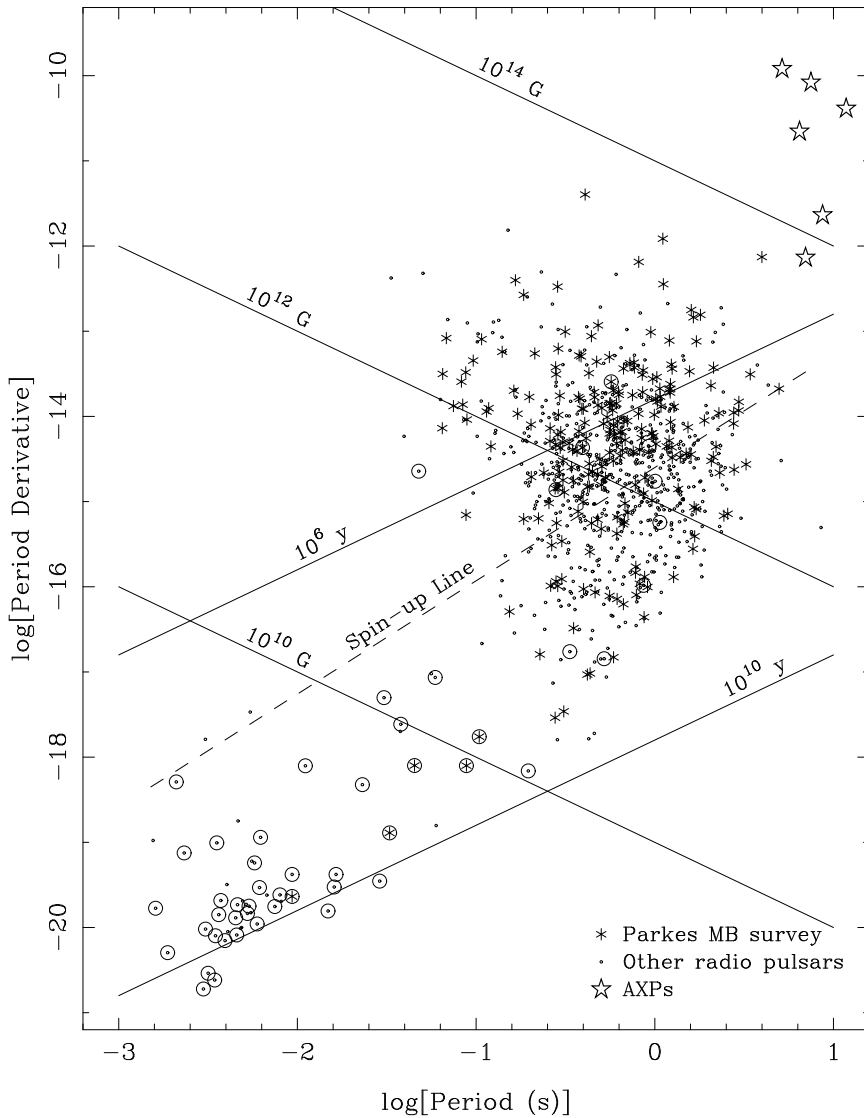
Figure 3.2. Distribution of pulsars and anomalous X-ray pulsars (AXPs) in the $P - \dot{P}$ plane. Binary systems are indicated by a circle around the point. Lines of constant pulsar characteristic age, $\tau_c = P/(2\dot{P})$, and surface dipole magnetic field strength, $B_s \sim (P\dot{P})^{1/2}$, are indicated. The spin-up line, representing the minimum period attainable by accretion from a binary companion, is also shown. Figure from Manchester (2001).

rotational frequency is equal to the spin of the NS:

$$R_{\text{co}} = \left[\frac{GMP^2}{4\pi^2} \right]^{1/3}, \tag{3.2}$$

where P is the pulsar period. If $R_{\text{m}} > R_{\text{co}}$, then matter will be ejected by the magnetic
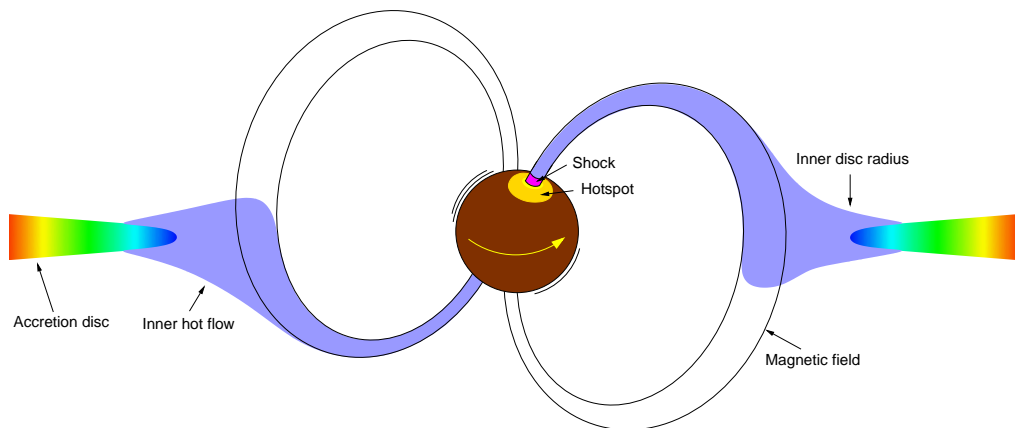
Figure 3.3. An artist's representation of a magnetically-driven accretion onto NS. Figure from Gierliński, Done, & Barret (2002).

field, as the field will have a field velocity greater than Keplerian. This will also cause the NS to slow down. In the opposite situation, accretion is possible and the momentum is transferred to the NS, causing it to spin up (since Keplerian motion of the accreting matter will be faster than the angular velocity of the NS and its magnetic field). A drop in the accretion rate can cause accretion to cease (since $R_{\mathrm{m}} \sim \dot{M}^{-2/7}$). The "spin-up" line in Fig. 3.2 corresponds to the situation when the "spin equilibrium" takes place ($R_{\mathrm{m}} = R_{\mathrm{co}}$).

How can a millisecond pulsar be born? Young pulsars have high magnetic fields and short periods (as during the collapse of the star the magnetic flux and angular momentum remain conserved). They emit relativistic winds, radio waves, photons and undergo magnetic field interactions with their surroundings, and hence lose their energy and spin down. Then, the accretion of gas from the companion, which also carries some angular momentum, spins the star up to millisecond periods.

Magnetized accretion is a rather complex problem. MHD simulations performed by Romanova with coauthors (see Romanova et al. 2003, 2004; Long, Romanova, & Lovelace 2007; Romanova, Kulkarni, & Lovelace 2008; Kulkarni & Romanova 2008; Long, Romanova, & Lovelace 2008) show that the flow of matter could be far from the "dipole-like" approximation under certain conditions. In fact, observed pulse profiles can be reasonably well explained by a simple accreting geometry, such as in Fig. 3.3.

3.2   Observational properties of millisecond pulsars

When a pulsar is detected, the first step is to obtain accurate parameters of the system. To obtain a pulsar ephemeris, one has to propose a "phase model", which predicts pulse times of arrival. By fitting such a model to the arrival time residuals, it is possible to constrain binary system and pulsar parameters (such as inclination, binary separation, eccentricity, pulsar frequency and frequency derivatives). While such

Table 3.1. Parameters of the accretion-powered millisecond pulsars. Table adopted from Poutanen (2006).

	Source	P_{orb}[a] (min)	ν_{spin}[b] (Hz)	$a_x \sin i$[c] (lt-ms)	f_x[d] ($M_\odot$)	$M_{c,min}$[e] ($M_\odot$)
1	SAX J1808.4−3658	121	401	62.809	3.779×10^{-5}	0.043
2	XTE J1751−305	42.4	435	10.113	1.278×10^{-6}	0.014
3	XTE J0929−314	43.6	185	6.290	2.9×10^{-7}	0.0083
4	XTE J1807−294	40.1	191	4.75	1.49×10^{-7}	0.0066
5	XTE J1814−338	257	314	390.3	2.016×10^{-3}	0.17
6	IGR J00291+5934	147	599	64.993	2.813×10^{-5}	0.039
7	HETE J1900.1−2455	83.3	377	18.39	2.00×10^{-6}	0.016
8	SWIFT J1756.9−2508	55	182	5.942	$1.66 \cdot 10^{-7}$	0.007

[a] Orbital period; [b] neutron star spin frequency; [c] projected semimajor axis; [d] pulsar mass function; [e] minimum companion mass for a $M_x = 1.4 M_\odot$ neutron star.
References: [1] Wijnands & van der Klis (1998); Chakrabarty & Morgan (1998); [2] Markwardt & Swank (2002); Markwardt et al. (2002); [3] Remillard et al. (2002); Galloway et al. (2002); [4] Markwardt et al. (2003a); Kirsch et al. (2004); Falanga et al. (2005a); [5] Markwardt & Swank (2003); Markwardt et al. (2003b); [6] Eckert et al. (2004); Markwardt et al. (2004a,b); Galloway et al. (2005); [7] Vanderspek et al. (2005); Morgan et al. (2005); Kaaret et al. (2005); [8] Krimm et al. (2007).

an approach, taken from research on radio pulsars, in principle is the same for the accretion-powered X-ray millisecond pulsars (AMSPs), their pulse shapes evolve with time, leading to the "timing noise" that complicates ephemeris determination (Hartman et al., 2008; Riggio et al., 2008; Papitto et al., 2008). Small occasional noise can be caused by, e.g., the movement of the accretion spot (Patruno, Wijnands, & van der Klis, 2009c), but dramatic changes in pulse profile, such as seen in SAX J1808.4–3658, are probably caused by the gradual unscreening of the antipodal emitting spot. We study the latter effect in our Paper V.

Currently known AMSPs are listed in Table 3.1 along with their basic physical characteristics. In addition to these sources, typically non-pulsating LMXBs such as Aql X-1 and SAX J1748.9−2021 are known to show episodes of "intermittent" pulsations, lasting for hundreds of seconds (Altamirano et al., 2008; Casella et al., 2008; Patruno et al., 2009a). AMSPs are transient sources: for example, SAX J1808.4–3658 goes into outburst approximately every two years and IGR J00291+5934 has an outburst period of about 3 years (Chakrabarty et al., 2008). Their orbital periods are quite close (40 min to 4.3h) and three of them, probably not coincidentally, have a nearly equal periods of 42 ± 2 minutes (three other binaries in NGC6652, namely 4U1626−67, 4U1916−05 and X1832−330, also have similar periods). The typical average accretion rate is about $10^{-11} M_\odot$/year.

The outburst profile of SAX J1808.4–3658 can be split into a few typical stages: "flare" (very high, constant flux), "slow decay" (exponential decay of flux, e-folding

factor is about 6-7 days), "rapid drop" (steep drop of flux) and "flaring tail" (jumps in the flux until the source becomes undetectable). Such a profile seems rather common among AMSPs, though many sources were observed mainly during their "slow decay" stage (Gierliński & Poutanen, 2005; Falanga et al., 2005b). However, some peculiarities are known: XTE J1807−294 shows a purely exponential decay with timescale of 120 days (Falanga et al., 2005a); in HETE J1900.1−2455, quasi-persistent emission remains present while pulsations had disappeared within two months of discovery.
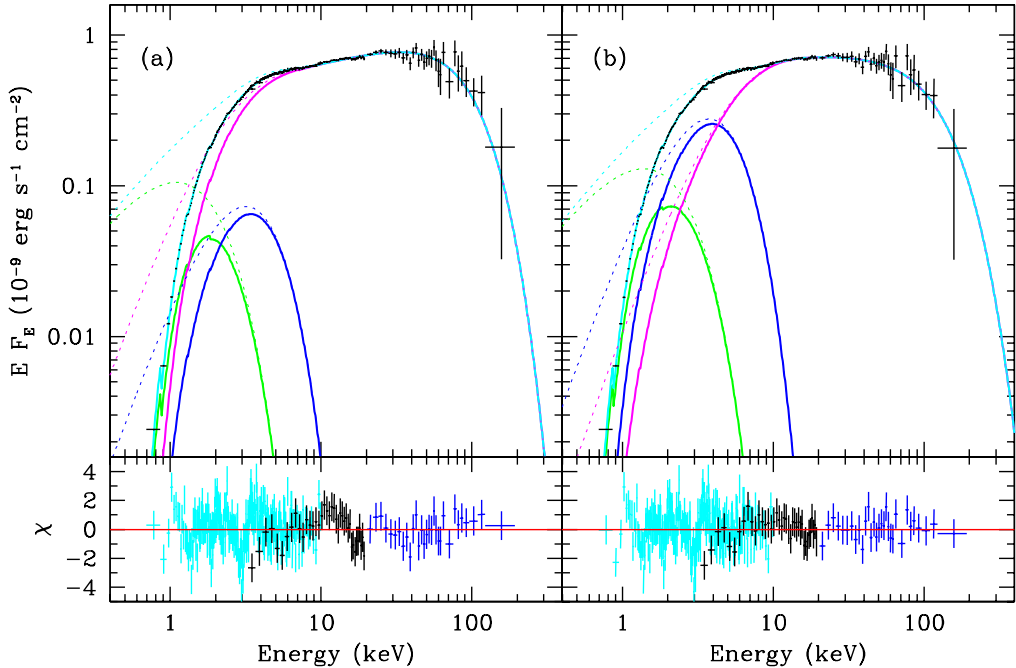
Figure 3.4. Broad-band spectrum of XTE J1751–305. The models consists of the multicolour disc (green curve), single temperature blackbody (blue curve), and thermal Comptonization of the blackbody photons (magenta curve). The dotted curves show unabsorbed spectral components. Panel (a) shows a best-fit for the case, when blackbody component temperature is equal to the "seed" photon temperature for Comptonization, and panel (b) shows fit for independent temperatures. The lower panels shows the residuals of *XMM*/EPIC-pn (cyan), *RXTE*/PCA (black) and *RXTE*/HEXTE (blue). Figure from Gierliński & Poutanen (2005).

Energy spectra of pulsars are quite similar to each other (see the example in Fig. 3.4). There are a few basic components: a powerlaw-like tail (due to the thermal Comptonization in the accretion shock, Zel'dovich & Shakura 1969; Alme & Wilson 1973; Lyubarskii & Syunyaev 1982; Viironen & Poutanen 2004), a blackbody-like component with effective temperature of about 1 keV (originating from the hot spot on the NS surface) and a colder blackbody with temperature of $\sim 0.4 - 0.6$ keV, probably due to the accretion disc. The signature of a reflecting medium is also present, but most of

the time it is very weak. The "case studies" of pulsar spectra can be found in Gierliński, Done, & Barret (2002); Gierliński & Poutanen (2005); Falanga et al. (2005a,b, 2007). Most of the time, *RXTE* data were used, however, *XMM-Newton* observations gave significant insights into what is happening at the soft energies unobservable by *RXTE*. For example, Patruno et al. (2009b) demonstrated that in SAX J1808.4–3658 below 2 keV the amplitude of millisecond pulsations drops dramatically, therefore the emission in this energy range can not be due to the rotating hot spot but likely originates from the accretion disc.

The pulse profiles at different energies do not arrive in phase, but have a "soft" phase lag (Fig. 3.5). The lag increases from ∼2 keV to about 7–10 keV, and then remain constant. However, in the special case of IGR J00291+5934 (Falanga et al., 2005b) the lags beyond 7 keV start decreasing again, and likely saturate at higher energies. The explanation of the existence of the lag comes from the fact that blackbody and Comptonized components have different emissivity patterns, see also Section 3.3.
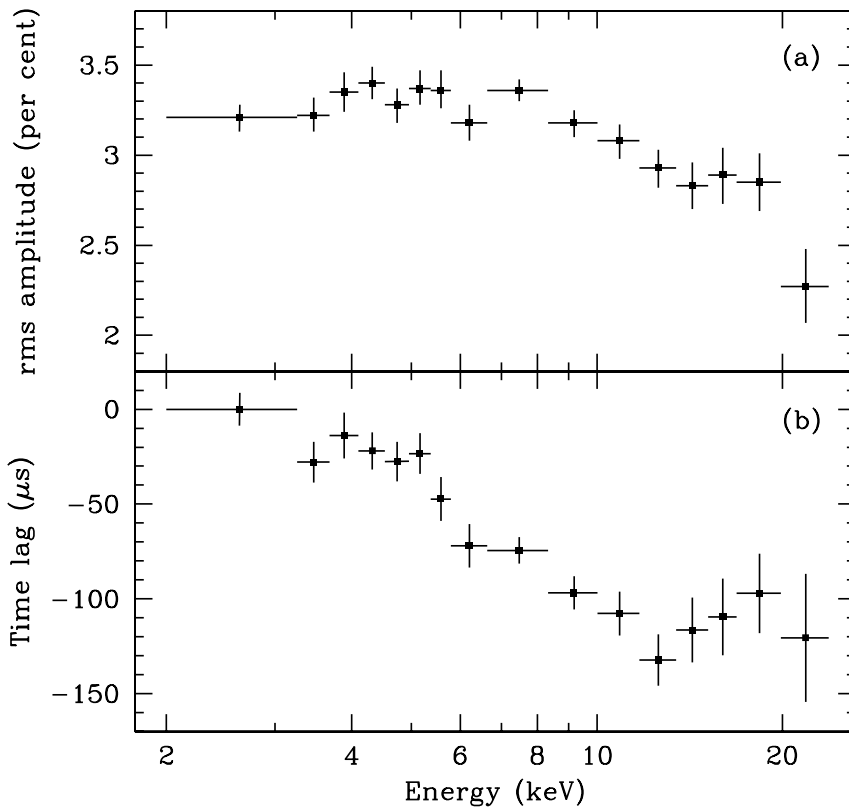

Figure 3.5. (a) The rms amplitude of the pulse profile of XTE J1751–305 as a function of energy. (b) The time lag of the pulse profile versus energy, with respect to the first energy channel, 2−3.3 keV. Figure from Gierliński & Poutanen (2005).

Phase-resolved spectra can be studied in order to track changes in spectral compo-

nents between various pulsar phases. They show that the blackbody and Comptonized continuum components remain similar in shape but their normalizations are "pulsating". The phase of blackbody normalization lags the Comptonized tail (e.g., Gierliński, Done, & Barret 2002; Gierliński & Poutanen 2005).

3.3 Modelling the pulse profiles

The pulse profile of an AMSP is usually rather simple and looks like a harmonic wave. However, this fact is not a general rule, as the SAX J1808.4–3658 pulse profiles show a sophisticated evolution and can be, in fact, very complicated. The pulse profile is very sensitive to the emissivity pattern, fractional contribution of an antipodal emitting spot (and therefore to the disc screening effects), and physical parameters of the system, including the mass and radius of the central star. Poutanen & Gierliński (2003) modelled the emission from a finite-size spot, taking into account relativistic effects (light bending, time delay and Doppler boosting, see Fig. 3.7) and fitted the obtained lightcurves to the observed pulses from the 1998 outburst of SAX J1808.4–3658 (these data belong to the "slow decay" phase, where only one spot is visible). They also present analytical expressions that describe emission from a fast-rotating, always visible finite-size spot. In a subsequent work, Poutanen & Beloborodov (2006) presented a large analytical study of a fast pulsar that has two very small spots. Similar work on pulsar shape modelling has been done by Leahy, Morsink, & Cadeau (2008); Leahy et al. (2009), where the additional effect of oblateness (important for very fast rotation with frequency ∼ 600 Hz, see Morsink et al. 2007) was considered. In our Papers IV and V, we present the further improvement of the model of Poutanen & Gierliński (2003) that now includes the effect of disc screening.
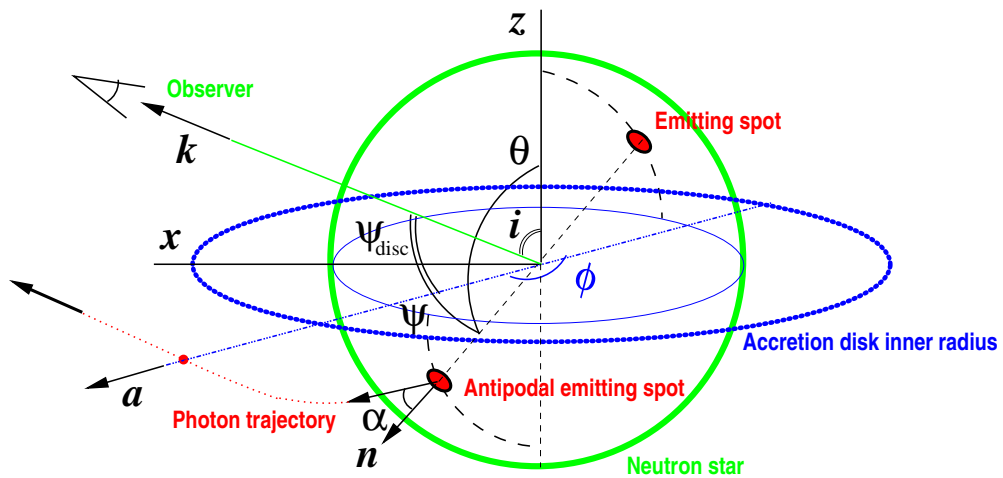

Figure 3.6. Geometry used in modelling of fast pulsar lightcurves. Figure adopted from Poutanen & Beloborodov (2006).
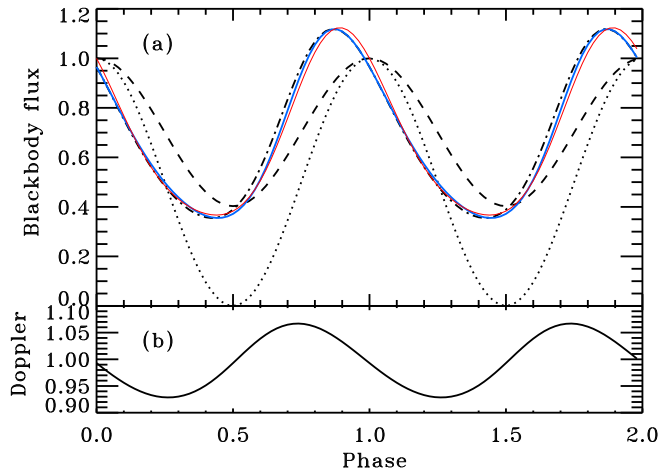
Figure 3.7. (a) The bolometric blackbody flux as a function of the observed phase. Dotted curve is for a slowly rotating star ignoring all relativistic effects. The pulse profile where gravitational light bending is accounted for is shown by the dashed curve. Dot-dashed curve gives the profile modified by the Doppler boost and aberration for a neutron star rotational frequency 600 Hz. Solid curve accounts also for the time delay. Thin solid curve is a pulse profile produced using the approximate Fourier amplitudes. (b) Doppler factor as a function of the observed phase. 600 Hz frequency, $i = \theta = 45°$, star radius $5R_g$ and $1.4M_\odot$ are assumed. Figure from Poutanen & Beloborodov (2006).

The geometry of the problem is illustrated in Fig. 3.6. The incident spectrum is expressed as $I_E = I_0(1 + h\cos\alpha)E^{-\Gamma}$, where the energy-independent parameter h characterizes the anisotropy of the emission. Here, $h = 0$ corresponds to the constant specific intensity (blackbody) case, $h = 2$ is for Chandrasekhar-Sobolev optically-thick electron scattering atmosphere (Chandrasekhar, 1960; Sobolev, 1963), and some values in the $-1 < h < 0$ range correspond to Comptonization in a slab with moderate optical depth (Sunyaev & Titarchuk, 1985; Viironen & Poutanen, 2004). Values of $h < -0.5$ correspond to the Thomson optical depth across the slab less than unity. $\Gamma \sim 1.9$ is typical for observed Comptonized spectra of AMSPs. Photons emitted toward direction α with respect to the normal of a current cell are bent towards the observer (Beloborodov, 2002). These photons could also be screened by a star or disc surface. The time delay effect will make photons emitted from different points within the hot spot arrive at the observer at different times. Integrating over the spot surfaces, we can obtain the modelled light curves in the observer frame. Fig. 3.7 illustrates how relativistic effects can affect the initial lightcurve.
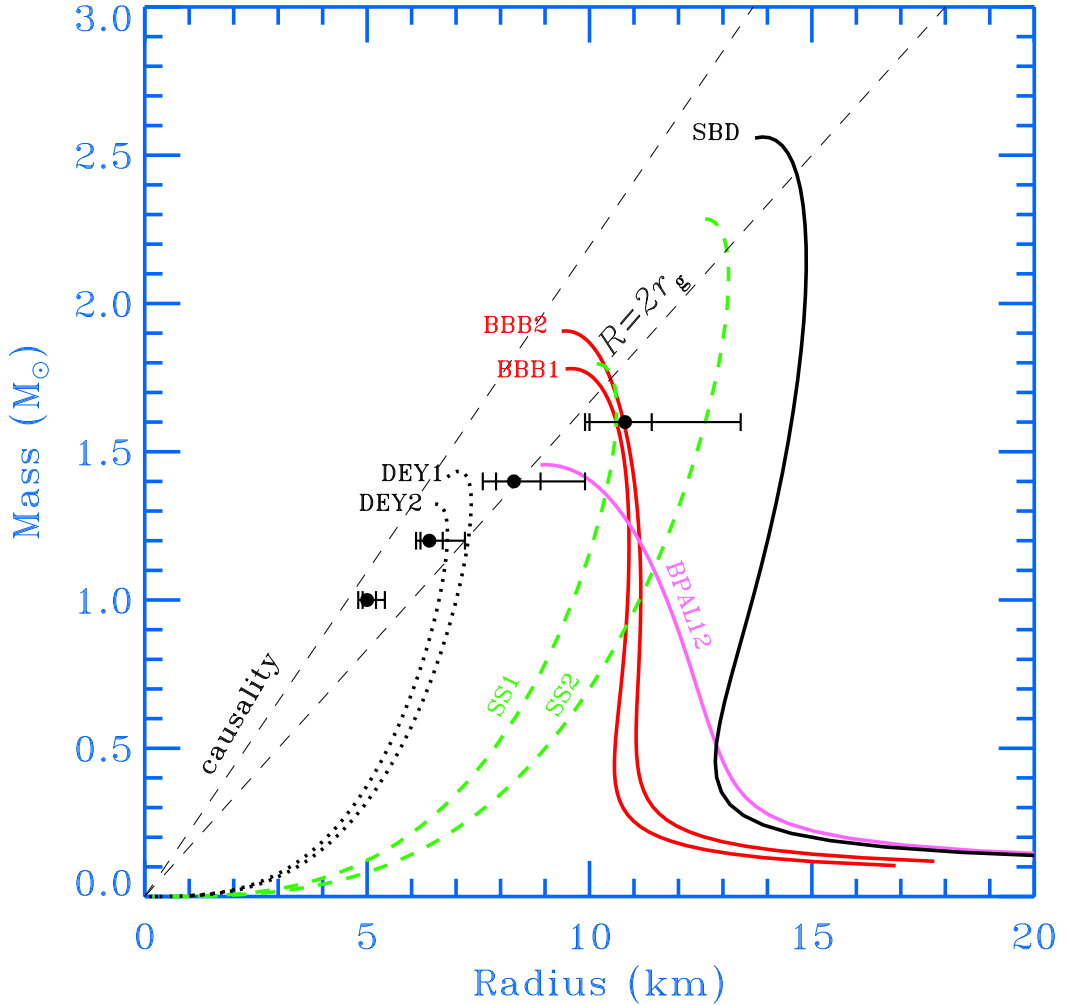
Figure 3.8. Equations of state and constraints on the radius of the compact star. Circles are for the masses and radii obtained by Poutanen & Gierliński (2003) from fitting the observed profiles of SAX J1808.4–3658 with the theoretical model developed by the authors (see also Paper V); double error bars are for 90 and 99 per cent confidence intervals. The relations between the star mass and its radius for several equations of state of neutron stars and strange stars are marked as follows: BBB1 and BBB2 – Baldo et al. (1997), BPAL12 – Prakash et al. (1997), SBD – Sahu et al. (1993), SS1 and SS2 – MIT bag model (Gondek-Rosińska et al., 2002), DEY1 and DEY2 – Dey (1998) computed as in Gondek-Rosińska et al. (2000). All realistic equations of state lie to the right of the causality line. The line $R = 2R_S$ is shown to guide the eye. Figure from Poutanen & Gierliński (2003).

3.4   Neutron star inner core equation of state

The structure of the inner core of a neutron star remains a challenging question. Several models exist (see Hansel, Potekhin, & Yakovlev 2007), and it is customary to compare these using a $M - R$ diagram, such as shown in Fig. 3.8. Fitting the pulse profiles can provide some constraint on NS mass and radius, which can be used for comparison with present NS equation of state theories. Poutanen & Gierliński (2003) have fitted the observed pulse profiles from the 118 ks of 1998 outburst of SAX J1808.4–3658 in the energy bands 3–4 and 12–18 keV. Since the mass of the object is not constrained, several choices of mass were made. For instance, for a mass of $1.4 M_\odot$, the authors obtain NS radius $R = 8.3^{+0.6}_{-0.4}$ km. The pulse profile analysis also provided constraints on system inclination, spot colatitude and emissivity pattern. Since the 1998 outburst of SAX J1808.4–3658 apparently show pulsations from a single non-eclipsed spot, further constraints on inclination and colatitude based on the analytical expression for pulse amplitude were also possible. As a result, the authors suggested the most probable mass to be in range 1.2–$1.6 M_\odot$ and system inclination in the range 65–82°. The upper limit of 82° comes from the absence of binary eclipses (Bildsten & Chakrabarty, 2001). However, previous determinations of the EOS were based on a limited amount of data, therefore these constraints are not conclusive.

Works of Leahy, Morsink, & Cadeau (2008); Leahy et al. (2009) were also dedicated to a similar analysis of a few pulse profiles of SAX J1808.4–3658 and XTE J1814-338. However, these results are inconclusive as well: these two objects constrain different regions on the mass-radius plane, thus favouring different equations of state. These works used just a limited number of pulse profiles and considered the one-spot model. As we demonstrated in Papers IV and V, a two-spot configuration that involves a disc screening is a far better approach for the description of complex pulse shapes. In our Paper V, we describe our model that takes these effects into account and show promising results describing sophisticated pulse shapes observed from SAX J1808.4–3658.

There are also other methods to constrain mass and radius from X-ray observations. Briefly, one can fit the spectra of spreading layers on NS surface (Suleimanov & Poutanen, 2006); Roche lobe constrains can be made (Falanga et al., 2005a); the "saturation" of the highest QPO frequency can be a measure of the innermost stable circular orbit, thus providing the upper limit for the star size.

Chapter 4

Rossi X-Ray Timing Explorer

The Rossi X-ray Timing Explorer (*RXTE*, Bradt, Rothschild, & Swank 1993) was launched on December 30th, 1995, and continues its operation till now. Most of the results of this thesis are owed to this observatory. The *RXTE* has three main instruments whose properties are described below.

4.1 All-Sky Monitor (ASM)

The ASM (Levine et al., 1996) consists of three wide-angle shadow cameras equipped with proportional counters with a total collecting area of 90 cm^2. It has three shadow cameras, each with 6 x 90 degrees FOV. The instrument has three channels that cover 1.5–3, 3–5 and 5–12 keV. The instrument can scan 80% of the sky every 90 minutes; spatial resolution is 3' x 15'. The detector is the position-sensitive proportional counter with sensitivity of 30 mCrab.

Despite its simplicity, this instrument serves several important tasks. It can monitor state transitions of the sources, thus triggering the Target-of-Opportunity observations of interesting phenomena. Another outcome is excellent long-term lightcurves from many sources covering the entire mission lifetime (about 13 years now). This provides a great source of information for the behaviour of many objects on timescales from days to years. In our Papers II and III we investigate the Cyg X-1 long-term variability using ASM data collected over several years.

4.2 Proportional Counter Array (PCA)

The Proportional Counter Array (PCA, Jahoda et al. 2006) is the main instrument of the mission. It contains five mechanically collimated counters (so-called PCUs) filled with Xenon, with a total collecting area of 6500 cm^2 and field of view about 1 square degree. It covers the energy range 2–60 keV (from which 3–20 keV are usually used for most analysis) with energy resolution about 18% at 6 keV. The instrument has quite a high time resolution of 1 microsec, that allows one to "see" very fast phenomena such as millisecond pulsations. The sensitivity of the instrument is 0.1 mCrab, background
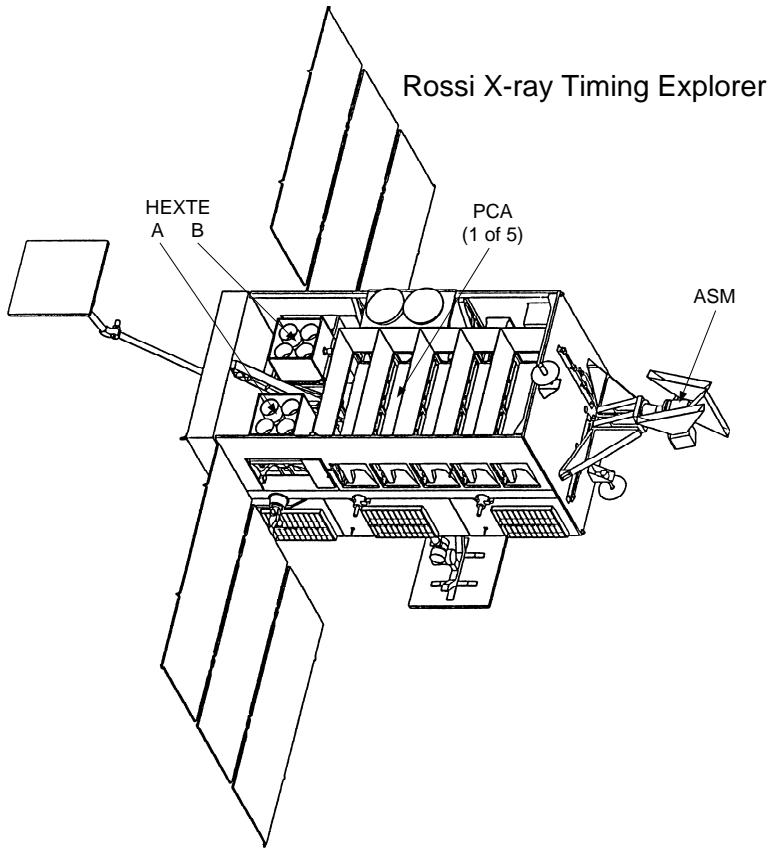
Figure 4.1. The RXTE spacecraft viewed from above to reveal the scientific instruments. The five PCA proportional counters and the two HEXTE clusters are shown in relation to the rest of the spacecraft components, such as the two high gain antennae for communications with the ground via the Tracking and Data Relay Satellite System, the two solar-power arrays that can rotate to face the sun, and the ASM on the end with clearance to view the sky. Figure from Rothschild et al. (1998).

level is 2 mCrab. The models of the background are built based on numerous "blank sky" observations, which are used in the course of the data reduction process to predict the background at a given date and pointing position. Deadtime of the detectors is about 10 microsecond for each photon. While the instrument can not produce images, scanning observations can localize bright sources up to the accuracy of $1' - 2'$. The large collecting area and high timing resolution makes this instrument unique for timing research. In our Paper IV, we used PCA data to obtain observed pulse profiles of SAX J1808.4–3658.

4.3   High Energy X-ray Timing Experiment (HEXTE)

The HEXTE (Rothschild et al., 1998) consists of two clusters each containing four photon counter NaI/CsI scintillation detectors. Each cluster can "rock" along mutually orthogonal directions to provide background measurements 1.5 or 3.0 degrees away from the source every 16 to 128 s (while the background varies on much slower timescales). Automatic gain control is provided by using a 241Am radioactive source mounted in each detector's field of view. The instrument energy range is 15–250 keV (of which, 20–200 keV range is used commonly) with energy resolution 15% at 60 keV. Time sampling is 8 microsecond, field of view is 1 square degree. Collecting area of each cluster is 800 cm^2, sensitivity is 360 count/s per HEXTE cluster, background rate per cluster is 50 count/s and deadtime is about 1–2 microsecond. Although timing with HEXTE is not often considered, the spectral results from this detector are very helpful in determining broad-band spectra of observed objects. In our Paper I, we used spectra obtained by PCA and HEXTE (together with coincidental *CGRO* observations) to analyze wide-range energy spectra of Cyg X-1. In Paper IV, PCA and HEXTE data of SAX J1808.4–3658 were used to track changes in the source during its outburst.

Chapter 5

Summary of the original publications

5.1 Paper I — Broad-band spectra of Cygnus X-1 and correlations between spectral characteristics

Broad-band spectral information is necessary for an accurate theoretical modeling of the source emission, as the data from narrow ranges provide only very limited constraints. In the paper, we present the results of spectral analysis of 42 simultaneous broad-band *Ginga–CGRO*/OSSE and *RXTE–CGRO*/OSSE observations of Cyg X-1 carried out in 1991 and 1996–1999. The broad-band spectra from 3 to ~ 1000 keV can be well described by a thermal Comptonization model with reflection from the cold disc, with an additional soft component visible below 10 keV. We show, that the additional soft component can result from thermal Comptonization by electrons with a low Compton parameter, or can be a part of a nonthermal, power-law like emission extending above 1 MeV.

We study correlations between parameters obtained from the spectral fits and confirm a general correlation between the photon index Γ and the amplitude of reflection R. We find that simple phenomenological models (like power-law plus Compton reflection) applied to the narrow band (3–20 keV) data overestimated the values of R and Γ. The dynamic corona model (Malzac, Beloborodov, & Poutanen, 2001) provides a satisfactory description of the observed correlation, while the truncated inner disc models have problems in reproducing it quantitatively. On the other hand, we show that the spectral parameters are well correlated with the timing characteristics of the source, which is difficult to explain using the dynamic corona model but seems natural in the truncated disc scenario.

5.2   Paper II — Superorbital variability of X-ray and radio emission of Cyg X-1. — I. Emission anisotropy of precessing sources

We study theoretical interpretations of the ∼150-d (superorbital) modulation observed in the X-ray and radio emission of Cyg X-1 in the framework of models connecting this phenomenon to the accretion disc precession. We consider, in particular, anisotropy patterns of blackbody-type emission, thermal Comptonization in slab geometry, jet/outflow beaming, and absorption in a coronal-type medium above the disc. We then fit these models to the data from the *RXTE*/All Sky Monitor, *CGRO*/BATSE, and the Ryle and Green Bank radio telescopes, and find angles between the precession and orbital planes to be $\sim 10^{\circ}$–20°. The thermal Comptonization model for the X-ray emission explains well the observed decrease of the variability amplitude from 1 to 300 keV as a result of a reduced anisotropy of the emission due to multiple scatterings. Our modelling also yields the jet bulk velocity of $\sim (0.3$–$0.5)c$, which is in agreement with the previous constraint from the lack of an observed counterjet and lack of short-term X-ray/radio correlations.

5.3   Paper III — Superorbital variability of X-ray and radio emission of Cyg X-1 — II. Dependence of the orbital modulation on the superorbital phase

We report the discovery of a pronounced dependence of the strength of the soft X-ray orbital modulation and the spectral hardness in Cyg X-1 in the hard state on its superorbital phase. We find our results can be well modelled as a combination of the precession of the accretion disc (which causes the superorbital flux modulation) and the orbital-phase dependent X-ray absorption in an accretion bulge. The bulge is located at the accretion disc edge close to the supergiant companion but displaced from the line connecting the stars by about 25°. Our findings are supported by the distribution of the X-ray dips showing concentration towards zero superorbital phase, which corresponds to the bulge passing through the line of sight. We Fourier analyse our model, and find that it explains the previous finding of asymmetric beat frequencies in the observed power spectrum, provided the disc precession is prograde.

There are statistically significant changes of the orbital modulation with the superorbital phase in the 15-GHz radio data, which are consistent with the radio being emitted by a jet in the system far from the central source. Additionally, we find that both the X-ray and radio fluxes of Cyg X-1 in the hard state on time scales $\geq 10^{4}$-s have lognormal distributions. We provide a correct formula for the uncertainty of rms of a light curve for the case when the uncertainty is higher than the measurement.

5.4 Paper IV — Accreting millisecond pulsar SAX J1808.4−3658 during its 2002 outburst: evidence for a receding disc

We analyse an outburst of the accreting X-ray millisecond pulsar SAX J1808.4−3658 in October–November 2002. For the first time, we demonstrate how the area covered by the hotspot at the neutron star surface is decreasing in the course of the outburst together with the reflection amplitude. These trends are in agreement with the natural scenario, where the disc inner edge is receding from the neutron star as the mass accretion rate drops. These findings are further supported by the variations of the pulse profiles, which clearly show the presence of the secondary maximum at the late stages of the outburst after October 29, when the disc has moved sufficiently far from the neutron star to open the view of the lower magnetic pole. We use this fact to estimate the disc inner radius, the inclination at $i = 60^{\circ} \pm 5^{\circ}$ and to put constraints on the stellar magnetic moment $\mu = (7 \pm 3) \times 10^{25}$ G cm^3, which corresponds to the surface field of about 10^8 G, and is in excellent agreement with the value obtained recently from the observed pulsar spin-down rate. We show that the timing noise and sharp changes in the phase of the fundamental are intimately related to the variations of the pulse profile, which we associate with the varying obscuration of the antipodal spot. Using the phase-resolved spectra, we also demonstrate that the strong dependence of the pulse profiles on photon energy and the observed soft time lags result from the different phase dependence of the two spectral components, the blackbody and the Comptonized tail, being consistent with the model, where these components have significantly different angular emission patterns. The pulse profile amplitude allows us to estimate the colatitude of the hotspot centroid to be ∼4°–10°.

5.5 Paper V — On the nature of pulse profile variations and timing noise in accreting X-ray millisecond pulsars

We consider the effect of timing noise, that is known to be present in the data on accretion-powered millisecond pulsars. The noise mostly appears as irregular pulse phase jumps on timescales from hours to weeks around a mean trend implied by ephemeris. Besides that, a large systematic drift is observed for example in the first discovered accretion millisecond pulsar SAX J1808.4–3658. To study the origin of the timing noise, we use here the data for the 2002 outburst of SAX J1808.4–3658, which has the best coverage. By directly fitting the pulse profile shapes with the theoretical model for pulse profiles, which includes the effect of partial screening of the antipodal emitting spot by the accretion disc, we are able to quantify the variations in the position of the spot centroid, its emissivity pattern and the inner accretion disc radius. We show that the main parameters of the emitting spot such as its mean latitude and azimuth as well as the emissivity pattern change irregularly causing small shifts in pulse phase. We stress that the sharp systematic shift in Fourier phases, observed together with the strong changes in the pulse form, can only be explained by the variations of the visibility of the antipodal spot associated with the receding accretion disc.

5.6　Contributions of the authors

In Paper I, the observational data were reduced and analysed by the author of the thesis, and the paper was written by him together with J. Poutanen, A. A. Zdziarski and M. Gilfanov, who provided the overall guidance of the process and contributed to the scientific discussion and interpretation. C. Shrader provided the OSSE data unavailable in the public archives.

In Paper II, the data analysis and all computational results were produced by the author of the thesis, who also wrote the main body of the manuscript. The idea of the work belongs to A. A. Zdziarski as a continuation of work by Lachowicz et al. (2006). J. Poutanen contributed greatly to the paper methodology and analysis approach.

The idea for Paper III, which led to the discovery of the effect, belongs to A. A. Zdziarski, who also contributed to the methodology and provided the section on the rms uncertainty. The author of the thesis performed the analysis of the observational data and confirmed the presence of the dependence. J. Poutanen made the theoretical modelling and fitted the data, as well as preparing a large part of the manuscript.

In Paper IV, all the data reduction and analysis was made by the author of the thesis. The theoretical section in the Discussion was contributed by J. Poutanen. The text was written jointly by the authors.

In Paper V, the original code of the light curve modelling has been written by J. Poutanen. Implementation of the disc screening condition and the fitting of the pulse profiles were made by the author of the thesis. The estimation of the spot size using dipole approximation was done by M. Annala. The manuscript was prepared by the author of the thesis and J. Poutanen.

5.7　Summary and future work

In the presented dissertation, the following main results were acquired:

- We studied a large number of broad-band energy spectra of Cyg X-1, analyzed the observed correlations between the model parameters, and concluded that the "soft excess" observed in the source can be produced by either thermal or non-thermal Comptonization. In the later case, the soft excess is also likely related to the spectral tail in the MeV range.

- We analysed in details the superorbital variability of Cyg X-1 and constrained the precession angle of the accretion disc. The changes of the variability amplitude with energy in the X-ray band are well explained by the energy-dependent emission pattern of the Comptonization in a slab geometry.

- We have discovered the dependence of the orbital variability on the superorbital phase in Cyg X-1. The effect can be explained as due to the existence of a "bulge" attached to the accretion disc in the place where it connects to the focused wind from the companion star.

- We studied the 2002 outburst of the accretion-powered millisecond pulsar SAX J1808.4–3658 and demonstrated how spectral parameters and the pulse shapes at different energies evolve in the course of the outburst. The data show an evidence that the accretion disc recedes with time from the neutron star. We also provide an estimation of the pulsar's magnetic field.

- The dramatic pulse evolution in SAX J1808.4-3658 (when, during approximately one day, the pulse completely changes its shape from nearly sinusoidal to a complex, double-peaked profile) is explained using our theoretical model, where the secondary antipodal emitting spot becomes visible as the disc retreats from the neutron star.

The amount of data on accretion-millisecond pulsars is enormous and is still growing as the *RXTE* observes them during their outbursts. We are looking forward to continue our work in the following directions. We aim to analyze other *RXTE* data on AMSPs and to track the evolution of spectral and timing properties during their outbursts.

Also, as we demonstrated in our work, the results of theoretical modeling of the pulse shapes strongly depend on the assumed spot geometry. We plan to include into our model the realistic spot shapes, obtained from the MHD simulations, in a hope that the obtained physical parameters become more reliable. As the amount of data on AMSPs grows, the simple models, that seem to be successful previously, fail and as a result more and more complexity is necessarily added to them. We hope, however, that our understanding of these enigmatic sources will become more complete in the very near future.

Bibliography

Abe Y., Fukazawa Y., Kubota A., Kasama D., Makishima K., 2005, PASJ, 57, 629

Abramowicz M. A., Igumenshchev I. V., 2001, ApJ, 554, L53

Alme M. L., Wilson J. R., 1973, ApJ, 186, 1015

Altamirano D., Casella P., Patruno A., Wijnands R., van der Klis M., 2008, ApJ, 674, L45

Axelsson M., Borgonovo L., Larsson S., 2005, A&A, 438, 999

Axelsson M., Borgonovo L., Larsson S., 2006, A&A, 452, 975

Axelsson M., Hjalmarsdotter L., Borgonovo L., Larsson S., 2008, A&A, 490, 253

Balbus S. A., 2005, ASPC, 330, 185

Balbus S. A., Hawley J. F., 1991, ApJ, 376, 214

Baldo M., Bombaci I., Burgio G. F., 1997, A&A, 328, 274

Bałucińska-Church M., Church M. J., Charles P. A., Nagase F., LaSala J., Barnard R., 2000, MNRAS, 311, 861

Barnard R., Balucińska-Church M., Smale A. P., Church M. J., 2001, A&A, 380, 494

Beckwith K., Done C., 2004, MNRAS, 352, 353

Belloni T., Mendez M., van der Klis M., Hasinger G., Lewin W. H. G., van Paradijs J., 1996, ApJ, 472, L107

Beloborodov A. M., 1999, ASPC, 161, 295

Beloborodov A. M., 2002, ApJ, 566, L85

Benlloch S., Wilms J., Staubert R., Nowak M. A., 2001, in Gimenez A., Reglero A., Winkler C., eds., ESA SP-459, Exploring the gamma-ray universe. ESA, Noordwijk, p. 263

Benlloch S., Pottschmidt K., Wilms J., Nowak M. A., Gleissner T., Pooley G. G., 2004, AIPC, 714, 61

Bildsten L., Chakrabarty D., 2001, ApJ, 557, 292

Bhattacharya D., van den Heuvel E. P. J., 1991, PhR, 203, 1

Blandford R. D., Begelman M. C., 1999, MNRAS, 303, L1

Bolton C. T., 1972, Nature, 235, 271

Bradt H. V., Rothschild R. E., Swank J. H., 1993, A&AS, 97, 355

Brocksopp C., Fender R. P., Larionov V., Lyuty V. M., Tarasov A. E., Pooley G. G., Paciesas W. S., Roche P., 1999a, MNRAS, 309, 1063

Brocksopp C., Tarasov A. E., Lyuty V. M., Roche O., 1999b, A&A, 343, 861

Brown G. E., Bethe H. A., 1994, ApJ, 423, 659

Campana S., Stella L., Israel G., D'Avanzo P., 2008, ApJ, 689, L129

Casella P., Altamirano D., Patruno A., Wijnands R., van der Klis M., 2008, ApJ, 674, L41

Chakrabarty, D., Morgan, E. H., 1998, Nature, 394, 346

Chakrabarty D., Swank J. H., Markwardt C. B., Smith E., 2008, ATel, 1660, 1

Chandrasekhar S., 1960, Radiative Transfer. Dover, New York

Coppi P. S., 1992, MNRAS, 258, 657

Coppi P. S., 1999, ASPC, 161, 375

Cui W., Feng Y. X., Zhang S. N., Bautz M. W., Garmire G. P., Schulz N. S., 2002, ApJ, 576, 357

Davis S. W., Blaes O. M., Hubeny I., Turner N. J., 2005, ApJ, 621, 372

Dey M., Bombaci I., Dey J., Ray S., Samanta B. C., 1998, Phys. Lett. B, 438, 123

Done C., Nayakshin S., 2001, ApJ, 546, 419

Done C., Wardziński G., Gierliński M., 2004, MNRAS, 349, 393

Done C., Gierliński M., Kubota A., 2007, A&ARv, 15, 1

Done C., Zycki P. T., 1999, MNRAS, 305, 457

Dovčiak M., Karas V., Yaqoob T., 2004, ApJS, 153, 205

Ebisawa K., et al., 1994, PASJ, 46, 375

Eckert, D., Walter, R., Kretschmar, P., et al., 2004, ATel 352, 2004

Esin A. A., McClintock J. E., Narayan R., 1997, ApJ, 489, 865

Falanga M., et al., 2005a, A&A, 436, 647

Falanga M., et al., 2005b, A&A, 444, 15

Falanga M., Poutanen J., Bonning E. W., Kuiper L., Bonnet-Bidaud J. M., Goldwurm A., Hermsen W., Stella L., 2007, A&A, 464, 1069

Falcke H., Körding E., Markoff S., 2004, A&A, 414, 895

Fender R. P., 2001, MNRAS, 322, 31

Feng Y. X., Cui W., 2002, ApJ, 564, 953

Galloway, D. K., Chakrabarty, D., Morgan, E. H., Remillard, R. A., 2002, ApJ, 576, L137

Galloway, D. K., Markwardt, C. B., Morgan, E. H., et al., 2005, ApJ, 622, L45

Gierliński M., Poutanen J., 2005, MNRAS, 359, 1261

Gierliński M., Done C., Barret D., 2002, MNRAS, 331, 141

Gierlinski M., Zdziarski A. A., Done C., Johnson W. N., Ebisawa K., Ueda Y., Haardt F., Phlips B. F., 1997, MNRAS, 288, 958

Gierliński M., Zdziarski A. A., Poutanen J., Coppi P. S., Ebisawa K., Johnson W. N., 1999, MNRAS, 309, 496

Gilfanov M., Churazov E., Revnivtsev M., 1999, A&A, 352, 182

Gleissner T., Wilms J., Pottschmidt K., Uttley P., Nowak M. A., Staubert R., 2004, A&A, 414, 1091

Gleissner T., et al., 2004, A&A, 425, 1061

Gold T., 1968, Nature, 218, 731

Gondek-Rosińska D., Bulik T., Zdunik L., Gourgoulhon E., Ray S., Dey J., Dey M., 2000, A&A, 363, 1005

Gondek-Rosińska D., Kluźniak W., Stergioulas N., 2002, astro-ph/0206470

Haardt F., Maraschi L., 1993, ApJ, 413, 507

Haberl F., 2007, Ap&SS, 308, 181

Hartman J. M., et al., 2008, ApJ, 675, 1468

Hirose S., Krolik J. H., Blaes O., 2009, ApJ, 691, 16

Ibragimov A., Poutanen J., Gilfanov M., Zdziarski A. A., Shrader C. R., 2005, MNRAS, 362, 1435

in't Zand J. J. M., Miller J. M., Oosterbroek T., Parmar A. N., 2002, A&A, 394, 55

Ichimaru S., 1977, ApJ, 214, 840

Jahoda K., Markwardt C. B., Radeva Y., Rots A. H., Stark M. J., Swank J. H., Strohmayer T. E., Zhang W., 2006, ApJS, 163, 401

Hansel P., Potekhin A. Y., Yakovlev D. G., 2007, ASSL, 326,

Heiselberg H., Pandharipande V., 2000, ARNPS, 50, 481

Kaaret, P., Morgan, E., Vanderspek, R., 2005, ATel 538

Karitskaya E. A., et al., 2001, Astron. Rep., 45, 350

Kirsch, M. G. F., Mukerjee, K. Breitfellner, M. G., et al., 2004, A&A, 423, L9

Krimm H. A., et al., 2007, ApJ, 668, L147

Kulkarni A. K., Romanova M. M., 2008, MNRAS, 386, 673

Lachowicz P., Zdziarski A. A., Schwarzenberg-Czerny A., Pooley G. G., Kitamoto S., 2006, MNRAS, 368, 1025

Lasota J.-P., 2001, NewAR, 45, 449

Leahy D. A., Morsink S. M., Cadeau C., 2008, ApJ, 672, 1119

Leahy D. A., Morsink S. M., Chung Y.-Y., Chou Y., 2009, ApJ, 691, 1235

Levine A. M., Bradt H., Cui W., Jernigan J. G., Morgan E. H., Remillard R., Shirey R. E., Smith D. A., 1996, ApJ, 469, L33

Li L.-X., Zimmerman E. R., Narayan R., McClintock J. E., 2005, ApJS, 157, 335

Lightman A. P., Eardley D. M., 1974, ApJ, 187, L1

Ling J. C., et al., 1997, ApJ, 484, 375

Liu Q. Z., van Paradijs J., van den Heuvel E. P. J., 2007, A&A, 469, 807

Long M., Romanova M. M., Lovelace R. V. E., 2007, MNRAS, 374, 436

Long M., Romanova M. M., Lovelace R. V. E., 2008, MNRAS, 386, 1274

Lyubarskii Y. E., Syunyaev R. A., 1982, SvAL, 8, 330

Magdziarz P., Zdziarski A. A., 1995, MNRAS, 273, 837

Malzac J., Beloborodov A. M., Poutanen J., 2001, MNRAS, 326, 417

Manchester R. N., 2001, PASA, 18, 1

Markwardt, C. B., Swank, J. H., 2002, IAUC 7867

Markwardt, C. B., Swank, J. H., 2003, IAUC 8144

Markwardt, C. B., Galloway, D. K., Chakrabarty, D., et al., 2004b, ATel 360

Markwardt, C. B., Smith, E., Swank, J. H., 2003a, IAUC 8080

Markwardt, C. B., Swank, J. H., Strohmayer, T. E., et al., 2002, ApJ 575, L21

Markwardt, C. B., Swank, J. H., Strohmayer, T. E., 2003b, ATel 164

Markwardt, C. B., Swank, J. H., Strohmayer, T. E., 2004a, ATel 353

McConnell M., et al., 1994, ApJ, 424, 933

McConnell M. L., et al., 2002, ApJ, 572, 984

Meier D. L., 2005, Ap&SS, 300, 55

Miyamoto S., Iga S., Kitamoto S., Kamado Y., 1993, ApJ, 403, L39

Miyamoto S., Kimura K., Kitamoto S., Dotani T., Ebisawa K., 1991, ApJ, 383, 784

Morgan, E., Kaaret, P., Vanderspek, R., 2005, ATel 523

Morsink S. M., Leahy D. A., Cadeau C., Braga J., 2007, ApJ, 663, 1244

Narayan R., Yi I., 1995, ApJ, 452, 710

Oppenheimer J. R., Snyder H., 1939, Phys. Rev. 56, 455

Özdemir S., Demircan O., 2001, Ap&SS, 278, 319

Paczyński B., Wiita P. J., 1980, A&A, 88, 23

Paizis A., et al., 2006, A&A, 459, 187

Page D., Reddy S., 2006, ARNPS, 56, 327

Papitto A., Menna M. T., Burderi L., di Salvo T., Riggio A., 2008, MNRAS, 383, 411

Patruno A., Altamirano D., Hessels J. W. T., Casella P., Wijnands R., van der Klis M., 2009a, ApJ, 690, 1856

Patruno A., Rea N., Altamirano D., Linares M., Wijnands R., van der Klis M., 2009b, MNRAS, 396, L51

Patruno A., Wijnands R., van der Klis M., 2009c, ApJ, 698, L60

Piran T., 1978, ApJ, 221, 652

Pooley G. G., Fender R. P., Brocksopp C., 1999, MNRAS, 302, L1

Poutanen J., 1998, in Abramowicz M. A., Bjornsson G., Pringle J. E., eds., Theory of Black Hole Accretion Disks. Camb. Univ. Press, Cambridge, p.100

Poutanen J., 2006, AdSpR, 38, 2697

Poutanen J., Beloborodov A. M., 2006, MNRAS, 373, 836

Poutanen J., Coppi P. S., 1998, PhST, 77, 57

Poutanen J., Gierliński M., 2003, MNRAS, 343, 1301

Poutanen J., Svensson R., 1996, ApJ, 470, 249

Poutanen J., Vurm I., 2009, ApJ, 690, L97

Pottschmidt K., et al., 2003, A&A, 407, 1039

Prakash M., et al., 1997, Phys. Rep., 280, 1

Remillard R. A., McClintock J. E., 2006, ARA&A, 44, 49

Remillard, R. A., Swank, J. H., Strohmayer, T. E., 2002, IAUC 7893

Reynolds C. S., Nowak M. A., 2003, PhR, 377, 389

Revnivtsev M., Gilfanov M., Churazov E., 1999, A&A, 347, L23

Revnivtsev M., Gilfanov M., Churazov E., 2000, A&A, 363, 1013

Riggio A., Di Salvo T., Burderi L., Menna M. T., Papitto A., Iaria R., Lavagetto G., 2008, ApJ, 678, 1273

Romanova M. M., Kulkarni A. K., Lovelace R. V. E., 2008, ApJ, 673, L171

Romanova M. M., Ustyugova G. V., Koldoba A. V., Wick J. V., Lovelace R. V. E., 2003, ApJ, 595, 1009

Romanova M. M., Ustyugova G. V., Koldoba A. V., Lovelace R. V. E., 2004, ApJ, 610, 920

Rothschild R. E., et al., 1998, ApJ, 496, 538

Ruffini R., Wheeler J. A., 1971, PhT, 24, 30

Sahu P. K., Basu R., Datta B., 1993, ApJ, 416, 267

Shakura N. I., Sunyaev R. A., 1973, A&A, 24, 337

Shakura N. I., Sunyaev R. A., 1976, MNRAS, 175, 613

Shapiro S. L., Lightman A. P., Eardley D. M., 1976, ApJ, 204, 187

Sobolev V. V., 1963, A Treatise on Radiative Transfer. Van Nostrand, Princeton

Suleimanov V., Poutanen J., 2006, MNRAS, 369, 2036

Sunyaev R. A., Titarchuk L. G., 1980, A&A, 86, 121

Sunyaev R. A., Titarchuk L. G., 1985, A&A, 143, 374

Sunyaev R. A., Truemper J., 1979, Nature, 279, 506

Tanaka Y., Lewin W. H. G., 1995, in Lewin W. H. G., van Paradijs J., van den Heuvel E. P. J., eds, X-Ray Binaries. Camb. Univ. Press, Cambridge, p. 126

Tanaka Y., Shibazaki N., 1996, ARA&A, 34, 607

Timmes F. X., Woosley S. E., Weaver T. A., 1996, ApJ, 457, 834

Thorsett S. E., Chakrabarty D., 1999, ApJ, 512, 288

Vanderspek, R., Morgan, E., Crew, G., et al., 2005, ATel 516

Viironen K., Poutanen J., 2004, A&A, 426, 985

Webster B. L., Murdin P., 1972, Nature, 235, 37

Wijnands, R., van der Klis, M., 1998, Nature, 394, 344

Wilms J., Nowak M. A., Dove J. B., Fender R. P., di Matteo T., 1999, ApJ, 522, 460

Wilms J., Nowak M. A., Pottschmidt K., Pooley G. G., Fritz S., 2006, A&A, 447, 245

Yuan F., 2001, MNRAS, 324, 119

Yuan F., 2003, ApJ, 594, L99

Yuan F., Zdziarski A. A., 2004, MNRAS, 354, 953

Zdziarski A. A., Gierliński M., 2004, PThPS, 155, 99

Zdziarski A. A., Grove J. E., Poutanen J., Rao A. R., Vadawale S. V., 2001, ApJ, 554, L45

Zdziarski A. A., Poutanen J., Paciesas W. S., Wen L., 2002, ApJ, 578, 357

Zel'dovich Y. B., Shakura N. I., 1969, SvA, 13, 175

Paper I

Ibragimov A., Poutanen J., Gilfanov M.,
Zdziarski A. A., Shrader C. R.
Broad-band spectra of Cygnus X-1 and correlations
between spectral characteristics

Broad-band spectra of Cygnus X-1 and correlations between spectral characteristics

Askar Ibragimov,[1,2]★ Juri Poutanen,[1]★† Marat Gilfanov,[3,4] Andrzej A. Zdziarski[5] and Chris R. Shrader[6]

[1]*Astronomy Division, PO Box 3000, FIN-90014 University of Oulu, Finland*
[2]*Kazan State University, Astronomy Department, Kremlyovskaya 18, 420008 Kazan, Russia*
[3]*Max-Planck-Institut für Astrophysik, Karl-Schwarzschild-Str. 1, 85740 Garching, Germany*
[4]*Space Research Institute, Russian Academy of Sciences, Profsoyuznaya 84/32, 117810 Moscow, Russia*
[5]*Centrum Astronomiczne im. M. Kopernika, Bartycka 18, 00-716 Warszawa, Poland*
[6]*Laboratory for High-Energy Astrophysics, NASA Goddard Space Flight Center, Greenbelt, MD 20771, USA*

ABSTRACT

We present the results of the spectral analysis of 42 simultaneous broad-band *Ginga*–OSSE and *RXTE*–OSSE observations of Cygnus X-1 carried out in 1991 and 1996–1999. The broad-band spectra from 3 to ~1000 keV can be well described by the thermal Comptonization model with reflection from the cold disc, with an additional soft component visible below 10 keV. The relative contribution of this component to the total energy flux appears to be higher in the spectra with larger reflection amplitude and steeper photon index of the thermal Comptonized component. We consider a number of physically realistic models to describe the shape of the $E \lesssim 10$ keV excess. The additional soft component can result from thermal Comptonization by electrons with a low Compton parameter, or can be a part of a non-thermal, power-law-like emission extending above 1 MeV.

We study correlations between parameters obtained from the spectral fits with different models. We confirm a general correlation between the photon index Γ and the amplitude of reflection R. We find that simple phenomenological models (such as power law plus Compton reflection) applied to the narrow band (3–20 keV) data overestimated the values of R and Γ, although the simple models did rank correctly the spectra according to R and Γ, as demonstrated in the original publications on this subject.

The dynamic corona model provides a satisfactory description of the observed correlation, while the hot inner disc models have problems in reproducing it quantitatively. On the other hand, in the context of the dynamic corona model it is difficult to understand correlations with the timing characteristics, which seems natural in the hot disc scenario. We do not find significant correlation between the electron temperature and other spectral parameters, while the optical depth of the hot medium seems to decrease when the spectrum becomes softer. It is also shown that spectral parameters are well correlated with the timing characteristics of the source.

Key words: accretion, accretion discs – black hole physics – stars: individual: Cygnus X-1 – gamma-rays: observations – X-rays: binaries.

1 INTRODUCTION

Matter accreting on to a black hole, whether supermassive in Seyfert galaxies or stellar mass in Galactic X-ray binaries, releases most of its gravitational energy in the form of X-rays deep in the potential well. Accretion may proceed in a number of regimes. The accreting gas can approach the black hole in a disc-like configuration (Shakura & Sunyaev 1973) if the gravitational energy is effectively transported away in the form of radiation, or in the form of an almost spherical flow if the energy exchange mechanism between protons (carrying most of the energy) and electrons is inefficient (Shapiro, Lightman & Eardley 1976; Ichimaru 1977; Narayan, Mahadevan &

★E-mail: askar.ibragimov@oulu.fi (AI); juri.poutanen@oulu.fi (JP)
†Corresponding Fellow, NORDITA, Copenhagen.

Quataert 1998). Magnetic fields can play an important role transporting a large fraction of the total available energy and dissipating it in a rarefied medium (corona) above the disc (Galeev, Rosner & Vaiana 1979; Tout & Pringle 1992; Svensson & Zdziarski 1994; Beloborodov 1999a; Miller & Stone 2000). However, every model is based on a number of assumptions that include prescriptions for the viscosity, the vertical distribution of the energy release through the flow, the energy transport mechanisms, etc. Given the difficulties in the accretion physics, observations should help in choosing among the different possibilities as well as guiding theoreticians in the right direction.

Cygnus X-1, one of the best studied black hole binaries (BHBs), has served as an accretion disc laboratory since the end of the 1960s. The most dramatic observed phenomena are the spectral state transitions occurring every few years, when the source, typically emitting most of its energy at about 100 keV in the hard state, switches to a soft state consisting of a prominent $\sim$1-keV blackbody and a power-law-like tail. The hard state spectrum was believed to originate from thermal Comptonization in a hot electron cloud (Shapiro et al. 1976; Ichimaru 1977; Sunyaev & Trümper 1979; Sunyaev & Titarchuk 1980). The blackbody-looking soft-state spectrum was associated with the optically thick accretion disc (Shakura & Sunyaev 1973), while the origin of $\sim$100-keV emission in that state was not discussed much, because the detailed spectrum was not available.

During the last decade, the quality of the X/γ-spectra increased dramatically improving our knowledge as well as producing many new questions. In the hard state, the spectrum turns out to be rather complicated containing a number of components. Thanks to the broad-band coverage by *Ginga* and *CGRO* (and later by *ASCA*, *RXTE* and *BeppoSAX*), and advances in modelling of Comptonization at mildly relativistic temperatures (Coppi 1992; Poutanen & Svensson 1996), the parameters of the electron cloud where Comptonization takes place were determined to a high accuracy. In Cyg X-1, the electron temperature of $kT_e \simeq 100 \pm 50$ keV and Thomson optical depth of $\tau \simeq 1$–2 were found to be typical (Zdziarski et al. 1996, 1997; Gierliński et al. 1997; Poutanen 1998; Di Salvo et al. 2001; Frontera et al. 2001; Zdziarski & Gierliński 2004). The Compton reflection bump, a signature of the presence of cold matter in the vicinity of the X-ray emitting source, was discovered (Done et al. 1992; Ebisawa et al. 1996; Gierliński et al. 1997). The blackbody associated with the cooler accretion disc (Balucińska & Hasinger 1991; Balucińska-Church et al. 1995; Ebisawa et al. 1996) and an additional soft excess at a few keV of unknown origin further complicate spectral decomposition (Di Salvo et al. 2001; Frontera et al. 2001). A high-energy excess at >500 keV discovered by *CGRO* (McConnell et al. 1994; Ling et al. 1997) gives some clues about the presence of non-thermal particles in the source.

The X/γ-ray soft-state spectrum has been studied extensively by simultaneous observations with *ASCA*, *RXTE*, *BeppoSAX* and *CGRO* during the summer of 1996. In addition to the dominating blackbody, a long power-law-like tail extending up to 10 MeV was discovered (McConnell et al. 2002). The high-energy spectrum could be well described by single Compton scattering off electrons having a nearly power-law distribution (Poutanen 1998; Poutanen & Coppi 1998; Gierliński et al. 1999, hereafter G99; Frontera et al. 2001). The Compton reflection was stronger than in the hard state, which was interpreted as a change in the geometry of the system, from the hot inner flow in the hard state to the standard Shakura–Sunyaev disc with a non-thermal corona in the soft state (Bisnovatyi-Kogan & Blinnikov 1977; Ichimaru 1977; Poutanen, Krolik & Ryde 1997; Li & Miller 1997; Esin et al. 1998; Poutanen & Coppi 1998).

Evaporation and condensation of the gas can provide a physical basis for the change of the transition radius between standard disc and hot inner flow (Meyer, Liu & Meyer-Hofmeister 2000; Różańska & Czerny 2000). A smaller reflection fraction in the hard state, however, can be explained by a beaming of the primary emission away from the disc due to mildly relativistic motion of the emitting plasma (ejection model; see Beloborodov 1999a,b; Malzac, Beloborodov & Poutanen 2001, hereafter MBP01). In order to distinguish among different possibilities, it is necessary to compare model predictions with other observational facts.

A few, well separated in time, broad-band spectra do not give us a good picture about relations between different components, such as, for example, Comptonized continuum and the reflection bump. It is possible to study these relations on a larger data set in a narrower energy band. Zdziarski, Lubiński & Smith (1999, hereafter ZLS99) and Gilfanov, Churazov & Revnivtsev (1999, hereafter GCR99) analysing data from *Ginga* and *RXTE*, respectively, have shown that the photon spectral slope of the Comptonized emission, Γ, is strongly correlated with the amplitude of Compton reflection component, $R = \Omega/2\pi$, where Ω is the solid angle the cool material covers as viewed from the source of primary X-rays. This correlation exists for individual BHBs and Seyfert galaxies as well as in a sample of sources (see also Gilfanov, Churazov & Revnivtsev 2000; Revnivtsev, Gilfanov & Churazov 2001). Zdziarski et al. (2003) studied possible statistical and systematic effects and concluded that the correlation exists beyond any reasonable doubt. Similar correlation also exists for Fourier-frequency resolved spectra, i.e. those corresponding to the variability in a given range of Fourier frequencies (Revnivtsev, Gilfanov & Churazov 1999).

The observed correlation provides extremely important clues to the geometry of the accreting material and can be used for testing the theoretical model. The fact that Γ and R are correlated is a natural consequence of coexistence of the cold media (accretion disc) and a hot Comptonizing gas in the vicinity of the black hole. The cold material acts as a source of seed photons for Comptonization and, at the same time, reflects and reprocesses the hard radiation produced in the hot gas.

The cold disc with the hot inner flow model naturally produces the correlation if there is an overlap between hot and cold phases (Poutanen et al. 1997; ZLS99). However, the Γ–R dependence observed in BHBs can be quantitatively reproduced only if the ratio of the seed photon temperature, kT_{seed}, to the electron temperature is about 10^{-4} (ZLS99; Gilfanov et al. 2000). For $kT_e \sim 100$ keV, this gives $kT_{seed} \sim 10$ eV, which is an order of magnitude smaller than the disc temperature in BHBs and closer to that expected from Seyferts. For $kT_{seed} \sim 300$ eV, the spectra are too hard for the given reflection fraction. In this model, the spectral slope is an extremely steep function of the overlap between the corona and the disc, while the reflection varies very little (Beloborodov 2001). Intrinsic dissipation in the disc can make spectra softer for the given reflection, but then the spectral slope will be an even steeper function of the overlap. Values of reflection larger than 1 sometimes observed in Seyferts also cannot be explained. On the other hand, all the data can be well described by the ejection model with the correct kT_{seed} (Beloborodov 1999a,b; MBP01).

The problem is that theoretical models try to reproduce the best-fitting Γ and R, which are subject to a number of systematic effects. The photon index and, especially, the strength of the Compton reflection depend crucially on the spectral shape of the underlying continuum and description of the reflection physics (see detailed discussion in Zdziarski et al. 2003). All the papers above, where this correlation was studied, assumed the underlying spectrum to be

a power law. Because the Comptonization spectrum has a cut-off at high energies, it gives fewer incident photons that are available for reflection (Weaver, Krolik & Pier 1998; Malzac & Petrucci 2002; Perola et al. 2002), and thus the fitted *R* would be larger. Fitting an exponentially cut-off power law to the broad-band data (e.g. Matt 2001; Perola et al. 2002) does not improve the situation, because this model does not reproduce well the shape of the Comptonization continuum (Malzac & Petrucci 2002; Zdziarski et al. 2003). The approximate treatment of ionization could be another source of errors.

As discussed above, the spectra of BHBs are rather complex having a number of components, and it is not possible to resolve different spectral components (e.g. thermal Comptonization and soft excess) in the narrow energy range of an instrument such as *RXTE*/Proportional Counter Array (PCA) or *Ginga*/Large Area Proportional Counter (LAC). There is a danger that different components overlap in that energy band producing effectively a power law of one index while in reality the slope of the primary emission could be rather different. The resulting reflection amplitude could be also influenced significantly. Thus, in order to obtain actual Γ and *R* to be used in theoretical models, the analysis of broad-band data with physical models (such as Comptonization) is absolutely necessary.

Additional sources of information are the width of the fluorescent Fe Kα line at 6.4 keV and the frequencies of the quasi-periodic oscillations (QPOs) that were also observed to correlate with the reflection fraction and the spectral slope (GCR99; Gilfanov et al. 2000). This seems to be consistent with the variations of the inner cold disc radius. Not much data exist on the variability of the electron temperature and Thomson optical depth of the Comptonizing source, which can provide information about the nature of the emitting plasma (electron–proton or electron–positron). It would be of interest to determine how the optical depth changes with the bolometric flux, because this can help in distinguishing the accretion mode the flow is in.

In this paper, we analyse a large set of simultaneous broad-band spectra. Four observations of Cyg X-1 by *Ginga*/LAC and *CGRO*/OSSE from 1991 as well as 38 observations by *RXTE*/PCA, *RXTE*/HEXTE and *CGRO*/OSSE from 1996–1999 are studied in detail. For the spectral analysis, we use physically motivated Comptonization models and study correlations between model parameters such as the spectral slope of the primary Comptonization continuum, the reflection amplitude, the width of the Fe line, the electron temperature of the hot gas, and its Thomson optical depth.

2 OBSERVATIONS AND DATA ANALYSIS

The observation log is presented in Table 1. Data reduction for *RXTE* has been carried out using LHEASOFT 5.3.1 software; PCA responses were generated using PCARSP v. 10.1 and HEXTE responses were used from 2000 May 26. In PCA data reduction, all five PCUs were taken into account, when possible. If not all PCUs were turned on, we use PCUs 0, 2 and 3. Judging from the Crab data, these two PCU configurations produce similar spectral slopes. Systematic errors of 0.5 per cent were added in quadrature to the PCA data. *CGRO*/OSSE spectra were prepared by adding per-orbit data (average exposure 2–5 ks), with total exposure up to 12 h and contemporary PCA observation in the middle of the period. The systematic error in OSSE spectra varies from 3 per cent at 50 keV to 0.3 per cent at 300 keV. The stability of the OSSE spectra was checked using hardness ratios (154–282/52–154 keV) for per-orbit spectra being added.

If orbital spectra within 12 h were apparently different, we lowered the total integration time to include only similar data.

We used PCA data from 3 to 20 keV, HEXTE data from 20–25 to 200 keV and OSSE data from 50 to 1000 keV. In addition, four *Ginga*/LAC and OSSE simultaneous observations from 1991, previously studied by Gierliński et al. (1997), were also analysed. The *Ginga*/LAC data are available from 1.7 keV, but we decided to use exactly the same energy interval as covered by the PCA. For the spectral analysis, we use XSPEC 11.3.1k (Arnaud 1996).

The spectra may be separated into two groups based on the difference of their photon index (see Fig. 1). Spectra from 1991 and 1997, represented by observation 6, have $\Gamma \sim 1.6$ (usual for the hard state) and those from 1999 (observations 25 and 31) have $\Gamma \sim 1.8$–2.2; hereafter, we call the corresponding state flat (because the spectrum is nearly flat in the EF_E plot). The spectra from 1996 and 1998 are close to the hardest ones from 1999. We do not consider here the broad-band soft-state spectra, for which a similar analysis has been performed by G99 and Frontera et al. (2001).

3 SPECTRAL ANALYSIS

In order to describe the observed broad-band spectra, we use the following models:

(0) power law (without or with an exponential cut-off) and Compton reflection (PEXRAV model; Magdziarz & Zdziarski 1995);

(1) two thermal Comptonization models and reflection, with the soft excess also modelled by thermal Comptonization;

(2) thermal Comptonization with reflection plus a non-thermal Comptonization corresponding to the soft state spectrum.

We use the EQPAIR code (Coppi 1999; G99) for modelling thermal and non-thermal Comptonization. All models include also a Gaussian line at 6.4 keV and interstellar absorption with column density N_H, which we find often larger than the value of 0.6×10^{22} cm^{-2} (derived from the reddening towards the companion star; see Balucińska-Church et al. 1995). To avoid unreasonably low values of this parameter, its low limit was set to 0.5×10^{22} cm^{-2}. The presented uncertainties are given at a 90 per cent confidence level for a single parameter ($\Delta \chi^2 = 2.71$). Fluxes, unless stated otherwise, correspond to the range covering all the model emission.

3.1 Power law and reflection model in the 3–20 keV data

The spectra of Cyg X-1 clearly show correlations between reflection amplitude and the spectral index (GCR99, ZLS99). Detailed analysis confirms (Zdziarski et al. 2003) that the extent of correlation is much larger than typical errors in the best-fitting parameters. However, because the PCA spectrum falls in a quite narrow energy interval, it is difficult to distinguish between various spectral components that may form an 'effective' power law. Therefore, it is not certain that the values for Γ and *R* obtained from the simple power-law/reflection fits indeed correspond to the actual physical situation.

Still, in order to compare our results with those of previous analysis, we have performed fits similar to those presented in ZLS99 and GCR99. We later compare them to the results obtained with more physical models (see Section 4.4). We use the XSPEC model PHABS*(PEXRAV+GAUSSIAN) (model 0), i.e. a power law with the photon index, Γ, and Compton reflection with the relative strength, *R* (Magdziarz & Zdziarski 1995), accompanied by a Gaussian fluorescence Fe Kα line (characterized by the relativistic smearing width σ and the equivalent width), all absorbed by interstellar material of

Table 1. Observation log.

| No	*RXTE* ObsID	*Ginga* or PCA exposure[a] (s)	HEXTE exposure[b] (s)	Date	Time (UT)	*CGRO* VP	OSSE exposure (s)	Time (UT)
				1991 hard state				
G1		2304		June 6	00:18–02:10	02	4121	00:03–02:11
G2		888		June 6	04:43–06:29	02	4040	04:29–06:51
G3		2828		June 6	11:03–14:25	02	5975	10:43–14:32
G4		1272		June 6	20:22–20:44	02	1629	20:02–20:33
				1996 flat state				
1	10238-01-08-000	14 592	5083	March 26	10:12–17:36	516.5	17 538	07:22–20:01
2	10238-01-07-000	8446	2922	March 27	23:06–05:20	516.5	23 018	20:20–07:47
3	10238-01-06-00	11 455	3713	March 29	11:43–17:33	516.5	21 868	08:24–21:06
4	10238-01-05-000	10 397	3524	March 30	19:54–01:58[c]	516.5	24 153	16:51–04:12[c]
				1997 hard state				
5	10239-01-01-00	9095	–	Feb 2	20:13–02:03	612.5	47 864	16:53–04:52[c]
6	10238-01-03-00	6441	1938	Feb 3	19:30–22:06	612.5	44 530	14:38–02:36[c]
7	30158-01-01-00	1175	809	Dec 10	07:08–08:30	705	7552	02:55–12:46
8	30158-01-02-00	2012	823	Dec 11	07:06–08:45	705	12 004	04:11–14:05
9	30158-01-03-00	2027	706	Dec 14	08:48–10:20	705	11 599	03:09–11:35
10	30158-01-05-00	2614	901	Dec 15	05:26–07:09	705	16 721	23:31–11:18[c]
11	30158-01-06-00	3210	941	Dec 17	00:40–02:05	706	13 017	20:13–07:32[d]
12	30157-01-02-00	2309	784	Dec 18	07:07–08:16	706	9924	01:49–08:46
13	30158-01-07-00	2275	766	Dec 20	07:11–08:29	706	11 847	02:46–12:52
14	30158-01-08-00	2581	878	Dec 21	05:28–07:05	706	14 924	00:51–12:31[c]
15	30157-01-03-00	2846	860	Dec 24	21:24–23:03	707	10 127	21:36–03:18[c]
16	30161-01-01-000	13 244	4136	Dec 28	13:56–21:03	707	13 717	11:33–00:24[c]
17	30158-01-12-00	2836	916	Dec 30	03:52–05:00	707	8979	23:49–07:57[d]
				1998 flat state				
18	30155-01-01-020	10 027	3897	Dec 23	00:07–05:58	804	2957	21:52–09:00[d]
19	30155-01-02-00	9625	3399	Dec 28	01:40–07:09	804	5124	23:14–10:29[d]
20	30161-01-03-01	9863	3371	Dec 28	13:08–18:37	804	5289	11:50–21:31
21	40100-01-04-00	8472	–	Dec 29	01:37–05:57	804	5476	22:51–10:08[d]
22	40100-01-05-00	8476	–	Dec 30	01:38–05:57	804	5288	22:30–09:46[d]
23	40100-01-06-00	7245	–	Dec 31	03:12–07:11	804	5552	23:44–11:00[d]
				1999 flat state				
24	40101-01-09-00	2405	665	Oct 5	18:39–19:45	831.5	29 605	15:04–01:12[c]
25	40101-01-11-00	731	165	Oct 6	19:22–20:03	831.5	25 960	14:39–00:50[c]
26	40101-01-12-00	865	–	Oct 7	07:10–07:40	831.5	28 389	03:08–12:55
27	40101-01-15-00	741	218	Oct 8	08:07–08:48	831.5	31 014	04:20–14:35
28	40101-01-16-00	757	215	Oct 9	09:41–10:22	831.5	33 770	03:55–15:48
29	40099-01-20-01	1228	354	Oct 12	17:33–19:56	831.5	37 186	12:11–01:23[c]
30	40100-01-11-01	4300	–	Oct 28	10:46–15:12	832	19 559	06:16–17:46
31	40099-01-22-00	1444	520	Nov 8	14:44–15:25	832	17 504	09:52–21:28
32	40099-01-23-01	3084	1453	Nov 23	15:26–17:32	834.5	8734	15:14–21:54
33	40100-01-13-01	770	–	Nov 24	20:08–20:59	834.5	19 652	14:51–02:13[c]
34	40100-01-14-02	479	–	Nov 25	20:05–20:56	834.5	16 683	14:24–01:47[c]
35	40100-01-15-03	1729	–	Nov 26	21:40–22:32	834.5	24 372	17:11–04:33[c]
36	40100-01-16-02	1448	–	Nov 27	19:59–20:50	834.5	19 063	15:13–02:34[c]
37	40100-01-17-03	1902	–	Nov 28	21:32–22:27	834.5	10 309	19:19–00:28[c]
38	40100-01-18-03	1961	–	Nov 29	21:29–22:25	834.5	19 999	16:03–03:19[c]

[a]The deadtime-corrected exposure. [b]HEXTE cluster 0 exposure. Symbol '–' means that no HEXTE data are available. [c]The observation finished on the following day. [d]The observation started on the previous day.

column density $N_{\rm H}$. Hereafter, we assume the disc inclination of $i = 50°$ and neutral reflector.

The fit results are presented in Table 2. Only the low-energy 3–20 keV (*RXTE*/PCA and *Ginga*/LAC) data were fitted, and therefore we did not apply any high-energy cut-off to the power law. We find that the correlations between spectral parameters (see Fig. 2) are similar to the results of GCR99.

As shown in Section 3.2, there is a likely overlap of different spectral components in the PCA energy range. Therefore, model 0

cannot represent a good approach for physical interpretations for the spectra. Taking into account also the OSSE data and including an exponential cut-off in the model, we can model the joint data only very roughly, with $\chi^2/\rm dof \sim 2$. This is likely to be due to the shape of the exponential cut-off (which is assumed in PEXRAV) being substantially different from the shape of the cut-off of thermal Comptonization (see, for example, Zdziarski et al. 2003). This provides an argument against utilizing simple phenomenological models in the analysis of BHB spectra.
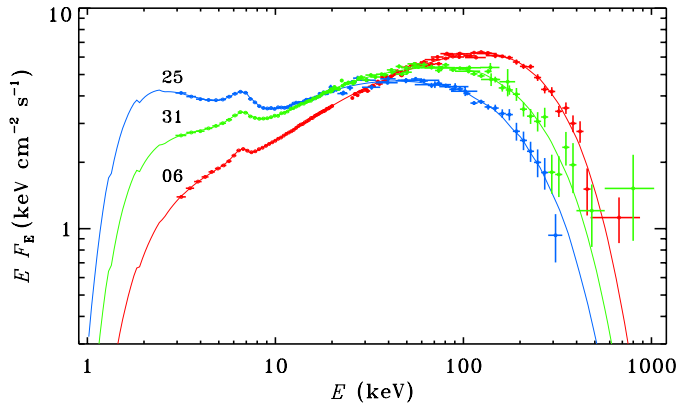
Figure 1. Broad-band spectra of Cyg X-1 as observed by *RXTE* and OSSE (with the respective observation number from Table 1) and the best-fitting models. Theoretical curves represent model 1 for observations 6, 25 and 31 (see Section 3). All of the figures are colour in the online version of the paper on *Synergy*.

3.2 Comptonization model and broad-band spectra

The hard-state spectra are well described by thermal Comptonization (Gierliński et al. 1997; Poutanen 1998; Frontera et al. 2001), with a weak soft excess. To describe Comptonization we use the XSPEC model EQPAIR (see Coppi 1999; G99). The spectrum of seed photons is from a pseudo-Newtonian accretion disc (see G99). The parameters of emission are expressed through the compactness

$$\ell = \frac{L\sigma_T}{\mathcal{R} m_e c^3}, \qquad (1)$$

where L is the source luminosity, $\mathcal{R}$ is the radius of the emitting spherical cloud, and σ_T is the Thomson cross-section. We consider here thermal plasma. The model is characterized by the following parameters: ℓ_s is the compactness of soft seed photons (assumed here to be 1); ℓ_h/ℓ_s is the ratio of the dimensionless energy dissipation rate in a hot cloud to ℓ_s; kT_{max} is the maximal colour temperature of the disc (at 9.5 gravitational radii, $R_g = GM/c^2$, or at the inner radius of the disc, if it is cut-off at larger value); τ_p is the Thomson optical depth corresponding to the ions; R is the reflection amplitude. Because there are large ($\sim$25 per cent at 1σ) errors on kT_{max}, we decided to fix it at the common value of 200 eV. The model computed the coronal temperature, kT_e, and the total optical depth, τ, from the background electrons and produced $e^{\pm}$ pairs self-consistently from the energy and pair balance. For the assumed compactness, pair production is negligible for all considered spectra, and thus the resulting total optical depth $\tau = \tau_p$. In the fits, we assume the inner disc radius of $6R_g$ (this parameter only has an effect on the relativistic smearing of the reflected component, which could hardly be resolved with present energy resolution).

The normalization of EQPAIR, corresponding to the disc component, is $f_c M^2 \cos i /(D^2 \beta_c^4)$, where f_c is the covering factor, M is the black hole mass in units of the solar mass, D is the distance to the source in units of kpc, and β_c is the ratio of the colour temperature to the effective temperature.

At low energies, the effect of the interstellar absorption is clearly visible. The addition of an additional soft component leads to further improvement of the fits. Such soft excesses were observed in both the hard state by Di Salvo et al. (2001) and in a flat state (similar to that analysed here) by Frontera et al. (2001) in *BeppoSAX* data. However, this component, whose nature we address below, is relatively weak in the case of 1991 and 1997 (observations G1–G4, 05–17) hard-state

data. The spectra observed in 1996, 1998 and 1999 (observations 1–4, 18–38) appear similar in overall shape to those of the hard state, but are significantly softer (see Fig. 2). The soft excess in the flat state is stronger.

We stress that the requirement of an additional soft excess is implied only by the joint PCA/HEXTE/OSSE data, because the PCA data cover a too narrow energy range. Even if the actual spectrum in the PCA 3–20 keV band is not a power law but is, for example, concave, a good fit with a power law plus reflection (model 0) can be still achieved. However, the real strength of Compton reflection can be significantly different.

Because the data require an additional component only in a relatively narrow range ($\sim$3–10 keV), the parameters of the soft excess cannot be constrained accurately. Below we consider a number of physically realistic scenarios of its nature. In each of the considered models, we restrict the parameters controlling its spectral shape to values that make its flux significant only at low energies, and we fit only its normalization. These fits allow us to completely describe the broad-band spectra and to constrain the parameters of main continuum.

3.2.1 High temperature of the optically thick disc

The additional component may, in principle, be emitted by the hottest part of the optically thick disc provided its temperature is high enough. We find that the spectra of the observations 1–4, 18–38 can be well fitted with $kT_{max} \sim 1$ keV. However, Di Salvo et al. (2001) have shown that the spectral decomposition of the *BeppoSAX* data of Cyg X-1 in the hard state requires the presence of both the soft blackbody disc photons (with $kT_{max} \simeq 0.1$–0.2 keV) and an additional soft excess component. Therefore, we consider this model to be not appropriate.

3.2.2 Hybrid model

We also tried to apply hybrid thermal + non-thermal EQPAIR model to the spectra. Most of the data require nearly non-thermal injection and the resulting spectrum becomes a power law directed by the PCA part of the spectrum. Because the observed hard tail is not a power law, large reflection appears to mimic the cut-off region, but it is still not enough to describe both the soft excess below 10 keV

Table 2. The best-fitting parameters for model 0 (fitted to the low-energy *Ginga* and *RXTE*/PCA data only).

| No.	N_H (10^{22} cm^{-2})	Γ	R	σ (keV)	EW (eV)	χ^2/dof
			1991			
G1	$0.5^{+1.2}_{-0}$	$1.63^{+0.09}_{-0.03}$	$0.39^{+0.19}_{-0.08}$	$0.46^{+0.81}_{-0.46}$	134^{+47}_{-66}	3/11
G2	$0.5^{+1.2}_{-0}$	$1.62^{+0.09}_{-0.03}$	$0.37^{+0.18}_{-0.09}$	$0.58^{+0.93}_{-0.58}$	152^{+54}_{-73}	4/11
G3	$1.3^{+1.3}_{-0.7}$	$1.60^{+0.10}_{-0.07}$	$0.26^{+0.17}_{-0.13}$	$0.60^{+0.95}_{-0.60}$	142^{+77}_{-75}	3/11
G4	$1.4^{+1.2}_{-0.9}$	$1.69^{+0.09}_{-0.08}$	$0.41^{+0.19}_{-0.16}$	$0.42^{+0.97}_{-0.42}$	82^{+36}_{-60}	5/12
			1996			
01	1.2 ± 0.2	1.80 ± 0.02	0.51 ± 0.05	0.68 ± 0.16	96 ± 19	24/43
02	0.6 ± 0.2	1.79 ± 0.02	0.48 ± 0.05	0.80 ± 0.12	148 ± 20	20/43
03	0.7 ± 0.2	1.80 ± 0.02	0.48 ± 0.04	0.72 ± 0.12	138 ± 19	20/43
04	1.2 ± 0.2	1.89 ± 0.02	0.66 ± 0.05	0.87 ± 0.16	112 ± 19	24/43
			1997			
05	1.3 ± 0.3	1.65 ± 0.02	0.25 ± 0.04	$0.40^{+0.22}_{-0.40}$	66 ± 20	19/39
06	1.2 ± 0.3	1.65 ± 0.02	0.24 ± 0.04	$0.38^{+0.19}_{-0.33}$	76 ± 20	27/39
07	1.0 ± 0.3	1.71 ± 0.02	0.35 ± 0.05	$0.52^{+0.21}_{-0.26}$	79 ± 22	16/39
08	1.0 ± 0.3	1.69 ± 0.02	0.29 ± 0.04	$0.44^{+0.19}_{-0.24}$	86 ± 21	35/39
09	1.2 ± 0.3	1.71 ± 0.02	0.36 ± 0.05	$0.56^{+0.21}_{-0.25}$	82 ± 22	26/39
10	1.2 ± 0.2	1.69 ± 0.02	0.32 ± 0.05	$0.43^{+0.20}_{-0.27}$	77 ± 20	22/39
11	1.2 ± 0.2	1.70 ± 0.02	0.32 ± 0.04	$0.35^{+0.20}_{-0.35}$	69 ± 19	15/39
12	3.1 ± 0.2	1.72 ± 0.02	0.38 ± 0.05	$0^{+0.42}_{-0}$	32 ± 12	23/39
13	2.1 ± 0.3	1.71 ± 0.02	0.37 ± 0.05	$0.30^{+0.55}_{-0.30}$	56 ± 19	21/39
14	1.1 ± 0.3	1.70 ± 0.02	0.37 ± 0.05	$0.43^{+0.20}_{-0.29}$	78 ± 21	21/39
15	2.1 ± 0.3	1.70 ± 0.02	0.35 ± 0.05	$0.15^{+0.53}_{-0.15}$	41 ± 18	17/39
16	2.1 ± 0.2	1.69 ± 0.02	0.41 ± 0.05	$0.17^{+0.43}_{-0.17}$	57 ± 16	22/39
17	2.7 ± 0.3	1.71 ± 0.02	0.36 ± 0.05	$0.03^{+2.79}_{-0.03}$	37 ± 17	19/39
			1998			
18	1.2 ± 0.2	1.87 ± 0.02	0.54 ± 0.05	0.73 ± 0.16	99 ± 20	19/39
19	1.2 ± 0.2	1.84 ± 0.02	0.48 ± 0.05	0.71 ± 0.17	95 ± 20	19/39
20	1.2 ± 0.2	1.85 ± 0.02	0.50 ± 0.05	0.71 ± 0.17	96 ± 20	17/39
21	1.1 ± 0.2	1.83 ± 0.02	0.47 ± 0.05	0.71 ± 0.17	93 ± 20	14/39
22	0.7 ± 0.2	1.83 ± 0.02	0.47 ± 0.05	0.69 ± 0.14	123 ± 21	20/39
23	0.7 ± 0.2	1.82 ± 0.02	0.46 ± 0.05	0.72 ± 0.13	135 ± 21	17/39
			1999			
24	$0.5^{+0.1}_{-0}$	2.09 ± 0.01	0.89 ± 0.07	0.93 ± 0.12	203 ± 23	28/33
25	$0.5^{+0.1}_{-0}$	2.30 ± 0.02	1.38 ± 0.16	1.12 ± 0.16	249 ± 34	48/33
26	$0.5^{+0.1}_{-0}$	2.23 ± 0.01	1.15 ± 0.10	1.09 ± 0.13	247 ± 27	43/33
27	$0.5^{+0.2}_{-0}$	2.05 ± 0.01	0.81 ± 0.08	0.95 ± 0.14	188 ± 25	14/33
28	0.7 ± 0.3	2.05 ± 0.03	0.84 ± 0.10	0.82 ± 0.15	161 ± 26	32/33
29	$0.5^{+0.1}_{-0}$	2.01 ± 0.01	0.74 ± 0.07	0.91 ± 0.15	185 ± 25	22/33
30	$0.5^{+0.1}_{-0}$	2.20 ± 0.01	1.07 ± 0.07	1.03 ± 0.11	237 ± 22	27/33
31	$0.5^{+0.2}_{-0}$	1.94 ± 0.02	0.61 ± 0.06	0.82 ± 0.13	170 ± 22	25/33
32	1.1 ± 0.3	1.85 ± 0.03	0.50 ± 0.06	0.54 ± 0.23	79 ± 22	20/33
33	$0.7^{+0.3}_{-0.2}$	1.87 ± 0.03	0.53 ± 0.07	0.63 ± 0.19	113 ± 26	30/33
34	$0.6^{+0.3}_{-0.1}$	1.86 ± 0.03	0.47 ± 0.08	0.61 ± 0.19	125 ± 28	14/33
35	$0.5^{+0.2}_{-0}$	1.88 ± 0.02	0.52 ± 0.05	0.65 ± 0.13	141 ± 18	25/33
36	$0.5^{+0.2}_{-0}$	1.88 ± 0.02	0.55 ± 0.06	0.72 ± 0.14	156 ± 22	25/33
37	1.2 ± 0.3	1.92 ± 0.03	0.62 ± 0.07	0.68 ± 0.18	109 ± 24	27/33
38	1.2 ± 0.3	1.98 ± 0.03	0.77 ± 0.08	0.78 ± 0.16	125 ± 24	39/33

and the hard tail, in which the systematic difference between the data and the model remains. Therefore, we ruled out this model.
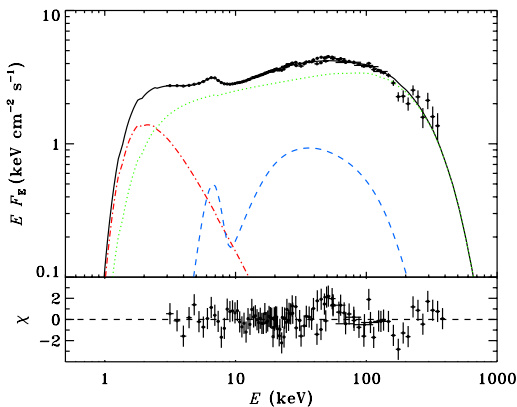
3.2.3 Two thermal Comptonization components

The soft component can be described by additional thermal Comptonization (Di Salvo et al. 2001; Frontera et al. 2001). We use the model 1, PHABS(COMPTT+EQPAIR+GAUSSIAN), where EQPAIR gives the main Comptonization and COMPTT (Titarchuk 1994) the additional soft component. Because the parameters of the soft excess are rather weakly constrained by our data, we fixed the parameters of COMPTT at $kT_e = 20$ keV and $\tau = 1$. Such a model produces a soft power law that does not extend to very high energies. This model fitted to the data of observation 24 is shown in Fig. 3. In
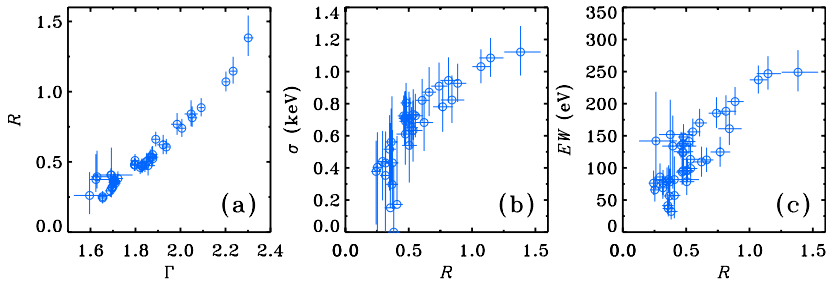
Figure 2. Correlations between parameters for model 0 (PEXRAV). (a) The reflection amplitude, R, versus the photon spectral index, Γ. (b) The relativistic smearing Gaussian width σ versus reflection R. (c) The Fe Kα 6.4-keV line equivalent width versus R.

Figure 3. The model spectrum with two thermal Comptonization components (model 1, Section 3.2.3) fitted to the *RXTE*+OSSE observation 24 (from 1999). The spectral components of the fit are shown by the dotted (green), dot-dashed (red) and dashed (blue) curves, which correspond to the main thermal Comptonization continuum, the additional thermal Comptonization with $kT_e = 20$ keV and $\tau = 1$, and the Compton reflection including the Fe line, respectively. The solid (black) curve shows the total spectrum. The lower panel shows the residuals of the fit.

spite of its simplicity, it yields a relatively good description of the data.

The fit parameters are given in Table 3, and the dependences between various model parameters are shown in Fig. 4. We also quote the values of the spectral index Γ of the power law obtained from the least-squares fitting of the logarithm of the intrinsic model flux at a logarithmic energy grid in the 2–10 keV range (chosen to enable comparison with the results of other papers).

The meaning of the normalization of EQPAIR has been described in Section 3.2. Substituting $f_c = 1$, $M = 10\,\mathrm{M_\odot}$, $i = 50°$, $D = 2.0$ kpc (see references in G99; Frontera et al. 2001) and $\beta_c = 1.7$ (Shimura & Takahara 1995), we expect the normalization of $\simeq 1.92$. The lower normalization of the obtained fits (see Table 3) is caused either by a larger $\beta_c \sim 1.77$–1.98 or by a smaller covering factor f_c. A slightly smaller, than the assumed disc temperature of 200 eV, can also reduce the normalization. On the other hand, some flat-state normalizations are larger than the expected value of 1.92. This cannot be explained by changing f_c (a smaller covering factor can only reduce the normalization), but could be a result of somewhat larger inner

disc radius or larger temperature. The largest observed normalizations correspond to $kT_{\max} \sim 220$–245 eV.

We see that there is a clear anticorrelation between the strength of the soft component and the hardness of spectrum expressed in terms of ℓ_h/ℓ_s. There is also a correlation between τ and ℓ_h/ℓ_s. The reflection amplitude is correlated with the Fe line equivalent width and anticorrelated with ℓ_h/ℓ_s (while at high values of ℓ_h/ℓ_s the anticorrelation possibly breaks down).

The electron temperature kT_e is a calculated parameter and no errors on it can be obtained from fitting. However, we estimated its 1σ limits using its extremal values within the uncertainties of the parameters controlling spectral shape, i.e. ℓ_h/ℓ_s and τ. This estimation gives us a possible conservative error on kT_e of about 15 keV for both models 1 and 2. Taking this into account, no correlations between kT_e–flux and $kT_e - \ell_h/\ell_s$ are apparent.

3.2.4 Thermal continuum and non-thermal Comptonization component

As an alternative to the second thermal Compton component, we consider here addition of a non-thermal Comptonization component. We find that such a non-thermal component can describe both the soft excess and the MeV non-thermal tail observed in hard states by the Compton Telescope (COMPTEL; McConnell et al. 2002), while neither of these components can be described by the main thermal Compton emission. This model fitted to the spectrum 24 is shown in Fig. 5. Note that the COMPTEL data are shown for illustration only and were not taken into account in the fitting. The used model 2 consists of PHABS(EQPAIR+EQPAIR+GAUSSIAN), in which the second EQPAIR component produces the non-thermal spectrum. In EQPAIR, the available power is supplied in part into heating electrons and in part into their acceleration, with the resulting steady-state electron distribution calculated self-consistently. The compactness corresponding to the acceleration is hereafter denoted as $\ell_{\rm nth}$. Then the relative fraction of the input power going into the non-thermal acceleration is $\ell_{\rm nth}/\ell_h$, where ℓ_h (as before) corresponds to the total rate of energy dissipation in the plasma.

For that additional component, we assumed that all the available power goes into non-thermal acceleration, i.e. $\ell_{\rm nth}/\ell_h = 1$. Note that the resulting self-consistent electron distribution is not purely non-thermal but hybrid, i.e. it does contain a low-energy Maxwellian heated by Compton and Coulomb interactions. We further assume $R = 0$, the power-law index of the accelerated electrons of $\Gamma_{\rm inj} = 2.4$ (see Poutanen & Coppi 1998; G99; Frontera et al. 2001; McConnell et al. 2002), the minimum and maximum Lorentz factors of the power law of $\gamma_{\min} = 1.3$ and $\gamma_{\max} = 1000$, respectively,

Table 3. The best-fitting parameters for model 1.

| Obs.	N_H^a	ℓ_h/ℓ_s	τ	R	σ	EW	N^b	F_{tot}^c	F_{add}^d	kT_e^e	Γ^f	χ^2/dof
G1	$1.1^{+0.8}_{-0.6}$	$13.8^{+0.9}_{-0.7}$	$1.39^{+0.07}_{-0.08}$	$0.38^{+0.04}_{-0.03}$	$0.67^{+0.32}_{-0.34}$	189^{+57}_{-51}	$1.36^{+0.05}_{-0.06}$	5.32	0.11	90	1.62	49/73
G2	1.3 ± 0.8	$15.6^{+1.3}_{-0.8}$	$1.58^{+0.12}_{-0.05}$	$0.35^{+0.04}_{-0.05}$	$0.87^{+0.36}_{-0.63}$	235^{+75}_{-63}	$1.63^{+0.06}_{-0.09}$	7.24	0.24	82	1.59	58/74
G3	1.4 ± 0.2	$14.0^{+0.9}_{-1.6}$	$1.34^{+0.08}_{-0.20}$	$0.26^{+0.06}_{-0.04}$	$0.60^{+0.92}_{-0.60}$	151^{+54}_{-47}	$1.13^{+0.10}_{-0.04}$	4.18	0	94	1.62	53/73
G4	$2.0^{+0.7}_{-0.9}$	13.4 ± 1.8	$1.36^{+0.29}_{-0.30}$	$0.26^{+0.09}_{-0.08}$	$0.63^{+0.41}_{-0.31}$	132^{+57}_{-48}	$1.04^{+0.14}_{-0.11}$	3.83	0.14	90	1.63	53/73
01	2.6 ± 0.2	$10.3^{+0.4}_{-0.1}$	$1.31^{+0.06}_{-0.03}$	$0.27^{+0.02}_{-0.01}$	$1.00^{+0.16}_{-0.13}$	173^{+26}_{-20}	$1.99^{+0.03}_{-0.09}$	7.32	1.26	86	1.68	501/478
02	2.1 ± 0.3	$9.76^{+0.18}_{-0.24}$	$1.32^{+0.02}_{-0.03}$	$0.29^{+0.01}_{-0.02}$	$1.11^{+0.12}_{-0.13}$	240^{+25}_{-27}	$2.50^{+0.06}_{-0.04}$	8.83	1.56	83	1.69	531/493
03	$2.2^{+0.3}_{-0.2}$	$10.2^{+0.1}_{-0.2}$	$1.47^{+0.05}_{-0.03}$	0.26 ± 0.02	$1.02^{+0.14}_{-0.13}$	227^{+28}_{-29}	2.18 ± 0.03	8.04	1.49	75	1.68	542/506
04	2.9 ± 0.2	$8.77^{+0.18}_{-0.14}$	$1.38^{+0.03}_{-0.02}$	0.31 ± 0.01	1.12 ± 0.11	215^{+23}_{-19}	$2.85^{+0.05}_{-0.07}$	10.0	2.44	77	1.71	529/493
05	$1.6^{+0.4}_{-0.3}$	$11.8^{+1.2}_{-0.4}$	$1.09^{+0.16}_{-0.05}$	0.22 ± 0.02	$0.48^{+0.22}_{-0.23}$	77^{+18}_{-16}	$1.30^{+0.03}_{-0.09}$	4.46	0.08	110	1.65	61/73
06	1.8 ± 0.4	$12.8^{+0.3}_{-0.5}$	$1.29^{+0.03}_{-0.08}$	$0.19^{+0.02}_{-0.01}$	$0.54^{+0.19}_{-0.21}$	96 ± 19	$1.05^{+0.04}_{-0.02}$	3.99	0.19	95	1.64	374/402
07	$1.9^{+0.3}_{-0.4}$	12.0 ± 0.4	$1.24^{+0.13}_{-0.07}$	0.22 ± 0.02	$0.75^{+0.19}_{-0.23}$	121^{+24}_{-27}	$1.54^{+0.04}_{-0.06}$	5.80	0.52	96	1.65	367/415
08	$2.0^{+0.3}_{-0.4}$	$11.9^{+0.3}_{-0.4}$	$1.41^{+0.03}_{-0.04}$	$0.20^{+0.02}_{-0.01}$	$0.68^{+0.19}_{-0.21}$	118^{+21}_{-22}	$1.47^{+0.04}_{-0.02}$	5.43	0.46	84	1.65	404/415
09	2.3 ± 0.3	$12.0^{+0.4}_{-0.2}$	$1.41^{+0.03}_{-0.06}$	0.23 ± 0.02	$0.85^{+0.20}_{-0.18}$	131^{+26}_{-21}	$1.56^{+0.03}_{-0.04}$	5.98	0.62	84	1.65	350/415
10	$1.6^{+0.5}_{-0.4}$	$11.3^{+0.3}_{-0.4}$	$1.18^{+0.08}_{-0.05}$	$0.24^{+0.02}_{-0.01}$	$0.56^{+0.19}_{-0.18}$	102^{+21}_{-18}	$1.43^{+0.02}_{-0.04}$	4.92	0.25	99	1.66	301/334
11	4.1 ± 0.3	$11.6^{+0.4}_{-0.5}$	$1.19^{+0.06}_{-0.03}$	0.23 ± 0.02	$0.41^{+0.74}_{-0.41}$	54^{+18}_{-17}	1.53 ± 0.04	5.72	0.58	99	1.65	193/236
12	4.2 ± 0.3	$11.8^{+0.6}_{-0.5}$	$1.20^{+0.10}_{-0.03}$	$0.23^{+0.02}_{-0.01}$	$0.43^{+0.78}_{-0.41}$	55^{+20}_{-17}	$1.52^{+0.04}_{-0.06}$	5.77	0.61	99	1.65	202/238
13	$2.5^{+1.0}_{-0.8}$	12.8 ± 0.4	$1.45^{+0.05}_{-0.03}$	0.22 ± 0.02	$0.58^{+0.24}_{-0.18}$	106^{+19}_{-20}	$1.45^{+0.04}_{-0.03}$	5.74	0.47	83	1.63	369/411
14	2.2 ± 0.3	$12.4^{+0.4}_{-0.3}$	1.34 ± 0.03	0.24 ± 0.02	$0.74^{+0.19}_{-0.17}$	126^{+23}_{-19}	$1.58^{+0.03}_{-0.04}$	6.25	0.63	90	1.64	397/415
15	3.2 ± 0.3	13.6 ± 0.5	$1.26^{+0.11}_{-0.04}$	0.19 ± 0.02	$0.60^{+0.19}_{-0.30}$	75^{+27}_{-19}	$1.29^{+0.03}_{-0.04}$	5.51	0.57	99	1.62	201/244
16	3.4 ± 0.3	13.7 ± 0.2	1.61 ± 0.04	0.24 ± 0.01	$0.55^{+0.19}_{-0.16}$	98^{+19}_{-14}	1.47 ± 0.02	6.53	0.76	76	1.62	446/402
17	3.8 ± 0.3	$12.9^{+0.6}_{-0.4}$	$1.33^{+0.15}_{-0.10}$	$0.19^{+0.02}_{-0.03}$	$0.60^{+0.29}_{-0.38}$	73 ± 21	$1.25^{+0.02}_{-0.05}$	5.12	0.55	92	1.63	345/415
18	2.5 ± 0.3	8.13 ± 0.15	$1.23^{+0.02}_{-0.03}$	$0.28^{+0.02}_{-0.01}$	$0.98^{+0.13}_{-0.11}$	182^{+23}_{-21}	2.32 ± 0.04	7.09	1.41	84	1.73	512/489
19	2.7 ± 0.3	$9.43^{+0.23}_{-0.09}$	$1.61^{+0.04}_{-0.03}$	0.21 ± 0.02	$1.02^{+0.15}_{-0.12}$	182^{+25}_{-21}	$1.67^{+0.02}_{-0.03}$	5.87	1.29	66	1.69	457/502
20	2.6 ± 0.3	$9.14^{+0.20}_{-0.09}$	$1.45^{+0.03}_{-0.06}$	$0.24^{+0.01}_{-0.02}$	$1.00^{+0.15}_{-0.12}$	182^{+26}_{-21}	$1.79^{+0.02}_{-0.03}$	6.11	1.29	73	1.70	472/502
21	2.6 ± 0.4	$9.91^{+2.16}_{-2.68}$	$1.36^{+0.59}_{-0.43}$	$0.20^{+0.11}_{-0.14}$	$0.94^{+0.18}_{-0.14}$	161^{+46}_{-42}	$1.83^{+0.56}_{-0.42}$	6.52	1.28	81	1.68	46/73
22	$2.1^{+0.3}_{-0.4}$	$8.96^{+2.38}_{-2.05}$	$1.19^{+0.43}_{-0.55}$	$0.24^{+0.08}_{-0.13}$	0.90 ± 0.12	188^{+25}_{-19}	$2.13^{+0.58}_{-0.55}$	6.86	1.21	90	1.71	45/73
23	2.0 ± 0.4	$8.57^{+1.55}_{-1.42}$	$1.29^{+0.25}_{-0.65}$	$0.26^{+0.14}_{-0.09}$	$0.89^{+0.12}_{-0.11}$	192^{+30}_{-23}	$2.14^{+0.58}_{-0.16}$	6.57	1.10	81	1.72	43/73
24	$1.6^{+0.3}_{-0.2}$	$5.43^{+0.68}_{-0.19}$	$1.08^{+0.13}_{-0.03}$	0.36 ± 0.03	$0.99^{+0.09}_{-0.08}$	337^{+28}_{-23}	$1.85^{+0.06}_{-0.27}$	4.71	1.46	83	1.82	389/409
25	1.5 ± 0.2	$4.70^{+0.57}_{-0.29}$	$1.04^{+0.17}_{-0.06}$	$0.36^{+0.04}_{-0.06}$	$0.98^{+0.08}_{-0.07}$	395^{+33}_{-33}	$2.46^{+0.14}_{-0.24}$	6.51	2.71	81	1.85	355/409
26	1.3 ± 0.3	$4.08^{+0.92}_{-0.49}$	$0.89^{+0.25}_{-0.14}$	$0.40^{+0.08}_{-0.09}$	1.01 ± 0.07	382^{+28}_{-28}	$2.54^{+0.29}_{-0.42}$	5.44	1.92	90	1.89	48/67
27	1.8 ± 0.3	5.95 ± 0.30	$1.10^{+0.05}_{-0.06}$	0.33 ± 0.03	1.02 ± 0.10	305 ± 30	$2.19^{+0.10}_{-0.09}$	5.92	1.81	84	1.80	386/409
28	$1.7^{+0.2}_{-0.3}$	$5.75^{+0.35}_{-0.50}$	$1.21^{+0.14}_{-0.16}$	$0.33^{+0.06}_{-0.04}$	$0.98^{+0.09}_{-0.09}$	335^{+31}_{-27}	1.74 ± 0.16	4.71	1.52	75	1.81	389/409
29	1.6 ± 0.3	$6.01^{+0.32}_{-0.24}$	$1.09^{+0.05}_{-0.04}$	0.33 ± 0.03	$0.99^{+0.11}_{-0.10}$	295^{+30}_{-29}	$1.98^{+0.07}_{-0.09}$	5.06	1.28	85	1.80	394/409
30	$0.9^{+0.2}_{-0.3}$	$2.71^{+1.06}_{-0.23}$	$0.46^{+0.26}_{-0.19}$	$0.62^{+0.08}_{-0.05}$	0.97 ± 0.08	328^{+19}_{-25}	$4.06^{+0.48}_{-0.15}$	5.67	1.46	141†	1.93	52/67
31	1.7 ± 0.3	$6.74^{+0.32}_{-0.39}$	$1.09^{+0.06}_{-0.14}$	$0.29^{+0.04}_{-0.03}$	0.93 ± 0.11	253^{+27}_{-26}	$1.91^{+0.11}_{-0.09}$	5.10	1.12	89	1.77	390/409
32	2.4 ± 0.3	$9.38^{+0.37}_{-0.40}$	$1.37^{+0.10}_{-0.08}$	$0.22^{+0.03}_{-0.02}$	0.83 ± 0.15	151^{+22}_{-25}	1.49 ± 0.06	5.08	1.01	79	1.70	393/409
33	$2.1^{+0.2}_{-0.6}$	$7.94^{+0.56}_{-1.26}$	$1.23^{+0.09}_{-0.24}$	$0.27^{+0.07}_{-0.02}$	$0.83^{+0.15}_{-0.19}$	179^{+33}_{-32}	$1.93^{+0.29}_{-0.10}$	5.76	1.16	84	1.73	62/67
34	$1.5^{+0.3}_{-0.5}$	$7.08^{+0.35}_{-0.89}$	$1.08^{+0.13}_{-0.19}$	$0.29^{+0.07}_{-0.04}$	$0.74^{+0.17}_{-0.18}$	174 ± 31	$1.83^{+0.25}_{-0.11}$	4.64	0.67	92	1.76	43/67
35	$1.4^{+0.3}_{-0.4}$	$7.05^{+0.53}_{-0.73}$	$1.08^{+0.11}_{-0.16}$	$0.30^{+0.06}_{-0.04}$	0.78 ± 0.11	206^{+25}_{-23}	$2.03^{+0.19}_{-0.12}$	5.26	0.85	91	1.76	40/67
36	$1.6^{+0.4}_{-0.6}$	$7.46^{+0.73}_{-1.24}$	$1.07^{+0.15}_{-0.20}$	$0.32^{+0.06}_{-0.05}$	$0.88^{+0.12}_{-0.17}$	230^{+27}_{-39}	$1.92^{+0.30}_{-0.14}$	5.35	0.96	94	1.75	62/64
37	$3.3^{+1.3}_{-1.3}$	$6.52^{+1.11}_{-1.01}$	$1.04^{+0.22}_{-0.21}$	$0.35^{+0.06}_{-0.07}$	$0.98^{+0.26}_{-0.23}$	179^{+31}_{-42}	$2.02^{+0.30}_{-0.23}$	5.53	1.39	92	1.78	40/62
38	$3.2^{+0.6}_{-1.2}$	$6.24^{+0.67}_{-0.72}$	$0.96^{+0.14}_{-0.13}$	0.37 ± 0.05	$0.96^{+0.19}_{-0.18}$	199 ± 28	$2.29^{+0.25}_{-0.18}$	6.33	1.80	98	1.78	41/62

[a]Hydrogen column density, in units of 10^{22} cm^{-2}. [b]Normalization of the EQPAIR model component. [c]The unabsorbed total model flux, in units of 10^{-8} erg cm^{-2} s^{-1}. [d]The unabsorbed model flux of the COMPTT component, in units of 10^{-8} erg cm^{-2} s^{-1}. [e]Temperature of the emitting plasma in keV (for the EQPAIR component). [f]Photon spectral index of the EQPAIR component in the 2–10 keV range.

kT_{max} equal to that of the main component, $\ell_h/\ell_s = 1$, and $\tau_p = 1$. No pair production is required, and τ is found to be equal to τ_p.

The best-fitting parameters are presented in Table 4 and correlations between them are shown in Figs 6 and 11. The normalization of the thermal EQPAIR component corresponds to $\beta_c = 1.63$–2.01,

values similar to those obtained with model 1. The strength of the additional (non-thermal) component is again clearly anticorrelated with the spectral hardness. The anticorrelation between R and ℓ_h/ℓ_s is apparent and corresponds to the R–Γ correlation that we discuss in Section 4.4. The values of R and the Fe line equivalent width are well correlated and can be approximated by a linear function
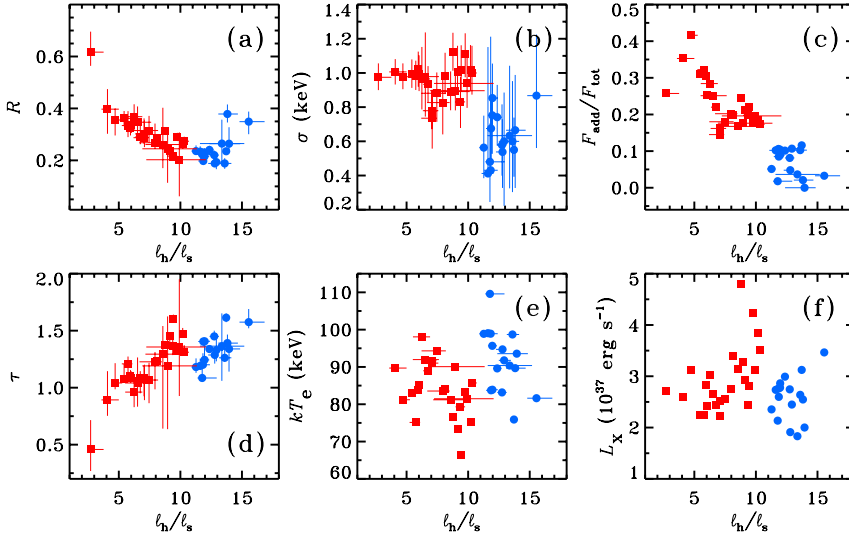
Figure 4. Dependences of the spectral parameters for model 1 (Section 3.2.3) fitted to the 1991 and 1997 (blue filled circles) and the 1996, 1998 and 1999 data (red filled squares) on the Compton amplification factor of the main Comptonization component ℓ_h/ℓ_s. (a) The reflection fraction R; (b) the relativistic smearing Gaussian width σ at 6.4 keV; (c) ratio of the additional thermal Comptonization flux to the total flux; (d) Thomson optical depth of the main Comptonization continuum component τ; (e) electron temperature of the main Comptonization component kT_e; (f) total luminosity of the Comptonizing cloud (assuming $D = 2$ kpc).
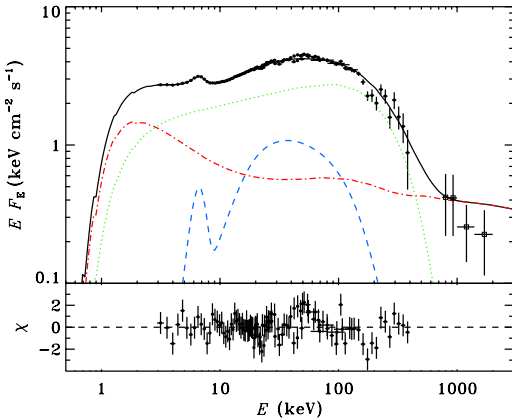
Figure 5. The model spectrum with the thermal and non-thermal Comptonization components (model 2, Section 3.2.4) fitted to the *RXTE*+OSSE observation 24 (from 1999) together with the COMPTEL (McConnell et al. 2002) hard-state data (marked by squares). The spectral components of the fit are shown by the dotted (green), dot-dashed (red) and dashed (blue) curves, which correspond to the main thermal Comptonization continuum, the additional non-thermal Comptonization and the Compton reflection including the Fe line, respectively. The solid curve shows the total spectrum. The lower panel shows the residuals of the fit.

passing through zero (see Fig. 11c). Again, there is a correlation between τ and ℓ_h/ℓ_s. The electron temperature does not seemingly depend on the hardness, but the spread becomes smaller at larger ℓ_h/ℓ_s where $kT_e \sim 90$ keV.

4 DISCUSSION

4.1 Absorption

As noted in Section 3, the hydrogen column density N_H was free in our fits. We find that our data require absorption significantly larger than $0.6 \pm 0.2 \times 10^{22}$ cm^{-2}, which is derived from the reddening towards the companion star (Balucińska-Church et al. 1995).

Cyg X-1 is known to show X-ray dips in its light curve, caused by obscuration by the stellar wind from the companion star. During dips, the absorption increases up to $N_H = 20 \times 10^{22}$ cm^{-2}. The absorption shows strong orbital phase dependence with maximal column density around phase 0, when companion star is in front of the black hole (Balucińska-Church et al. 2000; Feng & Cui 2002). We plotted the fitted values of N_H versus Cyg X-1 orbital phase (see Fig. 7), using the ephemeris with the time of the primary minimum at 50234.79 MJD and the period of 5.599829 d (LaSala et al. 1998; Brocksopp et al. 1999). We see a good correlation of N_H with the orbital phase, which indicates that variable absorption can indeed be caused by the companion's wind obscuring the X-rays from the black hole.

We note that because our models are relatively complicated in the range of 3–10 keV (consisting of absorption, Comptonization together with the seed photon emission and a soft excess), and also the PCA energy range is affected by absorption rather weakly, it is difficult to determine the exact values of N_H, even though the derived values of the parameter are in the range quoted by other authors and its relative changes are quite remarkable.

4.2 Spectral variability patterns

Using *CGRO*/BATSE and *RXTE*/ASM data, Zdziarski et al. (2002) showed that Cyg X-1 has two types of variability: changes of

Table 4. The best-fitting parameters for model 2.

| Obs.	$N_H{}^a$	ℓ_h/ℓ_s	τ	R	σ	EW	N^b	$F_{tot}{}^c$	$F_{add}{}^d$	$kT_e{}^e$	Γ^f	χ^2/dof
G1	$0.9^{+0.5}_{-0.4}$	$14.2^{+1.1}_{-0.9}$	1.41 ± 0.08	0.40 ± 0.04	$0.61^{+0.32}_{-0.38}$	182^{+59}_{-52}	1.29 ± 0.09	5.32	0.21	90	1.62	49/73
G2	$1.0^{+0.5}_{-0.6}$	$16.4^{+2.1}_{-1.2}$	$1.62^{+0.17}_{-0.08}$	0.37 ± 0.05	$0.78^{+0.34}_{-0.32}$	210^{+68}_{-60}	$1.50^{+0.12}_{-0.20}$	8.23	0.93	81	1.58	56/74
G3	$1.4^{+0.4}_{-0.2}$	$14.0^{+0.9}_{-1.7}$	$1.35^{+0.08}_{-0.21}$	$0.26^{+0.07}_{-0.03}$	$0.58^{+0.93}_{-0.58}$	144^{+57}_{-50}	$1.12^{+0.10}_{-0.06}$	4.19	0.01	93	1.62	53/73
G4	$1.6^{+0.5}_{-0.6}$	$13.8^{+2.9}_{-1.9}$	$1.37^{+0.34}_{-0.30}$	$0.30^{+0.09}_{-0.08}$	$0.56^{+0.95}_{-0.58}$	122^{+55}_{-48}	$0.97^{+0.13}_{-0.15}$	3.81	0.23	91	1.62	53/73
01	2.0 ± 0.2	11.4 ± 0.3	$1.39^{+0.02}_{-0.04}$	0.34 ± 0.02	$0.85^{+0.13}_{-0.14}$	148^{+19}_{-21}	$1.63^{+0.07}_{-0.05}$	7.55	1.98	83	1.66	498/478
02	1.4 ± 0.2	10.5 ± 0.2	1.36 ± 0.02	$0.35^{+0.02}_{-0.01}$	0.95 ± 0.10	203^{+21}_{-19}	2.12 ± 0.06	9.00	2.30	83	1.67	528/493
03	$1.6^{+0.1}_{-0.2}$	$11.1^{+0.1}_{-0.1}$	$1.55^{+0.03}_{-0.04}$	0.32 ± 0.02	0.85 ± 0.11	182^{+22}_{-17}	$1.81^{+0.05}_{-0.04}$	8.28	2.34	73	1.66	527/506
04	$2.1^{+0.1}_{-0.2}$	$9.86^{+0.19}_{-0.24}$	$1.49^{+0.03}_{-0.07}$	$0.41^{+0.02}_{-0.03}$	0.93 ± 0.12	167^{+23}_{-17}	$2.16^{+0.09}_{-0.06}$	10.45	3.86	73	1.69	515/493
05	$1.7^{+0.2}_{-0.3}$	$13.0^{+0.5}_{-0.6}$	$1.21^{+0.05}_{-0.03}$	0.21 ± 0.02	$0.51^{+0.21}_{-0.23}$	81^{+18}_{-17}	$1.17^{+0.05}_{-0.02}$	4.62	0.31	101	1.63	60/73
06	1.6 ± 0.2	$13.0^{+0.4}_{-0.5}$	$1.29^{+0.03}_{-0.07}$	0.20 ± 0.01	$0.47^{+0.18}_{-0.20}$	90^{+18}_{-16}	$1.01^{+0.04}_{-0.03}$	4.02	0.29	95	1.63	372/402
07	$1.5^{+0.2}_{-0.3}$	12.5 ± 0.4	$1.27^{+0.13}_{-0.08}$	0.25 ± 0.02	0.64 ± 0.18	108 ± 21	$1.42^{+0.06}_{-0.08}$	5.85	0.76	95	1.64	366/415
08	1.6 ± 0.2	$12.2^{+0.4}_{-0.3}$	1.42 ± 0.03	0.23 ± 0.02	$0.56^{+0.18}_{-0.19}$	106^{+20}_{-19}	$1.37^{+0.04}_{-0.05}$	5.45	0.65	84	1.64	401/415
09	$1.9^{+0.2}_{-0.3}$	$12.7^{+0.3}_{-0.4}$	$1.44^{+0.03}_{-0.07}$	0.27 ± 0.02	$0.72^{+0.20}_{-0.18}$	110^{+27}_{-18}	$1.40^{+0.06}_{-0.04}$	6.11	0.98	84	1.64	348/415
10	$1.4^{+0.4}_{-0.3}$	$11.5^{+0.7}_{-0.4}$	$1.17^{+0.13}_{-0.03}$	$0.26^{+0.02}_{-0.03}$	$0.55^{+0.19}_{-0.25}$	103^{+21}_{-26}	$1.37^{+0.05}_{-0.08}$	4.97	0.40	101	1.66	301/334
11	$3.7^{+0.1}_{-0.3}$	$12.3^{+0.4}_{-0.7}$	$1.22^{+0.10}_{-0.05}$	$0.27^{+0.03}_{-0.02}$	$0.07^{+0.56}_{-0.07}$	43^{+19}_{-10}	$1.38^{+0.07}_{-0.06}$	5.82	0.90	99	1.64	193/236
12	$3.6^{+0.4}_{-0.2}$	$12.3^{+1.1}_{-0.4}$	$1.22^{+0.18}_{-0.04}$	0.27 ± 0.03	$0.21^{+0.62}_{-0.21}$	46^{+21}_{-12}	$1.38^{+0.04}_{-0.06}$	5.78	0.85	99	1.64	201/238
13	2.5 ± 0.8	$13.4^{+0.6}_{-0.5}$	$1.47^{+0.06}_{-0.03}$	0.25 ± 0.02	$0.50^{+0.21}_{-0.19}$	88^{+21}_{-22}	$1.31^{+0.06}_{-0.07}$	5.96	0.91	83	1.62	365/411
14	1.7 ± 0.2	$13.0^{+0.5}_{-0.4}$	$1.37^{+0.13}_{-0.03}$	0.28 ± 0.02	$0.61^{+0.18}_{-0.19}$	109^{+20}_{-19}	$1.42^{+0.05}_{-0.06}$	6.35	0.96	89	1.63	391/415
15	$2.8^{+0.2}_{-0.4}$	$14.6^{+0.6}_{-0.8}$	$1.32^{+0.09}_{-0.08}$	0.23 ± 0.02	$0.42^{+0.34}_{-0.40}$	62^{+27}_{-17}	$1.14^{+0.07}_{-0.04}$	5.63	0.92	96	1.61	198/244
16	2.8 ± 0.2	14.0 ± 0.3	$1.49^{+0.02}_{-0.03}$	$0.30^{+0.01}_{-0.02}$	$0.41^{+0.17}_{-0.22}$	85^{+16}_{-15}	1.38 ± 0.04	6.67	1.02	84	1.62	436/402
17	3.3 ± 0.2	13.7 ± 0.5	$1.42^{+0.08}_{-0.13}$	0.22 ± 0.02	$0.37^{+0.30}_{-0.37}$	58^{+19}_{-15}	$1.11^{+0.05}_{-0.04}$	5.16	0.83	87	1.62	342/415
18	$2.0^{+0.1}_{-0.3}$	$9.53^{+0.40}_{-0.23}$	$1.59^{+0.04}_{-0.05}$	0.33 ± 0.02	$0.83^{+0.13}_{-0.12}$	150^{+32}_{-16}	$1.70^{+0.07}_{-0.08}$	7.34	2.47	67	1.69	481/489
19	$2.0^{+0.2}_{-0.3}$	$10.4^{+0.1}_{-0.3}$	$1.66^{+0.01}_{-0.05}$	0.29 ± 0.02	$0.86^{+0.13}_{-0.15}$	148^{+22}_{-21}	$1.34^{+0.06}_{-0.03}$	6.10	1.99	66	1.67	455/502
20	1.9 ± 0.2	$9.93^{+0.43}_{-0.18}$	$1.49^{+0.03}_{-0.06}$	$0.31^{+0.01}_{-0.02}$	0.85 ± 0.13	151^{+19}_{-20}	$1.47^{+0.04}_{-0.05}$	6.30	1.95	73	1.69	467/502
21	1.7 ± 0.2	$9.73^{+2.14}_{-1.38}$	$1.31^{+0.25}_{-0.36}$	$0.30^{+0.04}_{-0.06}$	0.82 ± 0.14	139 ± 20	$1.64^{+0.30}_{-0.46}$	6.47	1.73	84	1.69	47/73
22	1.3 ± 0.2	$8.70^{+2.75}_{-1.41}$	$1.08^{+0.32}_{-0.26}$	$0.34^{+0.05}_{-0.06}$	$0.76^{+0.13}_{-0.12}$	160^{+30}_{-20}	$1.98^{+0.39}_{-0.47}$	6.82	1.59	99	1.71	44/73
23	1.2 ± 0.3	$7.25^{+2.36}_{-0.56}$	$0.97^{+0.31}_{-0.42}$	0.39 ± 0.04	0.80 ± 0.12	171^{+22}_{-21}	$2.29^{+0.34}_{-0.46}$	6.32	1.11	103	1.75	43/73
24	$0.7^{+0.3}_{-0.1}$	$6.61^{+0.37}_{-0.31}$	$1.42^{+0.09}_{-0.05}$	$0.49^{+0.06}_{-0.04}$	$0.89^{+0.08}_{-0.11}$	301^{+22}_{-39}	$1.15^{+0.06}_{-0.09}$	5.03	2.55	66	1.78	379/409
25	0.5^{+0}_{-0}	$6.06^{+0.73}_{-0.67}$	$1.47^{+0.20}_{-0.22}$	$0.63^{+0.12}_{-0.09}$	$0.88^{+0.05}_{-0.07}$	346^{+26}_{-27}	$1.17^{+0.07}_{-0.14}$	4.28	2.22	62	1.80	354/409
26	0.5^{+0}_{-0}	$5.29^{+1.47}_{-1.15}$	$1.30^{+0.38}_{-0.29}$	$0.59^{+0.08}_{-0.06}$	0.93 ± 0.07	348 ± 27	$1.32^{+0.35}_{-0.28}$	3.69	1.70	67	1.83	52/67
27	$1.0^{+0.1}_{-0.2}$	$6.86^{+0.98}_{-0.78}$	$1.28^{+0.23}_{-0.17}$	$0.46^{+0.06}_{-0.05}$	$0.91^{+0.10}_{-0.11}$	263^{+28}_{-29}	$1.48^{+0.21}_{-0.14}$	4.21	1.39	76	1.77	380/409
28	0.8 ± 0.2	$6.63^{+0.36}_{-0.31}$	$1.43^{+0.08}_{-0.05}$	$0.50^{+0.05}_{-0.04}$	$0.90^{+0.08}_{-0.11}$	299^{+23}_{-35}	$1.14^{+0.07}_{-0.09}$	3.31	1.20	66	1.78	379/409
29	0.9 ± 0.2	$6.51^{+0.77}_{-0.39}$	$1.14^{+0.05}_{-0.06}$	$0.47^{+0.04}_{-0.05}$	0.91 ± 0.10	264 ± 27	$1.51^{+0.13}_{-0.17}$	3.74	1.01	83	1.78	388/409
30	0.6 ± 0.1	$3.68^{+0.81}_{-0.79}$	$0.86^{+0.49}_{-0.14}$	$0.75^{+0.09}_{-0.07}$	$0.93^{+0.08}_{-0.07}$	324^{+26}_{-23}	$2.17^{+0.65}_{-0.73}$	3.91	1.58	89	1.91	49/67
31	1.0 ± 0.2	$7.26^{+0.47}_{-0.41}$	$1.15^{+0.14}_{-0.12}$	0.38 ± 0.04	0.85 ± 0.11	228^{+26}_{-25}	$1.53^{+0.11}_{-0.15}$	3.86	0.84	87	1.75	388/409
32	1.8 ± 0.2	$10.4^{+0.3}_{-0.6}$	$1.47^{+0.04}_{-0.13}$	0.29 ± 0.02	$0.69^{+0.15}_{-0.16}$	128^{+22}_{-21}	$1.19^{+0.11}_{-0.04}$	4.03	0.75	76	1.67	388/409
33	$1.4^{+0.2}_{-0.4}$	$8.26^{+1.38}_{-0.82}$	$1.24^{+0.19}_{-0.20}$	$0.35^{+0.04}_{-0.05}$	$0.69^{+0.18}_{-0.15}$	151^{+38}_{-21}	1.63 ± 0.21	4.44	0.81	83	1.72	62/67
34	1.0 ± 0.3	$7.18^{+1.54}_{-0.83}$	$1.08^{+0.25}_{-0.16}$	$0.34^{+0.03}_{-0.04}$	$0.66^{+0.17}_{-0.16}$	160^{+30}_{-26}	$1.66^{+0.10}_{-0.30}$	3.65	0.46	92	1.75	42/67
35	0.9 ± 0.2	$7.48^{+1.20}_{-1.33}$	$1.13^{+0.21}_{-0.15}$	$0.36^{+0.05}_{-0.04}$	0.70 ± 0.11	189^{+23}_{-22}	$1.74^{+0.23}_{-0.25}$	4.15	0.63	89	1.75	41/67
36	1.1 ± 0.4	$8.15^{+1.22}_{-1.33}$	$1.16^{+0.17}_{-0.29}$	$0.38^{+0.07}_{-0.05}$	$0.78^{+0.12}_{-0.11}$	203^{+26}_{-25}	$1.56^{+0.31}_{-0.25}$	4.21	0.74	89	1.73	58/64
37	$2.3^{+1.0}_{-0.9}$	$7.27^{+2.05}_{-1.28}$	$1.14^{+0.35}_{-0.24}$	$0.45^{+0.08}_{-0.06}$	$0.79^{+0.19}_{-0.18}$	149^{+29}_{-27}	$1.54^{+0.35}_{-0.35}$	5.72	2.16	88	1.75	41/62
38	2.2 ± 0.9	$7.26^{+1.12}_{-1.02}$	$1.11^{+0.20}_{-0.19}$	$0.49^{+0.08}_{-0.06}$	$0.79^{+0.16}_{-0.13}$	169^{+25}_{-24}	$1.60^{+0.34}_{-0.25}$	4.58	1.32	89	1.75	45/62

^{a}Hydrogen column density, in units of 10^{22} cm^{-2}. ^{b}Normalization of the thermal EQPAIR model component. ^{c}The unabsorbed total model flux (without reflection) in units of 10^{-8} erg cm^{-2} s^{-1}. ^{d}The unabsorbed model flux from the non-thermal component, in units of 10^{-8} erg cm^{-2} s^{-1}. ^{e}Temperature of the emitting plasma in keV (for the thermal EQPAIR component). ^{f}Photon spectral index of the thermal EQPAIR component in the 2–10 keV range.

flux without spectral slope change and pivoting at ~50 keV, which produces anticorrelation of the fluxes in the soft and hard parts of the spectrum. However, these instruments do not provide detailed spectral information, giving fluxes only in some energy intervals. The effective photon spectral indices using fluxes in two energy bands and calculated in the wide (20–300 keV) energy interval, where real spectra experience a cut-off, should be treated with caution. Now it is possible to check the results of Zdziarski et al. (2002) using our set of observations, on which we have detailed spectral information in the wide energy
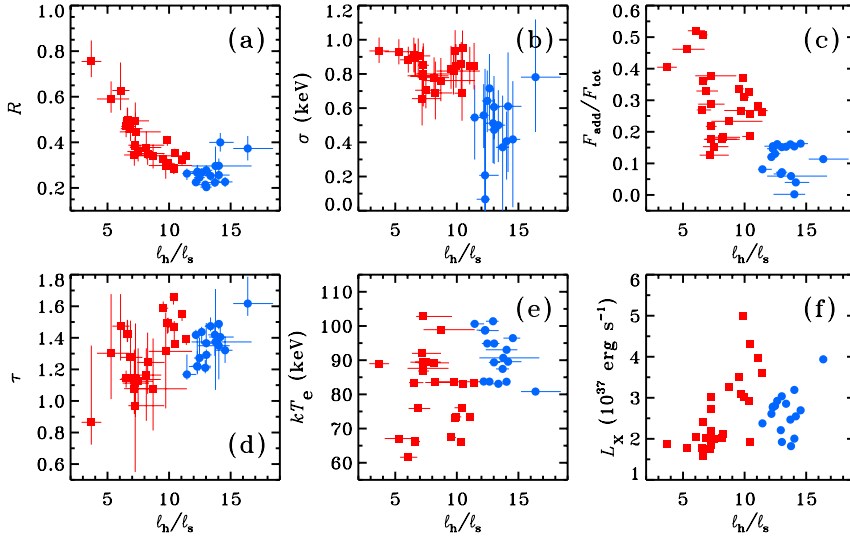
Figure 6. Dependences of the spectral parameters for model 2 (Section 3.2.4) fitted to the 1991 and 1997 (blue filled circles) and the 1996, 1998 and 1999 data (red filled squares) on the Compton amplification factor of the main Comptonization component ℓ_h/ℓ_s. The meaning of the axes is the same as in Fig. 4, except (c) the ratio of the additional non-thermal Comptonization flux in model 2 to the total flux.
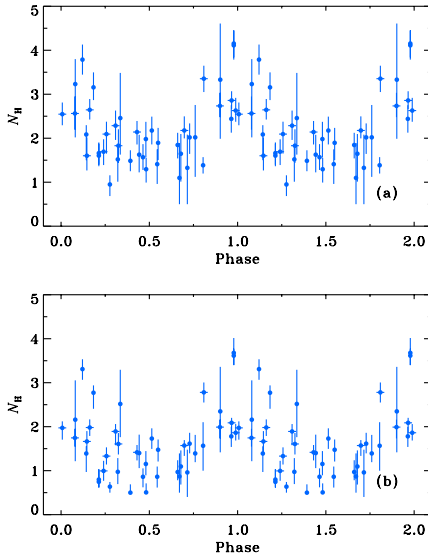
Figure 7. (a) Fitted value of absorption column density N_H for model 1 versus orbital phase of the binary system. (b) Same, for model 2. Distributions are repeated twice for clarity. N_H is in units of 10^{22} cm^{-2}.

range. For this purpose, we use the model spectra obtained from model 1.

In Fig. 8 we present the spectra related to different time periods. It is possible to see that 1991, 1996–1998 spectra only change their normalization. However, the spectral slope is different for various
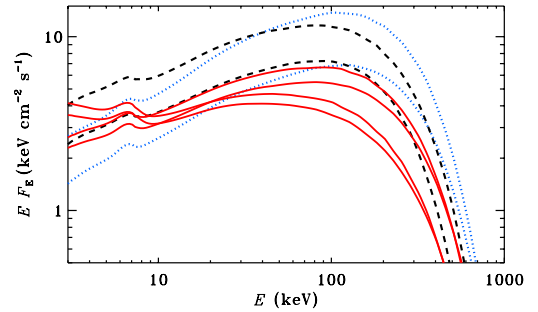
Figure 8. Sample of the spectra from different periods. Lowest and highest spectra from each time period are shown: red solid lines, 1999; blue dotted lines, 1991 (the 1997 spectra are similar to them); black dashed lines, 1996 and 1998. The 1991+1997 and 1996+1998 data form two groups with slightly different spectral slopes.

years and forms two groups: 1991 + 1997 and 1996 + 1998 spectra. In the 1999 data, we can again see normalization changes (see pairs of red solid curves) as well as pivoting behaviour.

The Γ–flux correlations are shown in Fig. 9. It is clearly seen that the 1991 and 1996–1998 data do not show dependence between flux and Γ. The 1999 data show clear anticorrelation between Γ and flux at low energies (3–12 keV) and correlation at high energies (20–100, 100–300 keV), which indicates the pivoting behaviour with the pivot energy between 12 and ~50 keV. In Fig. 9(d) (see also fig. 8 in Zdziarski et al. 2002), it can be seen that spectra from 1996 and 1998 are somewhat softer at high energies than the hard-state spectra from 1991 and 1997, but the fluxes in all energy intervals generally correlate with each other. The 1999 spectra show clearly different dependence: the high-energy fluxes are corre-
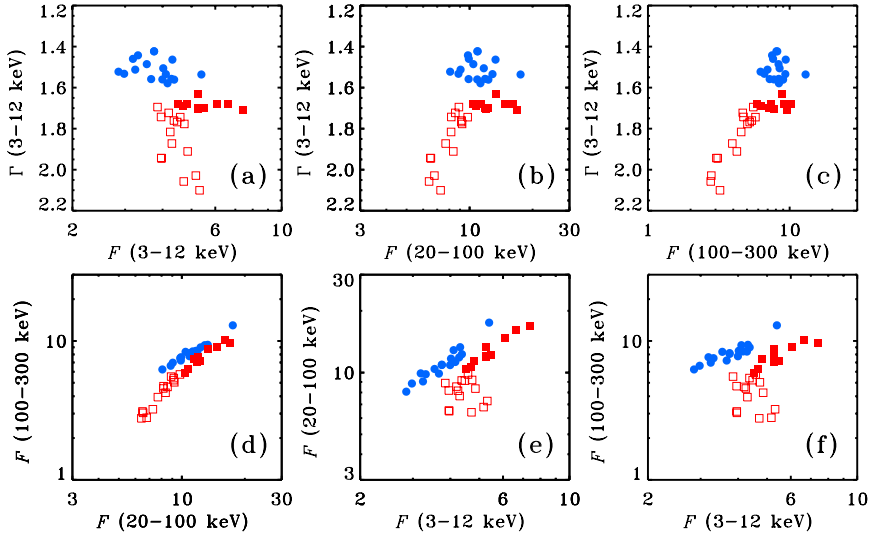
Figure 9. Flux–spectral index (3–12 keV) and flux–flux correlations. Respective energy intervals are indicated along the axis. The 1991 and 1997 data are indicated by blue filled circles, 1996 and 1998 by red filled squares, and 1999 by red open squares. All fluxes are in units of keV cm^{-2} s^{-1}.

lated, but there is a clear anticorrelation between 3–12 and 100–300 keV fluxes due to pivoting. The timing behaviour has also changed its nature in late 1998, as was pointed out by Pottschmidt et al. (2003).

4.3 Quasi-periodic oscillation frequencies

Among the data sets we have studied, there are timing data for 33 observations available from the recent paper by Axelsson, Borgonovo & Larsson (2005). This allows us to check the relation between the characteristic frequencies in the power density spectra and the spectral parameters. In the work of Axelsson et al. (2005), several values of QPO frequencies ν_{QPO} might be determined during one observation, and for these data points we assume the averaged middle frequency and consider the uncertainty from lower to higher of obtained values. In agreement with the earlier results of GCR99, we find a clear anticorrelation between the characteristic frequencies of the aperiodic variability and ℓ_h/ℓ_s (Fig. 10), indicating an apparent connection between QPO frequencies and the parameters of the Comptonizing region. This provides an argument (but not a proof) in favour of the presence of a hot inner corona and a variable inner radius of the surrounding disc.

The frequency–hardness correlation can be described by a power law $\nu_{QPO} \propto (\ell_h/\ell_s)^{-\alpha}$ with $\alpha = -1.48 \pm 0.04$. The best fit is shown by the solid curve in Fig. 10. A similar correlation was observed by Pottschmidt et al. (2003) and Nowak, Wilms & Dove (2002).

4.4 Comparison between phenomenological and physical spectral models and *R*–Γ correlation

Fig. 11 compares the results obtained with the simple phenomenological model of power law + reflection in the 3–20 keV energy range (model 0) with those from our model 2 applied to the 3–1000 keV range. More elaborate and physically justified models utilizing the full energy range of our data do not change the pic-
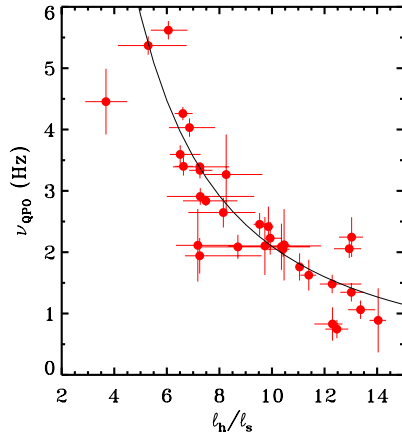
Figure 10. Dependence between QPO frequencies and ℓ_h/ℓ_s. The ℓ_h/ℓ_s are best-fitting values from model 2. The QPO frequencies are from Axelsson et al. (2005). The solid curve shows the best power-law fit $\nu_{QPO} \propto (\ell_h/\ell_s)^{-1.48}$.

ture qualitatively. On the quantitative level, we find that the simple power law + reflection spectral fits to the 3–20 keV data overestimated the amplitude of the reflected component *R* and the slope Γ of the primary Comptonization continuum. We confirm, however, that the simple models did correctly rank the spectra according to the strength of the reflected component and slope of the Comptonized radiation, as demonstrated in the original publications on this subject (GCR99; ZLS99). This is also illustrated by the lower three panels of Fig. 11. The difference of the obtained parameters comes from the fact that, for wide-energy observations, the main thermal
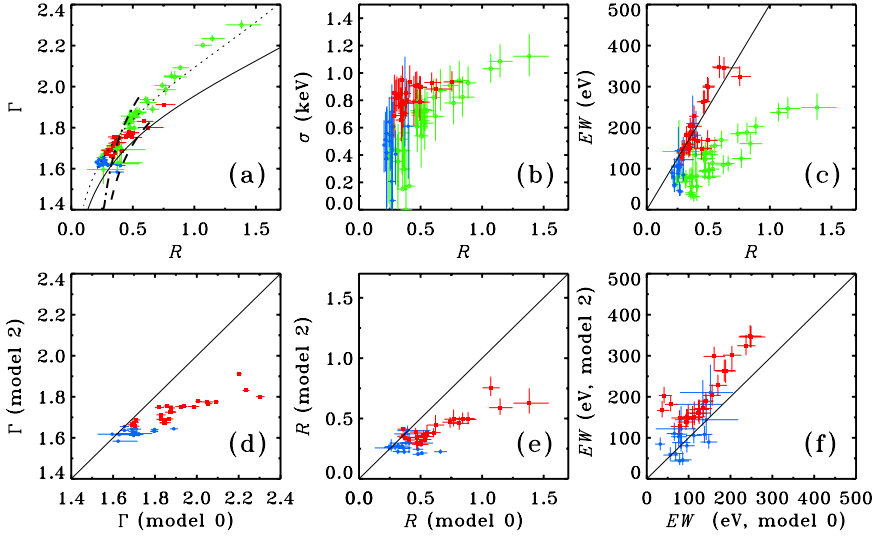
Figure 11. (a)–(c) Correlations obtained using model 0 (green open circles), model 1 (blue filled circles) and model 2 (red filled squares). (a) The spectral slope Γ versus reflection scaling factor R correlation. For model 0, Γ is a fitting parameter, for model 2 the index of a power-law fitted to the spectral model in the 2–10 keV range. The solid curve shows the dependence predicted for the ejection model (Beloborodov 1999a; MBP01) with the parameters of $i = 50°$, the albedo of 0.15, $\mu_s = 0.5$ and $\tau = 2$, the dotted curve shows the same for $\mu_s = 0.4$. The dashed curve shows the dependence predicted by the model with a hot spherical corona and cold overlapping disc (Poutanen et al. 1997; ZLS99) with the blackbody temperature of 0.2 keV (see Section 4.4 for details). The dot–dashed curve shows the same model with the dissipation effect taken into account (dissipation parameter $L_{int} = 1$, $L_{int}/4\pi = 1$ at $r < 1$; see Appendix A for details). (b) The relativistic smearing Gaussian width σ at 6.4 keV versus R. (c) The equivalent width of the 6.4-keV line equivalent width versus R. The straight line is EW (eV) = $500R$. (d)–(f) Γ, R and equivalent width obtained from model 2 versus those from model 0.

Comptonization component that describes well the hard energy tail may lie well below the observed flux in the 2–10 keV range (see Figs 3 and 5) and has a different slope in this band. The difference is largest for 1996, 1998 and 1999 data, while in the 1991 and 1997 cases the soft excess is weak and parameters obtained with the physical models are similar to those obtained with the phenomenological models.

In Fig. 11(a), we see a clear correlation between Γ and R. For comparison, we also show the dependences predicted by the plasma ejection model of Beloborodov (1999a,b) and MBP01 (cylindrical geometry with $h/r = 2$), using the geometric parameter of that model of $\mu_s = 0.4$ and 0.5, $i = 50°$, the albedo of the reflecting medium of 0.15 and $\tau = 2$. We used the dependence between the amplification factor A of Comptonization and Γ from MBP01. We also compared our data with the dependence expected in the model of ZLS99, assuming the blackbody temperature of 0.2 keV, appropriate for Cyg X-1, with one minor change. In the original paper, all the reflection luminosity was assumed to reach the observer. Reflection amplitude is an integral that consists of two parts, from the disc inside the corona and from the outer part of it. We multiplied the part of luminosity coming from the former part by $e^{-\tau}$, to approximately take into account scattering of radiation in the corona ($\tau = 1$ was chosen). We see that this model cannot quantitatively describe the presented data. Moreover, taking into account intrinsic dissipation in the disc (see Appendix A for details) will further increase the slope of the dependence, making the discrepancy larger. Intrinsic dissipation becomes important for a small inner disc radius (when reflection is relatively large) and the increase of the soft seed photon flux in that case makes the spectrum softer (see Beloborodov 2001).

4.5 Physical scenario

The hard spectral state of BHBs is commonly defined as the state in which the spectrum is dominated by the hard Comptonization component, without significant contribution of the blackbody-type emission from the optically thick accretion disc. Naturally, the hard state is not characterized by a single, uniquely defined spectrum, but rather includes a continuum of spectral shapes with the major spectral parameters varying in a rather broad range. The diversity of the hard-state spectra reflects the position of the source with respect to the 'bottom hard' state and the soft state. Quantitatively, this position can be characterized by the strength of the reflected component (reflection scaling factor R or Fe line equivalent width) or properties of the main Comptonized component (Comptonization parameter, or Compton amplification factor $A = \ell_h/\ell_s$, or the photon index Γ in the low-energy limit) or characteristic frequencies of the aperiodic variability. The existence of good correlations between all these quantities suggests that they all are an equally good measure of the source position within the hard state. The results found in earlier work (GCR99; ZLS99; Gilfanov et al. 2000; Gilfanov, Churazov & Revnivtsev 2004) and presented in the previous sections of this paper suggest the following pattern of spectral and temporal variability. An increase of the strength of the reflected component is accompanied by an increase of the width of the Fe line, an increase of the characteristic QPO frequencies and a softening of the Comptonized component observed as an increase of its photon index Γ in the low-energy limit.

We find from our spectral analysis that in the 'bottom hard' state the broad-band spectrum (3–1000 keV) is mostly described by the single thermal Comptonization spectrum with superimposed

component due to reflection of the primary emission from relatively cool and neutral, or partly ionized, optically thick matter (the accretion disc), with an additional relatively weak soft component. As the source moves towards the soft state, the strength of the reflected component increases, and the soft component becomes more significant. Considering the 3–1000 keV energy range covered by our data, this spectral component reveals itself most clearly in the $E \lesssim 10$ keV energy domain as the 'soft excess'. Another independent indication of spectral complexity is the gamma-ray power-law tail detected at MeV energies by the COMPTEL telescope (McConnell et al. 2002).

From the point of view of the formal fit quality, the $E \lesssim 10$ keV excess can be described equally well by an additional thermal Comptonization component due to low temperature, low Comptonization parameter plasma or by non-thermal Comptonization with the power-law index of accelerated electrons $\Gamma_{\rm inj} \sim 2$–3. Owing to the complex shape of the continuum at these energies defined by the superposition of several spectral components, these two possibilities cannot be easily discriminated based solely on the low-energy data. The task is further complicated by the rather limited low-energy coverage provided by the PCA instrument, $E > 3$ keV. However, the above possibilities predict very different behaviour in the $\sim$MeV energy domain, where the main thermal Comptonization component diminishes and the power-law tail due to the non-thermal Comptonization should reveal itself. As the OSSE sensitivity and energy range are insufficient to probe the existence of the MeV tail correlated with the $E < 10$ keV excess, we cannot, strictly speaking, give preference to either of these two models.

There are however several additional considerations to be taken into account. (i) COMPTEL detected a weak MeV tail in the averaged hard-state data for Cyg X-1 (McConnell et al. 2002). The slope and amplitude of this tail are qualitatively consistent with the extrapolation of the non-thermal Comptonized component, required to explain the $E \lesssim 10$ keV excess (Fig. 5). (ii) In the soft state, the non-thermal power law is the dominant (the only) high-energy component. (iii) The $E \lesssim 10$ keV excess is more pronounced in the spectra characterized by large reflection and the rather steep slope of the main Comptonized component, i.e. in those sufficiently close to the soft state. Its strength seems to increase with the increase of the reflection. These arguments suggest that the non-thermal origin of the $E \lesssim 10$ keV excess is more plausible. We note that the 1991 and 1997 data show much weaker excess. This may be explained by the lower relative luminosity of the non-thermal Comptonization component, which therefore reveals itself at lower energies, below the $E = 3$ keV threshold of the PCA instrument, but can be detected by instruments which have a response at lower energies, i.e. *BeppoSAX* (see Di Salvo et al. 2001; Frontera et al. 2001).

The overall qualitative picture can be outlined as follows. The overall geometry of the accretion flow is adequately represented by the truncated disc model with the inner radius of the standard optically thick geometrically thin disc varying from $\sim 6 R_{\rm g}$ to $\sim$ several tens of $R_{\rm g}$. Inside this radius, the accretion flow proceeds via quasi-spherical optically hot flow. The plausible mechanism governing the transition from the disc accretion to the coronal flow is the disc evaporation process as proposed by Meyer & Meyer-Hofmeister (1994). The geometrically thin disc gives rise to the soft blackbody-type component. In addition, due to dynamo, solar-type magnetic flares can be produced above the accretion disc (Galeev et al. 1979). The electrons there can be accelerated and form non-thermal distribution. Comptonization of the disc emission on these electrons results in the power-law-like Comptonized emission. The inner optically thin flow gives rise to the thermal Comptonization

component. The relative contributions of non-thermal and thermal Comptonized components are defined by the fractions of the gravitational energy released in the disc (i.e. outside $R_{\rm in}$) and in the inner hot flow (inside $R_{\rm in}$). The position of the transition radius is defined by the mass accretion rate and is modified by the irradiation-related effects. The transition radius decreases as the mass accretion rate increases.

The QPOs are due to some processes in the transition region near $R_{\rm in}$ and approximately scale with the Keplerian frequency and other characteristic time-scales of the coronal flow and standard accretion disc in the transition region.

The configuration with the large inner disc radius, probably $R_{\rm in} \gtrsim 50$–$100 R_{\rm g}$, corresponds to the classical hard state. The main features of this 'bottom hard' state are low strength of the reflected continuum, relatively narrow fluorescent Fe line of small equivalent width, large Comptonization parameter of the thermal Comptonized component (hard spectra with the low-energy photon index $\Gamma \sim 1.6$), and low frequencies of QPOs. As only a small fraction of the gravitational energy is released in the disc, the contribution of the non-thermal component is small and the spectrum is adequately described by thermal Comptonization.

As the mass accretion rate increases, the transition radius decreases, and the disc moves towards the compact object. This results in an increase of the reflection, broader fluorescent Fe line, larger QPO frequencies, and smaller $\ell_{\rm h}/\ell_{\rm s}$, i.e. a smaller Comptonization parameter in the inner hot flow. The contribution of the non-thermal component increases. The optical depth of the thermal plasma of the inner flow decreases due the shrinking of the inner hot flow as the disc extends towards the compact object.

The classical soft state (we ignore all the complications and substates here) corresponds to the accretion disc extending all the way towards the last stable orbit or very close to it. Correspondingly, the inner hot flow disappears and the dominant or the only hard component is that due to non-thermal Comptonization of the disc emission on the non-thermal electrons accelerated in the magnetic loops/flares above the disc.

The behaviour of the temperature of the thermal Comptonization component is unclear. It seems relatively constant, which suggests the possible presence of electron–positron pairs (see MBP01).

The physical scenario qualitatively outlined above is based on the truncated disc picture and on the assumption that the spectral evolution is governed by the change of the transition radius between the standard accretion disc and the hot inner flow. In this picture, many of the observed correlations can be explained naturally. However, the R–Γ correlation is significantly better quantitatively explained by the non-stationary corona model (MBP01), in which the governing parameter is the velocity of the blobs of emitting plasma relative to the accretion disc. We note that both models are geometrical in their nature and the predicted qualitative relations between the physical parameters are obtained with a number of simplifying assumptions. Therefore, the results of quantitative comparison of the model predictions with the observed pattern of the spectral variability should be interpreted with caution and any conclusions regarding the validity of either model based on such a comparison would be premature.

5 CONCLUSIONS

Based on the broad-band (3–1000 keV) data from simultaneous observations by *Ginga* and *CGRO*/OSSE in 1991 and PCA and HEXTE instruments aboard *RXTE* and OSSE in 1996–1999 we have studied the spectral variability of Cyg X-1.

(i) We confirm earlier results on R–Γ correlation. Considering the 3–20 keV data, we find very tight one-parameter relations between reflection, spectral index and the width of the Fe line.

(ii) More elaborate and physically justified models utilizing the full energy range of our data do not change the picture qualitatively. On the quantitative level, we find that the simple power law + reflection spectral fits to the 3–20 keV data overestimated the amplitude of the reflected component R and the slope Γ of the primary Comptonization continuum. We confirm, however, that the simple models did correctly rank the spectra according to the strength of the reflected component and slope of the Comptonized radiation, as demonstrated in the original publications on this subject (GCR99; ZLS99).

(iii) Based on the analysis of the broad-band data, we found that the spectra in our sample can be adequately described by the thermal Comptonized component with superposed reflection from the optically thick disc and a soft excess. This excess is relatively weak in the case of the hardest spectra of our sample ($\Gamma \sim 1.7$). As the strength of the reflection increases, the excess becomes much more significant. The presence of this excess was the primary reason for the simple spectral approximations of the 3–20 keV data to overestimate both R and Γ. The nature of this excess cannot be unambiguously determined from our data. Based on the circumstantial evidence we suggest that it is the lower energy part of the non-thermal Comptonized component with the power-law index of accelerated electrons $\Gamma_{\rm inj} \sim 2$–3. At higher energies, this non-thermal component reveals itself as a power law detected by COMPTEL at MeV energies in the average hard state spectrum of Cyg X-1.

(iv) We note the variability of the absorption correlated with the phase of binary system. These results confirm previous findings of the X-ray dips in the source.

(v) The overall pattern of spectral and temporal variability can be summarized as follows. An increase of the strength of the reflected component is accompanied by an increase of the width of the Fe line, an increase of the characteristic QPO frequencies and a softening of the Comptonized component observed as an increase of its photon index Γ in the low-energy limit or, equivalently, a decrease of the Compton amplification factor $\ell_{\rm h}/\ell_{\rm s}$. Simultaneously, the optical depth of the thermal Comptonization decreases and the fractional contribution of the non-thermal component to the total energy flux increases. The exact behaviour of the electron temperature in the hot inner flow is not constrained by our data.

(vi) We suggest a qualitative physical scenario naturally explaining the observed behaviour. In this scenario, the evolution of the spectral parameters is governed by the value of the transition radius between the standard optically thick accretion disc and the inner quasi-spherical hot flow. The thermal Comptonized component originates in the inner hot flow as a result of Comptonization of the soft photons emitted by the accretion disc. The origin of the non-thermal component is related to the optically thick disc; for example, it can be produced due to non-thermal electrons accelerated near the surface of the optically thick disc in the solar-type magnetic flares. The relative contributions of non-thermal and thermal components to the total energy flux depend on the fractions of the gravitational energy of accreting matter released in the optically thick disc and in the hot inner flow.

ACKNOWLEDGMENTS

REFERENCES

Arnaud K. A., 1996, in Jakoby G. H., Barnes J., eds, ASP Conf. Ser. Vol. 101, Astronomical Data Analysis Software and Systems V. Astron. Soc. Pac., San Francisco, p. 17
Axelsson M., Borgonovo L., Larsson S., 2005, A&A, 438, 999
Balucińska M., Hasinger G., 1991, A&A, 241, 439
Balucińska-Church M., Belloni T., Church M. J., Hasinger G., 1995, A&A, 302, L5
Balucińska-Church M., Church M. J., Charles P. A., Nagase F., LaSala J., Barnard R., 2000, MNRAS, 311, 861
Beloborodov A., 1999a, ApJ, 510, L123
Beloborodov A., 1999b, in Poutanen J., Svensson R., eds, ASP Conf. Ser. Vol. 161, High Energy Processes in Accreting Black Holes. Astron. Soc. Pac., San Francisco, p. 295
Beloborodov A., 2001, Adv. Space Res., 28, 411
Bisnovatyi-Kogan G. S., Blinnikov S. I., 1977, A&A, 59, 111
Brocksopp C., Tarasov A. E., Lyuty V. M., Roche P., 1999, A&A, 343, 861
Coppi P. S., 1992, ApJ, 258, 657
Coppi P. S., 1999, in Poutanen J., Svensson R., eds, ASP Conf. Ser. Vol. 161, High Energy Processes in Accreting Black Holes. Astron. Soc. Pac., San Francisco, p. 375
Di Salvo T., Done C., Życki P. T., Burderi L., Robba N. R., 2001, ApJ, 547, 1024
Done C., Mulchaey J. S., Mushotzky R. F., Arnaud K., 1992, ApJ, 395, 275
Ebisawa K., Ueda Y., Inoue H., Tanaka Y., White N. E., 1996, ApJ, 467, 419
Esin A. A., Narayan R., Cui W., Grove E. C., Zhang S.-N., 1998, ApJ, 505, 854
Feng Y. X., Cui W., 2002, ApJ, 564, 953
Frontera F. et al., 2001, ApJ, 546, 1027
Galeev A. A., Rosner R., Vaiana G. S., 1979, ApJ, 229, 318
Gierliński M., Zdziarski A. A., Done C., Johnson W. N., Ebisawa K., Ueda Y., Haardt F., Phlips B. F., 1997, MNRAS, 288, 958
Gierliński M., Zdziarski A. A., Poutanen J., Coppi P. S., Ebisawa K., Johnson W. N., 1999, MNRAS, 309, 496 (G99)
Gilfanov M., Churazov E., Revnivtsev M., 1999, A&A, 352, 182 (GCR99)
Gilfanov M., Churazov E., Revnivtsev M., 2000, in Zhao G., Wang J-J., Qiu H. M., Boerner G., eds, SGSC Conference Series, Vol. 1, Proceedings of the 5th Sino-German Workshop on Astrophysics, p. 114 (astro-ph/0002415)
Gilfanov M., Churazov E., Revnivtsev M., 2004, in Kaaret P., Lamb F. K., Swank J. H., eds, AIP Conf. Proc. 714, X-ray Timing: Rossi and Beyond. AIP, Melville, p. 97
Ichimaru S., 1977, ApJ, 214, 840
LaSala J., Charles P. A., Smith R. A. D., Balucinska-Church M., Church M. J., 1998, MNRAS, 301, 285
Li H., Miller J. A., 1997, ApJ, 478, L67
Ling J. C. et al., 1997, ApJ, 484, 375
McConnell M. L. et al., 1994, ApJ, 424, 933
McConnell M. L. et al., 2002, ApJ, 572, 984
Magdziarz P., Zdziarski A. A., 1995, MNRAS, 273, 837
Malzac J., Petrucci P.-O., 2002, MNRAS, 336, 1209
Malzac J., Beloborodov A., Poutanen J., 2001, MNRAS, 326, 417 (MBP01)
Matt G., 2001, in White N. E., Malaguti G., Palumbo G. G. C., eds, AIP Conf. Proc. 599, X-ray Astronomy. Stellar Endpoints, AGNs and the Diffuse X-ray Background. AIP, Melville, p. 209
Meyer F., Meyer-Hofmeister E., 1994, A&A, 288, 175
Meyer F., Liu B. F., Meyer-Hofmeister E., 2000, A&A, 354, L67

Miller K. A., Stone J. M., 2000, ApJ, 534, 398
Narayan R., Mahadevan R., Quataert E., 1998, in Abramowicz M. A., Björnsson G., Pringle J., eds, Theory of Black Hole Accretion Discs. Cambridge Univ. Press, Cambridge, p. 148
Nowak M. A., Wilms J., Dove J. B., 2002, MNRAS, 332, 856
Perola G. C., Matt G., Cappi M., Fiore F., Guainazzi M., Maraschi L., Petrucci P.-O., Piro L., 2002, A&A, 389, 802
Pottschmidt K. et al., 2003, A&A, 407, 1039
Poutanen J., 1998, in Abramowicz M., Björnsson G., Pringle J., eds, Theory of Black Hole Accretion Discs. Cambridge Univ. Press, Cambridge, p. 100
Poutanen J., Coppi P., 1998, Phys. Scr., T77, 57
Poutanen J., Svensson R., 1996, ApJ, 470, 249
Poutanen J., Krolik J. H., Ryde F., 1997, MNRAS, 292, L21
Revnivtsev M., Gilfanov M., Churazov E., 1999, A&A, 347, L23
Revnivtsev M., Gilfanov M., Churazov E., 2001, A&A, 380, 520
Różańska A., Czerny B., 2000, A&A, 360, 1170
Shakura N. I., Sunyaev R. A., 1973, A&A, 24, 337
Shapiro S. L., Lightman A. P., Eardley D. M., 1976, ApJ, 204, 187
Shimura T., Takahara F., 1995, ApJ, 445, 780
Sunyaev R. A., Titarchuk L. G., 1980, A&A, 86, 121
Sunyaev R. A., Trümper J., 1979, Nat, 279, 506
Svensson R., Zdziarski A. A., 1994, ApJ, 436, 599
Titarchuk L., 1994, ApJ, 434, 570
Tout C. A., Pringle J. E., 1992, MNRAS, 259, 604
Weaver K. A., Krolik J. H., Pier E. A., 1998, ApJ, 498, 213
Zdziarski A. A., Gierliński M., 2004, Progr. Theor. Phys. Suppl., 155, 99
Zdziarski A. A., Gierliński M., Gondek D., Magdziarz P., 1996, A&AS, 120, 553
Zdziarski A. A., Johnson W. N., Poutanen J., Magdziarz P., Gierliński M., 1997, in Winkler C., Courvoisier T. J.-L., Durouchoux Ph., eds, SP-382, The Transparent Universe, Proc. 2nd INTEGRAL Workshop. ESA Publications Division, Noordwijk, p. 373
Zdziarski A. A., Lubiński P., Smith D. A., 1999, MNRAS, 303, L11 (ZLS99)
Zdziarski A. A., Poutanen J., Paciesas W. S., Wen L., 2002, ApJ, 578, 357
Zdziarski A. A., Lubiński P., Gilfanov M., Revnivtsev M., 2003, MNRAS, 342, 355

APPENDIX A: DISSIPATION AND ATTENUATION IN THE DISC–HOT FLOW MODEL

ZLS99 have considered an idealized geometrical model for thermal Comptonization, reprocessing and reflection in an accretion flow consisting of a central hot sphere surrounded by a flat cold disc (see fig. 2 in ZLS99). The sphere has a unit radius, and the inner radius of the disc can assume any value, d. For $d < 1$, there is an overlap between the two components. The hot sphere Comptonizes soft seed photons emitted by the disc. In the original model of ZLS99, the disc reprocesses and re-emits only the photons emitted by the sphere incident on the disc.

Here, we generalize this model to include intrinsic dissipation in the cold disc (as expected in an accretion flow). Also, we take into account scattering of the Compton-reflected photons in the hot sphere, which was neglected in ZLS99. For completeness, we give here the full set of relevant equations, but refer the reader to ZLS99 for details of the derivation.

The hot sphere has a unit luminosity and emits isotropically. The total flux incident on the disc at a radius, r, is then given by (ZLS99)

$$F_{\mathrm{inc}}(r) = \frac{3h(r)}{16\pi^2}, \qquad (A1)$$

where

$$h(r) = (4/3)$$

$$\times \begin{cases} \left[(2 - r^{-2})E(r^2) + (r^{-2} - 1)K(r^2) \right], & r < 1, \\ \left[(2r - r^{-1})E(r^{-2}) + 2(r^{-1} - r)K(r^{-2}) \right], & r \geqslant 1, \end{cases} \qquad (A2)$$

where E and K are complete elliptic integrals. The luminosity of the disc due to re-emission of photons incident on it is

$$L_{\mathrm{inc}}(d) = 4\pi \int_d^\infty \mathrm{d}r\, r\, F_{\mathrm{inc}}(r). \qquad (A3)$$

This can be divided into the contributions to the integral from the parts of the disc at $d \leqslant 1$ and $d > 1$, $L_{\mathrm{inc}} = L_{\mathrm{inc}}^< + L_{\mathrm{inc}}^>$, where the first term is non-zero only for $d < 1$.

Then, the relative strength of Compton reflection can be identified (ZLS99) with the ratio of the luminosity of the disc due to irradiation to the fraction of the sphere luminosity that is not incident on the disc. However, we correct here for attenuation of the reflection from the parts of the disc with $d < 1$ because of scattering by the hot electrons in the sphere. For the radial optical depth of the sphere τ, we can then write

$$R \simeq \frac{\mathrm{e}^{-\tau} L_{\mathrm{inc}}^< + L_{\mathrm{inc}}^>}{1 - L_{\mathrm{inc}}}. \qquad (A4)$$

Another effect not included in the treatment of ZLS99 is the intrinsic dissipation in the disc. Far away from the centre (so any effect of the inner boundary condition is negligible), the dissipated flux per unit area is $\propto r^{-3}$, and we assume it for $r > 1$. On the other hand, the dissipation in the part of the disc inside the hot sphere, $r < 1$, is reduced due to the transfer of the power to the hot plasma. We assume here that dissipation is either null or constant matching that of the outside disc

$$F_{\mathrm{int}}(r) = \frac{L_{\mathrm{int}}}{4\pi} \begin{cases} 0 \quad \text{or} \quad 1, \ r \leqslant 1, \\ r^{-3}, & r > 1, \end{cases} \qquad (A5)$$

where we parametrized the relative intrinsic dissipation by the dimensionless factor, L_{int}, defined as the intrinsic luminosity of the disc extending from $r = 1$ to infinity (regardless of the actual value of d).

The power in seed photons scattered in the sphere from both the reprocessing and the intrinsic dissipation (assuming $\tau = 1$) is then

$$L_{\mathrm{s}}(d) \approx \frac{3(1-a)}{4\pi^2} \int_d^\infty \mathrm{d}r\, r h^2(r) + \frac{L_{\mathrm{int}}}{\pi} \int_{\max(d,1)}^\infty \mathrm{d}r\, \frac{h(r)}{r^2}$$

$$+ \frac{L_{\mathrm{int}}}{\pi} \int_d^1 \mathrm{d}r\, r h(r), \qquad (A6)$$

where a is the albedo and the term given by the second line of equation (A6) appears only in the case of non-zero dissipation within the sphere and when $d < 1$.

The amplification factor of the process of thermal Comptonization is then $A(d) \equiv 1/L_{\mathrm{s}}(d)$. It can be related to the spectral index of the power-law part of the Comptonization spectrum using, for example, the formula of MBP01

$$\Gamma = C(A - 1)^{-\delta}, \qquad (A7)$$

where $C = 2.19$ and $\delta = 0.14$ for BHBs with $kT_{\mathrm{seed}} = 0.2$ keV.

This paper has been typeset from a TEX/LATEX file prepared by the author.

Paper II

Ibragimov A., Zdziarski A. A., Poutanen J.
Superorbital variability of X-ray and radio emission
of Cyg X-1 — I. Emission anisotropy
of precessing sources

Superorbital variability of X-ray and radio emission of Cyg X-1 – I. Emission anisotropy of precessing sources

Askar Ibragimov,[1,2]* Andrzej A. Zdziarski[3]* and Juri Poutanen[1]

[1]*Astronomy Division, PO Box 3000, FIN-90014, University of Oulu, Finland*
[2]*Kazan State University, Astronomy Department, Kremlyovskaya 18, 420008 Kazan, Russia*
[3]*Centrum Astronomiczne im. M. Kopernika, Bartycka 18, 00-716 Warszawa, Poland*

ABSTRACT

We study theoretical interpretations of the $\sim$150-d (superorbital) modulation observed in X-ray and radio emission of Cyg X-1 in the framework of models connecting this phenomenon to precession. Precession changes the orientation of the emission source (either disc or jet) relative to the observer. This leads to emission modulation due to an anisotropic emission pattern of the source or orientation-dependent amount of absorbing medium along the line of sight or both. We consider, in particular, anisotropy patterns of blackbody-type emission, thermal Comptonization in slab geometry, jet/outflow beaming and absorption in a coronal-type medium above the disc. We then fit these models to the data from the *Rossi X-ray Timing Explorer* All-Sky Monitor, *CGRO* BATSE and the Ryle and Green Bank radio telescopes, and find relatively small best-fitting angles between the precession and the orbital planes, $\sim$10°–20°. The thermal Comptonization model for the X-ray emission explains well the observed decrease in the variability amplitude from 1 to 300 keV as a result of a reduced anisotropy of the emission due to multiple scatterings. Our modelling also yields the jet bulk velocity of $\sim$(0.3–0.5)c, which is in agreement with the previous constraint from the lack of an observed counterjet and the lack of short-term X-ray/radio correlations.

Key words: accretion, accretion discs – radiation mechanisms: thermal – stars: individual: Cyg X-1 – radio continuum: stars – X-rays: binaries – X-rays: stars.

1 INTRODUCTION

Periodic variability of emission from Cyg X-1 flux at various frequencies at the period of $\sim$150 d has been reported by, for example, Brocksopp et al. (1999a), Pooley, Fender & Brocksopp (1999), Özdemir & Demircan (2001), Benlloch et al. (2001, 2004), Karitskaya et al. (2001) and Lachowicz et al. (2006, hereafter L06). This period is much longer than the 5.6-d orbital period (Brocksopp et al. 1999b) and this type of periodicity (or quasi-periodicity) in binaries is called superorbital. The generally accepted interpretation of the underlying cause of superorbital periodicity in X-ray binaries is precession of the accretion disc and/or jet (e.g. Katz 1973, 1980; Larwood 1998; Wijers & Pringle 1999; Ogilvie & Dubus 2001; Torres et al. 2005; Caproni et al. 2006; L06; but with the exception of 4U 1820−303; e.g. Zdziarski, Wen & Gierliński 2007). However, the question arises in which way the precession causes the modulation of the observed flux. There appear to be a number of possibilities.

Considering the X-ray modulation first, the outer edge of the optically thick disc may partially cover the X-ray source. This, however,

would require extreme fine-tuning. Namely, the X-ray source has the size $\sim$10^2 R_g (where $R_g \equiv GM/c^2$) as indicated by the X-ray power spectrum and agreement with theoretical prediction on the range of radii where most of the accretion power is released, while the disc size is generally much larger, up to the order of the size of the Roche lobe ($\sim$10^6 R_g in Cyg X-1). Another possibility is that the outer part of the disc fully obscures the X-ray source, but we see the X-rays scattered in a large corona above the disc (this appears to take place e.g. in Her X-1; Leahy 2002). This, however, would dramatically affect the X-ray power spectrum, removing oscillations at all frequencies above 1 Hz, which effect is clearly not seen, and thus this scenario can be ruled out. The bound–free absorption in a spatially extended medium of moderate optical depth associated with the outer regions of the disc appears to be ruled out as there are rather weak or no energy dependencies of the modulation (see L06 and Section 3) (bound–free absorption in the wind from the companion is responsible for the *orbital* modulation of the X-rays in Cyg X-1; Wen et al. 1999). On the other hand, a viable scenario is the wind/corona around the outer disc being almost fully ionized, with scattering away from the line of sight being responsible for the X-ray superorbital modulation.

Yet another possibility is that the X-ray emission is intrinsically anisotropic. Such a possibility was considered by Brocksopp et al.

*E-mail: askar.ibragimov@oulu.fi (AI); aaz@camk.edu.pl (AAZ)

(1999b) who have relied on the blackbody-type anisotropy, where the flux is proportional to the projected area. However, there is overwhelming evidence that the dominant radiative process producing X-rays in the hard state of Cyg X-1 (and other black-hole binaries) is thermal Comptonization (e.g. Poutanen 1998; Zdziarski & Gierliński 2004). Therefore, it is of interest to study models of the anisotropy of the Comptonized emission to see whether they can reproduce the observed superorbital variability.

We note that the hot Comptonizing plasma most likely also forms the base of the jet, which is present in the hard state and radiates, at larger distances from the black hole, non-thermal synchrotron radio emission correlated with the X-rays (e.g. Gallo, Fender & Pooley 2003). However, the radiative process giving rise to the X-rays is still thermal Comptonization. Early models accounting for the radio–X-ray correlation postulated that the observed X-ray emission is due to non-thermal synchrotron emission of very energetic power-law electrons with a fine-tuned high-energy cut-off. However, that process cannot account, for example, for the sharpness of the observed cut-offs (Zdziarski et al. 2003). Then, recent X-ray jet models turned to thermal Comptonization to account for the high-energy cut-off. However, the electron temperature in that model is very high, $kT \sim$ 3–4 MeV (Markoff, Nowak & Wilms 2005), yet still fitted to the cut-off observed at $\sim$100 keV. Those authors do not explain how it is done; if it is due to the first-order scattering by the thermal electrons, very strong fine-tuning in all hard states of black-hole binaries is obviously required. Generally, assume the jet X-ray origin also leads to a number of other conflicts with the observations (e.g. Poutanen & Zdziarski 2003; Zdziarski et al. 2003, 2004; Maccarone 2005; Yuan et al. 2007).

The synchrotron, radio emission of the jet may be isotropic in the comoving frame (in the presence of a tangled magnetic field). However, if the jet bulk motion is at least mildly relativistic, the observed flux will depend on the jet angle, and will thus change with the jet precession. Indeed, Stirling et al. (2001) find that the absence of an observable counter jet requires such a velocity for the extended part of the jet. This constraint combined with one from the lack of radio–X-ray correlations on short time-scales (Gleissner et al. 2004) leads to the estimate on the jet velocity of $\sim$(0.5–0.7)c. If the jet precesses together with the disc, the radio emission will be modulated with the precession period. On the other hand, we have no information on the velocity in the core of the jet, which can be, in principle, much lower. In that case, the process responsible for the radio superorbital modulation may be free–free absorption in the wind from the companion star which will depend on the direction, the jet is inclined. This may provide an alternative explanation of the superorbital modulation of the radio emission (Szostek & Zdziarski 2007). Furthermore, both the Doppler beaming and the precession-dependent absorption may take place in Cyg X-1.

Here, we study the precession physical scenarios leading to superorbital modulations in a systematic way. In general, any emission anisotropic (in the rest frame of the system) with respect to the disc/jet axis will be observed to be modulated when the direction of that axis changes.
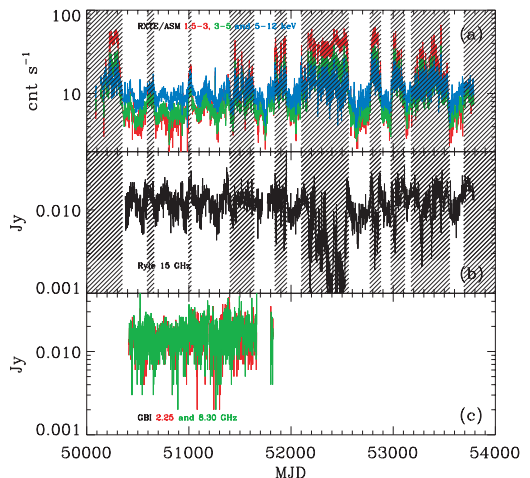
2 THE DATA

We use the X-ray dwell data from the All-Sky Monitor (ASM) aboard *Rossi X-ray Timing Explorer* (*RXTE*; Bradt, Rothschild & Swank 1993; Levine et al. 1996). We also use *Compton Gamma Ray Observatory* BATSE data in the 20–100 and 100–300 keV energy ranges, the 15-GHz radio data from the Ryle Telescope of the Mullard Radio Astronomy Observatory and the 2.25- and 8.30-GHz

data from the Green Bank Interferometer (GBI) of the National Radio Astronomy Observatory, Green Bank, WV, USA (see L06 for a detailed description of those data sets). Compared to the analysis of L06, we also include more recent ASM and Ryle data. We study the *RXTE*/ASM data for MJD 50087–53789 (1995 May 1–2006 February 23), the BATSE data for MJD 48371–51686 (1991 April 25–2000 May 22), the 15 GHz Ryle data for MJD 50377–53791 (1996 October 10–2006 February 25) and the GBI data for MJD 50409–51823 (1996 November 22–2000 October 6). Hereafter, we refer to the *RXTE*/ASM channels of 1.5–3, 3–5 and 5–12 keV as the ASM A, B and C, respectively, and the BATSE 20–100 and 100–300 keV data as the BATSE A and B, respectively.

Cyg X-1 is a highly variable source. Therefore, in order to accurately analyse its superorbital variability it is preferable to use observations affected in the least way by its aperiodic variability. Thus, we study only the hard state, in which Cyg X-1 is for majority of the time. We define it following Zdziarski et al. (2002), requiring the average photon spectral index derived from the *RXTE*/ASM fluxes to be <2.1. In addition, we exclude hard-state intervals with high X-ray variability following the criterion used by L06. Namely, we define MJD 50660–50990 as our reference interval. We then include only those 30-d intervals of the ASM data where <40 per cent of points exceed by 4σ the average flux in the reference interval. This has resulted in the removal of the following time intervals. MJD <50350, 50590–50660, 50995–51025, 51400–51640, 51840–51960, 52100–52565, 52770–52880, 52975–53115, 53174–53554, >53690. We apply the above selection to *RXTE*/ASM and Ryle data sets, as shown in Fig. 1.

On the other hand, the GBI data cover a relatively short-time interval, also shown in Fig. 1. That interval is entirely in the hard state. Therefore, we have not applied any additional screening criteria to those data except the removal of the data marked as bad. Then, for the BATSE data, we exclude the periods of the soft state of 1994 and 1996, that is, MJD 49250–49440 and MJD 50230–50307 (as in L06).

Figure 1. The panel (a) 1.5–3, 3–5 and 5–12 keV (red, greed and blue, respectively) *RXTE*/ASM, panel (b) Ryle and panel (c) 2.25 and 8.30 GHz (red and green, respectively) GBI light curves for the available span of the data. The shaded areas show the data not taken into account in our analysis.
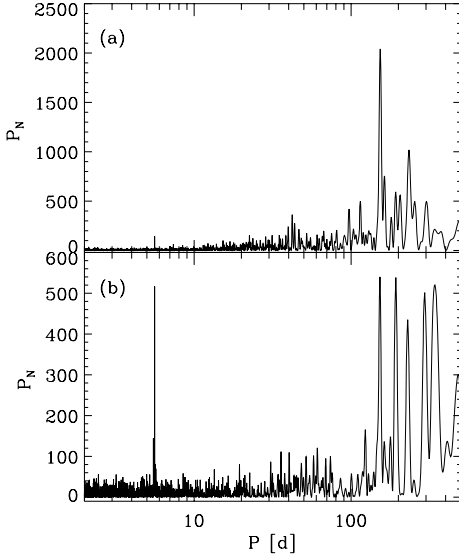
Figure 2. The Lomb–Scargle periodograms for panel (a) the ASM C and panel (b) the Ryle data (before pre-whitening; corresponding periodograms after pre-whitening are shown by L06).

3 PERIODIC MODULATIONS IN THE DATA

The currently most comprehensive analysis of the orbital and the superorbital modulations of Cyg X-1 has been done by L06. In particular, they found the superorbital period of $\sim$150 d consistent with constant in all the available data since approximately 1976. Furthermore, they found the phase of the superorbital also compatible with constant (see fig. 7 and table 3 in L06).

Here, we use the Lomb–Scargle method (Lomb 1976; Scargle 1982) to characterize the periodicities in the data analysed by us. The periodograms for the ASM C and Ryle data are shown in Fig. 2. We clearly see the peaks corresponding to 5.6 and $\sim$150 d for both data sets. In addition, we see strong peaks corresponding to periods longer than 150 d for the Ryle data. Their origin remains unclear though they are likely to be artefacts (see L06 for discussion).

We first consider the orbital modulation (caused by absorption in the wind; Wen et al. 1999; Brocksopp, Fender & Pooley 2002; Szostek & Zdziarski 2007; see the latter paper for corrections to Brocksopp et al. 2002). For it, we use the spectroscopic ephemeris (LaSala et al. 1998; Brocksopp et al. 1999a):

$$\min[\text{MJD}] = 50234.79 + 5.599829E, \qquad (1)$$

where E is an integer. At those times, the companion star is in front of the X-ray source. We then fit the light curves folded over the orbital period and averaged within each of 20 phase bins. We then use logarithm, $G = \ln F$, of the photon or energy fluxes or count rates, F, for fitting the sum of harmonics,

$$G_{\text{mod}}(\phi) = \langle G \rangle - \sum_{k=1}^{N} G_k \cos[2\pi k(\phi - \phi_k)], \qquad (2)$$

where ϕ is the 0–1 phase, $\langle G \rangle$ is the (fitted) average value of the logarithm of the flux, and G_k and ϕ_k are the amplitude and the offset phase, respectively, for the kth harmonic. We adopt the convention that $G_k > 0$ and $-0.5 < k\phi_k \leqslant 0.5$. The obtained parameters for $N = 3$ for the *RXTE*/ASM and Ryle data and $N = 1$ for the GBI data (see L06) are given in Table 1. We do not consider here the orbital modulation for the BATSE data since it is very weak, $\lesssim$3 per cent (L06).

We note that assigning errors to the folded and averaged fluxes is not a unique procedure. Here, we first divide the light curve into time bins of the 1/20 of the period (orbital or superorbital) and obtain the average of the flux, F_{ij}, where i is the number of the phase bin and j is the number of the time bin contributing to the ith phase bin, weighted by the inverse squares of their measurement error. In this way, we avoid any contribution to our folded/averaged light curves from the source variability on time-scales shorter than that corresponding to the length of our chosen phase bin. The resulting measurement uncertainties on F_{ij} are rather small, and we neglect them. Then, we consider the average and standard deviation of all time bins contributing to a given phase bin. Here, we want to take into account the actual aperiodic variability of the source not just the measurement errors. Therefore, we calculate the unweighted average within the ith phase bin, $F_i = (\sum_{j=1}^{N_i} F_{ij})/N_i$, where N_i is the number of time bins contributing to the ith phase bin and the corresponding rms standard deviation, σ_i, given by $\sigma_i^2 = [\sum_{j=1}^{N_i}(F_i - F_{ij})^2]/[N_i(N_i - 1)]$. Then, we take $G_i = \ln F_i$ and fit with equation (2).

Subsequently, we pre-whiten the logarithmic light curves by subtracting from them the orbital variability fitted above,

$$G'(t) = G(t) - G_{\text{mod}}(t) + \langle G \rangle. \qquad (3)$$

We now again apply the Lomb–Scargle method to the pre-whitened data. (We do not pre-whiten the BATSE data, as their orbital modulation is very small, see above.) The obtained main ($\sim$150-d) superorbital periods are presented in Table 2. The given 1σ errors have been estimated using the method described in section 4.4 of Schwarzenberg-Czerny (1991). The superorbital period of Cyg X-1 was determined by L06 using the weighted average, 151.43 d, of periods determined for a large number of data sets. For our data alone, we find 152.4 ± 0.6 d, and including the *Ginga* and *Ariel 5* data from L06, we obtain a similar value, $P = 152.0 \pm 0.4$ d (1σ error), consistent with that of L06. Thus, for consistency with L06,

Table 1. The coefficients for the orbital modulation fitted by equation (2). The units of exp $\langle G \rangle$ are s^{-1} for the *RXTE*/ASM data and Jy for the Ryle and GBI data.

Detector	$\langle G \rangle$	G_1	ϕ_1	G_2	ϕ_2	G_3	ϕ_3
RXTE/ASM A	1.829 ± 0.005	0.113 ± 0.008	0.007 ± 0.011	0.042 ± 0.008	-0.02 ± 0.01	0.017 ± 0.008	-0.01 ± 0.02
RXTE/ASM B	1.825 ± 0.004	0.066 ± 0.006	0.005 ± 0.013	0.022 ± 0.006	0.03 ± 0.02	0.008 ± 0.006	0.00 ± 0.04
RXTE/ASM C	2.188 ± 0.003	0.035 ± 0.005	0.005 ± 0.022	0.011 ± 0.005	-0.04 ± 0.04	0.007 ± 0.005	-0.02 ± 0.04
Ryle	-4.429 ± 0.007	0.167 ± 0.011	0.14 ± 0.01	0.035 ± 0.010	0.16 ± 0.02	0.017 ± 0.010	0.15 ± 0.03
GBI (8.30 GHz)	-4.122 ± 0.011	0.064 ± 0.015	0.17 ± 0.04	–	–	–	–
GBI (2.25 GHz)	-4.187 ± 0.010	0.024 ± 0.014	0.4 ± 0.1	–	–	–	–

Table 2. The periods and amplitudes of the superorbital modulation in the analysed data. The amplitudes have been calculated using the average superorbital period of L06, 151.43 d. The errors are 1σ. The second set of the A values gives the modulation amplitudes obtained by L06.

Detector	Energy	P [d]	A	A (L06)
RXTE/ASM A	1.5–3 keV	153.5 ± 1.5	0.120 ± 0.005	0.133 ± 0.005
RXTE/ASM B	3–5 keV	153.5 ± 1.5	0.105 ± 0.003	0.114 ± 0.003
RXTE/ASM C	5–12 keV	153.5 ± 1.3	0.103 ± 0.003	0.114 ± 0.003
BATSE A	20–100 keV	151.0 ± 1.1	0.083 ± 0.001	0.081 ± 0.001
BATSE B	100–300 keV	152.0 ± 3.0	0.075 ± 0.002	0.070 ± 0.001
Ryle	15 GHz	152.7 ± 1.4	0.140 ± 0.005	0.105 ± 0.002
GBI	8.30 GHz	148.8 ± 3.1	0.116 ± 0.004	0.123 ± 0.003
GBI	2.25 GHz	150.7 ± 3.5	0.122 ± 0.004	0.107 ± 0.003

we hereafter use their ephemeris,

$$\min[\mathrm{MJD}] = 50514.59 + 151.43E. \tag{4}$$

We then fold and average within each of 20 superorbital phase bins the pre-whitened data, and fit them using equation (2) with $N = 1$. The errors used in the fit are calculated in the way described above. The fits give us the amplitude of the variability, which we define as

$$A = \frac{F_{\max} - F_{\min}}{F_{\max} + F_{\min}} = \frac{R - 1}{R + 1}, \tag{5}$$

where $F_{\max}$ and $F_{\min}$ are, respectively, the maximum and the minimum fitted fluxes, ratio of which is $R \equiv F_{\max}/F_{\min}$ and $R = (1 + A)/(1 - A)$. For our harmonic fit with $N = 1$, $F_{\max,\min} = \exp(\langle G \rangle \pm G_1)$. The obtained values of A are listed in Table 2. We see that the amplitudes of the superorbital modulation in both the ASM and radio data are almost independent of the energy, confirming the previous result of L06. On the other hand, we confirm the result of L06 that the modulation amplitudes in the 20–300 keV energy range are significantly smaller than those in the 1.5–12 keV range. Two of the resulting superorbital phase diagrams are shown in Fig. 3.

We point out that the obtained amplitudes are somewhat affected by systematic uncertainties, in particular, those related to the selection criteria. We have tested that indeed changing the criteria used to choose the fitted parts of the light curves results in some changes of the values of A. To illustrate this effect, Table 2 also gives the values of A of L06, who used both somewhat different selection criteria and different pre-whitening method (namely, pre-whitening the data with all other significant modulations, not only the orbital one). We can see that their values differ from ours by typically 10 per cent, which can be taken as the systematic uncertainty of the values of A. The largest difference is for the Ryle data, which appears to result from not applying the selection criteria obtained from the ASM data to the Ryle data in L06. Also, we note that L06 treated each modulation as due to absorption which lead to increases of the average fluxes after each pre-whitening. In our method, we preserve the average fluxes (see equation 3).

4 FLUX VARIATION FROM PRECESSION

Let us consider a precessing slab model with a constant tilt angle, δ (see Fig. 4), and a constant angular velocity $\omega = 2\pi P^{-1}$ where P is the superorbital period. Then, the superorbital phase is proportional to time within each cycle, for example, $\phi_{\mathrm{so}} = t/P$ for $t \leqslant P$. Note that the precession is independent of the orbital motion of the system, that is, the disc inclination in an inertial frame does not directly depend on the orbital phase. The precession may also include any
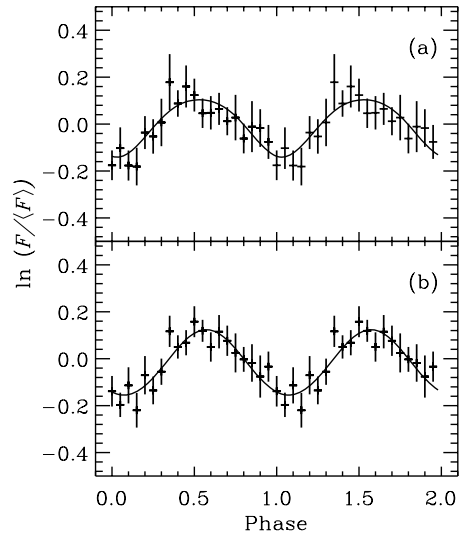

Figure 3. The superorbital phase diagrams for two of our data sets showing the light curves folded over the superorbital ephemeris, equation (4), and averaged within each phase bin. Panel (a): the ASM A X-ray data modelled by thermal Comptonization in the slab geometry. The best fit corresponds to $i = 32°$ and $\delta = 18°$ (see Section 4.2, Fig. 9). The Ryle radio data fitted with the jet model (see Section 4.1 and Fig. 6) with the assumed values of $i = 40°$ and $\beta = 0.4$, which yield the best fit of $\delta = 11°$.

structure attached to the disc, for example, a corona and/or a jet. The angle, ψ, between the normal to the disc and the direction towards the observer is given by

$$\cos\psi = |\cos\delta \cos i - \sin\delta \sin i \cos(2\pi\phi_{\mathrm{so}})|, \tag{6}$$

where i is the orbital inclination to the line of sight. Here, $\phi_{\mathrm{so}} = 0$ corresponds to the disc being most inclined with respect to the observer. The emissivity of the disc (and any additional structure e.g. a jet) integrated over its surface and over the orbital period can only be a function of the direction with respect to the normal, that is, ψ. The value of ψ varies between $i + \delta$ at $\phi_{\mathrm{so}} = 0$ and $|i - \delta|$ at $\phi_{\mathrm{so}} = 0.5$. We note that since no secondary maxima are observed in the X-ray folded superorbital light curves (Fig. 3), we see only one side of the disc, that is, always $\psi < 90°$, implying $i + \delta < 90°$. Otherwise, we would see at some moment only the disc edge and then its opposite side. Note also that equation (6) is symmetric with
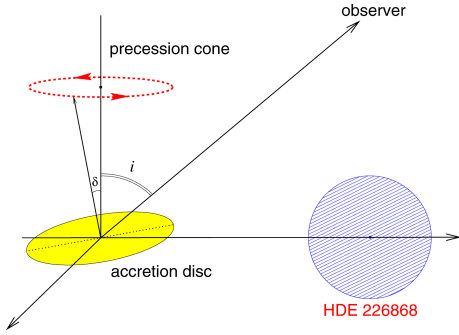
Figure 4. The assumed geometry of Cyg X-1 at the zero orbital phase (i.e. at the superior conjunction of the X-ray source).

respect to an exchange of i and δ. Thus, for any configuration with $i > \delta$ there is an equivalent one with $\delta > i$ but with the two values exchanged. Thus, we will consider only the case of $i > \delta$, keeping in mind the existence of the symmetry.

4.1 Analytical models

If the emission from the precessing structure is anisotropic, flux variations over the precession period take place. We consider first, a few simple models. Here, $0° \leqslant \psi \leqslant 90°$.

(a) $F(\psi) = C \cos \psi$. This case corresponds to a slab/disc emitting with a constant specific intensity, that is, blackbody like.

(b) $F(\psi) = C \cos \psi (1 + a \cos \psi)$. A more general case, where a is an anisotropy parameter parametrizing departures from the black-body. Here, $a = 0$ corresponds to the constant specific intensity (blackbody) case, $a = 2$ is for Chandrasekhar–Sobolev optically thick electron scattering atmosphere (Chandrasekhar 1960; Sobolev 1963) and some values in the $-1 < a < 0$ range correspond to Comptonization in a slab with a moderate optical depth (Sunyaev & Titarchuk 1985; Viironen & Poutanen 2004; see also Section 4.2 below). Values of $a < -0.5$ correspond to the Thomson optical depth across the slab $\tau \lesssim 1$.

(c) $F(\psi) = C[\gamma(1 - \beta \cos \psi)]^{-(1+\Gamma)}$, where F is the energy flux. This law corresponds to the emissivity pattern of a steady jet or disc outflow when the retardation effect is absent (see e.g. Rybicki & Lightman 1979; Sikora et al. 1997). Here, $\beta = v/c$ is the bulk velocity in units of c, $\gamma = (1 - \beta^2)^{-1/2}$, and Γ is the observed photon spectral index. Note that if this model is applied to the jet case, the counter jet may be visible as well (unless obscured by the disc and/or free–free absorbed in the wind, Szostek & Zdziarski 2007). If the counter jet is visible, a second term with β replaced by $-\beta$ should be added to the above expression for $F(\psi)$.

(d) $F(\psi) = C e^{-\tau/\cos \psi}$, where τ is the optical depth. This law corresponds to anisotropy caused by an absorber with the same symmetry as the disc.

Using these models, we relate either the amplitude, A, or the flux ratio, R, to the model parameters. We assume $\delta < 90° - i$, in which case the global flux minimum corresponds to $\psi = i + \delta$. For Case (a), we have,

$$A = \tan \delta \tan i. \tag{7}$$

In Case (b),

$$A = \frac{(1 + 2a \cos \delta \cos i) \sin \delta \sin i}{\cos \delta \cos i (1 + a \cos \delta \cos i) + a \sin^2 \delta \sin^2 i} \tag{8}$$

and

$$a = \frac{\sin \delta \sin i - A \cos \delta \cos i}{A \cos^2 \delta \cos^2 i - 2 \cos \delta \cos i \sin \delta \sin i + A \sin^2 \delta \sin^2 i}. \tag{9}$$

Note that in equations (8) and (9), we have assumed that the flux monotonously decreases with increasing disc viewing angle, ψ. This is generally the case for $a \geqslant -0.5$. If $a < -0.5$, the above formulae apply only in the range of $\psi \geqslant \arccos(-1/2a)$. Otherwise, the maximum flux is achieved either at $\psi = \arccos(-1/2a)$ or at the maximum value of ψ of the precession (i.e. $i + \delta$). In the former case, there will be two local minima of the flux, and in the latter, the minimum flux would be achieved at the minimum value of ψ. Both those cases can be ruled out for Cyg X-1. First, only one minimum per superorbital period is seen and secondly, the X-ray superorbital modulation is in phase with the radio one (L06), and it is highly unlikely that our Case (b) with $a < -0.5$ would apply to the jet radio emission. Therefore, we hereafter assume that the flux monotonously decreases with increasing ψ and equations (8) and (9) are applicable. If anisotropy is interpreted as resulting from Compton scattering in a slab, the above constraints on a also mean that the slab Thomson optical depth is $\tau \gtrsim 1$, which is consistent with the estimates of τ from the X-ray spectra (see Section 4.2).

In Case (c), we obtain formulae relating the flux ratio, R, to β (neglecting hereafter the counter jet emission),

$$R = \left[\frac{1 - \beta \cos(i + \delta)}{1 - \beta \cos(i - \delta)} \right]^{1+\Gamma}, \tag{10}$$

$$\beta = \frac{R^{1/(1+\Gamma)} - 1}{R^{1/(1+\Gamma)} \cos(i - \delta) - \cos(i + \delta)} \tag{11}$$

(see also Gregory et al. 1989). Note that for given R and i, there is a low limit on δ (as $\beta < 1$). The minimum β required to explain an observed flux ratio at a given inclination is achieved when the precession angle is given by

$$\tan \delta = \frac{R^{1/(1+\Gamma)} + 1}{R^{1/(1+\Gamma)} - 1} \tan i. \tag{12}$$

Note that this value of δ is generally $>i$, that is, the interchange symmetry between i and δ is no longer present here.

In Case (d), we find

$$R = \exp \left\{ \tau [\sec(i + \delta) - \sec(i - \delta)] \right\}, \tag{13}$$

$$\tau = \frac{\ln R}{\sec(i + \delta) - \sec(i - \delta)}. \tag{14}$$

Various authors have obtained different constraints on the inclination of Cyg X-1, for example, Gies & Bolton (1986), Wen et al. (1999), Abubekerov, Antokhina & Cherepashchuk (2004) and Ziółkowski (2005) got $i = 28°−39°$, $10°−40°$, $31°−44°$ and $23°−38°$, respectively. Hereafter in this section, we assume $i = 40°$. Relationships between δ and other model parameters are shown in Fig. 5.

We then fit the anisotropy laws (a–d) to the observed profiles of the superorbital variability (Section 3). The (blackbody like) model (a) yields $\delta = 8°.2 \pm 0°.5$, $7°.2 \pm 0°.5$, $7°.0 \pm 0°.5$, $9°.5 \pm 1°.5$, $8°.4 \pm 1°.7$ and $8°.0 \pm 1°.6$ for the ASM A, B and C bands, Ryle and GBI 2.25- and 8.30-GHz data, respectively. For the models (b–d), the correlations between the parameters (see Fig. 5) lead to elongated error contours,
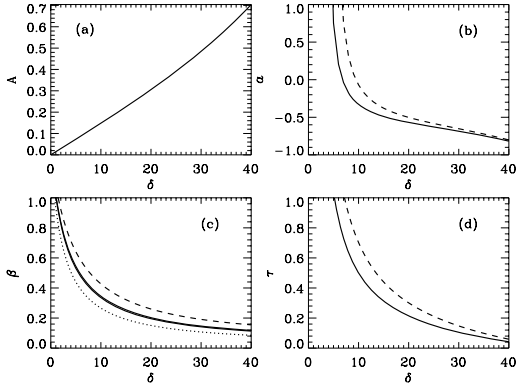
Figure 5. The relations between amplitude A, the precession angle, δ and other parameters of our analytical models for $i = 40°$. The panels (a–d) correspond to the models (a–d) described in Section 4.1. Panel (a): the dependence (7) between A and δ. Panels (b–d): the dependencies between model parameters and the precession angle δ. The assumed values of the variability amplitude of $A = 0.10$ and 0.14 are shown by the solid and the dashed curves, respectively. In Case (c), $\Gamma = 1$ was used. We also show the results at $\Gamma = 1.7$ for the above two values of A by the dotted and the dash–dotted curves, respectively.
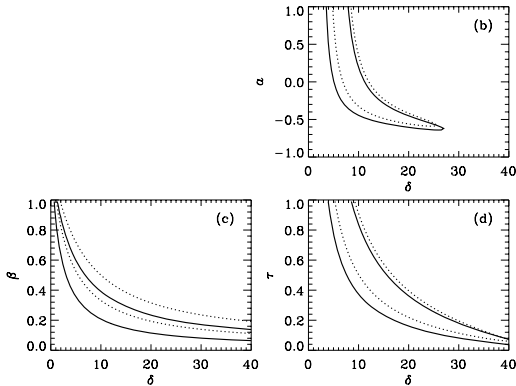
Figure 6. The 90 per cent confidence contours for the models (b–d) (marked on the panels) fitted to the observed superorbital variability profiles (Section 3) at the assumed $i = 40°$. In Case (c), we use $\Gamma = 1.7$ and 1 for the fits to the X-ray and radio data, respectively. The solid and dotted contours are for the ASM A data and the Ryle data, respectively. The ASM B, C and GBI data yield similar respective contours.

which we show in Fig. 6. The values of the statistic $\chi_\nu^2 = \chi^2 /$ degrees of freedom for the best fits are as follows for the ASM A, B and C bands, the 15-GHz Ryle data and the 2.25- and 8.30-GHz GBI data, respectively. For the model (a) $\chi_\nu^2 = (8/17, 11/17, 14/17, 10/17, 11/17, 21/17)$, (b) (8/16, 11/16, 14/16, 10/16, 11/16, 17/16), (c) (9/16, 11/16, 13/16, 11/16, 12/16, 22/16) and (d) (8/16, 11/16, 14/16, 10/16, 11/16, 17/16). Thus, we see that we cannot distinguish between the models based on the fit quality.

For the model (c), we use $\Gamma = 1.7$ (the average X-ray power-law index of the hard state of Cyg X-1) for the ASM data and $\Gamma = 1$ (corresponding to the observed 2.2–220 GHz radio emission

of Cyg X-1 in the hard state; Fender et al. 2000) for the Ryle data. In the latter case, we do not include emission of the counter jet. The results for those two cases are consistent with a coronal outflow at $\beta \simeq 0.3$ explaining the X-ray Compton reflection strength (Malzac, Beloborodov & Poutanen 2001), and the inferred radio jet velocity of $\beta \simeq 0.5$–0.7 in Cyg X-1 (Stirling et al. 2001; Gleissner et al. 2004), respectively. The model (c) fitted to the Ryle data superorbital phase diagram is shown in Fig. 3(b).

We point out that the jet in Cyg X-1 is embedded in the stellar wind from the companion, which causes the orbital modulation of the radio emission via free–free absorption (Szostek & Zdziarski 2007). Thus, a jet precession, which changes the path of the jet during the course of the orbital motion, will also change the average optical depth in the wind along the line of sight. This will give rise to a superorbital modulation, in addition to that caused by the jet beaming.

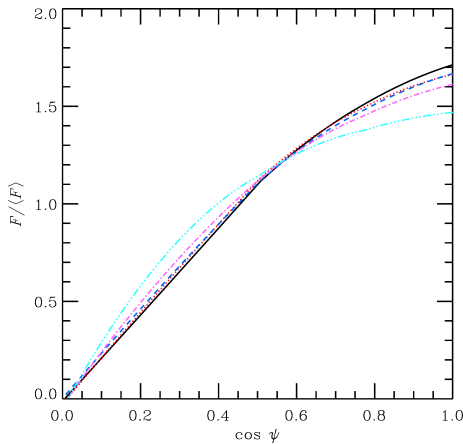### 4.2 Anisotropy of thermal Comptonization

The dominant radiative process giving rise to X-rays in the hard state of Cyg X-1 is, most likely, Comptonization of some soft seed photons by predominantly thermal electrons at the temperature of $\sim$50–100 keV (Gierliński et al. 1997; Poutanen 1998; Di Salvo et al. 2001; Frontera et al. 2001; McConnell et al. 2002; Zdziarski et al. 2002; Ibragimov et al. 2005). This is evidenced mostly by the characteristic form of its high-energy cut-off, present also in other black-hole binaries in the hard state (e.g. Grove et al. 1998; Zdziarski et al. 1998; Wardziński et al. 2002; Zdziarski & Gierliński 2004). The location of the thermally Comptonizing plasma is either a hot inner accretion flow (e.g. Poutanen, Krolik & Ryde 1997; Esin et al. 1998; Poutanen 1998; Zdziarski et al. 2002; Yuan et al. 2007) or a coronal outflow (Beloborodov 1999; Malzac et al. 2001).

Thus, we fit such a model to a representative hard-state spectrum of Cyg X-1. We choose the *RXTE* observation 10 238-01-03-00 together with the *CGRO*/OSSE observation VP 612.5 (spectrum 6 of Ibragimov et al. 2005), which gives us a broad-band energy coverage of $\sim$3–1000 keV. Our detailed model consists of the main component due to thermal Comptonization in a slab geometry calculated using the iterative scattering method of Poutanen & Svensson (1996) (COMPPS in XSPEC; Arnaud 1996). In addition, we include Compton reflection (Magdziarz & Zdziarski 1995), a fluorescent Fe Kα line and a soft excess. We attribute the last component to thermal Comptonization as well, but in a plasma with the Compton y parameter much smaller than that of the main Comptonizing plasma, and neglecting its Compton reflection (as in Frontera et al. 2001). Here, $y \equiv 4\tau kT_e/m_e c^2$, where τ is the optical depth of the plasma and T_e is its electron temperature. The seed photons for Comptonization are from a blackbody spectral component at the temperature of T_{bb}, which we keep equal to 0.2 keV in the fit. Also, we assume the inclination of $\psi = 40°$. The spectrum with the resulting fit components is shown in Fig. 7. The main fit parameters are $kT_e = 88$ keV and $\tau = 1.17$ for the main Comptonization component, the solid angle of the Compton reflector of $\Omega/2\pi = 0.17$ and $\tau = 0.87$ of the soft-excess Comptonizing plasma, for which $kT_e = 20$ keV was assumed. The absorber column density is $N_H = 2.3 \times 10^{22}$ cm^{-2}. The fit statistic is good, $\chi_\nu^2 = 371/401$.

We then vary the inclination of this model, and for each ψ, we integrate the photon flux in five energy bands, 1.5–3, 3–5, 5–12, 20–100 and 100–300 keV. The resulting dependences of $F(\psi)$ are shown in Fig. 8. We also compare the resulting functions to $F(\psi) = \cos\psi(1 + a\cos\psi)/(1/2 + a/3)$, that is, the normalized Case (b) of Section 4.1. We find $a \simeq -0.4$ as the closest overall approximation
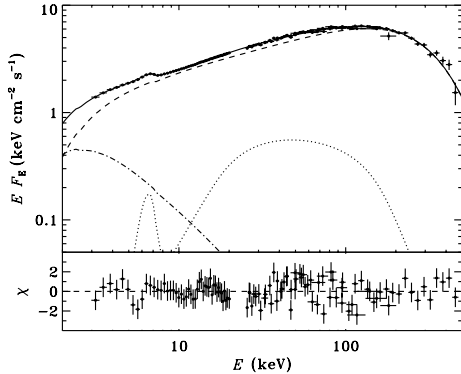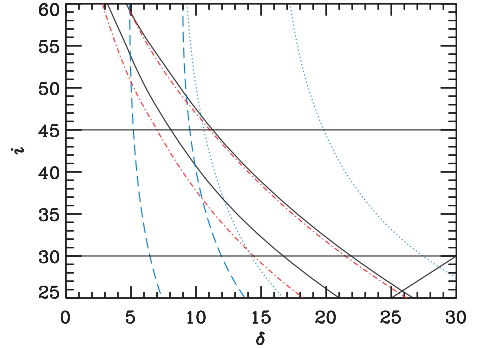
Figure 7. An example of the broad-band X-ray spectrum of Cyg X-1 in the hard state (data points) (see Section 4.2). The data are fitted by a thermal Comptonization and reflection model. The solid, dashed, dot–dashed and dotted curves represent the total model, the main Comptonization component, the soft excess (also fitted by Comptonization) and the reflection component together with an Fe Kα fluorescence line, respectively. At low energies, the spectrum is absorbed by interstellar and circumstellar media. The bottom panel shows the residuals to the fit.

Figure 9. The 90 per cent confidence contours for the inclination and the precession angle. The solid and dot–dashed curves correspond to the joint fit of all three ASM data and the BATSE A data, respectively. The dotted and dashed curves show the confidence contours of the fit to the Ryle data for the jet model with $\Gamma = 1$ for $\beta = 0.3$ and 0.5, respectively. The two horizontal lines mark $i = 30°$ and $45°$, approximately corresponding to the range of the inclination of Cyg X-1 allowed by other observational constraints. The line in the bottom right corner corresponds to $i = \delta$, below which there is a symmetric, $i < \delta$, solution (ruled out for Cyg X-1 by the $30 \lesssim i \lesssim 45°$ constraint).

ASM and the BATSE data. (Since the BATSE data are given as energy fluxes, we use the corresponding integrated energy fluxes for them.) This yields very good fits to all the data, for example, χ_ν^2 at the best fits to the ASM A, B, C data, and the joint fit for all three detectors equal 9/17, 11/17, 13/17 and 34/57, respectively. We have calculated the 90 per cent confidence contours for all the data, and found that they remain in excellent mutual agreement. We show the contours for the ASM joint fit and for the BATSE A data in Fig. 9 by the solid and the dot–dashed curves, respectively (the BATSE B contours are very similar to those of the BATSE A except for extending to a somewhat higher value of δ at a given i).

This agreement provides a strong argument for the correctness of our model of anisotropy as due to thermal Comptonization in a geometry similar to that of a slab. Namely, we see in Table 2 that the fractional X-ray modulation decreases monotonically with the increasing photon energy band from 1.5 to 300 keV. In particular, the ASM A channel shows the amplitude higher than that of the channels B and C, and the BATSE data show the amplitudes lower than those of the ASM. This is in excellent agreement with the theoretical anisotropy patterns shown in Fig. 8. Namely, we see there that the degree of anisotropy of thermal-Compton emission, as measured by the slope of the curves, decreases monotonically with the increasing energy (for $\cos \psi \gtrsim 0.3$, which is satisfied in all of our fits). This effect is due to the average number of scattering in the plasma increasing (thus leading to less anisotropic emission) with the photon energy. This then leads to a corresponding decrease in the relative amplitude of the precessional modulation, which is both present in the X-ray data sets (Table 2), and is very well fitted by our model.

On the other hand, we see the contours are very elongated, which results from a strong correlation between i and δ in the model. The 1σ contours are only slightly smaller than the shown 90 per cent ones, indicating that the minima of χ^2 are very shallow. Therefore, in order to constrain δ, we use the constraint of $30° \leqslant i \leqslant 45°$ (approximately corresponding to the constraints on i by various

Figure 8. Anisotropy patterns of thermal Comptonization in a slab obtained for our representative X-ray spectrum of Cyg X-1 in the hard state, Fig. 7. The solid, dotted, dashed, dot–dashed and three-dot–dashed curves give the photon flux integrated over the 1.5–3, 3–5, 5–12, 20–100 and 100–300 keV energy bands, respectively. The curves are normalized to $\langle F \rangle = \int_0^1 F(\cos\psi)\mathrm{d}\cos\psi$. The blackbody emission pattern would be represented by a diagonal straight line, whereas the anisotropy law of Case (b) of Section 4.1 with $a = -0.4$ lies between the shown dependencies for 5–12 and 20–100 keV.

for the shown angular dependencies. On the other hand, the normalized blackbody dependence equals $F(\psi) = 2 \cos \psi$, which yields less (more) emission than the normalized thermal Comptonization dependencies at $\cos \psi \lesssim 0.65$ ($\gtrsim 0.65$).

We now use the dependence, $F(\psi)$, in an energy band together with $\psi(i, \delta, \phi_{so})$ of equation (6) to fit the $F(\phi_{so})$ observed in that energy band, with i and δ as the fitted parameters. We use here the

authors listed in Section 4.1), with the boundaries of this region shown by the horizontal lines in Fig. 9. Then, we find $8° \lesssim \delta \lesssim 11°$ at $i = 45°$ and $17° \lesssim \delta \lesssim 22°$ at $i = 30°$. We then compare these results with the 90 per cent confidence contours for the radio emission as fitted with the jet model. We find that model is compatible with the Comptonization model for the X-ray data if $\beta = 0.3$–0.5 (shown by the dotted and dashed contours for $\beta = 0.3$ and 0.5, respectively), but not if $\beta = 0.7$. For $\beta = 0.3$–0.5 and $30° \leqslant i \leqslant 45°$, the radio data provide constraints on δ less restrictive than the X-ray data. We show the best-fitting ASM A model and a model for the Ryle data on the superorbital phase diagrams (see Fig. 3).

The main caveat to our results here is related to using the slab model for Comptonization. It is unlikely that the actual X-ray source in Cyg X-1 has exactly this geometry, and it is probably less anisotropic. This would yield somewhat higher precession angles than those obtained by us but it is unlikely to affect our qualitative conclusions. Also, we have used a specific (but rather typical) single spectrum to obtain $F(\psi)$. However, though there is some spectral variability in the hard state (e.g. Ibragimov et al. 2005), it is aperiodic and its effect will be averaged out over a number of superorbital cycles. Thus, using this assumption is unlikely to affect significantly our results.

5 DISCUSSION AND CONCLUSIONS

We have studied a general problem of how precession can affect the observed fluxes and spectra. Apart from an obvious case of a full or partial covering of the central source by an accretion disc (e.g. in Her X-1, Leahy 2002), the observed flux can be modulated if the emission pattern of the precessing source is anisotropic. We have studied a number of likely anisotropy patterns, due to either intrinsic anisotropy of the emission pattern in the source rest frame, or Doppler boosting of emission isotropic in the rest frame, or absorption/scattering by a corona covering the disc. We have derived formulae for the flux as a function of the precession phase for those processes. In addition, we have numerically calculated the X-ray anisotropy pattern due to thermal Comptonization and Compton reflection in a plasma with parameters characteristic to black-hole binaries in the hard state and assuming a slab geometry.

We have then applied these results to the superorbital modulation of the 2.25–15 GHz radio and 1.5–300 keV X-ray emission of Cyg X-1 in the hard state. We find that most models make similar predictions for the precession angle, that is, the tilt between the disc plane and the orbital plane, of the order of $\delta \sim 10°-20°$. The statistical quality of all the models is similar, thus, they cannot be distinguished on the basis of their χ^2. The model with absorption by a disc corona yields strongly anticorrelated the optical depth and the precession angle.

Our most physical model appears to be thermal Comptonization for the X-rays and jet Doppler boosting for the radio emission. The joint constraint to the X-ray and radio data yields for $\beta = 0.3$ the values of $\delta \gtrsim 10°$, $i \lesssim 47°$, and for $\beta = 0.5$, the values of $5° \lesssim \delta \lesssim 10°$, $40° \lesssim i \lesssim 60°$ (see Fig. 9). If we assume $30° \leqslant i \leqslant 45°$ (from other observational constraints on the inclination see Section 4.1), we obtain $8° \lesssim \delta \lesssim 22°$ from the X-ray data, which then implies $\beta \sim 0.3$–0.5 using the Ryle data. Thus, both the disc/jet precession angle and the jet velocity in Cyg X-1 appear relatively small. We also point out that our Comptonization model also explains and well fits the decrease in the fractional superorbital modulation amplitude with the increasing photon energy observed in the 1.5–300 keV X-ray emission of Cyg X-1. The decrease is explained by the Comptonization anisotropy decreasing with the photon energy

due to the correspondingly increasing average number of scatterings suffered by a photon before leaving the source.

Finally, it is interesting to compare our results for Cyg X-1 with those for the well-known precessing jet source SS 433. In that case, the jet velocity and the precession angle are very precisely determined based on the Doppler shift of spectral lines (formed in the jets). Their values are $\beta \simeq 0.265$ and $\delta \simeq 21°$ (Eikenberry et al. 2001; see Fabrika 2004 for a review). They are rather similar to those determined by us for Cyg X-1. However, the disc emission is not seen at all due to heavy obscuration, and the radio emission shows no periodic variability on either orbital or precessional period. This appears to be related to the rather large inclination of SS 433 of $i \simeq 78°$, at which the disc/jet system goes through the edge-on orientation at some point of each precessional cycle. Then, the counter jet is seen at a lower inclination than the primary jet during a part of the cycle, and both of them contribute comparably to the observed flux (see Section 4.1). Also, free–free absorption of the radio emission is of importance in that system (e.g. Fabrika 2004), which introduces a major complication to predictions of the precessional variability given that details of the wind geometry are unknown. On the other hand, the precessional modulation is very significant in the X-rays (Wen et al. 2006) emitted by the jets.

The disc/jet precession in SS 433 is probably caused by the precession of the companion star, with the rotation axis inclined with respect to the orbital plane (see Fabrika 2004, and references therein). On the other hand, this precession mechanism is unlikely in Cyg X-1, where the orbit is strictly circular (Brocksopp et al. 1999b), indicating that tidal forces have also brought the stellar rotation to alignment. Then, the precession may be caused, for example, by the gravitational force of the star acting on the inclined disc (e.g. Larwood 1998; L06).

REFERENCES

Abubekerov M. K., Antokhina E. A., Cherepashchuk A. M., 2004, Astron. Rep., 48, 550

Arnaud K. A., 1996, in Jakoby G. H., Barnes J., eds, ASP Conf. Ser. Vol. 101, Astronomical Data Analysis Software and Systems V. Astron. Soc. Pac., San Francisco, p. 17

Beloborodov A. M., 1999, ApJ, 510, L123

Benlloch S., Wilms J., Staubert R., Nowak M. A., 2001, in Gimenez A., Reglero A., Winkler C., eds, ESA SP-459, Exploring the Gamma-Ray Universe. ESA, Noordwijk, p. 263

Benlloch S., Pottschmidt K., Wilms J., Nowak M. A., Gleissner T., Pooley G. G., 2004, in Lamb F. K., Swank J. H., eds, AIP Conf. Ser. Vol. 714, X-ray Timing 2003: Rossi and Beyond. Am. Inst. Phys., New York, p. 61

Bradt H. V., Rothschild R. E., Swank J. H., 1993, A&AS, 97, 355
Brocksopp C., Fender R. P., Larionov V., Lyuty V. M., Tarasov A. E., Pooley G. G., Paciesas W. S., Roche P., 1999a, MNRAS, 309, 1063
Brocksopp C., Tarasov A. E., Lyuty V. M., Roche O., 1999b, A&A, 343, 861
Brocksopp C., Fender R. P., Pooley G. G., 2002, MNRAS, 336, 699
Caproni A., Livio M., Abraham Z., Mosquera Cuesta H. J., 2006, ApJ, 653, 112
Chandrasekhar S., 1960, Radiative Transfer. Dover, New York
Di Salvo T., Done C., Życki P. T., Burderi L., Robba N. R., 2001, ApJ, 547, 1024
Eikenberry S. S., Cameron P. B., Fierce B. W., Kull D. M., Dror D. H., Houck J. R., Margon B., 2001, ApJ, 561, 1027
Esin A. A., Narayan R., Cui W., Grove J. E., Zhang S., 1998, ApJ, 505, 854
Fabrika S., 2004, Astrophys. Space Phys. Rev., 12, 1
Fender R. P., Pooley G. G., Durouchoux P., Tilanus R. P. J., Brocksopp C., 2000, MNRAS, 312, 853
Frontera F. et al., 2001, ApJ, 546, 1027
Gallo E., Fender R. P., Pooley G. G., 2003, MNRAS, 344, 60
Gierliński M., Zdziarski A. A., Done C., Johnson W. N., Ebisawa K., Ueda Y., Haardt F., Phlips B. F., 1997, MNRAS, 288, 958
Gies D. R., Bolton C. T., 1986, ApJ, 304, 371
Gleissner T. et al., 2004, A&A, 425, 1061
Gregory P. C., Xu H.-J., Backhouse C. J., Reid A., 1989, ApJ, 339, 1054
Grove J. E., Johnson W. N., Kroeger R. A., McNaron-Brown K., Skibo J. G., 1998, ApJ, 500, 899
Ibragimov A., Poutanen J., Gilfanov M., Zdziarski A. A., Shrader C. R., 2005, MNRAS, 362, 1435
Karitskaya E. A. et al., 2001, Astron. Rep., 45, 350
Katz J. I., 1973, Nat. Phys. Sci., 246, 87
Katz J. I., 1980, ApJ, 236, L127
Lachowicz P., Zdziarski A. A., Schwarzenberg-Czerny A., Pooley G. G., Kitamoto S., 2006, MNRAS, 368, 1025 (L06)
Larwood J., 1998, MNRAS, 299, L32
LaSala J., Charles P.A., Sith R. A. D., Bałucińska-Church M., Church M. J., 1998, MNRAS, 301, 285
Leahy D. A., 2002, MNRAS, 334, 847
Levine A. M., Bradt H., Cui W., Jernigan J. G., Morgan E. H., Remillard R., Shirey R. E., Smith D. A., 1996, ApJ, 469, L33
Lomb N. R., 1976, Ap&SS, 39, 447
Maccarone T. J., 2005, MNRAS, 360, L68
Magdziarz P., Zdziarski A. A., 1995, MNRAS, 273, 837
Malzac J., Beloborodov A., Poutanen J., 2001, MNRAS, 326, 417
Markoff S., Nowak M. A., Wilms J., 2005, ApJ, 635, 1203

McConnell M. L. et al., 2002, ApJ, 572, 984
Ogilvie G. I., Dubus G., 2001, MNRAS, 320, 485
Özdemir S., Demircan O., 2001, Ap&SS, 278, 319
Pooley G. G., Fender R. P., Brocksopp C., 1999, MNRAS, 302, L1
Poutanen J., 1998, in Abramowicz M. A., Björnsson G., Pringle J. E., eds, Theory of Black Hole Accretion Discs. Cambridge Univ. Press, Cambridge, p. 100
Poutanen J., Svensson R., 1996, ApJ, 470, 249
Poutanen J., Zdziarski A. A., 2003, in Durouchoux Ph., Fuchs Y., Rodriguez J., eds, New Views on Microquasars. Center for Space Physics, Kolkata, p. 87
Poutanen J., Krolik J. H., Ryde F., 1997, MNRAS, 292, L21
Rybicki G. B., Lightman A. P., 1979, Radiative Processes in Astrophysics. Wiley, New York
Scargle J. D., 1982, ApJ, 263, 835
Schwarzenberg-Czerny A., 1991, MNRAS, 253, 198
Sikora M., Madejski G., Moderski R., Poutanen J., 1997, ApJ, 484, 108
Sobolev V. V., 1963, A Treatise on Radiative Transfer. Van Nostrand, Princeton
Stirling A. M., Spencer R. E., de la Force C. J., Garrett M. A., Fender R. P., Ogley R. N., 2001, MNRAS, 327, 1273
Sunyaev R. A., Titarchuk L. G., 1985, A&A, 143, 374
Szostek A., Zdziarski A. A., 2007, MNRAS, 375, 793
Torres D. F., Romero G. E., Barcons X., Lu Y., 2005, ApJ, 626, 1015
Viironen K., Poutanen J., 2004, A&A, 426, 985
Wardziński G., Zdziarski A. A., Gierliński M., Grove J. E., Jahoda K., Johnson W. N., 2002, MNRAS, 337, 829
Wen L., Cui W., Levine A. M., Bradt H. V., 1999, ApJ, 525, 968
Wen L., Levine A. M., Corbet R. H. D., Bradt H. V., 2006, ApJS, 163, 372
Wijers R. A. M. J., Pringle J. E., 1999, MNRAS, 308, 207
Yuan F., Zdziarski A. A., Xue Y., Wu X.-B., 2007, ApJ, 659, 541
Zdziarski A. A., Gierliński M., 2004, Progr. Theor. Phys. Suppl., 155, 99
Zdziarski A. A., Poutanen J., Mikołajewska J., Gierliński M., Ebisawa K., Johnson W. N., 1998, MNRAS, 301, 435
Zdziarski A. A., Poutanen J., Paciesas W. S., Wen L., 2002, ApJ, 578, 357
Zdziarski A. A., Lubiński P., Gilfanov M., Revnivtsev M., 2003, MNRAS, 342, 355
Zdziarski A. A., Gierliński M., Mikołajewska J., Wardziński G., Smith D. M., Harmon B. A., Kitamoto S., 2004, MNRAS, 351, 791
Zdziarski A. A., Wen L., Gierliński M., 2007, MNRAS, 377, 1006
Ziółkowski J., 2005, MNRAS, 358, 851

This paper has been typeset from a TEX/LATEX file prepared by the author.

Paper III

Poutanen J., Zdziarski A. A., Ibragimov A.
Superorbital variability of X-ray and radio emission
of Cyg X-1 — II. Dependence of the orbital
modulation and spectral hardness on the
superorbital phase

Superorbital variability of X-ray and radio emission of Cyg X-1 – II. Dependence of the orbital modulation and spectral hardness on the superorbital phase

Juri Poutanen,[1]★ Andrzej A. Zdziarski[2]★ and Askar Ibragimov[1,3]★

[1]*Astronomy Division, Department of Physical Sciences, PO Box 3000, FIN-90014 University of Oulu, Finland*
[2]*Centrum Astronomiczne im. M. Kopernika, Bartycka 18, 00-716 Warszawa, Poland*
[3]*Kazan State University, Astronomy Department, Kremlyovskaya 18, 420008 Kazan, Russia*

ABSTRACT

We discover a pronounced dependence of the strength of the soft X-ray orbital modulation and the spectral hardness in Cyg X-1 in the hard state on its superorbital phase. We find, our results can be well modelled as a combination of two effects: the precession of the accretion disc (which appears to cause the superorbital flux modulation) and the orbital-phase dependent X-ray absorption in an accretion bulge, located at the accretion disc edge close to the supergiant companion but displaced from the line connecting the stars by about $25°$. Our findings are supported by the distribution of the X-ray dips showing concentration towards zero superorbital phase, which corresponds to the bulge passing through the line of sight. We Fourier analyse our model, and find it explains the previous finding of asymmetric beat (between the orbital and superorbital modulations) frequencies in the observed power spectrum, provided the disc precession is prograde. On the other hand, we find no statistically significant changes of the orbital modulation with the superorbital phase in the 15-GHz radio data. This absence is consistent with the radio being emitted by a jet in the system, in which case the orbital modulation is caused by wind absorption far away from the disc. We also find that both the X-ray and radio fluxes of Cyg X-1 in the hard state on time-scales $\gtrsim 10^4$ s have lognormal distributions, which complements a previous finding of a lognormal flux distribution in the hard state on $\sim$1-s time-scales. We point out that the lognormal character of the flux distribution requires that flux logarithms rather than fluxes themselves should be used for averaging and error analysis. We also provide a correct formula for the uncertainty of rms of a light curve for the case when the uncertainty is higher than the measurement.

Key words: accretion, accretion discs – stars: individual: Cyg X-1 – stars: individual: HDE 226868 – radio continuum: stars – X-rays: binaries – X-rays: stars.

1 INTRODUCTION

A number of X-ray binaries show flux periodicities at their respective orbital period, which may be caused by a number of effects. First, the source associated with the compact object in a binary may be eclipsed by the companion (usually of high mass) (see e.g. a list in Wen et al. 2006). Secondly, a flux modulation may be caused by an optically thick disc rim (which is highest at the point of impact of the gas stream from the inner Lagrangian point in case of a donor filling its Roche lobe), obscuring the disc and/or its corona (e.g. White & Swank 1999; Hellier & Mason 1989). This obscuration may lead to

strong partial eclipses in so-called X-ray dippers. More generally, the disc and any associated structures may depart from its axial symmetry due to the influence of the companion, which may cause an orbital modulation. Third, wind from a high-mass companion may absorb/scatter the emission from the vicinity of the compact object, and the degree of absorption will depend on the orbital phase. In the case of Cyg X-1, both X-ray and radio emission are modulated by this effect, which modulations were modelled by, for example, Wen et al. (1999) and Szostek & Zdziarski (2007), respectively. Fourth, phase-dependent absorption (via photon-photon pair production) of high-energy γ-rays may occur in a photon field axially asymmetric with respect to the compact object, especially that of the stellar photons (e.g. Bednarek 2006). A fifth effect of the companion is reflection or reprocessing of the emission from around the compact object on the surface of the companion facing the compact object.

★E-mail: juri.poutanen@oulu.fi (JP); aaz@camk.edu.pl (AAZ); askar.ibragimov@oulu.fi (AI)

This effect appears to be responsible for, for example, the ultraviolet (UV) flux modulation from the X-ray binary 4U 1820–303 (Arons & King 1993; Anderson et al. 1997). Finally, the optical/UV emission of the companion will be modulated if its shape departs from the spherical symmetry by partially or fully filling its Roche lobe, which effect is seen in Cyg X-1, for example Brocksopp et al. (1999b).

Then, there will be an intrinsic dependence of the emitted flux on the orbital phase if the orbit is elliptical. This leads, for example to periodic outbursts at the periastron of Cir X-1 (Parkinson et al. 2003) and Be/X-ray binaries (see, e.g. Coe 2000; Negueruela 2004 for reviews) in X-rays, and sometimes, at other wavelengths. Also, some orbital flux modulation may be due to the Doppler effect, which is in principle observable (Postnov & Shakura 1987), but has not yet been detected in a binary. (Obviously, the Doppler effect leads to widely observed shifts of spectral lines from binaries.)

In addition, a number of X-ray binaries show modulation at periods much longer than their orbital periods, so-called superorbital periodicity, see, for example a partial list in Wen et al. (2006). In particular, Cyg X-1 shows such periodicity with the period of ~150 d (e.g. Brocksopp et al. 1999a; Karitskaya et al. 2001; Özdemir & Demircan 2001; Lachowicz et al. 2006, hereafter L06; Ibragimov, Zdziarski & Poutanen 2007, hereafter Paper I). The observed superorbital variability appears in most cases compatible with being caused by accretion disc and/or jet precession, which either results in variable obscuration of emitted X-rays as in Her X-1 (Katz 1973), or changes the viewing angle of the presumed anisotropic emitter, as in SS 433 (Katz 1980) or Cyg X-1 (e.g. L06, Paper I) or both. The only known exception, in which the superorbital periodicity is clearly caused by modulation of the accretion rate (and thus not by a changing viewing angle of the source), is 4U 1820–303 (Zdziarski, Wen & Gierliński 2007a).

A number of binaries show both orbital and superorbital modulations. Those currently known are LMC X-4, 2S 0114+650, SMC X-1, Her X-1, SS 433, 4U 1820–303 and Cyg X-1. An interesting issue then is whether there is any dependence of the parameters of the orbital modulation on the superorbital phase (or, similarly, on an average of the flux level). The shape of the profile of the orbital modulation in Her X-1 was found to depend on its superorbital phase (Scott & Leahy 1999), which appears to be due to the shadowing effect of the precessing accretion disc and scattering in its wind in that system. Recently, analogous dependencies of the shape of the orbital modulation on the average flux level have been found in LMC X-4, SMC X-1, Her X-1, as well as in Cen X-3 (Raichur & Paul 2008). Then, Zdziarski et al. (2007b) found such a dependence in 4U 1820–303 (of both the amplitude and the phase of the minimum flux) and interpreted it in terms of the size of the disc rim (partially obscuring the central source) changing with the variable accretion rate.

In addition, there is the case of the peculiar Be/X-ray binary LS I +61°303, which shows orbital variability in the radio, X-ray and TeV emission, and a superorbital variability of the peak radio flux during an orbit (Gregory, Peracaula & Taylor 1999; Gregory 2002). Gregory (2002) found a marked dependence of the phase of the peak of the orbital radio modulation on the superorbital phase in LS I +61°303. The presence of such a dependence may be due to interaction of the pulsar in that system with a variable circumstellar Be decretion disc (Gregory 2002; Zdziarski, Neronov & Chernyakova 2008).

It is of considerable interest to find out whether orbital modulation depends on the superorbital phase in Cyg X-1, the archetypical and very well-studied black-hole system with a high-mass companion,

the OB supergiant HDE 226868 (Walborn 1973). In this work, we study this issue and find that such dependence exists and is very strong in soft X-rays. We then explain it theoretically in terms of orbital-phase dependent absorption in the stellar wind interacting with the outer accretion disc.

## 2 THE LIGHT CURVES AND THEIR ANALYSIS

2.1 Data

We use the X-ray dwell data (MJD 50087-53789, i.e. 1996 January 5–2006 February 23; note a misprint in the start date in Paper I) obtained with three Scanning Shadow Cameras of the All-Sky Monitor (ASM) aboard *Rossi X-ray Timing Explorer* (*RXTE*; Bradt, Rothschild & Swank 1993; Levine et al. 1996), with the channels A, B and C corresponding to the photon energy intervals of 1.5–3, 3–5 and 5–12 keV, respectively. We also use the corresponding 15-GHz radio data from the Ryle Telescope of the Mullard Radio Astronomy Observatory (see, e.g. Pooley, Fender & Brocksopp 1999; L06 for earlier analyses of the observations of Cyg X-1).

Because Cyg X-1 is a highly variable source and the effects we search for are rather weak, we need to select accurately a homogeneous set of data. For most of the analysis in the paper, we use the data corresponding to the hard spectral state following the criteria defined in section 2 of Paper I. We require the average photon spectral index derived from the *RXTE*/ASM fluxes to be < 2.1 (Zdziarski et al. 2002), and additionally we exclude hard-state intervals with high X-ray variability, namely we include only those 30-d intervals of the ASM data where <40 per cent of points exceed by 4σ the average flux in the reference interval MJD 50660–50990. This has resulted in considering the following time intervals: MJD 50350–50590, 50660–50995, 51025–51400, 51640–51840, 51960–52100, 52565–52770, 52880–52975, 53115-53174 and 53554–53690 (see fig. 1 in Paper I).

2.2 Mean fluxes and variance

We generally follow the method of analysing light curves described in Paper I, but with some modifications necessitated by the scientific goal of the present work. We use the orbital ephemeris of Brocksopp et al. (1999b) and the superorbital ephemeris of L06, see equations (1) and (4), respectively, in Paper I. We use the values of the orbital and superorbital periods of $P = 5.599829$ d and $P_{sup} = 151.43$ d, respectively. We first divide an analysed light curve into bins with the length of $P/20$. Then, we average all points falling into a given bin weighted by the inverse squares of their measurement errors, obtaining the binned light curve, F_i. In this way, we avoid any contribution to our folded/averaged light curves from the source variability on time-scales shorter than that corresponding to the length of our chosen phase bin (see Paper I). Note that unlike the method in Paper I, we do not pre-whiten the light curves, that is, do not subtract variability at one period in order to detect more clearly variability at another period.

We have then looked into statistical properties of our distributions. We plot histograms of the fluxes for the ASM and Ryle data in Fig. 1. We see that each of the histograms follows a lognormal distribution and it is completely inconsistent with a normal one. Our finding of the lognormal form of the variability of Cyg X-1 in the hard state on long time-scales (~1/10-d to yr) in both X-rays and radio is supplemental to that of Uttley, McHardy & Vaughan (2005), who found the same type of distribution in X-rays on short time-scales, ~0.1–10 s, also in the hard state. This form of the flux
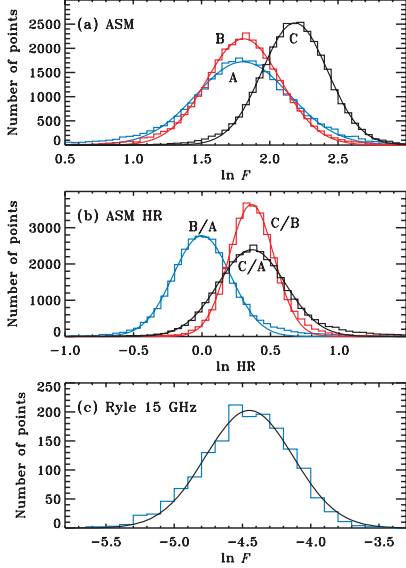
Figure 1. (a) The histogram of the count rates (dwell-by-dwell data) observed from Cyg X-1 for the ASM A, B and C detector channels. (b) Distribution of the HRs B/A, C/B and C/A. (c) Distribution of the flux in the Ryle data. The flux units for the ASM and Ryle data are count s^{-1} and Jy, respectively. The solid curves give the best-fitting lognormal distributions.

distribution has important implications for calculating flux averages and the intrinsic dispersion, that is the standard deviation in the data. Namely, the standard-deviation error estimate based on the rms, namely

$$\sigma^2 = \frac{\sum_{i=1}^{N} (x_i - \bar{x})^2}{N(N-1)}, \tag{1}$$

provides an unbiased estimate of the true standard-deviation error of the average of x_i only if the distribution of x_i is normal (Bevington & Robinson 1992). Therefore, for the purpose of calculating the averages and the rms standard deviations for our light curves, we have converted the count rates or fluxes in our binned light curves, F_i, into its logarithm, $G_i = \ln F_i$, with G_i having now the distributions close to normal.

We then separate the light curves binned based on the orbital phase into superorbital phase bins of the length of $P_{\rm sup}/8$, with the mid-point of the first and the fifth bin at $\Phi = 0$ and 0.5, respectively. Here, either the orbital phase, ϕ, or superorbital phase, Φ, is defined in the 0–1 interval, and zero corresponds to the flux minimum as defined by the respective ephemeris. Then, we calculate folded and averaged profiles (of $G_i = \ln F_i$) of the orbital modulation within each superorbital phase bin, that is

$$G_{jk} = \frac{\sum_{i \in (j,k)} G_i}{I_{jk}}, \tag{2}$$

where $i \in (j, k)$ counts over all points, i, falling into a given superorbital bin, j, *and* the orbital bin, k, and I_{jk} is the number of such points. We estimate the error of this average using equation (1), that is

$$\sigma_{jk}^2 = \frac{\sum_{i \in (j,k)} (G_i - G_{jk})^2}{I_{jk}(I_{jk} - 1)}. \tag{3}$$

Note that this error estimate accounts for both the aperiodic variability of the source, that is intrinsic dispersion of individual fluxes contributing to a given orbital/superorbital bin (usually dominating), and the dispersion due to measurement errors. Also, since we use logarithms, σ_{jk} represents a fractional error (and should not be divided by G_{jk}).

The average and the average-square error in a given superorbital bin are,

$$\bar{G}_j = \frac{\sum_{k=1}^{K} G_{jk}}{K}, \qquad \bar{\sigma}_j^2 = \frac{\sum_{k=1}^{K} \sigma_{jk}^2}{K}, \tag{4}$$

respectively, where $K = 20$ is the number of orbital bins.

We need to characterize the strength of a given modulation. One way of doing it without making any assumption about its shape is to measure the fractional rms of a given orbital modulation profile. To do it, we calculate the unweighted rms variance and then subtract from it the rms variance due to the uncertainties of the individual points, which is so-called excess variance (see e.g. Edelson et al. 2002),

$$S_j^2 = \frac{\sum_{k=1}^{K} (G_{jk} - \bar{G}_j)^2}{K - 1} - \bar{\sigma}_j^2. \tag{5}$$

Note that the variance difference above can be negative if the intrinsic variability is comparable or weaker than the measurement uncertainties. If this happens, we set this excess variance to zero. We again point out that S_j represent already the fractional rms, that is, it should not be further divided by $\bar{G}_j$ (which may be zero or negative). Then, we calculate the standard deviation of the above excess variance, ΔS_j^2, following equation (11) of Vaughan et al. (2003), hereafter V03,

$$\Delta S_j^2 = \left(\frac{2}{K}\right)^{1/2} \bar{\sigma}_j^2 \left(1 + \frac{2S_j^2}{\bar{\sigma}_j^2}\right)^{1/2}. \tag{6}$$

We note that the transformation of ΔS_j^2 into ΔS_j is not trivial. V03 have done it using the standard differential propagation of errors, obtaining their equations (B2) and (B3), which, however, we find not generally correct. Namely, the assumption behind using derivatives in propagating errors is that the uncertainty is much lower than the estimated quantity. This is often not the case for the excess variance, which can be null for either weak intrinsic variability or measurement errors comparable with that variability, see equation (5), whereas its uncertainty is always >0. Then, the error-propagation formula used by V03, $\Delta S_j = \Delta S_j^2/(\mathrm{d}S_j^2/\mathrm{d}S_j)$ (using our notation), obviously fails, leading to infinite uncertainties. The cause for that is the failure of the assumption of $\Delta S_j^2 \ll S_j^2$. To account for that, we calculate the uncertainty on the rms without that assumption, that is directly from the definition of the 1σ uncertainty range as $S_j^2 \pm \Delta S_j^2$,

$$\Delta S_j = (S_j^2 + \Delta S_j^2)^{1/2} - S_j. \tag{7}$$

Here, we have chosen the upper error, which is larger than the lower one, and which is the only one possible for $S_j^2 < \Delta S_j^2$. For $\Delta S_j^2 \ll S_j^2$, this becomes the usual $\Delta S_j \simeq \Delta S_j^2/(2S_j)$ (as in V03), which equals $\Delta S_j \simeq \bar{\sigma}_j/K^{1/2}$. On the other hand, for $\Delta S_j^2 \gg S_j^2$, the result is $\Delta S_j \simeq (\Delta S_j^2)^{1/2}$, which should be used to correct the upper part of equation (B3) in V03, and which equals $\Delta S_j \simeq (2/K)^{1/4}\bar{\sigma}_j$ (in our notation). Hereafter, we use equation (7) to estimate the rms uncertainty.

Note that the above uncertainty estimates are due to the measurement errors only, and they do not account for the long-term, red-noise, variability of the source properties (V03). This is a correct

procedure for our sample containing most of the currently available ASM data, for which we are interested in their actual properties, and are not hypothesizing about their behaviour over time-scales ≫10 yr.

2.3 Hardness ratio

We also would like to analyse the spectral variability of Cyg X-1 with orbital and superorbital phase. A useful measure of the spectral shape is the hardness ratio (HR) of the fluxes in various channels, which can be computed in a number of ways. The obvious one is to use already available mean fluxes and construct their ratio. This procedure, however, does not account for short-time-scale spectral variability. The HR can also be computed for each observation (dwell) and then the mean can be obtained. However, we have already seen that fluxes follow the lognormal distribution, and therefore expect that their ratio could also be distributed in such a way. Indeed, Fig. 1(b) demonstrates that the logarithm of HR have distributions close to normal. Therefore, for the unbiased estimation of the mean HR and its error, we take the logarithm of HR for each observation (using fluxes that are not pre-averaged within the $P/20$ bins) and average them within selected orbital and superorbital phase bins. We also note that the mean HR is computed without weighting the individual HRs according to their errors, because the error is systematically larger for harder spectra (as a result of a smaller flux in lower energy channels), and therefore accounting for errors would result in a strongly biased estimate of the mean.

## 3 STRENGTH OF THE ORBITAL MODULATION VERSUS THE SUPERORBITAL PHASE

The folded and averaged profiles of the orbital modulation for the ASM A data are shown in Fig. 2. We can see that the orbital mod-

ulation is variable, for example it appears to be the weakest at the superorbital phase $\Phi = 0.625$. However, there is also a fair amount of statistical noise, and the results of this figure need to be quantized. We can see here that the orbital modulation profiles are characterized by rather narrow minima, and thus would not be well fitted by a smooth function, for example a sinusoid. Thus, we first calculate the rms of each dependence to characterize its strength, following the method of Section 2.
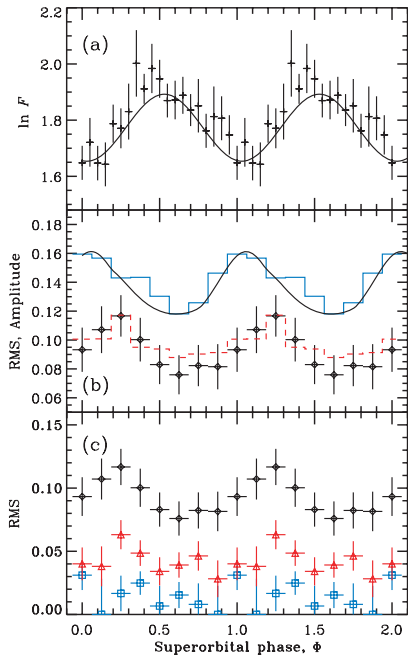
Fig. 3(a) shows the superorbital phase diagram for the ASM A channel. We can see the highly significant flux modulation with the superorbital period (cf. L06, Paper I). We also see that the minimum of the superorbital cycle is clearly offset from the ephemeris of L06 by $\Delta\Phi \simeq 0.1$ (which was based on ∼30 yr of data compared to 10 yr analysed by us). The crosses in Fig. 3(b) show the corresponding rms dependence. We very clearly see a strong dependence of the rms on Φ, with the rms being anticorrelated with the flux. It also appears that some phase lag, $\lesssim 0.1$, of the maximum of the rms with respect to the minimum of the flux is present.

Fig. 3(c) shows the results for all three ASM channels. The orbital modulation, due to bound-free absorption, is strongest in the 1.5–3 keV range and weakest in the 5–12 keV range (Wen et al. 1999; L06). Consequently, the statistical significance of the dependence on Φ decreases with the energy.

In order to test the robustness of our finding of the dependence of the strength of the orbital modulation on Φ, we have also calculated the rms for the ASM A taking into account the weights due to uncertainties of the individual points in the orbital phase diagrams (see Zdziarski et al. 2004). This alternative method gives only negligible differences with respect to the original one, and thus we do not show its results. Then, we have fitted the ASM A orbital modulation profiles with a sum of three sinusoidal harmonics, see equation (2) in Paper I, and calculated both the amplitude, $(F_{max} - F_{min})/(F_{max} + F_{min})$, and the rms for it. In this way, we largely avoid contributions to the rms from residual aperiodic variability. The results are shown in Fig. 3(b). We see
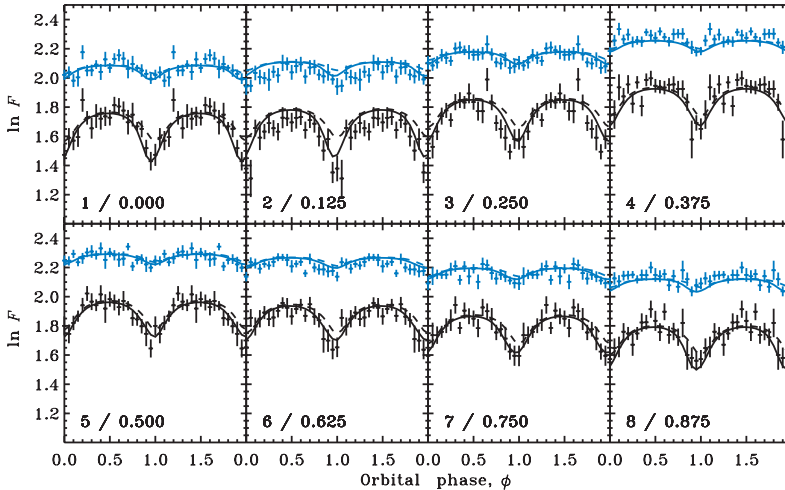

Figure 2. Profiles of the orbital modulation of the ASM A (1.5–3 keV, lower crosses) and C (5–12 keV, upper crosses) data at eight superorbital phase bins. The bin number and the phase of the bin centre are given on each panel. Note that the minimum and maximum modulation are offset from the 0 and 0.5 phase, and appear instead close to $\Phi = 0.125$ and 0.625, respectively. The unit of F is count s^{-1}. The solid curves give the best-fitting theoretical outflow model (model 8 in Table 1) described in Section 5, which involves the absorption in the isotropic stellar wind as well as in the bulge situated at the disc edge. The dashed curves shows the model component due to the wind only.

Figure 3. (a) The superorbital phase diagram for the ASM A channel. The unit of F is count s^{-1}. (b) Comparison of the characterization of the ASM A rms dependence using different methods. The crosses are the intrinsic rms, S, of the orbital modulation as a function of the superorbital phase. The solid histogram gives the amplitude of the orbital variability as fitted by sum of three harmonics, see Section 3. The dashed histogram gives the corresponding rms for the fitting functions. The solid curves in panels (a) and (b) show the dependencies for the theoretical outflow model (model 5 in Table 1). (c) The dependencies of the intrinsic rms of the orbital modulation on the superorbital phase for three ASM channels. The crosses with filled circles, open triangles and open squares correspond to the channels A, B and C, respectively.

that the values of the rms of the fitted functions are very similar to that calculated directly from the data in Fig. 2. On the other hand, the amplitude (which is sensitive only to the extremes of the fitted function) is larger than the rms simply due to their different definitions. The amplitude also shows a strong dependence of the superorbital phase similar in shape to that of the rms; however, it appears consistent with no phase shift with respect to the flux profile (Fig. 3a).

We have then searched for a similar effect in the Ryle 15 GHz data. We have found, however, that no apparent dependence is seen, and the Φ-dependent orbital modulation profiles look all similar, and consistent with the average orbital modulation (see fig. 4 in L06). Thus, we show here, in Fig. 4, only the results of calculating the rms of the orbital modulation as a function of Φ. In Fig. 4(b), we see that the strength of the orbital modulation is consistent with being constant, though we cannot rule out some dependence hidden in the statistical noise. We have also checked that the 2.25 and 8.30 GHz data from the Green Bank Interferometer (see L06; Paper I) also do not show any statistically significant dependencies.
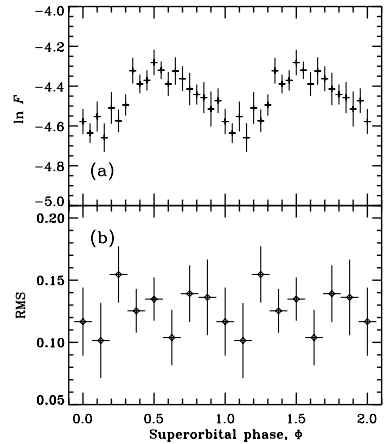
Figure 4. (a) The superorbital phase diagram for the Ryle 15 GHz data. The unit of F is Jy. (b) The dependence of the intrinsic rms of the 15 GHz orbital modulation on the superorbital phase, consistent with being constant.

4 SPECTRAL VARIABILITY

4.1 Hardness ratio

The X-ray modulations can also be tracked through the HR. The largest and easily detectable variability is shown by the ratio of count rates in ASM channels C and A (C/A). Fig. 5 presents the dependence of the mean C/A (computed from the logarithm of the ratio, see Section 2.3) on orbital and superorbital phases. We see a strong peak at orbital phase $\phi \sim 0$, which can be explained by absorption in the nearly isotropic wind (see Wen et al. 1999). The dependence of C/A on the superorbital phase also shows a very significant hardening around $\Phi \sim 0$. The two-dimensional dependencies on ϕ and Φ demonstrate a plateau with C/A$\approx$ 1.4, a significant increase in hardness around $\phi = 0.0 \pm 0.2$, and two peaks at superorbital phase $\Phi \sim -0.1$ and 0.1, which significance is not certain. Other HRs C/B and B/A show similar behaviour, but of smaller amplitude.

4.2 X-ray dips

X-ray dips, which are believed to result from absorption in blobs in the stellar wind, are characterized by significant drop in the count rate (see e.g. Bałucińska-Church et al. 2000, hereafter BC00; Feng & Cui 2002). However, most markedly they manifest themselves by spectral hardening (BC00). It is of interest to study their distribution over the orbital and superorbital phase and to compare these distribution to the corresponding dependencies of the HR.

In order to define the dips, we use the ratio of the ASM count rates in channels B and A, B/A (HR1 in BC00), and the analogous C to B ratio, C/B (HR2 in BC00). We then use the criteria of B/A >2 or C/B > 2.5, which is the same as that of BC00 (in spite of their statement that they used *both* criteria simultaneously; M. Bałucińska-Church, private communication). With the present ASM calibration, we found only 56 dips satisfying both criteria in the ASM data used by us. The cause for almost no dips with both hardnesses large appears to be caused by the dip absorption being partial, that is with some small fraction of the flux remaining unabsorbed, see fig. 4 of BC00. Then, at a relatively low
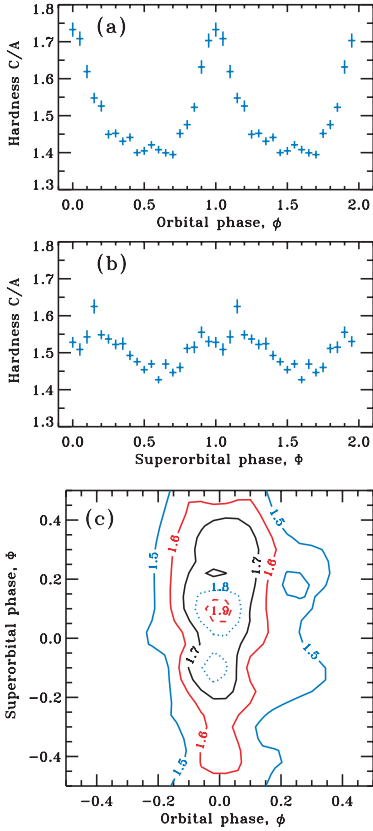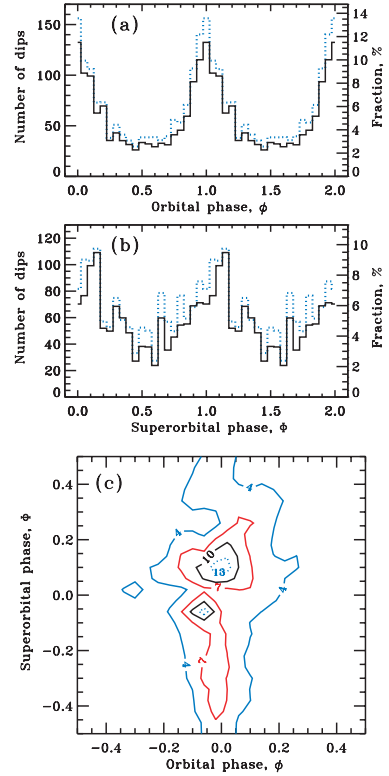
Figure 5. The mean HR in the ASM channels C and A in the hard state as a function of the (a) orbital and (b) superorbital phase. (c) Contour plot of the smoothed distribution of the HR C/A over the orbital and superorbital phases.

Figure 6. The distribution of X-ray dips over (a) orbital and (b) superorbital phase corrected for the coverage. The solid histogram is the hard state studied by us, while the dashed histogram is for the entire ASM data set. The fraction scale corresponds to the solid histograms. (c) Contour plot of the smoothed distribution of all X-ray dips over the orbital and superorbital phases.

absorbing column, the flux in the A channel is reduced but the B and C channels are only weakly affected, so this case yields a B/A ratio increase but not C/B. On the other hand, at a column yielding a substantial reduction of the B flux, the C/B ratio increases, but the absorbed flux in the A channel is so low that it is dominated by the constant unabsorbed component, which results in no substantial increase of the B/A hardness.

In the hard-state data, we have found 1151 dips (814 with B/A >2 and 387 with C/B > 2.5) among 31211 observations, while in the whole 10-yr data set without any selection we have found 1336 X-ray dips (995 with B/A >2 and 437 with C/B > 2.5) among 60127 independent observations. Thus, most of the dips happen during the hard state. This is expected because the spectral softening and increase of the luminosity in the soft state strongly increase the ionization level of the wind, which results in a weaker photoelectric absorption (BC00; Wen et al. 1999). This also strongly confirms the accuracy of our criterion defining the hard state.

Fig. 6(a) shows the distribution of the dips over the orbital phase renormalized to the number of ASM observations in each bin. Figure looks relatively similar to Fig. 5 in BC00 (based on ∼2 yr of the data, that is five times less than in our data set). The peak is at

$\phi \simeq 0$, and it is relatively symmetric, especially for the hard-state data only. We have also checked that the distributions of the dips selected separately in the B/A and C/B look very similar. On the other hand, the additional peak at $\phi \simeq 0.6$ claimed by BC00 is not found by us, and appears to be due to a statistical fluctuation in the previous data set. Indeed, the total number of counts in the three bins forming that excess was 34, whereas the continuum level (i.e, without the excess) in those three bins corresponds to about 25. Thus, the excess corresponds to only ∼1.5σ in the Poisson statistics. The existence of the feature at $\phi \simeq 0.6$ is also not supported by the dependence of the HR, which shows no signs of spectral hardening at this phase [see Fig. 5(a) and (c)].

Then, we have studied the distribution of the X-ray dips over the superorbital phase. The results are shown in Fig. 6(b). We see a maximum around $\Phi \simeq 0.05$–0.1, which is consistent with the position of the flux minimum [see Fig. 3(a)]. The distribution is clearly asymmetric relative to the peak, with a slower rise and faster decline, and it looks like the inverted flux (i.e. $-\ln F$) of Fig. 3(a).

Then, the two-dimensional distribution of the dips in ϕ and Φ is shown in Fig. 6(c). We see that most of the dips that give rise to the peak in the orbital phase distribution around $\phi \simeq 0.0 \pm 0.2$ happen around the superorbital phase of $\Phi \simeq 0.1 \pm 0.2$. (The statistical

significance of the presence of two, rather than one, separate peaks there is rather low, $\sim 2\sigma$.) The distributions of the dips resemble strongly that of the HR, which is natural because the dips just represent a tail of the HR distribution.

## 5 THEORETICAL INTERPRETATION

5.1 Wind geometry in Cyg X-1

Let us first summarize our findings. In the radio, we see no modulation of the orbital variability with the superorbital phase, while in the X-rays such a modulation is visible. In addition to the previously known spectral hardening at orbital phase $\phi \sim 0$ (visible in the HR and distribution of the X-ray dips), we find a significant increase in the HR around superorbital phase $\Phi = 0$. This effect can be tracked in the dependence of the HR as well as the distribution of the X-ray dips.

Our interpretation of the observed dependencies is as follows. The absence of statistically significant superorbital dependence of the orbital modulation of the 15-GHz radio emission is consistent with the radio being emitted by a jet in the system, in which case the orbital modulation is caused by wind absorption far away from the disc (Szostek & Zdziarski 2007). For the X-rays, the situation is more complicated.

The X-ray orbital modulation is due to variable absorption by the wind of the X-rays emitted close to the disc centre. The absorption can be separated into two components. One is independent of the superorbital modulation, and is due to absorption in the part of the wind steady in the comoving frame, as usually assumed. The other component is due to the part of the flow feeding the outer edge of the disc, and thus forming a bulge.

In Cyg X-1 system, though the OB star does not fill completely the Roche lobe, the wind density is enhanced inside the Roche lobe, which is an analog of the Roche lobe overflow but by the wind. Such a focused wind (Friend & Castor 1982; Gies & Bolton 1986b) in some way forms the accretion disc, known to exist in the system. The main argument for the existence of the disc is an overall similarity of the X-ray spectra and timing properties of Cyg X-1 to those of low-mass X-ray binaries, in which case accretion has to form a disc (see, e.g. Zdziarski & Gierliński 2004). The disc formation, most likely, leads to a condensation of the wind matter near the disc outer edge on the side of the companion in the form of a bulge, similar to the disc bulge inferred to be present in low-mass X-ray binaries, for example White & Holt (1982), White & Swank (1999), Parmar & White (1988), Hellier & Mason (1989), as illustrated in Fig. 7. On the other hand, the bulge can also be formed (see, e.g. Boroson et al. 2001) by a shock wave in the wind when it encounters the gravity of the companion, the disc, or a wind from the disc, which is also likely to be present. In any case, when the fast, $> 1000 \, \mathrm{km \, s^{-1}}$, wind is stopped, the density increases dramatically. A fraction of the focused wind might pass the black hole and be visible as additional absorption at orbital phase $\phi \sim 0.5$, however, we find no evidence for that in the X-ray data.

An issue in the above scenario is the position of the bulge relative to the line connecting the stars. Consider the accretion process in the corotating frame of the binary. In the case of low-mass X-ray binaries, the accretion stream leaves the L1 point with a small velocity and, being deflected by the Coriolis force, hits the disc (with the outer edge defined by the stream orbital angular momentum) at an azimuthal angle $\phi_b \sim 60°$, which is measured from the line connecting the stars with the origin at the compact object [see Fig. 7(c) and the entry for $\phi_h - 180°$ in table 2 in Lubow & Shu 1975]. For
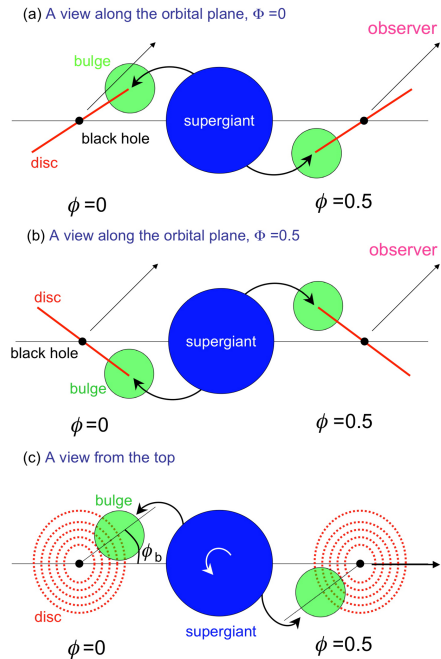
Figure 7. A drawing illustrating the effect of a bulge at the outer edge of a precessing inclined disc. The material in the bulge absorbs some of the X-ray emission originating close to the disc centre. The orbital modulation due to the bulge is seen to strongly depend on the superorbital phase. In addition, there will also be orbital modulation due to the direct wind from the supergiant, not shown here for clarity. The elongation of the supergiant, almost filling its Roche lobe, is not shown here. A view along the orbital plane: (a) the superorbital phase of zero, when the disc is seen closest to edge-on and the effect of the bulge is strongest; (b) the opposite case of the superorbital phase of 0.5. (c) A view from the top, with the arrow showing the direction of the observer. The angle ϕ_b gives the azimuthal displacement of the bulge centre relative to the line connecting the stars, and it is >0 in the case shown here. The maximum of the absorption corresponds then to $\phi = -\phi_b$. This view is for any value of Φ except for the shown orientation of the elliptical image of the disc, which corresponds to $\Phi = 0$ or 0.5.

the mass-ratio in Cyg X-1, $q = M_{BH}/M_C = 0.36 \pm 0.05$ (Gies et al. 2003), the gas freely falling from L1 point would hit the disc at $\phi_b \sim 70°$. However, these considerations neglect the radiative acceleration of the stream as well as the diffusive spreading of the accretion disc and therefore its potentially much larger size, with both effects significantly reducing ϕ_b.

An additional complexity is brought by a possibility of the non-synchronous rotation of the companion in high-mass systems. For example, a slower stellar rotation allows the wind to be launched with a non-zero angular momentum in the corotating frame and leads to the increase of ϕ_b, while the opposite is true for the faster rotation. The rotation of the companion in Cyg X-1 is compatible with corotation (Gies & Bolton 1986a), and therefore probably does not affect much the gas kinematics. Then, if we measure this angle, ϕ_b, in units of the 0–1 orbital phase, absorption of the X-ray emission in the bulge will peak at the orbital phase of $\phi \simeq 1 - \phi_b$. Indeed, the typical phase of major X-ray dips in low-mass X-ray binaries is $\simeq 0.8$–0.9 (Parmar & White 1988). Some other high-mass X-ray

binaries show dips at $\phi \simeq 0.8$–0.9, also thought to be caused by the accretion stream passing through the line of sight (Boroson et al. 2001 and references therein).

A crucial further complication in Cyg X-1 is that the disc is inclined with respect to the binary plane and thus precesses. The precession causes changes of the position of the bulge with respect to the line of sight. During a single binary revolution, the bulge moves up and down, while the inclination of the disc remains approximately constant (since $P_{\rm sup} \gg P$), see Figs 7(a) and (b). At Φ close to zero, we see the disc at the highest angle, that is most edge-on. The displacement of the bulge centre $\phi_{\rm b}$ relative to the line connecting the stars [see discussion above and Fig. 7(c)] will also cause a small shift of the superorbital phase at which the bulge absorption is maximal. On the other hand, we see the disc close to face-on at $\Phi = 0.5$, see Fig. 7(b), and then the bulge is always outside the line of sight to the X-ray source. Thus, that additional absorption component is absent.

The above considerations explain the dependence of HR on orbital and superorbital phases as well as the distribution of the X-ray dips. Based on the two-dimensional distribution of the dips [Fig. 6(c)], we have calculated that at least 1/3 of all the X-ray dips are caused by the bulge, and the rest are due to the isotropic part of the stellar wind. Fig. 7 can also be used to calculate the expected X-ray orbital profiles caused by the wind and bulge absorption. We can assume a specific density profile of the wind and the bulge, and calculate the optical depth during a revolution for a given superorbital phase.

5.2 Model

Let us consider first the isotropic component of the wind. The wind mass density as a function of distance from the centre of the star, r, can be estimated from the mass-conservation law

$$\rho_{\rm iso}(r) = \frac{\dot{M}}{4\pi r^2 v(r)}, \tag{8}$$

where $\dot{M}$ is the mass-loss rate. We assume $v(r) \propto (1 - R_*/r)^{\xi}$, where R_* is the stellar radius, and consider the attenuation cross-section independent of the distance. We thus get the absorption coefficient in the form

$$\alpha_{\rm iso}(r) = \alpha_0 \left(\frac{a}{r}\right)^2 \left(\frac{1 - R_*/a}{1 - R_*/r}\right)^{\xi}, \tag{9}$$

where a is the separation between the black hole and the companion, and α_0 is the absorption coefficient at $r = a$. We define here the characteristic optical depth, $\tau_{\rm iso,0} = a\alpha_0$.

The focused wind can be described by the cone of half-opening angle $\theta_{\rm max}$ centred around the line connecting the stars [see Fig. 8(a) for geometry]. The additional opacity can be scaled to the opacity of the isotropic component and its angular dependence can be approximated by a parabola (Friend & Castor 1982; Gies & Bolton 1986b)

$$\alpha_{\rm fw}(r, \theta) = \alpha_0(\eta_{\rm fw} - 1) \left[1 - \left(\frac{\theta}{\theta_{\rm max}}\right)^2\right], \quad \theta < \theta_{\rm max}, \tag{10}$$

where θ is the angle measured from the line connecting the stars and $\eta_{\rm fw}$ is the ratio of the wind density in the direction of the black hole to that of the isotropic component. The total wind absorption coefficient is defined by the sum $\alpha_{\rm w}(r, \theta) = \alpha_{\rm iso}(r) + \alpha_{\rm fw}(r, \theta)$.

Let us now compute the optical depth through the wind along the line of sight. It depends on the position of the observer. We introduce the coordinate system centred at the black hole with the
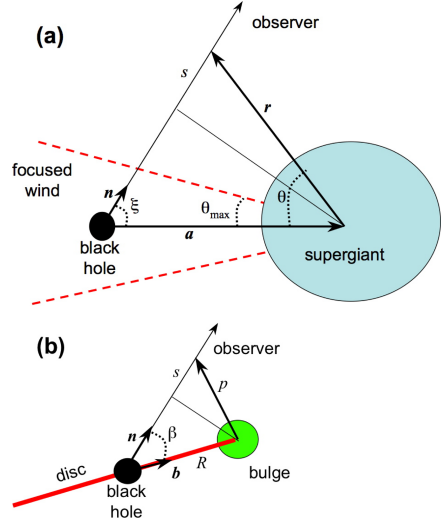

Figure 8. (a) Geometry of the wind. (b) Geometry of the bulge.

z-axis along the normal to the orbital plane, and the observer in the x–z plane, so that the direction to the observer is $\boldsymbol{n} = (\sin i, 0, \cos i)$. Position of the companion is then $\boldsymbol{a} = a(\cos\phi, \sin\phi, 0)$, where ϕ is the orbital phase. The angle between the line-of-sight $\boldsymbol{n}$ and $\boldsymbol{a}$ varies with phase:

$$\cos\xi = \boldsymbol{n} \cdot \frac{\boldsymbol{a}}{a} = \sin i \cos\phi. \tag{11}$$

The impact parameter is $a\sin\xi$ and the distance of some point in the wind to the supergiant centre is $r = \sqrt{s^2 + a^2 \sin^2\xi}$, where s is its distance to the point of the closest approach (which can be negative). The corresponding radius vector is $\boldsymbol{r} = \boldsymbol{n}(s + a\cos\xi) - \boldsymbol{a}$ [see Fig. 8(a)]. The angle between $\boldsymbol{r}$ and $-\boldsymbol{a}$ is then

$$\cos\theta = \frac{\boldsymbol{r}}{r} \cdot \frac{(-\boldsymbol{a})}{a} = \frac{1}{r}\left(a\sin^2\xi - s\cos\xi\right). \tag{12}$$

The optical depth through the wind is computed as

$$\tau_{\rm w}(\phi) = \int_{-a\cos\xi}^{\infty} \alpha_{\rm w}(r, \theta)\,{\rm d}s. \tag{13}$$

Let us apply this formalism to Cyg X-1. We take the ratio of the separation to the supergiant radius $a/R_* \approx 2.3$ (Ziółkowski 2005), the inclination $i = 40°$ (see Paper I and references therein), the velocity profile exponent $\zeta = 1.05$, and the focused wind parameters $\theta_{\rm max} = 20°$ and $\eta_{\rm fw} = 3$ (Friend & Castor 1982; Gies & Bolton 1986b). In this case, the optical depth through the isotropic component of the wind from the black hole to the infinity in the radial direction away from the companion is about $0.73\tau_{\rm iso,0}$, in the perpendicular direction it is $1.26\tau_{\rm iso,0}$ (i.e. at phases $\phi = 0.25,\ 0.75$) and at zero orbital phase along the line-of-sight $\tau_{\rm w}(0) \approx 3\tau_{\rm iso,0}$. The typical optical depth provided additionally by the focused wind across its cone is $\approx \theta_{\rm max}(\eta_{\rm fw} - 1)\frac{2}{3}\tau_{\rm iso,0} \approx 0.45\tau_{\rm iso,0}$. Thus, for Cyg X-1 at orbital phases $\phi \sim 0$, the focused wind adds only 15 per cent to the opacity produced by isotropic wind, while at $\phi \sim 0.5$, its contribution can reach 60 per cent, but the absorption itself at this phase is low. Thus, in the first approximation, we can use only the isotropic wind model and include the corrections introduced by the focused wind later.

In the case of the bulge, we first need to compute the position of the bulge centre, $\boldsymbol{b}$, relative to the black hole. For the prograde precession (see L06) the unit vector along the normal to the precessing accretion disc is $\boldsymbol{d} = (-\sin\delta\cos\Phi, -\sin\delta\sin\Phi, \cos\delta)$, where δ is the precession angle. Assume now that the bulge centre lies at the disc plane and the projection of $\boldsymbol{b}$ on the orbital plane x–y makes an angle ϕ_b with the line connecting the black hole to the companion [i.e. the azimuth of $\boldsymbol{b}$ is $\phi + \phi_b$, see Fig. 7(c)]. We then get the unit vector of the bulge centre

$$\boldsymbol{b} = \frac{[\cos(\phi+\phi_b), \sin(\phi+\phi_b), \tan\delta\cos(\phi+\phi_b-\Phi)]}{\sqrt{1+\tan^2\delta\cos^2(\phi+\phi_b-\Phi)}}. \quad (14)$$

The angle it makes to the line of sight is given by [see Fig. 8(b)]

$$\cos\beta = \boldsymbol{b}\cdot\boldsymbol{n}$$
$$= \frac{\sin i\,\cos(\phi+\phi_b) + \cos i\,\tan\delta\cos(\phi+\phi_b-\Phi)}{\sqrt{1+\tan^2\delta\cos^2(\phi+\phi_b-\Phi)}}. \quad (15)$$

Let us assume an exponential dependence of the absorption coefficient on the distance p from the bulge centre,

$$\alpha_b(p) = \alpha_{b,0}\exp(-p/r_b), \quad (16)$$

with r_b being the bulge scale-height. This gives the optical depth from the bulge centre to infinity of $\tau_{b,0} = r_b\alpha_{b,0}$. On the other hand, the optical depth from the black hole through the bulge along the line of sight,

$$\tau_b(\phi, \Phi) = \int_{-R\cos\beta}^{\infty}\alpha_b(p)\mathrm{d}s, \quad (17)$$

depends on the orbital as well as superorbital phase. Here, R is the distance to the bulge centre from the black hole (i.e. approximately the disc size) and $p = \sqrt{s^2 + R^2\sin^2\beta}$.

For simplicity, we assume that the wind and the bulge are independent and therefore the orbital modulation profile is given by

$$F(\phi, \Phi) = F_0(\cos\psi)\exp[-\tau_w(\phi)]\,\exp[-\tau_b(\phi, \Phi)], \quad (18)$$

where F_0 is the intrinsic flux (which depends on Φ) without absorption in the direction of the observer and ψ is the angle between the disc normal and the line of sight:

$$\cos\psi = \boldsymbol{n}\cdot\boldsymbol{d} = \cos i\cos\delta - \sin i\sin\delta\cos\Phi. \quad (19)$$

The retrograde precession can be modelled by substituting $\Phi \rightarrow -\Phi$ in the above formulae.

5.3 Modelling the data

In order to describe the profiles presented in Fig. 2 with the model of Section 5.2, we need to specify the angular distribution of the intrinsic flux, $F_0(\cos\psi)$. In Paper I, we have considered four simple analytical models.

(a) The blackbody, with the flux proportional to the projected area, $F_0(\cos\psi) = A\cos\psi$.

(b) An anisotropic model of $F_0(\cos\psi) = A\cos\psi(1+\eta\cos\psi)$ with parameter η giving the degree of deviation from the blackbody. Such anisotropy can be produced for example by thermal Comptonization (Paper I; Sunyaev & Titarchuk 1985; Viironen & Poutanen 2004), which the dominant radiative process giving rise to X-rays in the hard state of Cyg X-1 (e.g. Gierliński et al. 1997; Poutanen 1998; Poutanen & Coppi 1998).

(c) The steady jet model, $F_0(\cos\psi) = A[\gamma_j(1-\beta_j\cos\psi)]^{-(1+\Gamma)}$, where $\beta_j = v/c$ is the jet velocity, $\gamma_j = 1/\sqrt{1-\beta_j^2}$ is the jet Lorentz factor, and Γ is the photon index of the X-ray radiation. By

the 'jet', we mean here either the base of the jet in the direct vicinity of the black hole or an outflowing corona (see e.g. Beloborodov 1999; Malzac, Beloborodov & Poutanen 2001; Markoff, Nowak & Wilms 2005).

(d) The slab absorption model, $F_0(\cos\psi) = A\exp(-\tau/\cos\psi)$, which can be associated, for example, with some kind of a disc outflow.

All the models provide a good fit to the superorbital variability of Cyg X-1 (Paper I). Models (b) and (c) can be considered as more physically motivated, but we consider here all of them. In order to keep the number of parameters to minimum we fix the inclination of the system $i = 40°$. The precession angle δ is not well determined in models (b)–(d) as it is anticorrelated with other parameters (η, β_j, τ, see Paper I). Thus, we fix it at three values between $5°$ and $10°$.

The parameters describing the absorption of radiation are the characteristic optical depths $\tau_{iso,0}$ and $\tau_{b,0}$ for the wind and bulge, respectively. Additional parameters are the bulge-density scale measured in units of the disc size, r_b/R, and the phase shift, ϕ_b, of the position of the bulge centre. An arbitrary shift in the superorbital phase, $\Delta\Phi$ (due to the uncertainty of the superorbital ephemeris), is also introduced (i.e. we replace Φ by $\Phi - \Delta\Phi$ in all formulae of Section 5.2). The parameters describing the radiation pattern are the normalization, A (for ASM A channel), and the anisotropy parameter, η, in model (b), β_j in model (c) (where we fix Γ at a typical hard-state value of 1.7), and the slab optical depth, τ, in model (d).

We consider the prograde precession of the disc (L06). In order to understand the influence of the model complexity on the results, we consider first only the isotropic component of the wind (models W in Table 1) and fit the ASM A profiles only, which show strongest variability. We find that parameters r_b/R and $\tau_{b,0}$ are anticorrelated, and cannot be determined separately. This happens because various combinations of the two parameters can give the same optical depth through the bulge at a given impact parameter. Therefore, we fix $r_b/R = 0.2$. The best-fitting model parameters are presented in Table 1. For model (a), the precession angle agrees within the errors with the results of Paper I. The jet model, (c), provides a slightly better fit for smaller precession angles. The models (b) and (d) also give statistically similar fits. The phase shifts $\Delta\Phi$ and ϕ_b are well constrained by all the models. The fits require the shift of the bulge centre from the line connecting the stars by $\phi_b \approx 0.07$ [i.e. $25°$, see Fig. 7(c)]. All the models give similar optical depths through the wind and the bulge. The wind optical depth τ_w varies between 0.28 (i.e. $\approx 3\tau_{iso,0}$) and 0.08 (i.e. $\approx \tau_{iso,0}$) for ϕ varying between 0 and 0.5. For the bulge, τ_b varies between 0.15 and 0.007 at $\Phi = 0$ and between 0.05 and 0.008 at $\Phi = 0.5$.

We now add an additional focused wind component with the parameters specified in Section 5.2 and fit the data using jet model (c). The resulting best-fitting parameters are not very much different from those obtained with the isotropic wind model (compare entries 5 and 7 in Table 1). This is expected, because the focused wind affects the total opacity on average at about a 30 per cent level.

Finally, we fit the light curves in channels A and C simultaneously. Two additional parameters have to be introduced: the ratio of the absorption coefficients (and optical depths) in channels C and A, τ_C/τ_A, and the ratio of the normalizations (intrinsic HR), C/A. The best-fitting results for the main model parameters change only slightly (compare entries 5 and 8 in Table 1). Because the mean absorption coefficients in channels A and C differ only by a factor of 3, the absorbing gas has to be rather strongly ionized.

For the retrograde precession, all these models give much worse fits to the data.

Table 1. Best-fitting model parameters.

No.	Model[a]	δ[b] deg	$\tau_{iso,0}$[c]	$\tau_{b,0}$[d]	ϕ_b[e]	$\Delta\Phi$[f]	A[g]	η, β_j, τ[h]	τ_C/τ_A[i]	C/A[j]	χ^2/d.o.f.[k]
1	W+B a	7.5 ± 0.5	0.09 ± 0.03	$1.05^{+0.55}_{-0.44}$	0.07 ± 0.04	0.03 ± 0.02	9.2 ± 0.2	–			151.9/154
2	W+B b	10.0 (f)	0.09 ± 0.02	$0.8^{+0.4}_{-0.35}$	0.08 ± 0.03	0.04 ± 0.01	11.6 ± 0.8	-0.27 ± 0.06			155.2/154
3	W+B c	5.0 (f)	0.07 ± 0.03	$1.35^{+0.65}_{-0.6}$	0.07 ± 0.04	0.03 ± 0.01	2.90 ± 0.10	0.47 ± 0.03			148.8/154
4	W+B c	7.5 (f)	0.09 ± 0.03	$1.05^{+0.50}_{-0.45}$	0.07 ± 0.04	0.03 ± 0.01	3.55 ± 0.13	0.36 ± 0.03			151.8/154
5	W+B c	10.0 (f)	0.09 ± 0.02	$0.8^{+0.4}_{-0.35}$	0.08 ± 0.04	0.03 ± 0.02	4.04 ± 0.14	0.29 ± 0.02			154.7/154
6	W+B d	10.0 (f)	0.09 ± 0.02	$0.8^{+0.4}_{-0.35}$	0.08 ± 0.04	0.04 ± 0.01	14.8 ± 1.2	0.56 ± 0.05			155.9/154
7	F+W+B c	10.0 (f)	0.09 ± 0.02	$0.8^{+0.4}_{-0.35}$	0.08 ± 0.04	0.03 ± 0.01	4.20 ± 0.15	0.29 ± 0.02			155.4/154
8	W+B c	10.0 (f)	0.09 ± 0.02	$0.9^{+0.4}_{-0.35}$	0.08 ± 0.04	0.01 ± 0.02	4.15 ± 0.14	0.27 ± 0.02	0.3 ± 0.1	1.31 ± 0.03	359.2/318

[a]The models described in Section 5.2: W is the isotropic wind model, F is the focused wind and B stands for the bulge. Small letters giving the models of the intrinsic emission from Section 5.3. The model 8 is fitted to the ASM A and C channels simultaneously.
[b]The precession angle.
[c]Characteristic optical depth of the isotropic wind.
[d]Characteristic optical depth of the bulge.
[e]The shift of the bulge centre in orbital phase (fraction of the orbit).
[f]The shift in superorbital phase.
[g]The model normalization in the ASM A channel.
[h]The anisotropy parameter, the jet velocity, or the slab optical depth.
[i]The ratio of absorption coefficients in channels C and A.
[j]The ratio of model normalizations in channels C and A.
[k]χ^2 and the number of degrees of freedom. The errors on the parameters are given at 90 per cent confidence level for one parameter, that is for $\Delta\chi^2 = 2.71$. The size scale of the bulge in units of the disc size, r_b/R, is fixed at 0.2 and inclination $i = 40°$ in all of the models.

6 DISCUSSION

6.1 The origin of beat frequencies

A collateral effect of the coupling between the orbital and super-orbital modulations may be appearance of additional frequencies in the power spectrum. If the two modulations were independent, there would be simply two peaks in the power spectrum at the corresponding frequencies. On the other hand, if one modulation depends on the other, beat frequencies, at $\nu = 1/P \pm 1/P_{sup}$, may appear. Indeed, L06 reported finding the lower of the beat frequencies (albeit at a relatively limited statistical significance), and also found that its origin from X-ray reflection from the surface of the companion is unlikely.

Here, we have tested whether the discovered dependence of the orbital modulation on the superorbital phase may indeed cause beat frequencies to appear. Using our model (given by equation 18 and other formulae of Sections 5.2 and 5.3 with parameters of model 5 in Table 1), we have generated a light curve and computed Fourier power-density spectrum (PDS). We have found that our model gives rise to strong peaks at frequencies $1/P_{sup}$ and $1/P$ with harmonics as well as to two peaks in the power spectrum at the beat frequencies. Interestingly, the lower beat-frequency peak is 3.7–5.4 times stronger than the higher one (depending on whether we compute Fourier transforms from the flux or from the logarithm of the flux). Fig. 9 shows the flux Fourier transform for this case for the outflow model. We then compare these predictions with a simpler model where absorption in the bulge is neglected. In this case, there are two beat-frequency peaks of equal strength in the PDS of the flux (see the dashed curves in Fig. 9), while they are missing in the PDS computed from the logarithm of the flux, because the coupling disappears. If on the other hand, only bulge produces absorption, PDS shows both beat-frequency peaks with the strength ratio of 10 and 5 for the flux and its logarithm, respectively. Finally, we
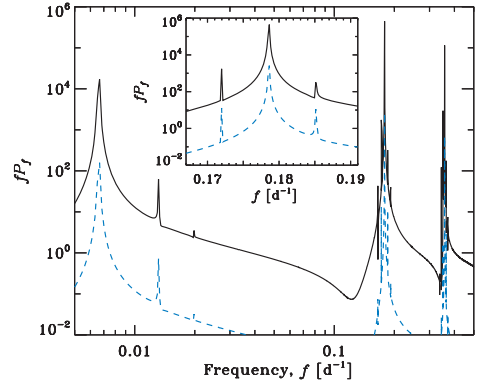
Figure 9. Power density spectra predicted by our models (arbitrary normalization). The solid curves show the power spectrum of the flux for the outflow model 5 in Table 1. The inset zooms on the frequency range near $1/P$. The dashed curves show the model with the absorption only in the wind, that is neglecting the presence of the bulge.

experimented with the model where intrinsic flux, F_0, as a function of superorbital phase was assumed to be constant and both bulge and wind are responsible for absorption. Now, the strength of the peak at $1/P_{sup}$ has diminished by three orders of magnitude, while the behaviour of PDS at $1/P$ and the beat frequencies was almost identical to the full model with variations of F_0 (the ratio of peak strengths is 6.5 and 5.5 for the flux and its logarithm, respectively).

We see that the lower beat-frequency peak is always stronger than the higher one when absorption is modulated by the bulge (for prograde precession). The coupling discovered in this work

thus predicts a presence of beat frequencies with a stronger low-frequency peak, which is consistent with the discovery by L06 of only the low-frequency peak.

6.2 Superorbital variability and outbursts of Cyg X-1

It is of interest to consider whether the superorbital variability of Cyg X-1 is related to other aspects of the source activity. Recently, the MAGIC collaboration (Albert et al. 2007) reported detecting TeV emission from Cyg X-1. That detection, on MJD 54 002, took place in the middle of a strong X-ray outburst of Cyg X-1 (Türler et al. 2006). We have checked that time corresponds to the peak of the superorbital cycle, $\Phi \simeq 0.5$, when the disc and jet of Cyg X-1 are most face-on. On the other hand, L06 found that the superorbital cycle was uncorrelated with the appearance of other strong X-ray outbursts of the source of duration of hours (Stern, Beloborodov & Poutanen 2001; Golenetskii et al. 2003). Thus, the significance of the coincidence of the TeV burst with the peak of the superorbital cycle in the present case remains unknown.

Interestingly, the orbital phase of the TeV outburst was at $\phi \simeq 0.9$ (Albert et al. 2007), at which absorption of TeV photons by pair production on the stellar photons is very strong. A possible way to obtain detectable TeV emission is then via pair cascades. We note that the statistical significance of the detection was relatively limited, 4.1σ, and thus an independent confirmation of this detection is desirable.

7 CONCLUSIONS

We have discovered the dependence of the orbital modulation strength and the HR on the superorbital phase of Cyg X-1. The observed effects can be explained by the presence of the absorbing material more or less fixed in the corotating frame of the stars. We associate this material with the bulge formed by the accreting stream impacting the accretion disc. Because of the disc precession (causing superorbital variability), the bulge moves up and down and its influence on absorption varies. At the superorbital phase 0.5, the line of sight does not pass through the bulge, while at $\Phi \approx 0$ the absorption in the bulge is maximal. We estimate the maximal optical depth at 1.5–3 keV through the bulge (for our line of sight) of about 0.15, while the stellar wind produces twice as much of the absorption.

Using a simple model of the bulge and the stellar wind incorporating the angular dependence of the intrinsic X-ray radiation from the black hole vicinity, we were able to reproduce the detailed shape of superorbital variability as well as of the orbital modulation at various superorbital phases. We find the bulge centre is displaced from the line connecting the stars by about $25°$. We also study the distribution of the X-ray dips over superorbital phase. We find their concentration towards the superorbital phase 0.1, which coincides with the position of the flux minimum. We thus are in position to claim that the X-ray dips observed in Cyg X-1 at around zero orbital phase have direct relation to the bulge which, in turn, causes variation of the orbital modulation with the superorbital phase. We Fourier analyse our model, and find it explains the finding of only the lower beat frequency between the orbital and superorbital frequencies in the observed power spectrum (L06), provided the disc precession is prograde.

We also find that both the X-ray and radio fluxes of Cyg X-1 in the hard state on time-scales $\gtrsim 10^4$ s have lognormal distributions, which complements the finding of a lognormal flux distribution in the hard state on $\sim$1-s time-scales (Uttley et al. 2005). We stress out that the lognormal character of the flux distribution requires that flux logarithms rather than fluxes themselves should be used for averaging and error analysis. We also correct a mistake in the treatment of V03 of the uncertainty of intrinsic rms variability of light curves in the case when the uncertainty is higher than the intrinsic rms (which is often close to null). The mistake stems from the failure of the assumption of the uncertainty to be much less than the estimated quantity, used in the standard propagation of errors.

REFERENCES

Albert J. et al., 2007, ApJ, 665, L51
Anderson S. F., Margon B., Deutsch E. W., Downes R. A., Allen R. G., 1997, ApJ, 482, L69
Arons J., King I. R., 1993, ApJ, 413, L121
Bałucińska-Church M., Church M. J., Charles P. A., Nagase F., LaSala J., Barnard R., 2000, MNRAS, 311, 861 (BC00)
Bednarek W., 2006, MNRAS, 368, 579
Beloborodov A. M., 1999, ApJ, 510, L123
Bevington P. R., Robinson K. D., 1992, Data Reduction and Error Analysis for the Physical Sciences, 2nd Edn. McGraw-Hill, New York
Boroson B., Kallman T., Blondin J. M., Owen M. P., 2001, ApJ, 550, 919
Bradt H. V., Rothschild R. E., Swank J. H., 1993, A&AS, 97, 355
Brocksopp C., Fender R. P., Larionov V., Lyuty V. M., Tarasov A. E., Pooley G. G., Paciesas W. S., Roche P., 1999a, MNRAS, 309, 1063
Brocksopp C., Tarasov A. E., Lyuty V. M., Roche O., 1999b, A&A, 343, 861
Coe M. J., 2000, in Smith M. A., Henrichs H. F., Fabregat J., eds, ASP Conf. Ser. Vol. 214, IAU Colloq. 175, The Be Phenomenon in Early-Type Stars. Astron. Soc. Pac., San Francisco, p. 656
Edelson R., Turner T. J., Pounds K., Vaughan S., Markowitz A., Marshall H., Dobbie P., Warwick R., 2002, ApJ, 568, 610
Feng Y. X., Cui W., 2002, ApJ, 564, 953
Friend D. B., Castor J. I., 1982, ApJ, 261, 293
Gierliński M., Zdziarski A. A., Done C., Johnson W. N., Ebisawa K., Ueda Y., Haardt F., Phlips B. F., 1997, MNRAS, 288, 958
Gies D. R., Bolton C. T., 1986a, ApJ, 304, 371
Gies D. R., Bolton C. T., 1986b, ApJ, 304, 389
Gies D. R. et al., 2003, ApJ, 583, 424
Golenetskii S., Aptekar R., Frederiks D., Mazets E., Palshin V., Hurley K., Cline T., Stern B., 2003, ApJ, 596, 1113
Gregory P. C., 2002, ApJ, 575, 427
Gregory P. C., Peracaula M., Taylor A. R., 1999, ApJ, 520, 376
Hellier C., Mason K. O., 1989, MNRAS, 239, 715
Ibragimov A., Zdziarski A. A., Poutanen J., 2007, MNRAS, 381, 723 (Paper I)
Karitskaya E. A., 2001, Astron. Rep., 45, 350

Katz J. I., 1973, Nat. Phys. Sci., 246, 87

Katz J. I., 1980, ApJ, 236, L127

Lachowicz P., Zdziarski A. A., Schwarzenberg-Czerny A., Pooley G. G., Kitamoto S., 2006, MNRAS, 368, 1025 (L06)

Levine A. M., Bradt H., Cui W., Jernigan J. G., Morgan E. H., Remillard R., Shirey R. E., Smith D. A., 1996, ApJ, 469, L33

Lubow S. H., Shu F. H., 1975, ApJ, 198, 383

Malzac J., Beloborodov A., Poutanen J., 2001, MNRAS, 326, 417

Markoff S., Nowak M. A., Wilms J., 2005, ApJ, 635, 1203

Negueruela I., 2004, preprint (astro-ph/0411335)

Özdemir S., Demircan O., 2001, Ap&SS, 278, 319

Parkinson P. M. S. et al., 2003, ApJ, 595, 333

Parmar A. N., White N. E., 1988, Mem. Soc. Astron. Ital., 59, 147

Pooley G. G., Fender R. P., Brocksopp C., 1999, MNRAS, 302, L1

Postnov K. A., Shakura N. I., 1987, Sov. Astron. Lett., 13, 122

Poutanen J., 1998, in Abramowicz M. A., Björnsson G., Pringle J. E., eds, Theory of Black Hole Accretion Discs. Cambridge Univ. Press, Cambridge, p. 100

Poutanen J., Coppi P. S., 1998, Phys. Scr. T, 77, 57

Raichur H., Paul B., 2008, MNRAS, 387, 439

Scott D. M., Leahy D. A., 1999, ApJ, 510, 974

Stern B. E., Beloborodov A. M., Poutanen J., 2001, ApJ, 555, 829

Sunyaev R. A., Titarchuk L. G., 1985, A&A, 143, 374

Szostek A., Zdziarski A. A., 2007, MNRAS, 375, 793

Türler M. et al., 2006, ATel, 911, 1

Uttley P., McHardy I. M., Vaughan S., 2005, MNRAS, 359, 345

Vaughan S., Edelson R., Warwick R. S., Uttley P., 2003, MNRAS, 345, 1271 (V03)

Viironen K., Poutanen J., 2004, A&A, 426, 985

Walborn N. R., 1973, ApJ, 186, 611

Wen L., Cui W., Levine A. M., Bradt H. V., 1999, ApJ, 525, 968

Wen L., Levine A. M., Corbet R. H. D., Bradt H. V., 2006, ApJS, 163, 372

White N. E., Holt S. S., 1982, ApJ, 257, 318

White N. E., Swank J. H., 1982, ApJ, 253, L61

Zdziarski A. A., Gierliński M., 2004, Prog. Theor. Phys. Suppl., 155, 99

Zdziarski A. A., Poutanen J., Paciesas W. S., Wen L., 2002, ApJ, 578, 357

Zdziarski A. A., Gierliński M., Mikołajewska J., Wardziński G., Smith D. M., Harmon B. A., Kitamoto S., 2004, MNRAS, 351, 791

Zdziarski A. A., Wen L., Gierliński M., 2007a, MNRAS, 377, 1006

Zdziarski A. A., Wen L., Gierliński M., Kostrzewa Z., 2007b, MNRAS, 377, 1017

Zdziarski A. A., Neronov A., Chernyakova M., 2008, MNRAS, submitted (arXiv:0802.1174)

Ziółkowski J., 2005, MNRAS, 358, 851

This paper has been typeset from a TEX/LATEX file prepared by the author.

Paper IV

Ibragimov A., Poutanen J.
Accreting millisecond pulsar SAX J1808.4-3658
during its 2002 outburst: evidence for
a receding disc

Accreting millisecond pulsar SAX J1808.4−3658 during its 2002 outburst: evidence for a receding disc

Askar Ibragimov[1,2]⋆ and Juri Poutanen[1]⋆

[1]*Astronomy Division, Department of Physics, PO Box 3000, FIN-90014 University of Oulu, Finland*
[2]*Kazan State University, Astronomy Department, Kremlyovskaya 18, 420008 Kazan, Russia*

ABSTRACT

An outburst of the accreting X-ray millisecond pulsar SAX J1808.4−3658 in 2002 October–November was followed by the *Rossi X-ray Timing Explorer* for more than a month. A detailed analysis of this unprecedented data set is presented. For the first time, we demonstrate how the area covered by the hotspot at the neutron star surface is decreasing in the course of the outburst together with the reflection amplitude. These trends are in agreement with the natural scenario, where the disc inner edge is receding from the neutron star as the mass accretion rate drops. These findings are further supported by the variations of the pulse profiles, which clearly show the presence of the secondary maximum at the late stages of the outburst after October 29. This fact can be interpreted as the disc receding sufficiently far from the neutron star to open the view of the lower magnetic pole. In that case, the disc inner radius can be estimated. Assuming that disc is truncated at the Alfvén radius, we constrain the stellar magnetic moment to $\mu = (9 \pm 5) \times 10^{25}$ G cm³, which corresponds to the surface field of about 10^8 G. On the other hand, using the magnetic moment recently obtained from the observed pulsar spin-down rate we show that the disc edge has to be within factor of two of the Alfvén radius, putting interesting constraints on the models of the disc-magnetosphere interaction. We also demonstrate that the sharp changes in the phase of the fundamental are intimately related to the variations of the pulse profile, which we associate with the varying obscuration of the antipodal spot. Using the phase-resolved spectra, we further argue that the strong dependence of the pulse profiles on photon energy and the observed soft time lags result from the different phase dependence of the normalizations of the two spectral components, the blackbody and the Comptonized tail, being consistent with the model, where these components have significantly different angular emission patterns. The pulse profile amplitude allows us to estimate the colatitude of the hotspot centroid to be $\sim 4°$–$10°$.

Key words: accretion, accretion discs – methods: data analysis – pulsars: individual: SAX J1808.4−3658 – stars: neutron – X-rays: binaries

1 INTRODUCTION

SAX J1808.4−3658 (hereafter J1808) is the first detected accretion-powered millisecond pulsar (AMSP) (in 't Zand et al. 1998; Wijnands & van der Klis 1998). J1808 experiences outbursts lasting a few weeks roughly once in two years, during which the coherent ∼401 Hz pulsations are observable. The neutron star accretes matter from a $\sim 0.05 M_\odot$ brown dwarf (Bildsten & Chakrabarty 2001) at a 2 hr orbit (Chakrabarty & Morgan 1998). The magnetic field strength is estimated to be about 10^8–10^9 G (Psaltis & Chakrabarty 1999). A recent analysis of the pulsar spin-down between the outbursts gives a narrower range of $B \sim (0.4$–$1.5) \times 10^8$ G (Hartman et al. 2008a, hereafter H08). Among eight AMSP discovered since 1998 showing coherent pulsations over ex-

tended intervals during their outbursts (see Wijnands 2006; Poutanen 2006 for reviews and Krimm et al. 2007), J1808 is the best studied thanks to its five outbursts and their good coverage with the *Rossi X-ray Timing Explorer (RXTE)*.

The analysis of the broad-band spectra of J1808 reveals the presence of at least two major components: soft, blackbody-like emission below 7 keV and a power-law tail with the cut-off at ∼100 keV (Gierliński, Done & Barret 2002; Poutanen & Gierliński 2003, hereafter PG03). Both components are pulsating at the pulsar frequency and therefore are associated with the impact of the accretion stream to the neutron star surface. The hard power-law is most probably produced in the accretion shock, while the blackbody might be the heated neutron star surface underneath and around this shock (see Gierliński & Poutanen 2005, for the geometry and observational signatures supporting this interpretation). These components have been identified in other AMSP too (Falanga et

⋆ E-mail: askar.ibragimov@oulu.fi, juri.poutanen@oulu.fi
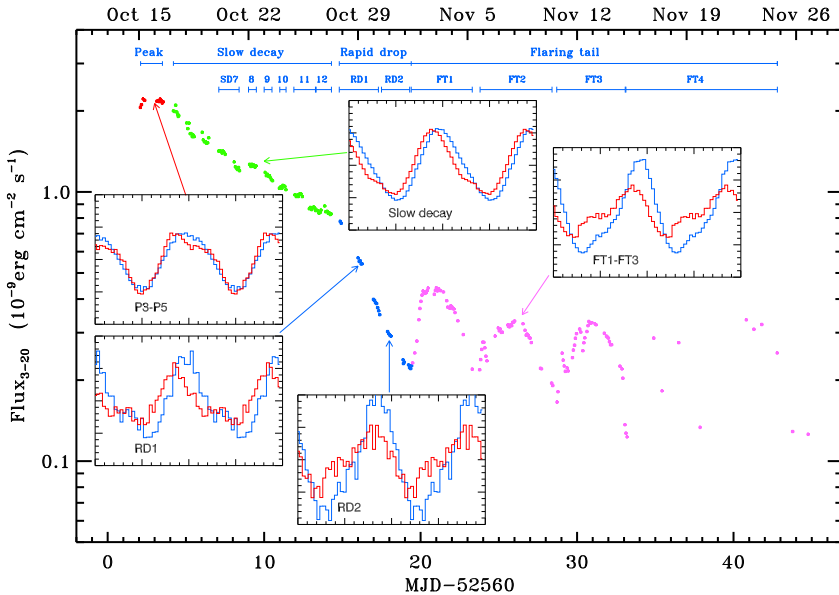
Figure 1. The light curve of SAX J1808.4−3658 during the 2002 outburst. The flux is computed in the 3–20 keV energy band. We divide the outburst into 4 stages: P, SD, RD and FT, which are coloured in red, green, blue and magenta, respectively. Stripes indicate different outburst stages, see Table 1. The inserts show the pulse profiles at different times in the 2–3.7 and 10–24 keV energy bands (blue and red histograms, respectively).

al. 2005a,b; Gierliński & Poutanen 2005; Falanga et al. 2007). The spectral shapes are very similar for individual objects over the course of the outbursts (see e.g. Gilfanov et al. 1998) as well as for different objects (Poutanen 2006). The accretion disc signatures have been also revealed with the *XMM-Newton* data either spectroscopically by the presence of the softer component as in XTE J1751–305 (Gierliński & Poutanen 2005) or by reduction of the pulse variability amplitude below ∼2 keV as in J1808 (Patruno et al. 2009a). Also the spectral features observed around 6–7 keV in J1808 are a clear signature of the iron line produced by reflection from the neutral matter, presumably the accretion disc.

Understanding of the physical nature of the spectral components has important implications for the correct interpretation of the pulse profiles and particularly their strong energy dependence. Phase-resolved spectroscopy reveals that the two major components do not vary in phase (Gierliński et al. 2002; Gierliński & Poutanen 2005), resulting in prominent soft time lags (i.e. hard photons arriving earlier), which have a steep energy dependence up to 7 keV, the energy where the contribution of the blackbody becomes negligible. The corresponding pulse profiles associated with the components also are significantly different, with the harder photons showing more harmonic content. A natural interpretation of these phenomena is related to the different angular pattern of the blackbody and the shock emission (PG03).

The variability of the pulse profiles in the course of the outburst also gives us a clue to the origin of the X-ray emission. J1808 demonstrates remarkably similar evolution of the profiles during its outbursts in 1998, 2002, 2005, and 2008 (H08; Hartman et al. 2009). During most of the outburst (at SD stage, see Fig. 1), at high flux level, the profile is very stable and is nearly sinusoidal with a low harmonic content. The profiles observed during the SD stages

of the 1998 and 2002 outbursts are almost identical (see profiles 2 and 4 in fig. 3 in H08). Also in 2005, profiles 4A and 4B that appeared during a large fraction of the outburst are rather similar to those in the SD stages of the 1998 and 2002 outbursts. Even in 2008, the pulsar had a similar profile at high flux period (see profiles 1 and 2 in fig. 1 of Hartman et al. 2009). Such profile is consistent with being produced by only one hotspot as discussed and modelled by PG03. The pulse stability allows to obtain a high photon statistics and use the average pulse profile to get constraints on the neutron star mass-radius relation and the equation of state (see PG03 and Leahy, Morsink & Cadeau 2008).

However, there are clear deviations from this profile both at high- and low- flux levels. In the peak of the outburst in 2002 and 2005, the profile has a dip in the middle of the broad maximum (see profiles for the P3–P5 period in Fig. 1). On the other hand, at low fluxes, the pulse has either a clearly double-peaked profile or a significant skewness opposite to that observed at SD stage (H08). This variability also results in jumps in the phases of the harmonics (timing noise) with the most dramatic example being a glitch-like feature in the phase of the fundamental in 2002 and 2005 outbursts (Burderi et al. 2006; H08). Such variations seriously complicate the study of the spin evolution of the pulsar. In 1998, this kind of jumps have not been detected as the *RXTE* data do not cover well enough the low-flux periods (see fig. 1 in Gilfanov et al. 1998 or fig. 1 in H08).

There are plenty of reasons why the pulse profile might change (see Poutanen 2008, for a review). At high accretion rate, the absorption in the accretion stream might play a role. The effect should be largest close to the phase where the flux is large, when the stream impact point (i.e. the hotspot) is visible at presumably lowest inclination to the normal. As the accretion rate changes, we expect,

for example, some variations of the angular emissivity pattern of the hotspots, and changes in the spot area, their shape, as well as their position at the stellar surface (Lamb et al. 2008; Patruno et al. 2009c), as the gas follows different magnetic field lines. Also, the visibility of the antipodal spot, hidden at high accretion rates, can vary dramatically as the accretion disc retreats, causing a strong pulse shape variability.

Changes in the accretion disc inner radius are expected on physical grounds as the magnetospheric radius increases with the dropping accretion rate. In addition, there is an indirect evidence for increasing inner radius from the drop of the kilohertz quasi-periodic oscillation (QPO) frequency during the 2002 outburst (van Straaten et al. 2005), if interpreted as a signature of Keplerian rotation.

In the present work, we track the changes in spectral and timing characteristics through the 2002 outburst of J1808 with the aim to determine the variations in the geometry of the system. We first analyse the phase-averaged spectra and their evolution. We study the variations of the apparent hotspot area and the amplitude of the reflection features (which are signatures of cool material in the vicinity of X-ray source) during the outburst. We then study the pulse profiles, their dependence on energy, the corresponding time lags, and finally the phase-resolved spectra. Furthermore, we estimate the physical size of the hotspot and put constraints on the geometry, in particular the inner disc radius and the displacement of the magnetic dipole from the rotational axis. Using two alternative methods, we determine the magnetic moment of the neutron star. Finally, we introduce a simple model of the pulsar with two antipodal spots and a variable inner accretion disc radius and compare the predictions of the model to the data.

2 OBSERVATIONS

We focus on the data obtained during the most data-rich outburst of J1808 happened in 2002. The observations are made by the *RXTE* during MJD 52562–52604 (October 15 – November 26) and belong to the ObsID 70080. For the analysis, we used the standard HEADAS 6.1 package and the CALDB. We use the data taken by *RXTE*/PCA (3–20 keV) and HEXTE (25–200 keV); 1 per cent systematics has been added to the PCA spectra (see Jahoda et al. 2006 for a complete review on PCA calibration). To keep the calibration uniform throughout our data set, we used the data from PCA units 2 and 3 only.

The outburst can be divided into four periods. The peak (P) stage (MJD 52562.1–52563.5; 2002 October 15–16) marks the very beginning of the observations, when the 3–20 keV flux (corrected for absorption) is relatively constant at $\sim 2.2 \times 10^{-9}$ erg cm^{-2} s^{-1} and fast (up to ~ 700 Hz) QPOs are present. The slow decay (SD) stage (MJD 52564.2–52574.3; October 17–27) shows QPOs twice as slow and the exponential decrease of the flux. At the rapid drop (RD) stage (MJD 52574.8–52579.3; October 27 – November 1), the flux falls even faster, and the secondary maximum appears in pulse profiles after October 29. During the flaring tail (FT), the last stage (MJD 52579.4–52602.8; November 1–24), the flux was rising and fading with the period of ~ 5 days till the source became undetectable. The power density spectrum at this stage is dominated by a strong 1 Hz QPO (van Straaten et al. 2005; Patruno et al. 2009b). The outburst lightcurve and the sample pulse profiles are shown on Fig. 1 (see also figs 2 and 3 in H08); note the shape differences between various energies.

While the photon count rate is rather high at the beginning of

Table 1. Data groupings for spectral and timing analysis.

| MJD interval	Group code	Outburst stage
52562.13 – 52563.55	P	P
52562.13 – 52562.46	P1	P begins
52562.46 – 52562.55	P2	
52563.11 – 52563.14	P3	
52563.18 – 52563.21	P4	
52563.25 – 52563.55	P5	P ends
52564.25 – 52574.29	SD	SD
52564.17 – 52564.50	SD1	SD begins
52564.50 – 52564.53	SD2	
52565.09 – 52565.42	SD3	
52565.42 – 52565.53	SD4	
52566.08 – 52566.11	SD5	
52566.14 – 52566.45	SD6	
52567.07 – 52568.42	SD7	
52569.04 – 52569.48	SD8	
52570.03 – 52570.28	SD9	
52570.95 – 52571.39	SD10	
52571.94 – 52573.30	SD11	
52573.33 – 52574.29	SD12	SD ends
52574.84 – 52579.36	RD	RD
52574.84 – 52577.40	RD1	
52577.40 – 52579.36	RD2	
52579.40 – 52602.79	FT	FT
52579.40 – 52583.30	FT1	FT begins
52583.75 – 52588.44	FT2	
52588.67 – 52592.92	FT3	
52593.02 – 52602.79	FT4	FT ends

the outburst, at its end it is necessary to co-add many individual observations to obtain the pulse profiles and spectra with reasonably small errors. Therefore, we group the data (based on similar count rate and pulse shape) as shown in Table 1. For pulse extraction, we used the pulsar ephemeris obtained by H08.

The spectral analysis (both phase-resolved and phase-averaged) was done using the XSPEC 11.2 spectral package (Arnaud 1996). All uncertainties correspond to a 90 per cent confidence interval.

3 SPECTRAL ANALYSIS

3.1 Evolution of the spectral shape

The comparison of the spectral shapes at different observation dates may help to determine the contribution of various emitting components. Thoughout the paper, we plot the so-called unfolded spectra, which show the assumed underlying model multiplied by the ratio of the observed data to the spectral model folded with the detector's response matrix. In Fig. 2, we present the *RXTE*/PCA spectra (unfolded using power-law model with spectral index 2.0) for several moments of the outburst. In the brightest observations at the P stage we find the flux excess below 4 keV; this feature is much less noticeable in the later data. Most probably, the soft excess is the accretion disc emission. This interpretation is supported by the reduced variability at the pulsar frequency below 2 keV in the *XMM-Newton* data obtained during the 2008 outburst (Patruno et al. 2009c). A similar component was found also in the *XMM-Newton* data on XTE J1751–305 (Gierliński & Poutanen 2005). As the disc temperature is below 0.5 keV in these cases, it is not sur-
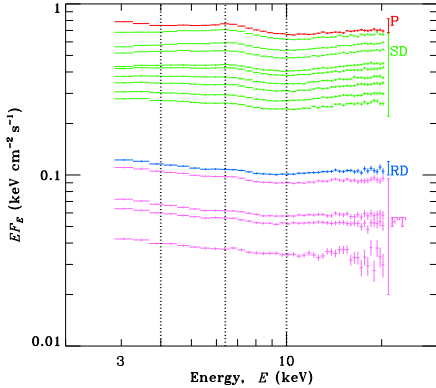
Figure 2. The unfolded spectra for *RXTE*/PCA range. Vertical lines indicate the boundaries for spectral components, from left to right: extra flux below 4 keV, 6.4 keV Fe line, blackbody hotspot emission below 10 keV and thermal Comptonization above 10 keV. The outburst stages coloured as in Fig. 1 are indicated at the right-hand side.

prising why *RXTE* sees the excess only at highest fluxes, when the accretion disc is expected to be hottest.

In the 3–10 keV range, the spectrum does not resemble a power-law and is likely the blackbody-like emission from the neutron star surface (the similar results were obtained for other AM-SPs, see Gierliński, Done & Barret 2002; Falanga et al. 2005a,b; Gierliński & Poutanen 2005; Falanga et al. 2007). Above 10 keV, we observe a power-law-like emission with the spectral index slightly changing in time. The hard X-ray data from *RXTE*/HEXTE (see Section 3.2) displays a cut-off at ~ 100 keV, which is consistent with thermal Comptonization in ~ 50 keV electron gas. A bump in the spectrum around 6–7 keV and the hardening above 10 keV are clear signatures of fluorescent iron line at ~ 6.4 keV and Compton reflection of the underlying continuum from the cold material. The amplitude of the corresponding residuals reduces as the flux drops.

3.2 Phase-averaged spectra

In this section, we describe the results of fitting the phase-averaged spectra with various models. All our models include interstellar absorption, with the hydrogen column density fixed at the Galactic absorption value of 1.13×10^{21} cm^{-2} (obtained from the HEADAS tool NH using the pulsar's coordinates). The distance to the source is assumed to be $D = 3.5$ kpc (Galloway & Cumming 2006). Because the relative normalization of the PCA and HEXTE instruments is uncertain, we allowed this to be an addition free parameter in all spectral fits.

3.2.1 Power-law-based models

A power-law model with an exponential cut-off (XSPEC model CUTOFFPL), described by the photon index Γ and cut-off energy $E_{\rm cut}$, produces rather bad fits. Adding a gaussian iron line at 6.4 keV and a blackbody component (BBODYRAD), described by the temperature $T_{\rm bb}$ and normalization $K = [(R_{\infty}/{\rm km})/(D/10\ {\rm kpc})]^2$, significantly improves the fits giving $\chi^2/{\rm dof} \sim 1$. The apparent residuals remain in the low energy
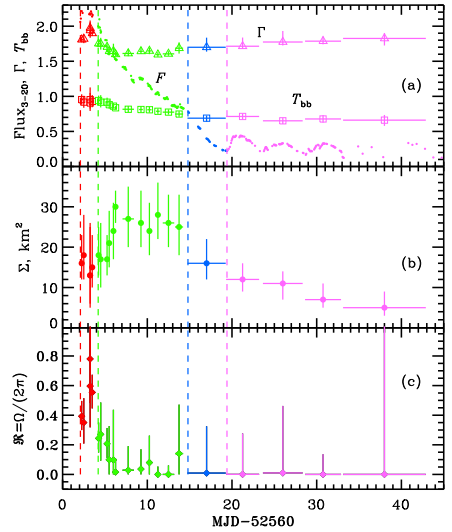
Figure 3. The best-fitting parameters for the blackbody and the cut-off power-law plus reflection model. Evolution of (a) the photon index Γ and blackbody temperature $T_{\rm bb}$ together with the flux in 3–20 keV band corrected for absorption (shown by circles) in units of 10^{-9} erg cm^{-2} s^{-1}, (b) blackbody apparent emitting area, and (c) reflection amplitude. The vertical dashed lines separate various outburst stages.

channels below 4 keV, at the earlier stages of the outburst (groups P1–SD4). We model this feature with another blackbody (representing the accretion disc) with the temperature of 0.2 keV and free normalization. The resulting fits show that the temperature of the main blackbody component decreases from about 0.9 to 0.7 keV and the apparent area $\Sigma = \pi R_{\infty}^2$ also decreases from about 30 to 10 km^2 as the outburst progresses. At the same time, the underlying power-law softens from $\Gamma \approx 1.5$ to 1.9 and the cut-off energy increases from about 40 to 80 keV, and during the FT stage it becomes unconstrained. The amplitude of the additional (disc) blackbody decreases with time, but it is badly constrained as this component is mostly outside of the *RXTE* energy band.

The residuals relative the power-law fit seen in Fig. 2 imply the presence of the Compton reflection and an iron line in the spectrum. Consequently, we add Compton reflection to the cut-off power-law model (PEXRAV model, Magdziarz & Zdziarski 1995), with the additional fitting parameters being the reflection amplitude $\Re = \Omega/(2\pi)$ (where Ω is the solid angle covered by the cold reflector as viewed from the isotropic X-ray source) and inclination which we fix at $i = 60°$. The inclination parameter affects only weakly the shape of the Compton reflection continuum in the X-ray band (Magdziarz & Zdziarski 1995; Poutanen, Nagendra & Svensson 1996) and does not affect any other spectral components. Therefore, any other value of i would be also acceptable.

The limited statistics does not allow to simultaneously constrain $\Re$ and the cut-off energy for the spectra taken only during short time intervals. We have fitted the averaged spectrum for the SD phase and obtained $E_{\rm cut} = 63^{+13}_{-10}$ keV; hense we assume $E_{\rm cut} = 65$ keV in all spectra. Our results are shown in Fig. 3. We see that the underlying power-law index is almost constant $\Gamma \sim 1.8$. The apparent blackbody area Σ reaches the maximum

of ∼30 km² (corresponding to the radius of only 3 km) at the SD stage and decreases at the later outburst stages. The reflection amplitude is clearly larger at the peak and drops rapidly during the SD stage, this explains the apparent softening of the power-law seen in the model without reflection. The absolute amplitude of reflection depends on assumed inclination, scaling roughly as $\propto 1/\cos i$.

3.2.2 Thermal Comptonization model

The physical origin of the power-law-like spectrum with a cut-off is most probably related to thermal Comptonization. Because this component is pulsating, it is natural to assume that it is produced in the accretion shock above the neutron star surface. Although the detailed shock structure can be rather complicated, one often approximates it by a single temperature plane-parallel slab. To simulate the Comptonized emission, we use the COMPPS model of Poutanen & Svensson (1996) in slab geometry. We set the inclination $i = 60°$ following Gierliński et al. (2002). As in power-law-based models of Section 3.2.1, inclination is not constrained from the spectral data alone and a particular choice of i will affect only the resulting reflection fraction, which scales as $\propto 1/\cos i$. The fitting parameters are the temperature and the Thomson optical depth of the Comptonizing electron slab T_e and τ and the temperature and the effective emitting area of the blackbody seed photons for Comptonization T_{seed} and Σ_{hard}. Reflection is described by the amplitude $\Re$ and the iron 6.4 keV line (DISKLINE) by the normalization. The statistical limitations of the data and the energy resolution of PCA do not allow us to fit the inner disc radius (that controls relativistic smearing of the line and reflection), therefore we fix it (for spectral fits only) on $10r_s$ (statistically acceptable for all observations, $r_s = 2GM/c^2$ is the Schwarzschild radius),[1] and assume the radial profile of the emissivity $\propto r^{-3}$. The heated surface around the shock is modeled by an additional blackbody emission component BBODYRAD (see also Gierliński et al. 2002; PG03; Gierliński & Poutanen 2005; Falanga et al. 2005b, 2007) of temperature T_{bb} and area Σ_{soft}. To account for the excess flux below 4 keV in groups P1 – SD4, we used an additional (disc) blackbody component with the temperature of 0.2 keV and free normalization.

On the physical grounds, we expect that the blackbody emitting area Σ_{soft} is similar to the area covered by the Comptonizing slab Σ_{hard}. Attempts to fit these normalizations independently lead to unreasonably large effective emitting areas of one of the components (see also Gierliński & Poutanen 2005, section 4.5). We have fitted the spectrum of group SD, which has the best statistic among our data set, with both Σ_{soft} and Σ_{hard} being free parameters, and obtained $\Sigma_{soft} = 75^{+31}_{-15}$ km² and $\Sigma_{hard} = 30^{+30}_{-15}$ km². Fixing the ratio $\Sigma_{soft}/\Sigma_{hard} = 2$, gives a good fit and results in a reasonable area of $\Sigma_{hard} = 37 \pm 7$ km². We then assumed equal areas $\Sigma_{soft} = \Sigma_{hard} = \Sigma$, and were also able to get good fits for all data sets and obtained reasonable values for the areas $\Sigma \sim 30$–110 km², which imply the apparent spot radius of $R_\infty \sim$3–6 km. These examples clearly demonstrate that on the quantitative level the results are affected by the assumed relations between the COMPPS and BBODYRAD normalizations. In the following we assume equal areas and keep in mind that the systematic error for the spot area is about a factor of two, which translates to a 50 per cent uncertainty in R_∞. We also note that to obtain the actual spot size at the stellar

---

[1] Here we assume fixed inner disc radius, because of the limited spectral data. Later in the paper, we show that the variations of the reflection amplitude and the pulse profiles require the disc inner radius to change.
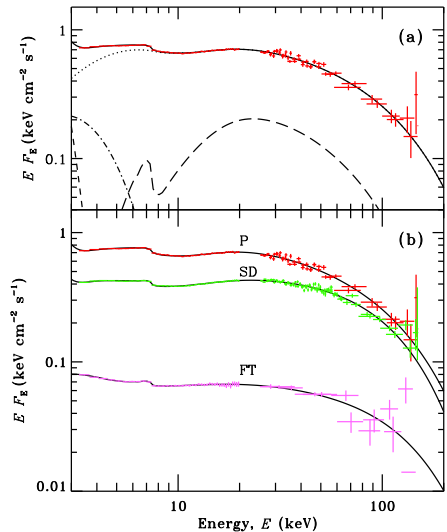
Figure 4. Broad-band spectra of J1808 and the best-fitting thermal Comptonization-based model. (a) Unfolded observed spectrum at the P stage. Solid, dotted, dot-dashed, long dashed and short-dashed curves represent the total model spectrum, thermal Comptonization continuum COMPPS, blackbody component, reflection with the 6.4 keV line, and an additional soft blackbody below 4 keV, respectively. (b) Unfolded observed spectra at the P, SD and FT stages. Solid curves represent the best-fitting thermal Comptonization model from Section 3.2.2.

surface the apparent areas should be corrected for the inclination and gravitational light bending effect, as discussed in Section 5.1.

The spectral fits to the broad-band spectra averaged over the outburst stages and the contribution of individual spectral components are shown on Fig. 4. We see that the overall spectral shape does not seem to vary much during the whole outburst as was noticed also by Gilfanov et al. (1998) for the 1998 outburst. However, the fitting parameters do change significantly (see Fig. 5). We clearly see that the seed photon temperature T_{seed} as well as the temperature of the additional blackbody are decreasing with time, which is natural as the total luminosity drops. The area Σ also seems to decrease. This trend is independent of the assumed ratio $\Sigma_{soft}/\Sigma_{hard}$. Such a behaviour is expected when the magnetospheric radius increases at lower accretion rate. The values of Σ in the Comptonization model are significantly larger than those in the power-law model fits (cf. Fig. 3), because in the Comptonization model only a fraction of the blackbody seed photons escape through the Comptonizing slab and the Comptonized continuum has a low-energy cut-off unlike the power-law which continues to lower energies without a break. Despite the large uncertainties, the reflection $\Re$ shows the decreasing amplitude which is consistent with the trend obtained with PEXRAV model. The Thomson optical depth and the electron temperature of the Comptonizing slab are rather constant, $\tau \sim$1.0–1.2 and $T_e \approx$40–45 keV, which is consistent with the stability of the underlying power-law in the PEXRAV model. The decreasing of the reflection together with the drop of the QPO frequencies (if related to the Keplerian frequencies) is consistent with the increasing inner disc radius in the course of the outburst.
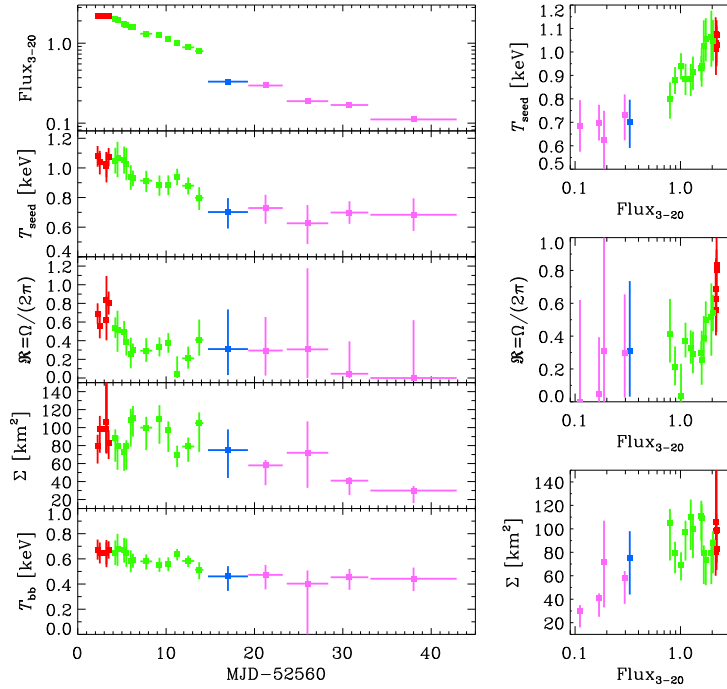
Figure 5. The evolution of the spectral parameters for the Comptonization model of Section 3.2.2 and the correlations between them. The flux corrected for absorption is in 3–20 keV band in units of 10^{-9} erg cm^{-2} s^{-1}. The points at various outburst stages are coloured as in Fig. 1.

4 TEMPORAL PROPERTIES

4.1 Pulse profiles and their energy dependence

The pulse profiles of J1808 evolve substantially during the 2002 outburst (H08). During the P stage, the energy-averaged pulse is close to sinusoidal, but skewed to right. The small secondary minimum is noticeable at energies above 10 keV. During the SD stage, the pulse is very stable and nearly symmetric, with a slightly faster rise than decay. In the end of RD1 stage (MJD 52576, October 29), the secondary maximum (signature of the second hotspot) becomes pronounced. At stage RD2 (after MJD 52577, October 30), the pulse becomes skewed to the left, and the secondary maximum shifts to the rising part of the main peak. On MJD 52581 (November 3), the pulse has a clear double-peak profile leaving no doubts that the second hotspot is visible. At the FT stage, the pulse continues to be skewed to the left. The strength of the first overtone (i.e. at double pulsar frequency) clearly anticorrelates with the flux at later stages as was pointed out by H08.

We are also interested in the energy dependence of the pulse profiles as this provides us with the clues of the origin of pulse variability. The evolution during the outburst of the pulse profiles in two energy intervals 2–3.7 keV and 10–24 keV is presented in Fig. 1. These energy bands are of particular interest, because the soft one has the largest contribution of the blackbody component, while the hard one contains only the Comptonized continuum. For most of the observations, the pulse shapes can well be described just by two harmonics:

$$F(\phi) = \overline{F}\{1 + a_1 \cos[2\pi(\phi - \phi_1)] + a_2 \cos[4\pi(\phi - \phi_2)]\}. \quad (1)$$

We have extracted pulse profiles in various energy intervals for every satellite orbit and fitted them with equation (1). The best-fitting (positive) relative amplitudes a_1, a_2 and the phases ϕ_1, ϕ_2 for the fundamental and first overtone for the two energy intervals are presented in Fig. 6. We also fitted pulse profiles averaged over the outburst stages in four different energy band (see left-hand panels of Fig. 7). We see that the profiles depend strongly on energy. During the P and SD stages, the relative amplitude of the first overtone is larger at hard energies (above 10 keV). The rms drops with increasing energy only slightly. At the later stages, the rms at energies above 10 keV is 2–3 times smaller than that below 4 keV and the oscillation amplitude at the fundamental is much more pronounced at soft energies comparing to the hard ones (see also Fig. 6).

We also notice that the phase of the overtone behaves differently below 4 keV and above 10 keV. There is a clear increasing trend at low energies, while the phase is consistent with being constant at higher energies (compare lower panels in Fig. 6). This serves as a warning against using such phase-connecting solutions to determine the pulsar frequency evolution (cf. Burderi et al. 2006). Clearly the pulse profile energy dependence and variability introduces a strong bias.

4.2 Time lags

The pulse profile dependence on energy can also be quantified by studying the time lags. Although they contain less information than the pulse shape, it is customary to study them as the function of energy. In J1808 the lags are soft, i.e. the pulse peaks at softer en-
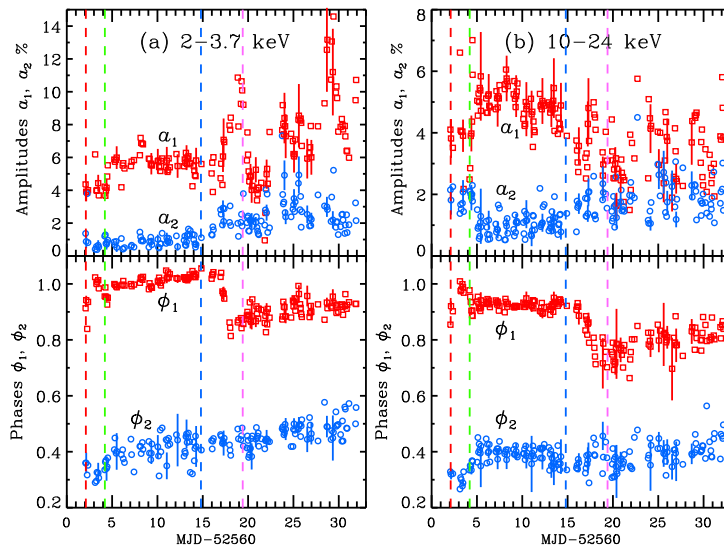
Figure 6. Fourier amplitudes and phases of the best-fitting curves (1) to the per-orbit pulse profiles in (a) 2–3.7 keV and (b) 10–24 keV energy bands. Top panels: amplitudes of the fundamental a_1 (squares) and the first overtone a_2 (circles). Bottom panels: phases of the fundamental ϕ_1 (squares) and the overtone ϕ_2 (circles). The vertical dashed lines separate various outburst stages. The typical errors are shown for some points.

ergies at a later phase (Cui, Morgan & Titarchuk 1998; Gierliński et al. 2002). We compute the time lags by fitting the pulse profiles at a given energy bin with equation (1) and finding the phase difference relative to the reference energy.[2] The 90 per cent confidence interval for one parameter is estimated from $\Delta\chi^2 = 2.71$. For the four outburst stages, the lags relative to the 2–3.3 keV band at the fundamental frequency and the first overtone computed from the best-fitting phases ϕ_1 and ϕ_2 are presented in the right-hand panels of Fig. 7 by circles and triangles, respectively. The absolute value of the lags is increasing from 3 up to ∼10 keV, and saturates there. Such a behaviour is similar to what is observed in the J1808 data during the 1998 outburst (Cui et al. 1998; Gierliński et al. 2002) as well as in other sources (see e.g. Galloway et al. 2002; Gierliński & Poutanen 2005), except IGR J00291+5934, where the lags seem to change the trend around 15 keV (Galloway et al. 2005; Falanga et al. 2005b). The lags at the fundamental increase when the accretion rate drops (see also Hartman, Watts & Chakrabarty 2008b). They are nearly zero at the peak of the outburst and reach -300 μs at the latter outburst stages. The lags at the first overtone seem to follow similar trends, being consistent with zero at the peak of the outburst and reaching -200 μs latter on.

[2] Alternatively, we can use the standard discrete Fourier transform of the pulse profile to compute the relative amplitudes and phases:

$$a_k e^{2\pi i k \phi_k} = 2/N_{\mathrm{ph}} \sum_{j=1}^{n} x_j e^{2\pi i j k/n}, \qquad (2)$$

where n is the number of phase bins, x_j ($j = 1, ..., n$) is the number of counts in the jth bin, $N_{\mathrm{ph}} = \sum_{j=1}^{n} x_j$ is the total number of counts, and $k = 1, 2$ correspond to the fundamental and the first overtone, respectively. The amplitudes and phases obtained by the two methods become similar in the limit of small errors and only when the profile can be well represented by equation (1).

An alternative measure of the lag is the shift with energy of the maximum of the best-fitting curve (1). To estimate the uncertainties of the lag value, we perturb the fitting parameters within 90 per cent confidence interval and find the maximal displacements of the curve maximum. The results are shown by squares in Fig. 7. These lags in general follow the energy dependence obtained from the fundamental, except at the P stage, where they are significantly larger. This difference originates in the existence of the absorption-like feature at zero phase in the pulse profile at high energies and the corresponding shift of the maximum to an early phase.

The lags have their origin most probably in difference of the emissivity patterns of blackbody and Comptonization emission, affected, in addition, by the fast stellar rotation (Gierliński et al. 2002; PG03). This explains not only why the lag change dramatically below 7 keV, where the blackbody's contribution varies significantly, but also the shape of the pulse profile as well as its energy dependence. On the other hand, models involving multiply Compton down- (or up-) scattering (see e.g. Cui et al. 1998; Falanga & Titarchuk 2007) pay attention only to the lags ignoring the pulse profiles. A specific time-lag model of Falanga & Titarchuk (2007) suffers also from other problems. The soft lags there are explained by multiply scattering of the hotspot's hard radiation in the accretion disc. However, the hard photons above 10 keV are actually mostly reflected (by single Thomson scattering), while the photons at a few keV are immediately absorbed (by photoelectric absorption) because the disc is rather cool. Thus, the role of multiply scattering is negligible in any case and the lags cannot possibly be produced this way.

4.3 Phase-resolved spectroscopy

The phase-resolved spectroscopy of J1808 for its 1998 outburst has been performed by Gierliński et al. (2002) and for XTE 1751–305
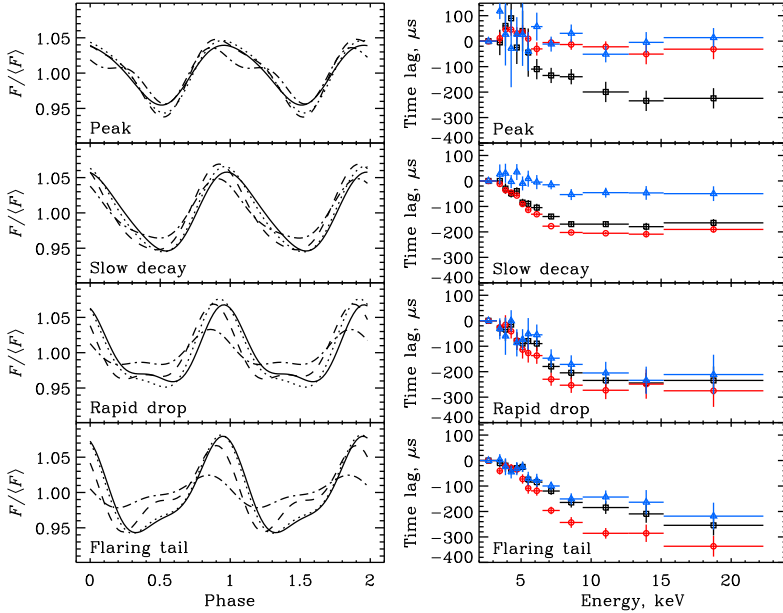
Figure 7. Pulse profiles (left-hand panels) in the 2–3.3, 4.5–4.9, 6.5–7.7 and 15.2–22.3 keV energy bands (solid, dotted, dashed and dash-dotted lines, respectively) as shown by their best-fitting expression (1). Time lags (right-hand panels) as a function of energy relative to the 2–3.3 energy band for various outburst stages. The time lags obtained from the pulse maximum, and the lags for the fundamental and the first overtone are shown by black squares, red circles, and blue triangles, respectively.

by Gierliński & Poutanen (2005). It has been concluded, that the energy dependence of the pulse profiles and the soft time lags can be explained with a simple model where only the normalizations of the Comptonized tail and the blackbody vary. The pulse shapes of these two components are different with the Compton component having stronger harmonic content and peaking at an earlier phase. Such profiles in their turn can be reproduced in a physical model proposed by PG03, where the angular dependence of the emissivity of the spectral components is different. In addition to normalization, one would expect variations of the blackbody temperature caused by Doppler shift, but this is a small effect at the level of 1–2 per cent (PG03).

We have generated the phase-resolved spectra for the P, SD and FT outburst stages. Following Gierliński et al. (2002), we used the corresponding thermal Comptonization model fits of the phase-averaged spectra (presented in Section 3.2.2) as a reference. We fixed all the model parameters and fitted the normalizations of the blackbody and thermal Comptonization (denoted as K_{soft} and K_{hard}, respectively). These normalizations can be directly related to the apparent emitting areas (measured in km^2) as $\Sigma_{soft|hard} = \pi D^2 K_{soft|hard}$ (where $D = 0.35$ is the source distance in units of 10 kpc). The results are shown on Fig. 8. The parameters of the fits with harmonic function (1) are given in Table 2.

At the P stage, the blackbody variations are consistent with a sine-wave, while the Comptonized component shows a dip at zero phase, which is reflected in the energy-resolved pulse profiles at high energies (left-hand panel, Fig. 7). This dip (probably associated with absorption in the accretion column) causes the shift of the maximum to earlier phase. The profiles during the SD stage are

Table 2. Harmonic fits by expression (1) to the phase-resolved apparent areas.

	Peak		Slow decay		Flaring tail	
	soft	hard	soft	hard	soft	hard
$\overline{\Sigma}$	77	74	67	67	40	52
a_1	0.08	0.04	0.10	0.06	0.60	0.05
ϕ_1	0.01	0.93	0.04	0.88	0.98	0.79
a_2	0.03	0.02	0.01	0.01	0.21	0.02
ϕ_2	−0.01	0.27	−0.03	0.35	0.01	0.38

almost identical to those observed in 1998 (Gierliński et al. 2002), with the hard tail being less variable and having a stronger harmonic. It arrives earlier than the blackbody, resulting in the soft lags. At the FT stage, the blackbody shows enormous variability by a factor of 3, while the rms variability of the Comptonized tail is still only ∼5 per cent. Although the absolute value for the blackbody emitting area and the amplitude of its variation is model-dependent (because of our assumption of the equal phase-averaged areas and because the ∼0.6 keV blackbody contributes little to the *RXTE* energy band above ∼3 keV), it is clear that the blackbody is much stronger variable than the tail. These profile shapes are reflected in strong variations of the energy-resolved pulse profiles shown in Fig. 7, with the low-energy pulses (where the blackbody contributes more) having larger rms and the high-energy ones looking exactly as the Comptonized tail. The nature of such strong variations of the blackbody is not clear.
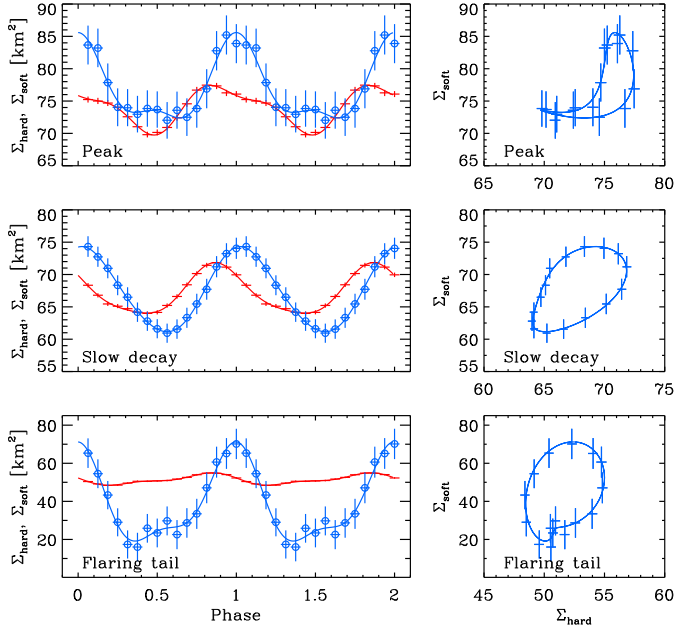
Figure 8. Results of the phase-resolved spectral analysis. The best-fitting parameters, except the normalizations of the Comptonization and blackbody components, are frozen at the values obtained for the phase-averaged spectra (groups P, SD and FT). Left panels: effective emitting area of the two components ($\Sigma_{\rm soft}$ and $\Sigma_{\rm hard}$, blue circles and red crosses, respectively) together with the fits by expression (1) and parameters given in Table 2. Right panels: $\Sigma_{\rm soft}$ versus $\Sigma_{\rm hard}$. The outburst stages are indicated on the panels.

5 THEORETICAL IMPLICATIONS

5.1 Spot size

The actual spot radius at the neutron star surface can be estimated from the apparent spot area $\Sigma = \pi R_\infty^2$ correcting for the light bending and geometry. Using Beloborodov (2002) analytical expression for light bending, PG03 obtained the observed bolometric flux produced by a circular blackbody spot of angular radius ρ (visible at all phases) as a function of phase ϕ of a slowly rotating pulsar:

$$F(\phi) = (1-u)^2 \frac{I_0}{D^2} \pi R_*^2 \sin^2\rho \left(Q + u\tan^2\frac{\rho}{2} + U\cos\phi\right), \quad (3)$$

where I_0 is the intrinsic radiation intensity, R_* is the neutron star radius, $u = r_{\rm s}/R_*$ and

$$U = (1-u)\sin i \, \sin\theta, \quad Q = u + (1-u)\cos i \, \cos\theta, \quad (4)$$

and i is the observer inclination and θ is the magnetic inclination, i.e. the colatitude of the spot centre. The phase-averaged value of $F(\phi)$, corresponding to the expression (3) without the last term in brackets, is related to the apparent radius as

$$\overline{F} = I\pi\frac{R_\infty^2}{D^2}, \quad (5)$$

where the observed intensity is $I = I_0(1-u)^2$. Thus for the apparent size of the spot we get

$$R_\infty = R_* \, \sin\rho \left(Q + u\tan^2\frac{\rho}{2}\right)^{1/2}, \quad (6)$$

which can be reduced to the biquadratic equation for $\sin(\rho/2)$ with the only physical solution:

$$\sin\frac{\rho}{2} = \frac{R_\infty}{R_*\sqrt{2}}\left[Q + \sqrt{Q^2 - \frac{R_\infty^2}{R_*^2}(1-u)\,\cos i\,\cos\theta}\right]^{-1/2}. \quad (7)$$

This relation breaks down when parts of the spot are eclipsed, and for the homogeneously bright star we have $R_* = R_\infty/\sqrt{1-u}$ (obviously, then no pulsations can be observed).

If the apparent size is significantly smaller the stellar radius, there exists a simple relation between the physical and the apparent sizes (PG03):

$$\rho R_* = R_\infty \, Q^{-1/2}. \quad (8)$$

The smallest possible spot radius is close to the apparent radius as $Q = 1$ for $i = 0$ and $\theta = 0$. As the oscillation amplitude is small, we expect that θ is rather small, thus the reasonable upper limit on the spot size is reached at $i = 90°$ (taking $\theta = 0$):

$$\rho R_* = R_\infty/\sqrt{u}. \quad (9)$$

Using equation (7) we compute the dependence of ρ on i and θ for a given R_∞. The results for $R_\infty = 5$ km (corresponding to the apparent area of 80 km^2) and two stellar compactnesses are shown in Fig. 9. The actual spot radius ρR_* is about 5–8 km depending on the inclination and compactness. The effect of rapid rotation changes the results only slightly. However, the apparent spot size obtained from the fitting of the spectra of J1808 is model dependent. The power-law-based model (Fig. 3) gives an apparent radius R_∞ between 3 and 1 km (for the assumed distance of $D = 3.5$
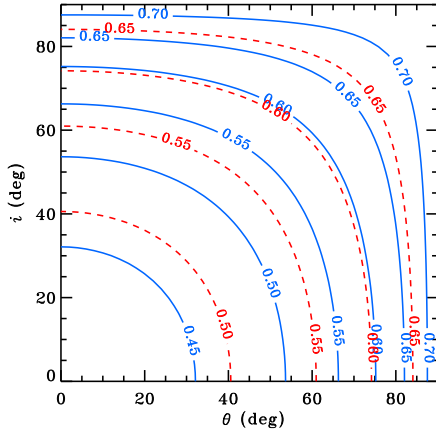
Figure 9. Contour plot of constant angular size (in radians) of the emitting spot ρ for the apparent spot radius $R_\infty = 5$ km. Solid curves correspond to the neutron star of $M = 1.4M_\odot$ and radius $R_* = 12$ km. The actual radius of the spot reaches minimum of 5.1 km at $i = 0$ and $\theta = 0$ and maximum of 8.7 km at $i = 90°$ and $\theta = 90°$. The dashed curves correspond to $M = 1.7M_\odot$ and $R_* = 11$ km. In that case, the actual spot size is between 5.1 and 7.6 km.

kpc). The radius estimated from the thermal Comptonization models (Fig. 5) is significantly larger, varying from about 5.6 to 3.6 km (corresponding to $\Sigma = $100–40 km^2) during the outburst. The main reason for this discrepancy is that the power-law continues to lower energies without a cut-off, while thermal Comptonization turns over at energies corresponding to seed photons. In addition, for Thomson optical depth of the order unity in the Comptonizing slab, only about 1/3 of the seed photons can escape directly, the rest being scattered and Comptonized to higher energies. Thus on the physical grounds we prefer the larger apparent size.

The apparent area is still uncertain within a factor of two as we discuss in Section 3.2.2, because of the unknown ratio of the areas of the blackbody and Comptonized components. The corresponding 50 per cent uncertainty in R_∞ means that the actual spot sizes of course are also uncertain by about the same amount, as it is clear from equation (8). An additional complication comes from the deviation of the spectrum from the blackbody. The actual spot size can be larger by the colour correction factor $f_{col} = T_{col}/T_{eff}$, which describes the shift of the spectral peak relative to the blackbody. However, for the atmospheres heated from above, this correction should not play a significant role (see discussion in PG03). In that case, the spot size during the whole outburst is smaller than the stellar radius for the typical neutron star masses and radii.

5.2 Oscillation amplitude and constraints on the geometry

Some constraints on the system geometry can be obtained from the observed oscillation amplitude. For a blackbody emitting spot at a slowly rotating star, the relative amplitude a_1 of the fundamental is (see PG03 and equation [3]):

$$a_1 = \frac{U}{Q + u\tan^2(\rho/2)}. \tag{10}$$

Comparing this expression to the observed oscillation amplitudes, we can constrain the geometrical parameters i and θ. The spot angular size ρ is estimated from equation (7) and substituted to equation (10). The resulting constraints on i and θ are shown in Fig. 10(a) as the contours of constant amplitude a_1 of 5 and 10 per cent. We see that for most probable inclinations, the displacement of the spot centre from the rotational axis is just $3°$–$7°$. These results only weakly depend on the assumed stellar compactness and stellar rotation (Poutanen & Beloborodov 2006). A stronger effect comes from the deviation of the emissivity pattern from the blackbody, as the Comptonization tail is expected to have a broader beaming pattern and therefore smaller amplitude (PG03, Viironen & Poutanen 2004). The same observed a_1 requires a slightly larger θ for a given i (see Gierliński & Poutanen 2005), but still $\theta \lesssim 10°$. Inclination smaller than about $40°$ (and thus possibly larger θ) can be ruled out on the basic of the X-ray (Chakrabarty & Morgan 1998) and optical (Giles, Hill & Greenhill 1999; Homer et al. 2001; Wang et al. 2001; Deloye et al. 2008) orbital modulations.

5.3 Visibility of the antipodal spot and the inner disc radius

The simplicity of the sine-like pulse profiles observed during the SD stage can be used to argue that the antipodal spot is not visible at this stage. The appearance of the antipodal spot later in the outburst is natural as the accretion disc is expected to recede from the neutron star opening the view of the lower stellar hemisphere. If we associate the appearance of the secondary peak in the pulse profile (on 2002 October 29) with the appearance of the antipodal spot, we can estimate the disc radius at this specific moment. This then can be used to get independent constraints on the magnetic field. The results depend somewhat on the spot size. We first assume $R_\infty = 5$ km (corresponding to apparent area of 80 km^2, see Fig. 5), and then vary it by 50 per cent within the uncertainty range.

Let us consider the parameter space where the antipodal spot can be eclipsed by the disc. As parameters we take the inclination i and the spot centroid colatitude θ. We take the spot size ρ given by equation (7) and shown in Fig. 9 and numerically compute photon trajectories from the spot elements towards the observer at every pulsar phase and check whether it crosses the disc (see Appendix C). This allows us to estimate the maximally allowed inner disc radius R_{in}, which fully blocks the spot. The contours of R_{in} at the plane i–θ for $R_\infty = 5$ km are shown in Fig. 10(a). We see that at large inclinations $i \sim 80°$, the disc fully covers the antipodal spot even when the inner radius is rather large $R_{in} \sim 40$ km. At $i \sim 50°$, the disc has to extend to < 20 km to cover the spot. The disc extending to the corotation radius

$$R_{cor} = 31 \left(\frac{M}{1.4M_\odot}\right)^{1/3} \left(\frac{\nu}{401\ \text{Hz}}\right)^{-2/3}\ \text{km} \tag{11}$$

blocks the antipodal spot from any observer at $i \gtrsim 67°$ (for $M = 1.4M_\odot$ and $R_* = 12$ km).

If we assume a smaller spot $R_\infty = 3$ km, the inner disc radius needed to fully block the spot increases by about 20 per cent compared to the $R_\infty = 5$ km case (compare solid to dashed curves in Fig. 10b). On the other hand, increasing the apparent spot size to 7 km, necessarily decreases the disc radius by 20 per cent (see dotted contours). The stellar compactness influences the results very little, for example, taking a higher mass of $M = 1.7M_\odot$ and $R_* = 11$ km, lead to the decrease in the disc radius by only $\sim$1 km (compare dashed and solid curves in Fig. 10a).

If the accretion is centrifugally inhibited at $R_{in} > R_{cor}$, the
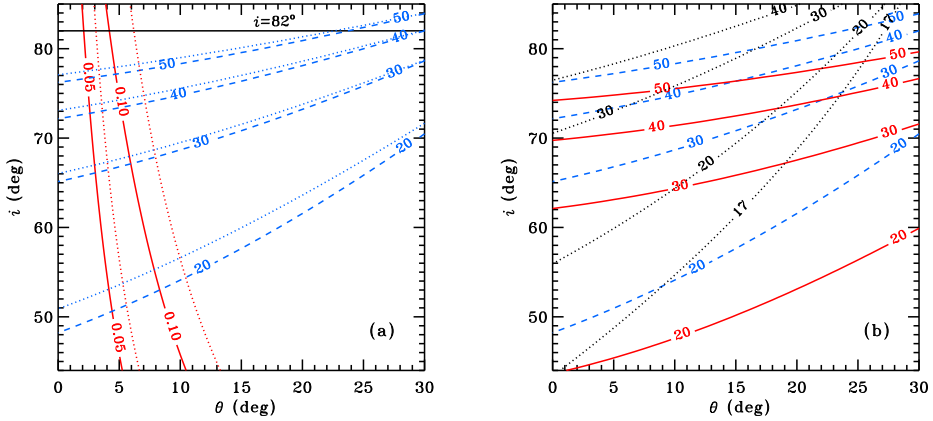
Figure 10. Constraints on inclination and colatitude of the emitting spot. (a) The solid (nearly vertical) curves show the contours of constant oscillation amplitude a_1 (given by equation [10]) of 5 and 10 per cent expected from a blackbody spot at a neutron star of mass $M = 1.4 \mathrm{M}_\odot$ and radius $R_* = 12$ km. The spot size corresponding to $R_\infty = 5$ km is computed using equation (7) (see Fig. 9). The dashed curves correspond to the upper limit on the inner disc radius (in km) that is required to fully block the view of the antipodal emitting spot. The corresponding results for the neutron star of $M = 1.7 \mathrm{M}_\odot$ and $R_* = 11$ km are shown by dotted curves. The upper limit on the inclination of $82°$ (Bildsten & Chakrabarty 2001) is shown by the horizontal line. (b) The inner disc radii required to block the antipodal spot ($M = 1.4 \mathrm{M}_\odot$ and $R_* = 12$ km) for various apparent spot sizes $R_\infty = 3$ (solid curves), 5 (dashed), and 7 km (dotted).

Table 3. Estimation of the inner disc radius and stellar magnetic moment μ from the apparent spot area at 2002 October 29.

	$M = 1.4\mathrm{M}_\odot$ $R_* = 12$ km			$M = 1.7\mathrm{M}_\odot$ $R_* = 11$ km		
i (deg)	50	60	70	50	60	70
			$R_\infty = 3$ km			
R_{in} (km)	21.5	27.5	40	20.5	27	38
$\mu\, k_{\mathrm{A}}^{7/4} f_{\mathrm{ang}}^{-1/2}$ ($10^{25}\mathrm{G\,cm^3}$)	4.4	6.8	13.2	3.6	5.9	10.7
			$R_\infty = 5$ km			
R_{in} (km)	19.5	24	34	18	23	33
$\mu\, k_{\mathrm{A}}^{7/4} f_{\mathrm{ang}}^{-1/2}$ ($10^{25}\mathrm{G\,cm^3}$)	3.7	5.4	9.9	2.9	4.5	8.4
			$R_\infty = 7$ km			
R_{in} (km)	17	20	27	14	18	26
$\mu\, k_{\mathrm{A}}^{7/4} f_{\mathrm{ang}}^{-1/2}$ ($10^{25}\mathrm{G\,cm^3}$)	2.9	3.9	6.6	1.9	2.9	5.5

clear signatures of the antipodal spot during the FT stage, give us an upper limit on the inclination $i \lesssim 64°, 67°, 73°$ for $R_\infty = 3, 5, 7$ km, respectively (for $M = 1.4\mathrm{M}_\odot$), which is lower than the constraint $i < 82°$ obtained from the absence of binary eclipses (Bildsten & Chakrabarty 2001). For a more massive star $M = 1.7\mathrm{M}_\odot$, the corresponding limits on the inclinations increase by 3 degrees. If, however, the inclination actually is $\gtrsim 75°$, this would imply that accretion proceeds even when $R_{\mathrm{in}} > R_{\mathrm{cor}}$ (see Spruit & Taam 1993; Rappaport, Fregeau & Spruit 2004; Kluźniak & Rappaport 2007).

The constraints on the oscillation amplitudes (see Section 5.2 and solid curves in Fig. 10a) reduce dramatically the allowed region in the (i, θ) plane. Combining this together with the fact that the antipodal spot has just appeared to the view, gives directly the estimation on the inner disc radius at that moment. The results are

presented in Table 3 for various inclinations and two sets of stellar compactness. We see that the largest uncertainty comes from the unknown inclination. The compactness affects the results at less than 10 per cent level, while a factor of 2 error in the apparent spot area (i.e. 50 per cent error in R_∞) results in only a 20 per cent error in R_{in}.

5.4 Constrains on stellar magnetic field

Having the information about the inner disc radius allows us to estimate the stellar magnetic moment. We need to know the accretion rate, which can be obtained from the observed bolometric flux F:

$$L = 4\pi D^2 F f_{\mathrm{ang}} = \eta \dot{M} c^2, \qquad (12)$$

where L is the total luminosity, $\eta = 1 - \sqrt{1-u}$ is the accretion efficiency in Schwarzschild metric, and f_{ang} is the factor correcting for the angular anisotropy of radiation and general relativity effects. It depends on the inclination, stellar compactness and spin, as well as position of the emitting spot and its emission pattern (see Appendix A for details of calculations). We approximate the angular distribution of radiation from the spot by a law

$$I_*(\alpha) = I_0(1 + h\cos\alpha), \qquad (13)$$

where α is the angle relative to the stellar normal and h is the anisotropy parameter. The value of $h = 0$ corresponds to the blackbody-like emission pattern and the negative h correspond to the Comptonized emission from an optically thin slab (see PG03; Viironen & Poutanen 2004). For inclinations in the range $50°$–$70°$ and a circular spot, f_{ang} varies in a rather narrow range 1.3 ± 0.2 (see Fig. A1). It depends very little on the assumed spot size, when R_∞ varies from 3 to 7 km, this factor changes only by 2–3 per cent.

The inner disc radius depends on the accretion rate $\dot{M}$ and scales with the classical Alfvén radius as

$$R_{\mathrm{in}} = k_{\mathrm{A}} (2GM)^{-1/7} \dot{M}^{-2/7} \mu^{4/7}, \qquad (14)$$

where μ is the neutron star magnetic moment. The coefficient k_A is rather uncertain, with the numerical simulations giving $k_A = 1/2$ (Long, Romanova & Lovelace 2005). Thus, we finally can express the magnetic dipole moment as

$$\mu_{25} = 0.56 \times k_A^{-7/4} \left(\frac{M}{1.4M_\odot}\right)^{1/4} \left(\frac{R_{in}}{10 \text{ km}}\right)^{7/4}$$
$$\times \left(\frac{f_{ang}}{\eta}\frac{F}{10^{-9} \text{ erg cm}^{-2} \text{ s}^{-1}}\right)^{1/2} \frac{D}{3.5 \text{ kpc}}, \quad (15)$$

where $\mu_{25} = \mu/10^{25}$ G cm^3.

The antipodal spot appears after 2002 October 29 at the flux level in the 3–20 keV band of $F_{3-20} \approx 0.4 \times 10^{-9}$ erg cm^{-2} s^{-1} and the corresponding bolometric flux $F \approx 0.8 \times 10^{-9}$ erg cm^{-2} s^{-1} and luminosity of about $L = 1.1 \times 10^{36}$ erg s^{-1}. Substituting this to equation (15), we get the magnetic dipole moments, which are presented in Table 3 for two sets of stellar parameters and various inclinations. Rather conservative limits are $\mu_{25} \approx (9 \pm 5) k_A^{-7/4}$ (for anisotropy factor $f_{ang} = 1.3 \pm 0.2$), with the largest uncertainty coming from the unknown inclination and parameter k_A. The estimated surface magnetic dipole field is about $B_0 \approx (0.8 \pm 0.5) \times 10^8 k_A^{-7/4}$ G (assuming neutron star radii 10–15 km), which is in excellent agreement with the value obtained recently from the pulsar long-term spin-down rate in the quiescence (H08), if $k_A \sim 1$. A similar value (close to the upper end) can be obtained (see Gilfanov et al. 1998) assuming that a sharp break (at 2002 October 28) in the pulsar light curve is associated with the onset of the propeller effect (Illarionov & Sunyaev 1975).

On the other hand, an independent knowledge of the stellar magnetic field provides constraints on parameter k_A. Taking $\mu_{25} = 5 \pm 3$ as obtained by H08, together with our estimations of the inner disc radius from Table 3, we get very conservative limits (for inclinations $50° < i < 70°$)

$$0.4 \lesssim k_A \lesssim 2.5. \quad (16)$$

These limits include all systematic and statistical uncertainties, including uncertainties in inclination, stellar mass, anisotropy factor, spot size and magnetic moment. As all theoretical models predict $k_A < 2^{1/7} \approx 1.1$ (see discussion in Psaltis & Chakrabarty 1999; Kluźniak & Rappaport 2007), this limits the inner disc radius to $R_{in} \lesssim 31$ km and gives some constraints on the inclination $i \lesssim 75°$.

5.5 Varying reflection

Variation of the reflection amplitude $\Re$ during the outburst and its correlation with the flux (see Figs 3 and 5) are clear signatures of the changes in the geometry happening when the accretion rate decreases. At the P stage, our thermal Comptonization fits require reflection to be $\Re \sim 0.6$–0.8 and power-law-based models give $\Re \sim 0.4$–0.6. The reflection substantially decreases during the SD phase and is not constrained at the FT stage. Although the actual reflection amplitude is model dependent (depends on the model of the underlying continuum and inclination), the trend is not. The dramatic changes in $\Re$ can only be explained if the geometry of the accretion flow varies significantly and the inner radius of the accretion disc in the peak of the outburst is close to the neutron star surface. Assuming R_{in} in the range 12–15 km at the peak flux level of $F_{3-20} \approx 2 \times 10^{-9}$ erg cm^{-2} s^{-1}, we can get a rough estimate of the stellar magnetic moment using equation (15). Taking anisotropy factor $f_{ang} = 1.3 \pm 0.2$ (see Fig. A1) and stellar masses in 1.4–1.7M$_\odot$ range, we get $\mu_{25} = (6 \pm 2) k_A^{-7/4}$, where the largest uncer-
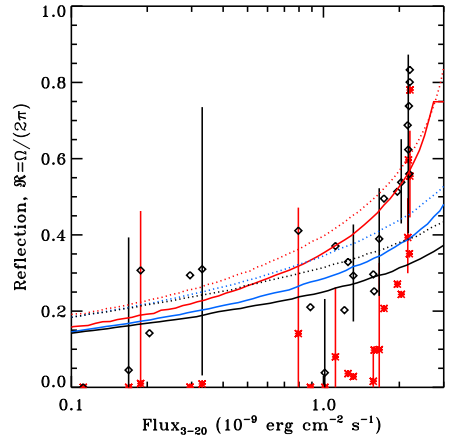

Figure 11. Reflection amplitude $\Re = \Omega/(2\pi)$ as a function of the flux in 3–20 keV band. The data points shown by diamonds and stars (with representative error bars) are for the fits using thermal Comptonization model of Section 3.2.2 and power-law-based model of Section 3.2.1, respectively. The set of three curves give the theoretical dependence expected for three different geometries of the emitting spot: (from top to bottom) a narrow ring with the outer angular radius ρ_{max} defined by the dipole formula (17) and the inner angular radius $\rho_{min} = 0.9\rho_{max}$; a ring with inner angular radius $\rho_{min} = \rho_{max}/2$; and a circle of radius ρ_{max} centred at the rotational pole. The solid curves are for the black body emitting spot (anisotropy parameter $h = 0$), and the dashed curves correspond to the angular pattern of the Comptonized emission with $h = -0.7$, with the magnetic moments of $\mu_{25} = 6$ and 7, respectively, and $k_A = 1$. Neutron star mass is $M = 1.4M_\odot$ and inclination $i = 60°$.

tainty comes from a strong dependence on R_{in}. Such μ is consistent with the estimation from the antipodal spot eclipse in Table 3.

For illustration, we simulate the expected dependence of the reflection amplitude on flux. For various h, we compute the flux F as a function of $\dot{M}$ at a given inclination i (as described in Appendix A). The reflection amplitude $\Re$ of course depends on the inner disc radius R_{in} (see details of calculations in Appendix B), which varies with $\dot{M}$ according to equation (14). Both flux and reflection depend on the geometry of the emitting spot. As the constraints obtained in Section 5.2 imply a rather small displacement of the spot centroid from the rotational axis, for estimating the reflection, we can neglect it and assume that magnetic dipole is aligned with the rotational axis. We consider three geometrical arrangements: a full circle centred at the rotational pole, a ring-shaped spot with the inner angular radius equal half of the outer radius and a very narrow ring. In all cases, we take the maximum spot extend from the rotation axis ρ_{max} given by the dipole formula:

$$\sin^2 \rho_{max} = \frac{R_*}{R_{in}}. \quad (17)$$

The theoretical reflection-flux dependence are shown in Fig. 11 together with the data. We see that the circular spot does not reproduce a sharp dependence of $\Re$ on flux. On the other hand, a narrow ring is more consistent with the data, as in that case at high fluxes, when the inner disc is close the star, the emission region is closer to the equator giving a strong increase in the reflection fraction. A sharp increase of reflection and its high value at high fluxes,
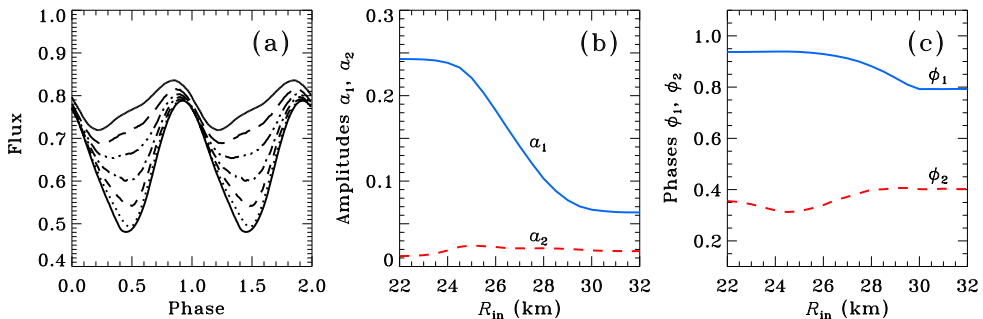
Figure 12. (a) Pulse profiles from two antipodal spots with the inner disc radius $R_{\rm in}$ varying from 24 to 30 km (from bottom to top). At $R_{\rm in} = 24$ km, the view of the antipodal spot is fully blocked by the disc, while for $R_{\rm in} = 30$ km the whole spot is visible. (b) The amplitudes and (c) the Fourier phases of the fundamental and first overtone of the pulse profiles, computed using equation (2), as a function of $R_{\rm in}$. Parameters of the simulations: neutron star mass $M = 1.4{\rm M}_\odot$ and radius $R_* = 2.5r_{\rm s} = 10.3$ km, inclination $i = 65°$, circular blackbody spots of angular radius $\rho = 30°$ centred at a colatitude $\theta = 16°$.

can also be explained if the inner disc is puffed up (see e.g. Long et al. 2005) because of the interaction with the magnetosphere.

5.6 Pulse profile variations with receding disc

As we argued above, the decreasing area of the emitting spot Σ and of the reflection amplitude $\Re$ when the flux is dropping are strong evidences of the receding disc. This is natural as the magnetosphere radius is expected to increase. Let us now look at the pulse profile variation in the course of the outburst and compare to the expected behaviour.

When the accretion rate is high, the disc should be close to the star and may fully blocks the view of the antipodal spot as we discussed in Section 5.3. The accretion flow itself can be optically thick and emission from the hotspot can be partially absorbed by the flow. Using the mass conservation equation $\dot{M} = 4\pi R_*^2 fV\rho$ (where $f \sim 0.1$ is a fraction of the stellar surface covered by the accretion stream, which corresponds to the spot area of about 100 km^2) and taking accretion velocity of $V \approx c/3$, we get the Thomson optical depth through the accretion stream at a typical distance R_* from the star:

$$\tau_{\rm T} \approx \rho R_* \frac{\sigma_{\rm T}}{m_{\rm p}} = 0.3 \frac{\dot{M}}{10^{16}{\rm g\ s}^{-1}} \frac{0.1}{f}, \qquad (18)$$

where $\sigma_{\rm T}$ is the Thomson cross-section, $m_{\rm p}$ is the proton mass. At the peak of the outburst, the bolometric flux is $\sim 4 \times 10^{-9}$ erg cm^{-2} s^{-1}, and luminosity $\sim 6 \times 10^{36}$ erg s^{-1}, which gives the accretion rate of about 2×10^{16} g s^{-1} and $\tau_{\rm T} \sim 0.6$. Thus, we see that at the peak of the outburst the flow is marginally optically thick and can produce dips in the light curves blocking the hotspot, while at lower fluxes corresponding to most of the outburst, the flow is transparent. It is possible that this effect is the cause of the observed non-sinusoidal pulse shape at the peak of the outburst (see the inset for P3–P5 in Fig. 1 and upper left-hand panel in Fig. 7). The effect is clearly largest at hard energies, which might imply that the hard Comptonized radiation is coming from a smaller area (which is easier to block) that the softer blackbody radiation.

As we discussed in the Introduction, the pulse profile during SD stage is very stable and is similar to the profiles observed during other outbursts at similar flux level. The profiles are well described by a one-spot model, implying that the disc is still rather close to the star blocking the view of the antipodal spot. The dependence

of the profiles on energy is consistent with the being produced by the different emissivity pattern of the blackbody and Comptonized radiation modified by Doppler effect (PG03). The pulse stability implies that the position of the spot at the neutron star surface does not change significantly. During the SD stage, the flux drops by a factor of 3, which corresponds to an increase of the inner disc radius by 40 per cent and corresponding increase of the outer spot angular radius by 20 per cent according to equations (14) and (17). However, these variations seem to have little impact on the pulse profile, which is expected if the centroid of the spot does not move and the spot size is smaller than the stellar radius (Poutanen & Beloborodov 2006).

With the dropping accretion rate, the disc moves sufficiently far so that the observer can see at least part of the antipodal pole. We thus expect that the pulse profiles change correspondingly. Significant variations in the pulse profile are observed from the middle of the RD phase. These changes are also reflected in sharp jumps in the phase of the fundamental (see Fig. 6). This motivates us to model theoretically variations of the pulse profiles with the varying inner disc radius.

As an illustration, we consider two circular antipodal spots emitting as a blackbody and displaced from the rotational axis by angle θ. The light curve produced by each spot is computed following techniques described in PG03 and Poutanen & Beloborodov (2006), accounting for Doppler boosting, time delays, and gravitational light bending. Now we also account for the effect of absorption by the disc of varying inner radius $R_{\rm in}$. We compute the trajectory for photons emitted by each spot element at every phase and check whether it crosses the disc plane at radius smaller or larger than $R_{\rm in}$ (see Appendix C for details). Fig. 12(a) shows the pulse profile variations as a function of the inner disc radius. Noticeable signatures of the second spot appear when $R_{\rm in} > 27$ km (for $i = 65°$), the dramatic change in the pulse profile happens when the inner radius changes from 28 to 30 km, as most of the antipodal spot then appears to our view. These fast changes are also reflected in a rather large phase shift $\Delta\phi_1 \approx 0.2$ of the fundamental, but small variations of the phase of the overtone, as shown in Fig. 12(c). This behaviour is qualitatively similar to that observed in J1808 (see Figs 6 and 7). Thus the phase jumps can be explained by changing visibility of the antipodal spot as the accretion disc recedes from the neutron star. The timing noise observed in other pulsars (Papitto et al. 2007, 2008; Riggio et al. 2008) may also have

its origin in this effect. In addition, spot wandering (Lamb et al. 2008; Patruno et al. 2009c) and variations in the spot size, shape, and emissivity pattern might be involved.

We also show the variation of the amplitudes in Fig. 12(b). We see that the fundamental amplitude decreases smoothly as R_{in} grows[3], while the amplitude of the first overtone increases slightly. Such a behaviour is consistent with that observed in Fig. 6(b) (see also fig. 1 in Hartman et al. 2009), but is not consistent with that seen in Fig. 6(a). We note, however, that in real situation the spots are probably not circular and emission is not a blackbody.

6 SUMMARY

In this paper, we present the detailed analysis of the 2002 outburst data of SAX1808. Below we summarize our findings.

(i) The phase-averaged spectra of the pulsar are roughly described by a power-law with the photon index ∼2. However, additional features are significantly detected: iron line at around 6.4 keV and Compton reflection, as well as a soft blackbody-like component below 5 keV. The dominating power-law-like component shows a clear cut-off above 50 keV, and the spectral shape is consistent with being produced by thermal Comptonization in plasma of electron temperature ∼40 keV. At the peak of the outburst, we also detect a soft excess below 3–4 keV, which we associate with the presence of the accretion disc.

(ii) The amplitude of Compton reflection is correlated with the flux. In spite of the fact, that the actual value for this amplitude is model dependent, the trend is not. This behaviour is generally consistent with the scenario where the disc recedes as the accretion rate drops and the magnetospheric radius grows. The observed sharp increase of the reflection at the highest fluxes is inconsistent with the simple circular model of the hard X-ray emitting region, but more consistent with a narrow ring. The high reflection fraction and its sharp dependence on flux might also imply that the inner disc is puffed up because of the interaction with the magnetosphere. In any case, the observations require the inner disc radius to be close to the stellar surface at the peak of the outburst.

(iii) The spectral analysis of the phase-averaged spectra also indicates a strong correlation of the apparent emitting area with the flux during the outburst. This result is largely model independent. The thermal Comptonization model with equal areas of the blackbody and Comptonization components give the area dropping from about 100 to 40 km² in the course of the outburst. The actual value for the apparent area of the emitting spot depends on the assumed ratio of the two components, and has a factor of two uncertainty.

(iv) We study the variations of the pulse profiles during the outburst and their dependence of photon energy. The profile is very stable during the SD stage and is similar to those observed during other outbursts at similar flux level. However, we observe significant variations of the profiles at both high and low fluxes.

At the P stage, the deviations are stronger at higher energies. We estimate the optical depth through the accretion stream and show that at highest fluxes, it is marginally optically thick and can absorb part of the radiation at certain pulsar phase resulting in the observed

dips close to the pulse maximum. The energy dependence of the effect seems to indicate that the Comptonizing region occupies a smaller area compared to the blackbody emitting spot.

When the flux drops below a certain level, after 2002 October 29, a secondary maximum appears in the pulse profiles. This is accompanied by the jump in the phase of the fundamental. We interpret these facts in terms of appearance of a secondary antipodal spot. We further develop a theoretical model of the pulse profile with the varying inner disc radius. We show that varying obscuration of the antipodal spot can produce phase jump and pulse profile variability similar to those observed.

(v) Our energy-resolved pulse profile analysis show that the pulse shapes at various energies are considerably different. One of the quantitative measure of this effect are the time lags, which show a complicated variability during the outburst, mostly as a result of changing the pulse profile. Relative to the 2–3 keV range, the lags are negative (i.e. high-energy emission is coming earlier than the softer emission), strongly increasing up to 7–10 keV and saturating at higher energies (see Fig. 7).

The phase-resolved spectra are well described by two major components (blackbody and Comptonized tail) with varying normalizations, representing the apparent areas of the emission components. In all outburst phases, the blackbody component are lagging the Comptonized one resulting in soft time lags and explaining their energy dependence. These facts could be explained by the model where the blackbody and Comptonization emissivity patterns are different. However, the physical nature of the very strong blackbody variability observed during the FT stage remains unknown.

(vi) The flux at the moment of significant change in the pulse profile, if associated with the appearance of the antipodal spot, can be used to put a constraint on the inner disc radius at that moment (see Table 3). It strongly depend on the unknown inclination i, giving radii from about 20 to 35 km, when i varies between 50° and 70°. The remaining uncertainty, because of the unknown stellar compactness and the size of the emitting spot, is about 20 per cent.

(vii) The information about the flux and the inner disc radius at the moment of appearance of the antipodal spot allows us to estimate the stellar magnetic dipole moment $\mu \approx (9 \pm 5) \times 10^{25} k_{A}^{-7/4}$ G cm³, where k_A is the ratio of the inner disc radius to the Alfvén radius. The uncertainties here are dominated by the unknown inclination. A similar value $\mu \approx (6 \pm 2) \times 10^{25} k_{A}^{-7/4}$ G cm³ is obtained from the fact that at the peak of the outburst, the inner disc radius is in close vicinity of the neutron star as implied by the observed high reflection fraction. The corresponding surface magnetic field (for neutron star radii 10–15 km) is $B_0 \approx (0.8 \pm 0.5) 10^8 k_{A}^{-7/4}$ G. These results are in excellent agreement with the values obtained recently from the pulsar spin-down rate (H08) assuming $k_A \sim 1$. To be consistent with the results of H08, one requires k_A to deviate from unity by not more than factor of 2, which give interesting constraints on the physics of accretion on to a magnetized star.

The analysis of the 2002 outburst of J1808 led us to the following coherent picture of the outburst. At highest observed luminosities, the accretion disc is very close to the star. It fully blocks the view of the antipodal spot and results in a high reflection fraction. The accretion stream at this stage is marginally optically thick and absorbs part of the radiation at a phase close to the pulse maximum. The behaviour of the reflection seems to indicate a rather narrow ring-like emission region and/or puffed up inner disc. As the flux drops, during the SD stage, the decreasing reflection indicates that the disc is retreating. The pulse profile is however very

---

[3] We note that for a slowly rotating star, two antipodal blackbody spots which are visible all the time produce no pulsations whatsoever (see e.g. Beloborodov 2002; Poutanen & Beloborodov 2006). Thus it is not surprising that even for a star rotating at 400 Hz, the amplitude of the fundamental decreases when both spots become visible.

stable, indicating that the accretion stream is now optically thin and the antipodal spot is still blocked from the view by the disc. During the rapid decay phase, the disc is far enough and the antipodal spot opens to the observer's view. This is accompanied by the fast changes in the pulse profile and sharp jump in the phase of the fundamental. The outlined scenario is consistent with all the data on J1808 obtained during its five outbursts.

There are still a number of uncertainties and unanswered questions. In our analysis and interpretation of the data, we have made somewhat contradicting assumptions. For spectral modelling, we have assumed a fixed inner disc radius of $10r_{\rm s}$, while the pulse variability and changes in the reflection indicate a varying radius. This is not a problem, as the obtained reflection fraction is not affected much by the assumption on the disc radius. For estimations of the inner disc radius and stellar magnetic moment from the flux at the moment of appearance of the antipodal spot, we assumed a circular emitting spot. On the other hand, the reflection-flux dependence indicates that the correct hotspot geometry might be closer to a ring. This difference does not affect the conclusions as long as the ring thickness is not much smaller than half of its radius, which is consistent with the numerical simulations (Romanova et al. 2004; Kulkarni & Romanova 2005). Our theoretical calculations of the pulse profile variations as a function of the inner radius would not be affected much in that case.

There are other effects not yet accounted in modelling. For example, we have assumed equal areas of the blackbody and Comptonization components. A dip in the high-energy profile at the peak of the outburst might indicate, however, that the high-energy component is produced in a smaller area. This discrepancy does not affect our conclusions regarding the decreasing spot area during the outburst and the estimations of the inner disc radius as we accounted for a factor of two uncertainty. However, the calculations of the pulse profile will be affected, because the retreating disc would affect the pulse profiles at low and high energies in a different way. This is an interesting problem for further studies. In order to reduce the uncertainties still present in the model and to get better constraints on geometrical parameters (e.g. inner disc radius), it would be useful to know the exact spot shape as a function of the magnetic inclination and the inner disc radius. A progress in this direction is possible with the detailed MHD simulations of the accretion disc-magnetosphere interaction (see e.g. Romanova et al. 2004; Kulkarni & Romanova 2005). A further progress would also require a detailed model of the shocked region, where the high-energy radiation is produced, together with the radiative transfer modelling in order to predict the angular emission pattern from first principles.

REFERENCES

Arnaud K. A., 1996, in Jakoby G. H., Barnes J., eds, ASP Conf. Ser. Vol. 101, Astronomical Data Analysis Software and Systems V. Astron. Soc. Pac., San Francisco, p. 17

Beloborodov A. M., 2002, ApJ, 566, L85

Bildsten L., Chakrabarty D., 2001, ApJ, 557, 292

Burderi L., Di Salvo T., Menna M. T., Riggio A., Papitto A., 2006, ApJ, 653, L133

Chakrabarty D., Morgan E. H., 1998, Nature, 394, 246

Cui W., Morgan E. H., Titarchuk L. G., 1998, ApJ, 504, L27

Deloye C. J., Heinke C. O., Taam R. E., Jonker P. G., 2008, MNRAS, 391, 1619

Falanga M. et al., 2005a, A&A, 436, 647

Falanga M. et al., 2005b, A&A, 444, 15

Falanga M., Poutanen J., Bonning E. W., Kuiper L., Bonnet-Bidaud J. M., Goldwurm A., Hermsen W., Stella L., 2007, A&A, 464, 1069

Falanga M., Titarchuk L., 2007, ApJ, 661 1084

Galloway D. K., Cumming A., 2006, ApJ, 652, 559

Galloway D. K., Chakrabarty D., Morgan E. H., Remillard R. A., 2002, ApJ, 576, L137

Galloway D. K., Markwardt C. B., Morgan E. H., Chakrabarty D., Strohmayer T. E., 2005, ApJ, 622, L45

Gierliński M., Done C., Barret D., 2002, MNRAS, 331, 141

Gierliński M., Poutanen J., 2005, MNRAS, 359, 1261

Giles A. B., Hill K. M., Greenhill J. G., 1999, MNRAS, 304, 47

Gilfanov M., Revnivtsev M., Sunyaev R., Churazov E., 1998, A&A, 338, L83

Hartman J. M. et al., 2008a, ApJ, 675, 1468 (H08)

Hartman J. M., Watts A., Chakrabarty D., 2008b, ApJ, 697, 2102

Hartman J. M., Patruno A., Chakrabarty D., Markwardt C. B., Morgan E. H., van der Klis M., Wijnands R., 2009, ApJ, 702, 1673

Homer L., Charles P. A., Chakrabarty D., van Zyl L., 2001, MNRAS, 325, 1471

Illarionov A. F., Sunyaev R. A., 1975, A&A, 39, 185

in 't Zand J. J. M., Heise J., Muller J. M., Bazzano A., Cocchi M., Natalucci L., Ubertini P., 1998, A&A, 331, 25

Jahoda K., Markwardt C. B., Radeva Y., Rots A. H., Stark M. J., Swank J. H., Strohmayer T. E., Zhang W., 2006, ApJS, 163, 401

Kluźniak W., Rappaport S., 2007, ApJ, 671, 1990

Krimm H. A. et al., 2007, ApJ, 668, L147

Kulkarni A. K., Romanova M. M., 2005, ApJ, 633, 349

Lamb F. K., Boutloukos S., Van Wassenhove S., Chamberlain R. T., Lo K. H., Clare A., Yu W., Miller M. C., 2008, ApJ, submitted (arXiv:0808.4159)

Leahy D. A., Morsink S. M., Cadeau C., 2008, ApJ, 672, 1119

Long M., Romanova M. M., Lovelace R. V. E., 2005, ApJ, 634, 1214

Magdziarz P., Zdziarski A. A., 1995, MNRAS, 273, 837

Papitto A., di Salvo T., Burderi L., Menna M. T., Lavagetto G., Riggio A., 2007, MNRAS, 375, 971

Papitto A., Menna, M. T., Burderi L., di Salvo T., Riggio A., 2008, MNRAS, 383, 411

Patruno A., Rea N., Altamirano D., Linares M., Wijnands R., van der Klis M., 2009a, MNRAS, 396, L51

Patruno A., Watts A. L., Klein-Wolt M., Wijnands R., van der Klis M., 2009b, ApJ, submitted (arXiv:0904.0560)

Patruno A., Wijnands R., van der Klis M., 2009c, ApJ, 698, L60

Poutanen J., 2006, Adv. Space Res., 38, 2697

Poutanen J., 2008, in Wijnands R., Altamirano D., Soleri P., De-

genaar N., Rea N., Casella P., Patruno A., Linares M., eds, AIP Conf. proc. 1068, A decade of accreting X-ray millisecond pulsars, AIP, Melville, p. 77

Poutanen J., Beloborodov A. M., 2006, MNRAS, 373, 836

Poutanen J., Gierliński M., 2003, MNRAS, 343, 1301 (PG03)

Poutanen J., Svensson R., 1996, ApJ, 470, 249

Poutanen J., Nagendra K. N., Svensson R., 1996, MNRAS, 283, 892

Psaltis D., Chakrabarty D., 1999, ApJ, 521, 332

Rappaport S. A., Fregeau J. M., Spruit H., 2004, ApJ, 606, 436

Riggio A., di Salvo T., Burderi L., Menna, M. T., Papitto A., Iaria R., Lavagetto G., 2008, ApJ, 678, 1273

Romanova M. M., Ustyugova G. V., Koldoba A. V., Lovelace R. V. E., 2004, ApJ, 610, 920

Spruit H. C., Taam R. E., 1993, ApJ, 402, 593

van Straaten S., van der Klis M., Wijnands J., 2005, ApJ, 619, 455

Viironen K., Poutanen J., 2004, A&A, 426, 985

Wang Z. et al., 2001, ApJ, 563, L61

Wijnands R., 2006, in Lowry J. A., ed., Trends in Pulsar Research. Nova Science Publishers, New York, p. 53

Wijnands R., van der Klis M., 1998, Nature, 394, 344

APPENDIX A: FLUX FROM A RING-SHAPED SPOT

For approximate calculation of the flux and reflection, we neglect magnetic inclination, and consider the emitting region in the form of a ring symmetric around the stellar rotational axis. The boundaries of the ring are described by colatitudes $\rho_{\min}$ and $\rho_{\max}$. We assume that the light from the antipodal ring below the equator is blocked by the accretion disc.

Let us first compute the observed flux from the ring. Consider a surface element $dS = R_*^2 d\cos\theta d\phi$ at a slowly rotating star. We neglect here the effects related to rapid rotation because the flux averaged over the ring is affected by them very little. The element position is described by the unit vector $\boldsymbol{n} = (\sin\theta\cos\phi, \sin\theta\sin\phi, \cos\theta)$ that points to it from the star center. Let the unit vector along the line of sight be $\boldsymbol{k} = (\sin i, 0, \cos i)$ with i being the inclination. The angle between $\boldsymbol{n}$ and the line of sight is denoted by ψ so that

$$\cos\psi = \boldsymbol{k} \cdot \boldsymbol{n} = \cos i \, \cos\theta + \sin i \, \sin\theta \, \cos\phi. \tag{A1}$$

The observed flux from this surface element in approximation of Beloborodov (2002) for light bending is (see PG03; Poutanen & Beloborodov 2006):

$$dF(i, \theta, \phi) = (1-u)^2 \frac{dS}{D^2} I_*(\alpha) \cos\alpha, \tag{A2}$$

where the angular distribution of intensity at the stellar surface $I_*(\alpha)$ is assumed to follow the dependence (13), α is the angle of the photon emission relative to the stellar normal related to other parameters as

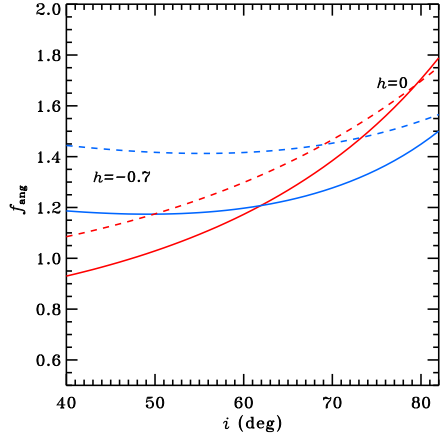$$\cos\alpha \approx u + (1-u)\cos\psi = Q + U\cos\phi, \tag{A3}$$

with Q and U given by equation (4).

Integrating (A2) over the ring surface, we get

$$F(i) = I_0 \frac{\Sigma}{D^2}(1-u)^2 \zeta \tag{A4}$$

where $\Sigma = R_*^2 2\pi(\mu_2 - \mu_1)$ is the ring area, $\mu_1 = \cos\rho_{\max}$, $\mu_2 = \cos\rho_{\min}$, and

$$\zeta = u + \frac{1-u}{2}(\mu_1 + \mu_2)\cos i$$

Figure A1. The anisotropy correction factor as a function of inclination computed from equations (A5) and (A7). The solid curves correspond to stellar parameters $M = 1.4 M_\odot$ and $R_* = 12$ km, while the dashed curves to $M = 1.7 M_\odot$ and $R_* = 11$ km. More inclined curves are for blackbody-like radiation pattern with $h = 0$ and almost horizontal curves are for $h = -0.7$. Here a circular spot centred at the rotational pole with $R_\infty = 5$ km is assumed.

$$+ \quad h\left[u^2 + u(1-u)(\mu_1 + \mu_2)\cos i + \frac{1}{2}(1-u)^2\sin^2 i\right]$$

$$+ \quad h\frac{1}{6}(1-u)^2(3\cos^2 i - 1)(\mu_1^2 + \mu_1\mu_2 + \mu_2^2), \tag{A5}$$

which is strictly valid when the whole ring is visible.

The total emitted luminosity at the stellar surface (for two symmetric about equator, ring-shaped emitting regions) is

$$L_* = 2\Sigma \, 2\pi \int_0^1 I_*(\alpha)\cos\alpha \, d\cos\alpha = 2\Sigma \, I_0 \, 2\pi\left(\frac{1}{2} + \frac{h}{3}\right), \tag{A6}$$

and the total luminosity at infinity $L = (1-u)L_*$. We thus get the anisotropy correction factor relating the observed flux to the luminosity in equation (12):

$$f_{\text{ang}} = \frac{L}{4\pi D^2 F(i)} = \frac{\frac{1}{2} + \frac{h}{3}}{(1-u)\zeta}. \tag{A7}$$

As an example, let us consider a circular spot (i.e. $\rho_{\min} = 0$) centred at the rotational pole. For a given apparent spot size R_∞, we compute the physical spot angular size $\rho_{\max} = \rho$ from equation (7). The dependence of f_{ang} on the inclination is shown in Fig. A1. Variations of R_∞ within 3–7 km, lead to only 2–3 per cent changes in f_{ang}.

APPENDIX B: REFLECTION FROM THE ACCRETION DISC

Let us now estimate the reflection amplitude expected for the emitting ring. By definition, it is given by the ratio of the luminosity reflected from the disc to that directly observed:

$$\Re = \frac{L_{\text{refl}}}{4\pi D^2 F(i)} = f_{\text{ang}} P_{\text{refl}}, \tag{B1}$$

where $P_{\rm refl}$ is the fraction of emitted photons that hit the disc surface at radii $r > R_{\rm in}$.

Because of the axial symmetry, the surface element in a ring is described only by colatitude with the corresponding unit vector pointing towards it, $\boldsymbol{n} = (\sin\theta, 0, \cos\theta)$. The photon direction (in the frame related to the element, with z-axis along its normal) is described by two angles, polar angle α and azimuth φ measured from the southern direction of the meridian. At large distances from the star the photon direction is given by vector $\boldsymbol{k}$. For a given α, the angle ψ its makes to $\boldsymbol{n}$ can be obtained from equation (A3). Using spherical trigonometry it is easy to show that

$$\boldsymbol{k} = \begin{pmatrix} \cos\psi\sin\theta + \sin\psi\cos\theta\cos\varphi \\ \sin\psi\sin\varphi \\ \cos\psi\cos\theta - \sin\psi\sin\theta\cos\varphi \end{pmatrix}. \tag{B2}$$

The necessary condition that the trajectory crosses the disc is

$$\cos\psi\cos\theta < \sin\psi\sin\theta\cos\varphi, \tag{B3}$$

that translates to the limits on α and φ. In the stellar polar region $\sin\theta < \kappa \equiv u/(1-u)$ (existing if $u < 1/2$), the limits are

$$\begin{array}{ll} 0 < \varphi < 2\pi, & \text{if } 0 < \cos\alpha < \cos\alpha_-, \\ \cos\varphi > \cos\varphi_0, & \text{if } \cos\alpha_- < \cos\alpha < \cos\alpha_+, \end{array} \tag{B4}$$

where $\cos\alpha_\pm = u \pm (1-u)\sin\theta$ and $\cos\varphi_0 = \cot\psi\cot\theta$. Thus photons emitted close to the surface will always cross the disc plane irrespectively of the azimuth, and those emitted close to the zenith $\cos\alpha > \cos\alpha_+$ do not cross it at all. In the intermediate case, photons have to be emitted in the southward direction to cross the disc plane. Outside the polar region $\sin\theta > \kappa$, the limits are

$$\cos\varphi > \cos\varphi_0, \quad \text{if } 0 < \cos\alpha < \cos\alpha_+. \tag{B5}$$

Now let us compute the radius where the photon trajectory crosses the disc plane. The unit vector along the intersection line of the disc and photon trajectory planes is

$$\boldsymbol{d} = \frac{(\cos\varphi,\ \cos\theta\sin\varphi,\ 0)}{\sqrt{1 - \sin^2\theta\sin^2\varphi}}, \tag{B6}$$

and thus the angle it makes with $\boldsymbol{k}$ is given by

$$\cos\psi_{\rm d} = \boldsymbol{d}\cdot\boldsymbol{k} = \frac{\sin\psi\cos\theta + \cos\psi\sin\theta\cos\varphi}{\sqrt{1 - \sin^2\theta\sin^2\varphi}}. \tag{B7}$$

For the given emission angle α and the impact parameter

$$b = R_* \sin\alpha/\sqrt{1-u}, \tag{B8}$$

an approximate photon trajectory is (Beloborodov 2002):

$$r(\psi) = \left[\frac{r_{\rm s}^2(1-\cos\psi)^2}{4(1+\cos\psi)^2} + \frac{b^2}{\sin^2\psi}\right]^{1/2} - \frac{r_{\rm s}(1-\cos\psi)}{2(1+\cos\psi)}. \tag{B9}$$

Substituting here $\psi = \psi_{\rm d}$, we obtain the disc radius, where photon trajectory crosses the disc plane.

Calculation of the reflected fraction now involves simple integration over the ring area (upper hemisphere) and photon emission angles:

$$P_{\rm refl} = \frac{4\pi R_*^2}{L_*}\int {\rm d}\cos\theta \int I_*(\alpha)\cos\alpha\,{\rm d}\cos\alpha \int {\rm d}\varphi\, H(r[\psi_{\rm d}] - R_{\rm in}), \tag{B10}$$

where H is the Heaviside step function and the limits on α and ϕ are given by conditions (B4) and (B5).

APPENDIX C: ANTIPODAL SPOT ECLIPSE BY THE ACCRETION DISC

The pulse profiles produced by the spots on a rapidly rotating star are computed following techniques described in PG03 and Poutanen & Beloborodov (2006). However, the effect of the accretion disc needs to be accounted for, because the photons emitted by the lower antipodal spot can be absorbed on the way to the observer by the disc. We divide the spot into a number of elements and compute the light curve from each of it independently. The position of each element can be described, as in Appendix A, by the unit vector $\boldsymbol{n} = (\sin\theta\cos\phi, \sin\theta\sin\phi, \cos\theta)$, where now $\theta > \pi/2$. The angle ψ this vector makes with the direction to the observer $\boldsymbol{k} = (\sin i, 0, \cos i)$ is given by equation (A1).

The element in principle (without the disc) is visible to the observer at all phases if $\cos(\theta + i) > -\kappa$, not visible at all if $\cos(\theta - i) < -\kappa$, and visible only when $\cos\phi > -Q/U$ if $\cos(\theta + i) < -\kappa < \cos(\theta - i)$ (see Poutanen & Beloborodov 2006, for details). If the element with the given (θ, ϕ) can be visible, we substitute ψ given by equation (A1) to the light bending formula (A3) getting the emission angle α and the impact parameter b using equation (B8), which fully define the photon trajectory. Its plane intersects with the disc plane along the line described by the unit vector

$$\boldsymbol{d} = \frac{(-\cos\theta\sin i + \cos i\sin\theta\cos\phi,\ \sin\theta\cos i\sin\phi,\ 0)}{\sqrt{\cos^2 i + \cos^2\theta - 2\cos i\cos\theta\cos\psi}}. \tag{C1}$$

The angle it makes with $\boldsymbol{k}$ is

$$\cos\psi_{\rm d} = \boldsymbol{d}\cdot\boldsymbol{k} = \frac{\cos i\cos\psi - \cos\theta}{\sqrt{\cos^2 i + \cos^2\theta - 2\cos i\cos\theta\cos\psi}}. \tag{C2}$$

We find the radius, where trajectory crosses the disc $r(\psi_{\rm d})$, using equation (B9). If it is larger than $R_{\rm in}$, the element is invisible.

Paper V

Poutanen J., Ibragimov A., Annala M.
On the nature of pulse profile variations and timing noise in accreting X-ray millisecond pulsars.

ON THE NATURE OF PULSE PROFILE VARIATIONS AND TIMING NOISE
IN ACCRETING MILLISECOND PULSARS

Juri Poutanen, Askar Ibragimov[1] and Marja Annala
Astronomy Division, Department of Physics, PO Box 3000, FIN-90014 University of Oulu, Finland

ABSTRACT

Timing noise is known to be present in the data on accretion-powered millisecond pulsars (AMP). The noise mostly appears as irregular pulse phase jumps on timescales from hours to weeks around a mean trend implied by ephemeris. Besides that, a large systematic drift is observed for example in the first discovered AMP SAX J1808.4−3658. To study the origin of the timing noise, we use here the data for the 2002 outburst of SAX J1808.4−3658, which has the best coverage. By directly fitting the pulse profile shapes with the theoretical model for AMP pulses, which includes the effect of partial screening of the antipodal emitting spot by the accretion disk, we are able to quantify the variations in the position of the spot centroid, its emissivity pattern and the inner accretion disk radius. We show that the main parameters of the emitting spot such as its mean latitude and azimuth as well as the emissivity pattern change irregularly causing small shifts in pulse phase. We stress that the sharp systematic shift in Fourier phases, observed together with the strong changes in the pulse form, can only be explained by the variations of the visibility of the antipodal spot associated with the receding accretion disk.

Subject headings: accretion, accretion disks – methods: data analysis – pulsars: individual: SAX J1808.4−3658 – stars: neutron – X-rays: binaries

1. INTRODUCTION

The first accreting millisecond X-ray pulsar (hereafter AMP) SAX J1808.4−3658 was discovered in 1998 (Wijnands & van der Klis 1998; Chakrabarty & Morgan 1998). Since then, eight objects of this class have been discovered, with frequencies in range 191–599 Hz (Poutanen 2006; Krimm et al. 2007). SAX J1808.4−3658 (with the rotational frequency of 401 Hz) is the best observed AMP to date with five registered outbursts since 1998.

Most of AMPs show rather simple sine-like profiles. This is consistent with the fact that one sees only one hotspot, because the accretion disk extends very close to the stellar surface. The general stability of the pulse profile allows to obtain a high photon statistics and to use the average pulse profile to get constraints on the neutron star mass-radius relation and the equation of state (Poutanen & Gierliński 2003). However, sometimes the profiles do show variations. At high fluxes, the absorption in the accretion column can cause a deep observed around the pulse maximum. At low fluxes, the pulsar follows amazingly similar evolution in 2002, 2005 and 2008 outbursts (Hartman et al. 2008, 2009) showing the profile skewed to the left and sometimes clearly double-peaked. This is accompanied by a large (0.2 cycles) jump in the phase of the fundamental (see Burderi et al. 2006; Hartman et al. 2008; Ibragimov & Poutanen 2009, hereafter IP09). IP09 proposed that strong pulse profile variations results from the appearance of the secondary antipodal spot to our view when the magnetospheric radius increases and the accretion disk recedes from the neutron star with the dropping accretion rate. This interpretation is supported by the fact that the amount of Compton reflection in the spectra is decreasing during the outburst.

Besides these noticeable profile changes, the timing noise is known to be present in AMP data, when the measured pulse phase delays show fluctuations around a mean trend implied

by ephemeris with timescales from hours to weeks (Papitto et al. 2007, 2008; Riggio et al. 2008; Patruno et al. 2009). Random phase irregularities can be imagined to appear because of changes in the geometry and position of the hotspots (Lamb et al. 2008; Patruno et al. 2009) or the emissivity pattern (Poutanen 2008). However, it is difficult to imagine that these can cause qualitative changes in the pulse form (such as transformation of the single-peaked profile to a double-peaked) and correspondingly large phase shifts. On the other hand, the visibility of the secondary spot might change even with small fluctuations of the accretion rate producing timing noise.

In this Letter, we directly fit the pulse profiles of SAX J1808.4−3658 during its 2002 outburst with the theoretical model for AMP pulses (Poutanen & Gierliński 2003; Viironen & Poutanen 2004; Poutanen & Beloborodov 2006) including the effect of partial screening of the antipodal emitting spot by the accretion disk. We aim at quantifying the variations in the position of the hotspot centroid, its emissivity pattern and the inner accretion disk radius, and determining the causes of the variations in the pulse shape and the timing noise.

2. MODEL

We assume that a magnetic dipole is displaced by angle θ from the rotational axis. The accretion disk is disrupted by the stellar magnetic field at some radius which scales with the classical Alfvén radius and is a function of the accretion rate and the neutron star magnetic moment. Matter following magnetic field lines hits the stellar surface making two antipodal hot spots. For the dipole field, the outer spot edge is displaced from the magnetic pole by an angle ρ:

$$\sin \rho = \cos \theta \sqrt{\frac{R}{r_{\mathrm{in}}}}. \qquad (1)$$

where R is the neutron star radius. This gives us a rough estimation of the spot size as a function of r_{in}. The spot size and shape depend on the magnetic inclination and the inner disk radius in a complicated fashion. When $\theta \ll 1$ and $r_{\mathrm{in}} \gg R$,

Electronic address: [juri.poutanen,askar.ibragimov,marja.annala]@oulu.fi
[1] also at Kazan State University, Astronomy Department, Kremlyovskaya 18, 420008 Kazan, Russia
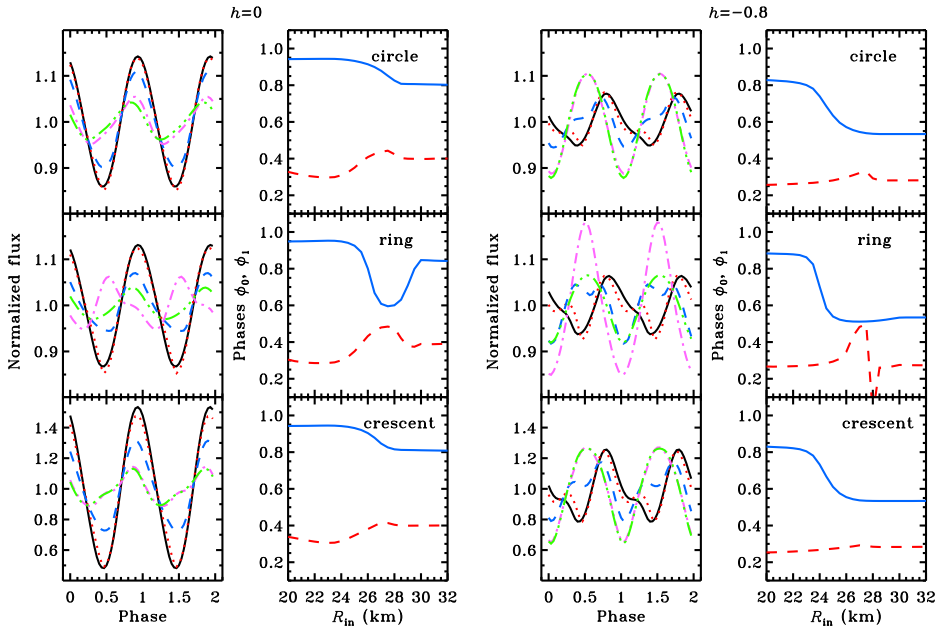
FIG. 1.— Pulse profiles and the corresponding Fourier phases for two antipodal spots and two cases of emissivity pattern $h = 0$ and $h = -0.8$ as a function of the inner disk radius. The pulse profiles are shown for r_{in} varying (with step 2.5 km) from 20 to 30 km (solid, dotted, dashed, dot-dashed and triple-dot-dashed curves, respectively). At lowest radii, the view of antipodal spot is almost fully blocked by the disk, while at highest radii, the whole spot is visible. Fourier phases of the fundamental and overtone given by equation (2) are shown in 2nd and 4th column of panels by solid and dashed curves. Three panels from top to bottom correspond to the filled circle, the ring and the crescent spot geometries, respectively. Stellar parameters: $M = 1.4 M_\odot$, $R = 2.5 r_s$, $i = 65°$, $\theta = 10°$. The spot angular size ρ is given by equation (1), and for the ring and crescent geometries, the inner radius is $\rho/\sqrt{2}$.

the hotspot is nearly a circle. When the disk is close to the star, the spot becomes a ring-like because the matter accretes via field lines penetrating the disk within a narrow ring. If the magnetic dipole is sufficiently inclined, the spot becomes a crescent-like (Romanova et al. 2004; Kulkarni & Romanova 2005). Thus we consider three simple geometries which incorporate all these cases: (1) a homogeneously emitting circle, (2) a ring, and (3) a crescent, which we approximate as a part of the ring.

For a given spot geometry and stellar parameters, we then compute the pulse profile. We account for general and special relativity effects (such as gravitational light bending, redshift, aberration, Doppler boosting), and time delays. We also need to specify the spectral shape and the angular emissivity pattern of radiation from the spot. We follow the general methodology as described in details in Poutanen & Gierliński (2003); Viironen & Poutanen (2004); Poutanen & Beloborodov (2006). As the accretion disk might be rather close to the stellar surface, we account also for the absorption of the disk as described in Appendix C of IP09. We also approximate the theoretical profile by a sum of two harmonics:

$$F(\phi) = \overline{F}\{1 + a_0 \cos[2\pi(\phi - \phi_0)] + a_1 \cos[4\pi(\phi - \phi_1)]\}, \quad (2)$$

with the phases and relative amplitudes computed using discrete Fourier transforms.

For the illustration, we assume the following parameters: $M = 1.4 M_\odot$, $R = 2.5 r_s$ (where $r_s = 2GM/c^2$ is the Schwarzschild radius), inclination $i = 65°$, magnetic inclination $\theta = 10°$ and a spot of angular radius ρ given by equation (1). The spectrum and angular distribution of radiation at the

stellar surface is given by the expression

$$I(\alpha) = I_0(1 + h\cos\alpha)E^{-(\Gamma - 1)}, \quad (3)$$

where $\Gamma = 2$ is the spectral index, α is the angle relative to the stellar normal, and h is the anisotropy parameter. For a ring- and a crescent-like spots we assume the spot thickness of $8°$, and for the crescent we consider half a ring furthest away from the rotational pole similar to what is obtained in MHD simulations (Romanova et al. 2004; Kulkarni & Romanova 2005).

Fig. 1 shows the pulse profile variations for as a function of the inner disc radius for these three geometries and emissivities $h = 0$ (blackbody) and $h = -0.8$ (corresponding to the angular distribution of radiation multiply scattered in an optically thin slab, see Poutanen & Gierliński 2003; Viironen & Poutanen 2004). The noticeable signatures of the second spot appears when $r_{in} > 20$ km, the dramatic change in the pulse profile happens when the inner radius changes from 24 to 26 km, as most of the antipodal spot then appears to our view. These fast changes are also reflected in a rather large phase shift ~ 0.2 of the fundamental, but generally smaller variations of the phase of the overtone, similar to what is observed in SAX J1808.4−3658 (see figs 6 and 7 in IP09).

While blackbody pulse shapes are rather smooth, the emissivity pattern ($h < 0$) lead to the presence of narrower features and more pronounced secondary maxima; the ring spot generates sharper features in the lightcurves and more rapid evolution with r_{in} comparing to the circle case. The crescent gives higher variability amplitude, because of its larger displacement with respect to the rotational pole of the star. However, the initial (when only one spot is visible) and the final
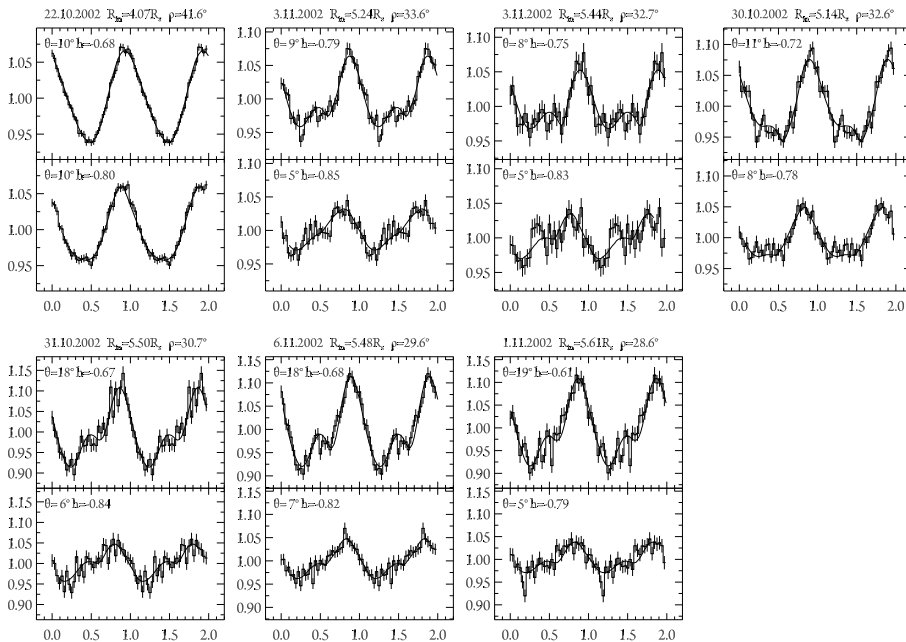
Fig. 2.— Pulse profiles of SAX J1808.4−3658, observed during October–November 2002 outburst, in order of decreasing flux. Top and bottom panels correspond to the profiles in 3.7–5.7 keV and 9.8–23.2 keV energy bands, respectively. The corresponding best-fit models parameters are indicated. The solid curves give the modeled pulse shapes (see Sect. 3).

(when both spots are visible) pulse profiles depend very little on the spot geometry, and changes of the Fourier phases with inner radius are also very similar.

3. COMPARISON WITH THE OBSERVED PROFILE EVOLUTION

Now we make a detailed comparison of the theoretical pulse profiles predicted by the model to the data on SAX J1808.4−3658 obtained during its 2002 outburst. *RXTE* followed the source during the period October 15 – November 26, 2002 obtaining the best coverage for any AMP. The data and their reduction are described in details in IP09.

At the peak stage (see H08 and IP09 for the definition of outburst stages), profiles are nearly sinusoidal with a deep noticeable at the pulse maximum at energies above 10 keV. This might be caused by absorption in the accretion column (see IP09) complicating the pulse modeling, and therefore we do not consider this stage in the paper. During the slow decay stage on October 17–27, the pulse profile, slightly skewed to the right (see Fig. 2a), was extremely stable, in spite of the fact that the flux was changing by a factor of four. At the rapid drop stage (October 27 – November 1) the flux fell down rapidly, while the pulse profile was evolving: on October 29 the secondary maximum – a signature of the second hot spot – becomes pronounced and after October 30 the pulse became skewed to the left and the secondary maximum shifted to the rising part of the main peak. The profile remains double-peaked till the end of the outburst (flaring tail stage), slightly varying in shape. On Fig. 2 we present a subset of the observed pulse shapes.

The pulse profiles can be rather well described by a sum of two Fourier harmonics, fundamental and overtone, given by equation (2). The dramatic variability of the pulse profiles is reflected in a phase shift of the fundamental by 0.2 observed within a couple of days around October 30, while the phase of the overtone did not change significantly (Burderi et al. 2006; Hartman et al. 2008; IP09). The behavior of the pulse phases and amplitudes varies with energy: for example, the amplitude of the high-energy pulse decreases with time, while the pulsation amplitude at low energies noticeably increases (IP09). The reason for that most probably lies in the fact that the soft blackbody that contributes significantly to the total spectrum below ∼7 keV (Gierliński et al. 2002; Poutanen & Gierliński 2003; IP09), might be produced in a region displaced from the accretion shock where the hard Comptonized tail is produced.

For comparison of the model described in Sect. 2 to the data, we consider a filled circle geometry of the spot. We fit simultaneously the pulse profiles in two broad energy bands 3.7–5.7 and 9.8–23.2 keV. The second band is dominated by the Comptonized components, while the blackbody contributes at the lower-energy band. We consider a possibility that photons at these energies can be produced predominantly at different positions, determined by the colatitude $\theta_{s,h}$ and azimuth $\varphi_{s,h}$ of the spot center. The angular emissivities of the radiation in the two bands are described by equation (3) with parameters $h_{s,h}$. The inner disk radius r_{in} of course is the same for both energies at each moment of the outburst, and the spot size is given by equation (1). The best-fit parameters are given in Table 1 and the pulse profiles are shown in Fig. 2.

We see that the model describes the pulse profiles rather

TABLE 1
Best fit parameters

Date	F[a]	$\theta_{\rm s}$[b] deg	$\theta_{\rm h}$[b] deg	$\varphi_{\rm s}$[c]	$\varphi_{\rm h}$[c]	$h_{\rm s}$[d]	$h_{\rm h}$[d]	$r_{\rm in}/r_{\rm s}$[e]	χ^2/d.o.f.[f]
Oct 22	15.6	10.2	10.8	0.10	0.13	-0.68	-0.80	4.07	34/56
Nov 3	4.2	9.7	5.2	0.14	0.10	-0.79	-0.85	5.24	80/56
Nov 3	3.6	8.2	5.4	0.15	0.06	-0.75	-0.83	5.44	62/56
Oct 30	3.5	11.6	8.1	0.13	0.08	-0.72	-0.78	5.14	86/56
Oct 31	2.4	18.4	6.6	0.13	0.09	-0.67	-0.84	5.50	92/56
Nov 6	1.9	18.1	7.0	0.15	0.12	-0.68	-0.82	5.48	61/56
Nov 1	1.5	19.3	5.7	0.12	0.11	-0.61	-0.79	5.61	74/56

NOTE. — The parameters of the model corresponding to the fits presented in Fig. 2, order according to the decreasing flux. We assume that the spots dominating at two different energy bands 3.7–5.7 keV and 9.8–23.2 keV (with the corresponding indices s and h) have a different location at the stellar surface with their centroids having coordinates θ and ϕ.

[a] Flux in 2.5–25 keV band in units 10^{-10} erg cm^{-2} s^{-1}.
[b] Colatitude of the spot center.
[c] Azimuth of the spot center (fraction of period).
[d] Anisotropy parameter at a given energy.
[e] Inner disk radius in units of $r_{\rm s}$.
[f] Reduced χ^2 and number of degrees of freedom.

well, except some narrow features. In general, the resulting $r_{\rm in}$ increases when the flux decreases, but not monotonically. We also see some variations in positions of the spot centroids, both in latitudinal and in azimuthal directions. These changes can be associated with the timing noise (i.e. erratic variations of the Fourier phases). However, the jump in the fundamental phase observed around October 30, which happened together with the dramatic change in the pulse profile, can be explained only by the appearance of the antipodal spot when the inner disk radius is at about 25 km.

The origin of some discrepancies between the model and the data probably lies in a simplified spot geometry assumed here, assumption of the equal area spots producing emission are different energies as well as in a possible inhomogeneity of the disk, which might cause narrow absorption features at some phases. Likely an important issue is the spot shape, as demonstrated in Sect. 2, the pulse shapes do depend considerably on that.

4. CONCLUSIONS

We have developed a model of pulse profile formation in AMPs by accounting for the partial screening of the antipodal emitting spot by the accretion disk. We have demonstrated that the appearance of the antipodal spot leads to sharp changes in the pulse profile and corresponding jump in Fourier phases. By directly fitting the model to the pulse shapes of SAX J1808.4−3658 observed during its 2002 outburst, we were able to quantify the variations in the position of the spot centroids, their emissivity pattern and the inner accretion disk radius. We argue that these variations are the main source of the timing noise observed in AMPs. We stress that the sharp jumps in Fourier phases, observed together in the strong changes in the pulse form, can only be explained by the variations of the visibility of the antipodal spot associated with the receding accretion disk. Further progress in detailed understanding of the accretion process onto a millisecond pulsar is possible by using the exact shape of the emitting spots obtained from the numerical simulations to fit the data.

REFERENCES

Burderi, L., Di Salvo, T., Menna, M. T., Riggio, A., & Papitto, A. 2006, ApJ, 653, L133
Chakrabarty, D. & Morgan, E. H. 1998, Nature, 394, 346
Gierliński, M., Done, C., & Barret, D. 2002, MNRAS, 331, 141
Hartman, J. M., Patruno, A., Chakrabarty, D., Kaplan, D. L., Markwardt, C. B., Morgan, E. H., Ray, P. S., van der Klis, M., & Wijnands, R. 2008, ApJ, 675, 1468
Hartman, J. M., Patruno, A., Chakrabarty, D., Markwardt, C. B., Morgan, E. H., van der Klis, M., & Wijnands, R. 2009, ApJ, 702, 1673
Ibragimov, A. & Poutanen, J. 2009, MNRAS, in press (arXiv:0901.0073)
Krimm, H. A., et al. 2007, ApJ, 668, L147
Kulkarni, A. K. & Romanova, M. M. 2005, ApJ, 633, 349
Lamb, F. K., Boutloukos, S., Van Wassenhove, S., Chamberlain, R. T., Lo, K. H., Clare, A., Yu, W., & Miller, M. C. 2008, ApJ, submitted (arXiv:0808.4159)
Papitto, A., di Salvo, T., Burderi, L., Menna, M. T., Lavagetto, G., & Riggio, A. 2007, MNRAS, 375, 971

Papitto, A., Menna, M. T., Burderi, L., di Salvo, T., & Riggio, A. 2008, MNRAS, 383, 411
Patruno, A., Wijnands, R., & van der Klis, M. 2009, ApJ, 698, L60
Poutanen, J. 2006, Adv. Space Res., 38, 2697
Poutanen, J. 2008, in A decade of accreting X-ray millisecond pulsars, AIP Conf. Ser. 1068, ed. R. Wijnands et al. (Melville, NY: AIP), 77
Poutanen, J. & Beloborodov, A. M. 2006, MNRAS, 373, 836
Poutanen, J. & Gierliński, M. 2003, MNRAS, 343, 1301
Riggio, A., Di Salvo, T., Burderi, L., Menna, M. T., Papitto, A., Iaria, R., & Lavagetto, G. 2008, ApJ, 678, 1273
Romanova, M. M., Ustyugova, G. V., Koldoba, A. V., & Lovelace, R. V. E. 2004, ApJ, 610, 920
Viironen, K. & Poutanen, J. 2004, A&A, 426, 985
Wijnands, R. & van der Klis, M. 1998, Nature, 394, 344